TU Delft

Delft University of Technology

Applied and fundamental studies of vibrating 2D membranes

Lee, M.

DOI
10.4233/uuid:92e07324-cb8b-43fa-86d5-8bfa6eb6e7b1

Publication date
2021

Document Version
Final published version

Citation (APA)
Lee, M. (2021). *Applied and fundamental studies of vibrating 2D membranes*. [Dissertation (TU Delft), Delft University of Technology]. https://doi.org/10.4233/uuid:92e07324-cb8b-43fa-86d5-8bfa6eb6e7b1

Important note
To cite this publication, please use the final published version (if applicable).
Please check the document version above.

Copyright
Other than for strictly personal use, it is not permitted to download, forward or distribute the text or part of it, without the consent of the author(s) and/or copyright holder(s), unless the work is under an open content license such as Creative Commons.

Takedown policy
Please contact us and provide details if you believe this document breaches copyrights.
We will remove access to the work immediately and investigate your claim.

This work is downloaded from Delft University of Technology.
For technical reasons the number of authors shown on this cover page is limited to a maximum of 10.

Applied and fundamental studies of vibrating 2D membranes

Applied and fundamental studies of vibrating 2D membranes

Dissertation

for the purpose of obtaining the degree of doctor
at Delft University of Technology
by the authority of the Rector Magnificus, prof. dr. ir. T. H. J. J. van der Hagen
chair of the Board for Doctorates
to be defended publicly on
Wednesday 6 Oct 2021 at 17:30h

by

Martin Lee

Master of Science,
McGill University,
born in Seoul, South Korea.

This dissertation has been approved by the promotors

prof.dr. P.G. Steeneken	Promotor
prof.dr.ir. H.S.J. van der Zant	Promotor

Rector Magnificus,	chairperson
Prof.dr. P.G. Steeneken	Delft University of Technology, promotor
Prof.dr.ir. H.S.J. van der Zant	Delft University of Technology, promotor
Independent members:	
Prof.dr.ir. P. M. Sarro	Delft University of Technology
Dr. S. Caneva	Delft University of Technology
Dr. A. Castellanos-Gomez	ICMM-CSIC Madrid
Prof.dr.ing. M. C. Lemme	RWTH Aachen
Prof.dr. H. Y. Hwang	Stanford University
Reserve member:	
Prof.dr. Y. M. Blanter	Delft University of Technology

Keywords: graphene, nanomechanics, pressure sensor, phase transition, complex oxide, membranes.

Printed by: ProefschriftMaken

Front & Back: A sketch of a device with a membrane being pulled down. Image: Sara Han.

Copyright © 2021 by M. Lee

Casimir PhD Series, Delft-Leiden 2021-24

ISBN 978-90-8593-490-5

An electronic version of this dissertation is available at
http://repository.tudelft.nl/.

Contents

Summary

This thesis encompasses both applied and fundamental studies of suspended van der Waals materials. Chapters 1 and 2 give an introduction to the field of 2D materials and some of the critical methods which facilitate the study of the suspended structures. In Chapters 3 and 4 we focus on the applications of graphene in barometric pressure sensors and develop a technique to improve their performance by hermetically sealing them. In Chapters 5 and 6 we use the mechanical resonance as a probe to study the magnetic and electronic phase transitions of suspended van der Waals materials.

Chapter 1 provides an overview of the field of 2D materials, complex oxides and microelectromechanical systems (MEMS) and discusses our motivation to combine these concepts together in an interdisciplinary field of nanomechanics.

Chapter 2 deals with various techniques used throughout the thesis. It starts with the nano fabrication of devices consisting of cavities and electrodes then to the exfoliation and transfer of 2D materials. In the case of complex oxides, pulsed laser deposition and the technique to release the films after epitaxy are discussed.

Chapter 3 and Chapter 4 focus on the application of graphene membranes in the next generation barometric pressure sensors. Chapter 3 deals with the massively parallel graphene drums used to capacitively measure the changes in the ambient pressure. This work demonstrates that graphene pressure sensors can already outperform the best silicon based capacitive pressure sensors on the market even with a with a sub-optimal yield of sealed cavities. In Chapter 4 we address the issue of low hermeticity in graphene drums by studying the pathways through which gases permeate. A novel sealing technique is presented which involves the deposition of additional SiO_2 along the edge of exfoliated graphene. After sealing we see an increase of hermeticity by four orders of magnitude. By combining sealing techniques with the graphene based capacitive pressure sensors from Chapter 3, we expect that the long-term stability of the sensors can be significantly improved.

Chapter 5 and Chapter 6 demonstrate that temperature dependent measurements of the nanomechanical resonance frequency of suspended 2D materials can be a powerful method for studying phase transitions. In Chapter 5 we show that both magnetic and electronic phase transitions can be probed by the temperature dependent nanomechanical resonance which has an anomaly as a result of the discontinuities in the thermodynamic properties. After establishing the basis of phase transitions, we focus on the charge density wave transitions in Chapter 6. First, the charge density wave transitions in archetypal systems 2H-TaS_2 and 2H-$TaSe_2$ are studied in their pristine states. Then the effect of disorder on the charge density wave transition temperature of 2H-TaS_2 is investigated. By comparing the nanomechanics before and after prolonged exposure to ambient air, we discovered

that degradation caused by air can enhance the transition temperature by more than 50 K.

Chapter 7 is a collection of preliminary results from currently on-going projects. These projects include piezoelectric actuators based on suspended single crystal $BaTiO_3$, curvature dependent anomalous Hall effect in suspended single crystal $SrRuO_3$ and superconducting microbridges made of 2H-TaS_2. Finally we conclude with Chapter 8 which summarizes the findings in this thesis.

Samenvatting

Dit proefschrift omvat zowel toegepaste als fundamentele onderzoeken van gesuspendeerde van der Waals-materialen. Hoofdstukken 1 en 2 geven een inleiding in het vakgebied van 2D materialen en een aantal van de essentiële technieken die de studie van gesuspendeerde structuren mogelijk maken. In Hoofdstukken 3 en 4 spitsen we ons toe op de toepassingen van grafeen in barometrische druksensoren en ontwikkelen we een techniek om hun prestaties te verbeteren door ze hermetisch af te dichten. In Hoofdstukken 5 en 6 gebruiken we de mechanische resonantie als meetinstrument voor magnetische en elektronische faseovergangen van gesuspendeerde van der Waals-materialen.

Hoofdstuk 1 verschaft een overzicht van het vakgebied van 2D materialen, complexe oxiden en micro-elektromechanische systemen (MEMS) en bespreekt onze drijfveer om deze concepten te combineren in een interdisciplinair vakgebied van de nanomechanica.

Hoofdstuk 2 beschrijft de verscheidene technieken die gebruikt zijn dit proefschrift. Het begint met de nanofabricage van apparaten bestaande uit holtes en elektroden en daarna de exfoliatie en overdracht van 2D-materialen. In het geval van complexe oxiden, wordt gepulseerde-laser depositie en de techniek om de films na epitaxie los te weken besproken.

Hoofdstuk 3 en Hoofdstuk 4 spitsen zich toe op de toepassing van grafeen membranen in de volgende generatie barometrische druksensoren. Hoofdstuk 3 behandelt de massaal parallelle grafeen nanotrommels die gebruikt worden om capacitief de veranderingen in de omgevingsdruk te meten. Dit werk toont aan dat grafeen druksensoren nu al de beste op silicium gebaseerde capacitieve druksensoren op de markt kunnen overtreffen, zelfs met een suboptimale opbrengst van afgedichte holtes. In Hoofdstuk 4 pakken we het probleem van lage hermeticiteit in grafeen nanotrommels aan door de paden waardoor gassen permeëren te bestuderen. Een nieuwe afdichtingstechniek wordt gepresenteerd welke betrekking heeft op de depositie van aanvullend SiO_2 langs de rand van geëxfolieerd grafeen. Na afdichting zien we een toename van de hermeticiteit van vier ordes van grootte. Door de afdichtingstechniek te combineren met de op grafeen gebaseerde capacitieve druksensoren uit Hoofdstuk 3, verwachten we dat de langetermijn stabiliteit van de sensoren significant kan worden verbeterd.

Hoofdstuk 5 en Hoofdstuk 6 tonen aan dat de temperatuurafhankelijke meting van de nanomechanische resonantiefrequentie van gesuspendeerde 2D materialen een krachtige methode kan zijn voor het bestuderen van faseovergangen. In Hoofdstuk 5 laten we zien dat zowel magnetische als elektronische faseovergangen gemeten kunnen worden door de temperatuurafhankelijke nanomechanische resonantie, welke een anomalie heeft ten gevolge van de discontinuïteiten in de thermodynamische eigenschappen. Na het vaststellen van de oorsprong van fase-

overgangen, spitsen we ons in Hoofdstuk 6 toe op de overgangen van ladingsdichtheidsgolven. Als eerst wordt de overgangstemperatuur van de ladingsdichtheidsgolven in de modelsystemen 2H-TaS_2 en 2H-$TaSe_2$ bestudeerd in hun ongerepte toestand. Daarna wordt het effect van wanorde op de overgangstemperatuur van de ladingsdichtheidsgolf onderzocht. Door de nanomechanische eigenschappen voor en na langdurige blootstelling aan omgevingslucht te vergelijken, ontdekten we dat verval veroorzaakt door lucht de overgangstemperatuur met meer dan 50 K kan verhogen.

Hoofdstuk 7 is een verzameling van voorlopige resultaten van lopende projecten. Deze projecten omvatten piezoelektrische aandrijvers gebaseerd op gesuspendeerd mono-kristallijn $BaTiO_3$, het krommingsafhankelijk anomalous Hall-effect in gesuspendeerd monokristallijn $SrRuO_3$ en supergeleidende microbruggen bestaande uit 2H-TaS_2. Tot slot sluiten we af met Hoofdstuk 8, wat de bevindingen in dit proefschrift samenvat.

1

1

Introduction

In this chapter we give an introduction to 2D materials and microelectromechanical systems (MEMS). 2D materials are attractive alternatives to Si in MEMS sensors and MEMS are becoming a versatile platform to study the properties of 2D materials.

1

1.1. Graphene

Until the discovery of graphene in 2004 by Novoselov and Geim [1], the term "2D materials" often referred to 3D systems that host 2D electron gas (2DEG) such as $LaAlO_3/SrTiO_3$ (LAO/STO) [2], silicon [3] and GaAs/AlGaAs [4]. In graphene, a true 2D material composed of a single layer of carbon atoms arranged in a hexagonal lattice, both crystal lattice and charge carriers are defined as 2D. Graphene is a single atomic layer isolated from its bulk counter part, graphite (Fig. 1.1). Graphene was first isolated in 2004 through mechanical exfoliation using Scotch tape. Since then, many thousands of other 2D materials have been discovered both experimentally and computationally [5–14]. In this thesis, graphene is employed in an application thanks to its scalability and its mechanical and electronic properties while other 2D materials such as $FePS_3$ and 2H-TaS_2 are investigated in fundamental studies.

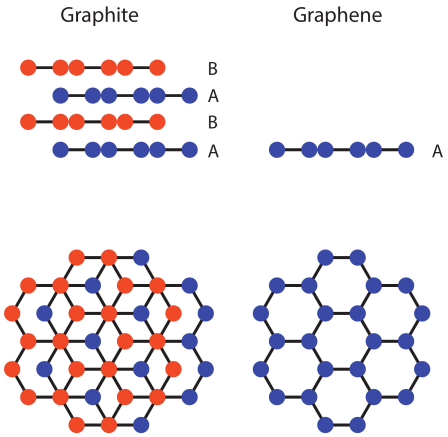

Figure 1.1: Cross sectional (top) and bird's eye view (bottom) illustrations of graphite (left) and graphene (right). Naturally occurring graphite consists of repeating AB stacked bilayers. Graphene is an isolated single layer from graphite.

Graphene boasts some exceptional properties. It is among the strongest materials with a Young's modulus of 1 TPa [15], has a flat 2.3 % optical absorption in the visible range [16], extremely high thermal conductivity [17], carrier mobility of up to 3×10^6 $cm^2/V{\cdot}s$ [18], relativistically fast massless fermions [1] and is impermeable to all gasses [19–21]. These properties make graphene an attractive material for the development of next generation consumer microelectromechanical devices. Now that the growth of monolayer graphene in large scale is realized in both roll-to-roll productions using copper foils [22, 23] and directly on wafers [24–27] graphene based devices are one step closer to commercialization.

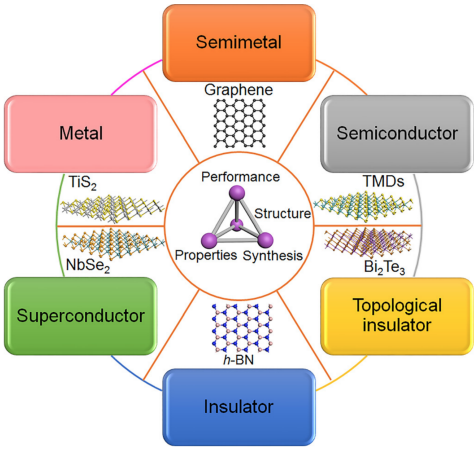

Figure 1.2: Examples of van der Waals with different ground states (figure adapted from [28]).

1.2. Other 2D materials

Since the discovery of graphene, many thousands of other 2D materials have been discovered [5–14]. This collection of 2D materials now encompass many of the electronic and magnetic ground states of condensed matter (Fig. 1.2) such as superconductivity, topological insulator and (anti)ferromagnetism. Fundamental studies of some of these phases of matter are conducted in the later half of the thesis, namely the phase transitions of antiferromagnetism and charge density waves.

1.2.1. Phase transition

Many 2D materials such as those studied in this thesis exhibit phase transitions. Phase transitions such as water turning into ice when cooled down below the critical temperature T_c can be described by Landau's theory of phase transitions [29]. The order of phase transitions are defined by the order of the derivative of the free energy F at which the parameter becomes discontinuous. For the first order phase transitions such as the solidification of water into ice, the discontinuity occurs in the entropy, the first derivative of the free energy ($S = \frac{\partial F}{\partial T}|_p$). In second order phase transitions such as the magnetic transitions or superconducting transitions, the discontinuity occurs in the specific heat c_p, the second order derivative of the free energy ($c_p = -\frac{\partial^2 F}{\partial T^2}|_p$). Differences between the first and second order phase transitions in F, S and c_p are shown in Fig. 1.3.

The phase transitions discussed in this thesis are paramagnetic to antiferromagnetic transitions and normal metal to charge density wave transitions which are both second order phase transitions. The free energy for second order phase transitions are of the form

$$F[\eta] = \begin{cases} F_0, & T > T_c \\ F_0 + F_2\eta^2 + F_4\eta^4, & T < T_c \end{cases} \tag{1.1}$$

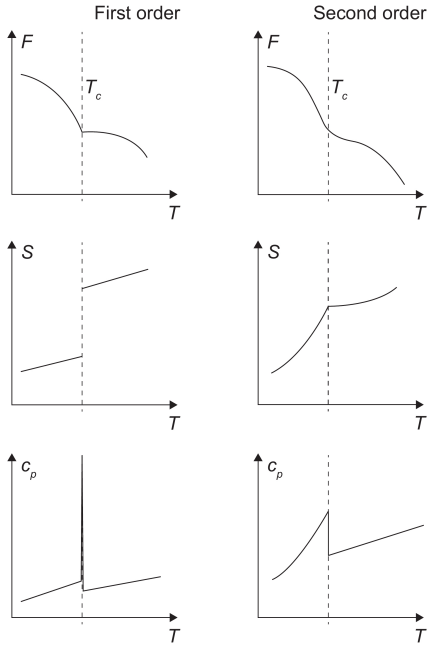

Figure 1.3: Free energy F, entropy S and specific heat c_p of first order transition (left column) and second order transition (right column).

where η is the order parameter obtained by minimizing the free energy. This is illustrated in Fig. 1.4 where above T_c, there is only one ground state. Below T_c, there are two ground states arising from the even order of F.

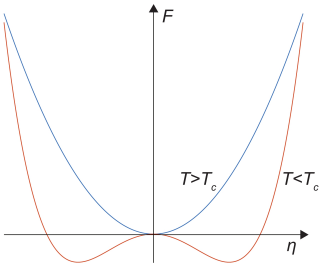

Figure 1.4: Free energy F as a function of the order parameter η. Above T_c, there is only one minimum (blue) and below T_c there are two possible orders (orange).

1.3. MEMS and sensors

Microelectromechanical systems (MEMS) have become ubiquitous in everyday consumer electronics. MEMS are used as high frequency clocks [36], actuators [37],

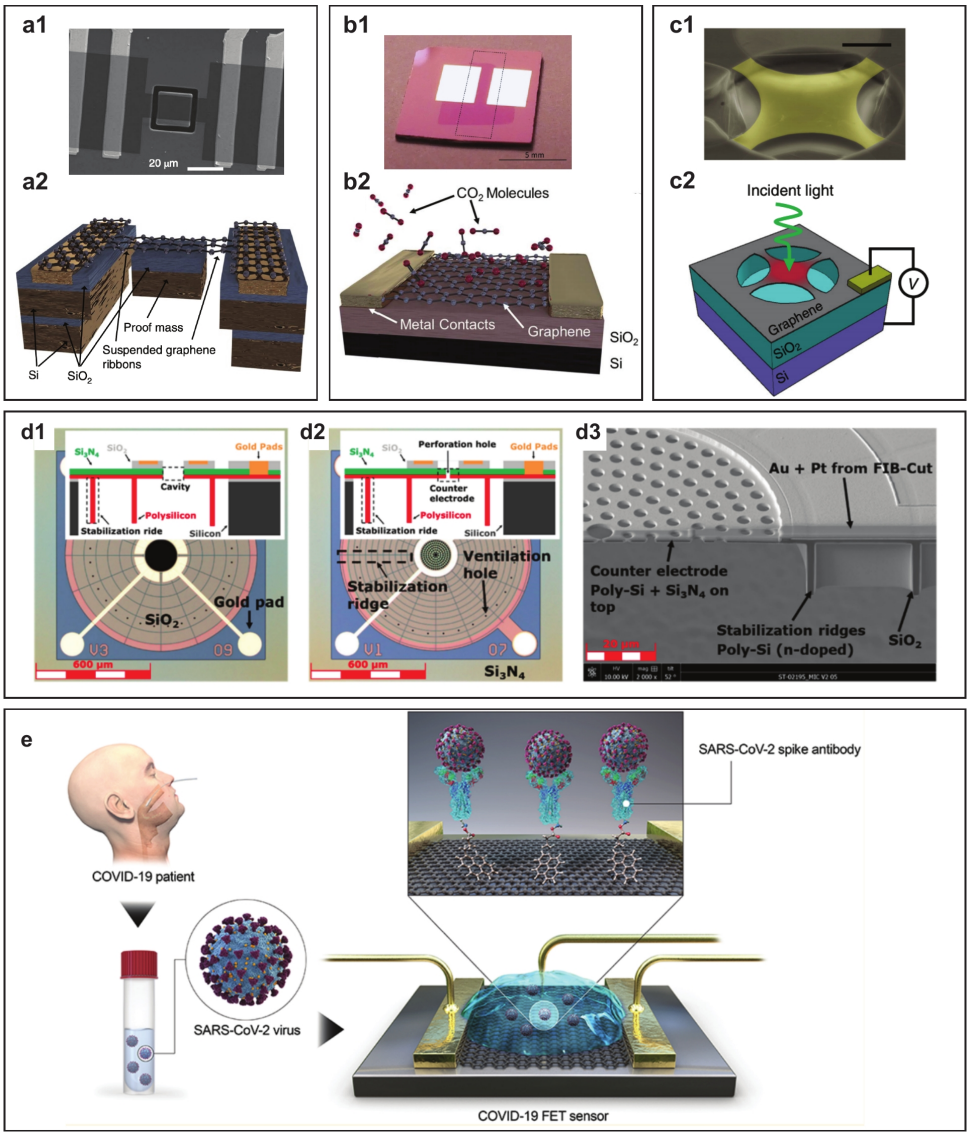

Figure 1.5: Few examples of graphene based MEMS devices and sensors. **a** Graphene based accelerometer with suspended proof mass (figure adapted from [30]). **b** Gas sensor. **b1** Graphene functionalized with V_2O_5 for sensing NH_3 (figure adapted from [31]). **b2** Graphene CO_2 sensor (figure adapted from [32]) **c** Suspended graphene bolometer (figure adapted from [33]). Suspended graphene based **d1** Hall sensor, **d2** microphone and **d3** a cross- sectional scanning electron microscopy image of device (figure adapted from [34]). **e** Graphene based COVID sensor (figure adapted from [35]).

filters [38] and sensors [39] among a myriad of applications. In consumer products, there is a general push for the reduction of dimensionality in MEMS devices. Size reduction in MEMS generally reduces cost, Si foot print, power consumption

and increases the frequency range. In this regard, 2D materials are expected to be superior to the current Si technologies due to their ultimate thinness and mechanical strength. Recently, 2D materials, especially graphene, have slowly been making their way to the frontiers of MEMS and sensors research [40]. Some examples include accelerometers [30, 41], gas sensors [31, 42, 43], Hall sensors [34], mass sensors [44], bio sensors [45–47], pH sensors [48], microphones [34, 49, 50], bolometers [33] and perhaps most relevant for the era this dissertation is written in, COVID sensors [35]. Some of the aforementioned graphene based devices are shown in Fig. 1.5.

1.3.1. Pressure sensors

One of the most auspicious areas that graphene and many other 2D materials shine in is for barometric pressure sensing applications. Owing to its high flexibility, mechanical strength and impermeability to gases, graphene based pressure sensors promise ultra high sensitivity to pressure changes and large working ranges. Several pressure readout mechanisms are being explored which include piezoresistive, squeeze film, Pirani and capacitive, each with their own advantages and disadvantages. Piezoresistive pressure sensors operate by reading out the change in the resistance due to the mechanical deflection of the membrane [51, 52], squeeze film pressure sensors measure the change in the stiffness arising from the membrane interacting with the gas molecules [53], Pirani pressure sensors measure the heat loss to the surrounding gases from the Pirani bridge [54] and capacitive pressure sensors measure the change in the capacitance due to the deflection of the membrane [55–57]. The advantages and disadvantages of each readout methods are listed in Table 1.1. Due to the low energy consumption, high sensitivity from large parallel readout and the ability to differentiate over and under pressures, we investigate the capacitive pressure sensors in Chapter 3.

Readout	Advantage	Disadvantage
Piezoresistive[51, 52]	simple DC circuit	large gauge factor desired, hermeticity required, over and under pressures have same signal
Squeeze film[53]	does not require hermeticity	non-trivial readout
Pirani[54]	does not require hermeticity	restricted pressure range
Capacitive[55–57]	low power consumption, both over and under pressure are unique	requires hermeticity, proper microwave shielding required

Table 1.1: Comparison of pressure readout methods used in graphene sensors thus far.

1.3.2. MEMS actuators for fundamental studies

Just as 2D materials are auspicious for the next generation MEMS devices, MEMS actuators are promising platforms for fundamental studies of 2D materials. Strain is a powerful tuning parameter which can affect the electronic properties of a material [62–70]. In this thesis, strain is applied by electrostatic gating a suspended material which is difficult to fabricate and difficult to analyse the strain. Due to the nature of the electrostatic strain, there is always some contribution to the Fermi

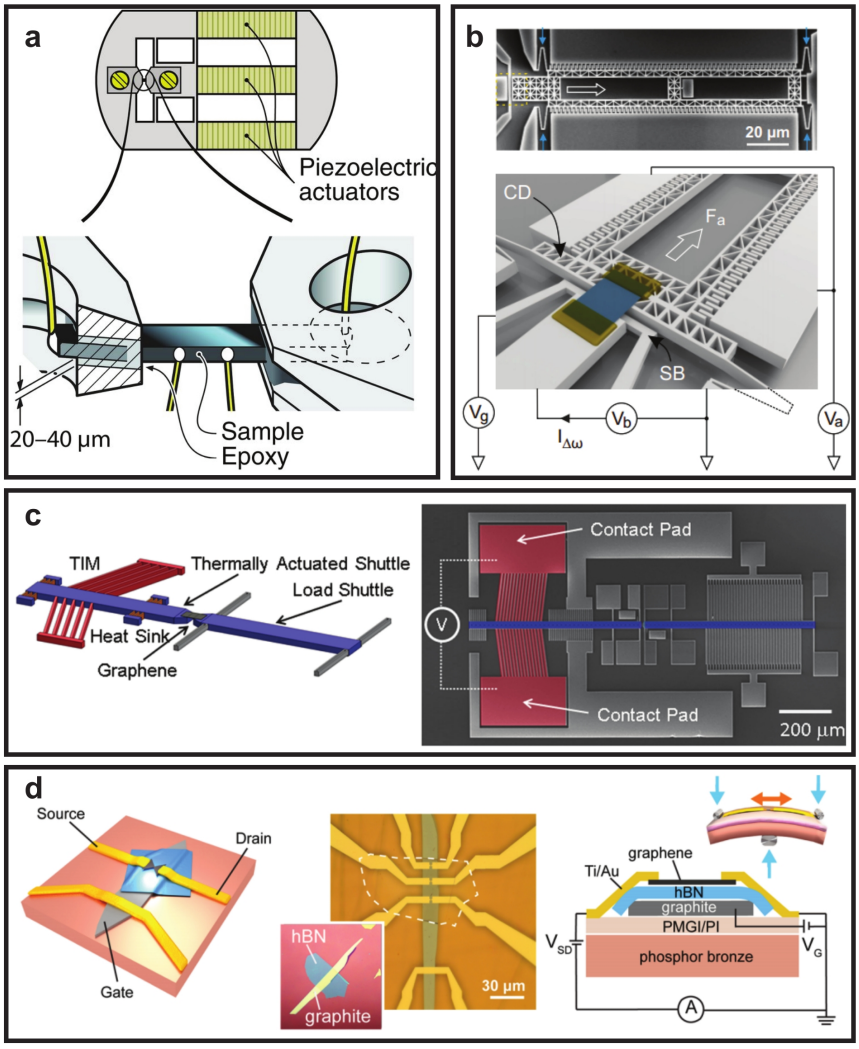

Figure 1.6: Images and reported examples of actuators being used to strain 2D materials in-situ. **a** Razorbill Ltd. strain cell operates by using piezoelectric actuators to apply force on a bulk crystal (figure adapted from [58]). **b** Comb-drive actuator operates by applying d.c. electric field to electrostatically move suspended Si structures away from another thereby stretching a 2D material suspended in between the Si structures (figure adapted from [59]). **c** Thermal actuator uses Joule heating to apply force to a central shuttle which supports a graphene flake thereby straining it (figure adapted from [60]). **d** Three-point bending setup bends the substrate with 2D flakes on top (figure adapted from [61]).

level. This system is therefore more suitable for large gap insulators and high density metals. Alternatively, there are several platforms that can induce strain in-situ independently to the electrostatic field. This includes Razorbill Ltd. piezo strain cell [71], comb-drive actuator [59, 72, 73], thermal actuator [60] and three-point

bending system [61, 74–77]. These platforms offer the strain and electric field to be independent parameters in the study of strain dependent magneto transport in quantum materials. Although this thesis does not contain any works on these systems, these systems are promising platforms for the next generation cutting-edge research of strain dependent quantum properties.

1.4. Complex Oxides

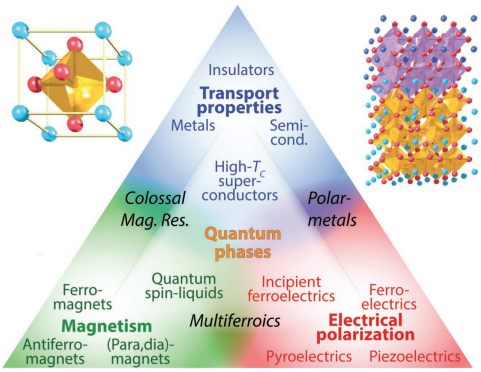

Figure 1.7: Various electronic phases available in the complex oxide family (figure adapted from [78]).

Complex oxides are a family of materials rich with interesting physics that span a myriad of electronic properties similar to 2D materials (Fig. 1.7) including magnetism [79], 2DEG [2], gate tunable superconductivity [80, 81], charge density waves [82], ferroelectricity [83], Mott insulators [84] and high temperature superconductivity (HTSC) [85]. Due to their long history, and useful properties, many applications already utilize complex oxides in their core operation. These applications include magnetic resonance imaging (MRI) [86], superconducting quantum interference devices (SQUID) [87] and sensors and actuators [88]. Furthermore, they hold promise for next generation energy applications such as high efficiency wind turbines [89, 90], fusion reactors [91] and hydrogen sensors [92, 93].

Due to their out of plane chemical bonds, typical complex oxides are not considered to be exfoliatable. Some layered HTSC such as $Bi_2Sr_2Ca_{n-1}Cu_nO_{2n+4+x}$ are exceptions being complex oxides with van der Waals interaction between the layers, allowing for mechanical exfoliation to be used to thin down from a bulk crystal [95]. However, this is not the case for most complex oxides. Illustrated in Fig. 1.8 are a few Ruddlesden-Popper phases of complex oxides consisting of a stoichiometric combination of rare earth metal element A, transition metal B and oxygen X [94]. As illustrated in the figure, these phases of oxides have out-of-plane chemical bonds. Although there exist several preferential cleavage planes [96] within the unit cell, extracting a single unit cell flake is of extreme difficulty.

However, recent developments to produce 2D-like free-standing complex oxides have opened the doors to probe the properties of complex oxides in their ultrathin form [97]. Many of these techniques such as the liquid phase exfoliation have

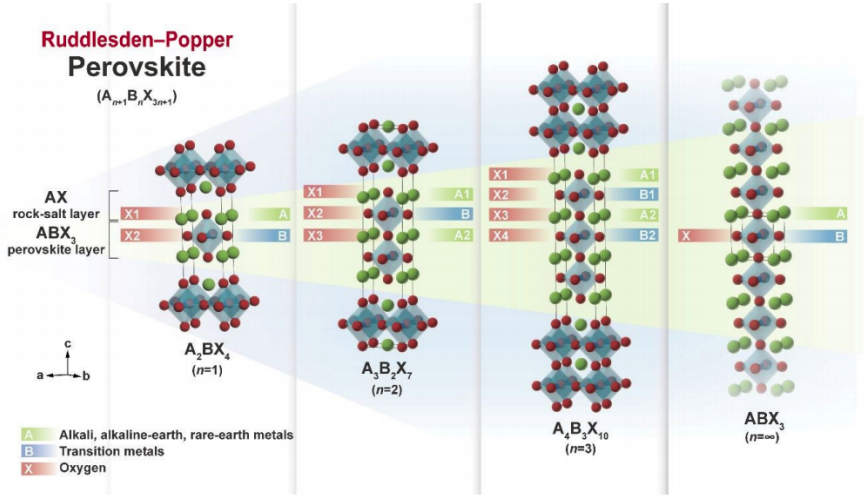

Figure 1.8: A schematic illustrating a few Ruddlesden-Popper phases of complex oxides with n = 1, 2, 3 and ∞.(figure adapted from [94]).

been adapted from the 2D materials community where a global push to develop and enhance the technology of producing 2D materials have allowed for a rapid advancement and maturity of the techniques. Some of these techniques to release single crystal complex oxides into their free-standing form are discussed in Chapter 2. In particular, we focus on the method developed by Lu *et al.* where the material of choice is epitaxially grown on top of a sacrificial water soluble layer which is itself epitaxially grown using a pulsed laser deposition technique [98]. Using this method, Ji *et al.* have demonstrated that complex oxides too can be isolated and suspended down to the single unit cell limit just like van der Waals materials [99]. The results regarding the complex oxides are shown in Chapter 7.

1.5. This thesis

This thesis is composed of three parts. The first part (chapters 3 and 4) studies the pressure sensing applications of graphene. In Chapter 3 we study graphene based capacitive pressure sensors. In this study, we come across one of the major hurdles in graphene based pressure sensors, the gas leakage. In Chapter 4 the origin of the leakage as well as a technique to suppress the leakage is presented. The second part (chapters 5 and 6) deals with fundamental studies of phase transitions in 2D nanomechanical resonators. In Chapter 5, we set up the basis for the nanomechanical study of phase transitions and show examples in antiferromagnets and charge density wave materials. In Chapter 6, we dig deeper into the study of charge density wave transitions and the influence of disorder on the charge density wave transitions. Finally, the third part (chapter 7) is a collection of on-going research and their preliminary results spanning both fundamental and applied studies.

1

References

[1] K. S. Novoselov, A. K. Geim, S. V. Morozov, D. Jiang, Y. Zhang, S. V. Dubonos, I. V. Grigorieva, and A. A. Firsov, "Electric field effect in atomically thin carbon films," *science*, vol. 306, no. 5696, pp. 666–669, 2004.

[2] A. Ohtomo and H. Y. Hwang, "A high-mobility electron gas at the $LaAlO_3/SrTiO_3$ heterointerface," *Nature*, vol. 427, no. 6973, pp. 423–426, 2004.

[3] A. B. Fowler, F. F. Fang, W. E. Howard, and P. J. Stiles, "Magneto-oscillatory conductance in silicon surfaces," *Physical review letters*, vol. 16, no. 20, p. 901, 1966.

[4] H. Störmer, R. Dingle, A. C. Gossard, W. Wiegmann, and M. D. Sturge, "Two-dimensional electron gas at a semiconductor-semiconductor interface," *Solid state communications*, vol. 29, no. 10, pp. 705–709, 1979.

[5] G. R. Bhimanapati, Z. Lin, V. Meunier, Y. Jung, J. Cha, S. Das, D. Xiao, Y. Son, M. S. Strano, V. R. Cooper, *et al.*, "Recent advances in two-dimensional materials beyond graphene," *ACS nano*, vol. 9, no. 12, pp. 11509–11539, 2015.

[6] A. Gupta, T. Sakthivel, and S. Seal, "Recent development in 2d materials beyond graphene," *Progress in Materials Science*, vol. 73, pp. 44–126, 2015.

[7] S. Das, J. A. Robinson, M. Dubey, H. Terrones, and M. Terrones, "Beyond graphene: progress in novel two-dimensional materials and van der waals solids," *Annual Review of Materials Research*, vol. 45, pp. 1–27, 2015.

[8] D. Akinwande, C. J. Brennan, J. S. Bunch, P. Egberts, J. R. Felts, H. Gao, R. Huang, J.-S. Kim, T. Li, Y. Li, *et al.*, "A review on mechanics and mechanical properties of 2d materials—graphene and beyond," *Extreme Mechanics Letters*, vol. 13, pp. 42–77, 2017.

[9] A. Chaves, J. G. Azadani, H. Alsalman, D. R. da Costa, R. Frisenda, A. J. Chaves, S. H. Song, Y. D. Kim, D. He, J. Zhou, A. Castellanos-Gomez, F. M. Peeters, Z. Liu, C. L. Hinkle, S.-H. Oh, P. D. Ye, S. J. Koester, Y. H. Lee, P. Avouris, X. Wang, and T. Low, "Bandgap engineering of two-dimensional semiconductor materials," *npj 2D Materials and Applications*, vol. 4, no. 1, pp. 1–21, 2020.

[10] S. Z. Butler, S. M. Hollen, L. Cao, Y. Cui, J. A. Gupta, H. R. Gutiérrez, T. F. Heinz, S. S. Hong, J. Huang, A. F. Ismach, *et al.*, "Progress, challenges, and opportunities in two-dimensional materials beyond graphene," *ACS nano*, vol. 7, no. 4, pp. 2898–2926, 2013.

[11] F. A. Rasmussen and K. S. Thygesen, "Computational 2d materials database: electronic structure of transition-metal dichalcogenides and oxides," *The Journal of Physical Chemistry C*, vol. 119, no. 23, pp. 13169–13183, 2015.

[12] N. Mounet, M. Gibertini, P. Schwaller, D. Campi, A. Merkys, A. Marrazzo, T. Sohier, I. E. Castelli, A. Cepellotti, G. Pizzi, and N. Marzari, "Two-dimensional materials from high-throughput computational exfoliation of experimentally known compounds," *Nature nanotechnology*, vol. 13, no. 3, pp. 246–252, 2018.

[13] S. Haastrup, M. Strange, M. Pandey, T. Deilmann, P. S. Schmidt, N. F. Hinsche, M. N. Gjerding, D. Torelli, P. M. Larsen, A. C. Riis-Jensen, J. Gath, K. W. Jacobsen, J. J. Mortensen, T. Olsen, and K. S. Thygesen, "The computational 2d materials database: high-throughput modeling and discovery of atomically thin crystals," *2D Materials*, vol. 5, no. 4, p. 042002, 2018.

[14] G. Cheon, K.-A. N. Duerloo, A. D. Sendek, C. Porter, Y. Chen, and E. J. Reed, "Data mining for new two-and one-dimensional weakly bonded solids and lattice-commensurate heterostructures," *Nano letters*, vol. 17, no. 3, pp. 1915–1923, 2017.

[15] C. Lee, X. Wei, J. W. Kysar, and J. Hone, "Measurement of the elastic properties and intrinsic strength of monolayer graphene," *science*, vol. 321, no. 5887, pp. 385–388, 2008.

[16] R. R. Nair, P. Blake, A. N. Grigorenko, K. S. Novoselov, T. J. Booth, T. Stauber, N. M. Peres, and A. K. Geim, "Fine structure constant defines visual transparency of graphene," *Science*, vol. 320, no. 5881, pp. 1308–1308, 2008.

[17] A. A. Balandin, S. Ghosh, W. Bao, I. Calizo, D. Teweldebrhan, F. Miao, and C. N. Lau, "Superior thermal conductivity of single-layer graphene," *Nano letters*, vol. 8, no. 3, pp. 902–907, 2008.

[18] L. Banszerus, M. Schmitz, S. Engels, M. Goldsche, K. Watanabe, T. Taniguchi, B. Beschoten, and C. Stampfer, "Ballistic transport exceeding 28 μm in cvd grown graphene," *Nano letters*, vol. 16, no. 2, pp. 1387–1391, 2016.

[19] J. S. Bunch, S. S. Verbridge, J. S. Alden, A. M. Van Der Zande, J. M. Parpia, H. G. Craighead, and P. L. McEuen, "Impermeable atomic membranes from graphene sheets," *Nano letters*, vol. 8, no. 8, pp. 2458–2462, 2008.

[20] P. Z. Sun, Q. Yang, W. J. Kuang, Y. V. Stebunov, W. Q. Xiong, J. Yu, R. R. Nair, M. I. Katsnelson, S. J. Yuan, I. V. Grigorieva, M. Lozada-Hidalgo, F. C. Wang, and A. K. Geim, "Limits on gas impermeability of graphene," *Nature*, vol. 579, no. 7798, pp. 229–232, 2020.

[21] V. Berry, "Impermeability of graphene and its applications," *Carbon*, vol. 62, pp. 1–10, 2013.

[22] S. Bae, H. Kim, Y. Lee, X. Xu, J.-S. Park, Y. Zheng, J. Balakrishnan, T. Lei, H. R. Kim, Y. I. Song, *et al.*, "Roll-to-roll production of 30-inch graphene films for transparent electrodes," *Nature nanotechnology*, vol. 5, no. 8, p. 574, 2010.

[23] T. Kobayashi, M. Bando, N. Kimura, K. Shimizu, K. Kadono, N. Umezu, K. Miyahara, S. Hayazaki, S. Nagai, Y. Mizuguchi, *et al.*, "Production of a 100-m-long high-quality graphene transparent conductive film by roll-to-roll chemical vapor deposition and transfer process," *Applied Physics Letters*, vol. 102, no. 2, p. 023112, 2013.

[24] K. V. Emtsev, A. Bostwick, K. Horn, J. Jobst, G. L. Kellogg, L. Ley, J. L. McChesney, T. Ohta, S. A. Reshanov, J. Röhrl, *et al.*, "Towards wafer-size graphene layers by atmospheric pressure graphitization of silicon carbide," *Nature materials*, vol. 8, no. 3, pp. 203–207, 2009.

[25] J.-H. Lee, E. K. Lee, W.-J. Joo, Y. Jang, B.-S. Kim, J. Y. Lim, S.-H. Choi, S. J. Ahn, J. R. Ahn, M.-H. Park, *et al.*, "Wafer-scale growth of single-crystal monolayer graphene on reusable hydrogen-terminated germanium," *Science*, vol. 344, no. 6181, pp. 286–289, 2014.

[26] J. Hwang, M. Kim, D. Campbell, H. A. Alsalman, J. Y. Kwak, S. Shivaraman, A. R. Woll, A. K. Singh, R. G. Hennig, S. Gorantla, *et al.*, "van der waals epitaxial growth of graphene on sapphire by chemical vapor deposition without a metal catalyst," *Acs Nano*, vol. 7, no. 1, pp. 385–395, 2013.

[27] L. Tai, D. Zhu, X. Liu, T. Yang, L. Wang, R. Wang, S. Jiang, Z. Chen, Z. Xu, and X. Li, "Direct growth of graphene on silicon by metal-free chemical vapor deposition," *Nano-micro letters*, vol. 10, no. 2, pp. 1–9, 2018.

[28] X. Li, L. Tao, Z. Chen, H. Fang, X. Li, X. Wang, J.-B. Xu, and H. Zhu, "Graphene and related two-dimensional materials: Structure-property relationships for electronics and optoelectronics," *Applied Physics Reviews*, vol. 4, no. 2, p. 021306, 2017.

[29] L. D. Landau and E. M. Lifshitz, *Course of theoretical physics. Vol. 5: Statistical physics.*, vol. 5. Pergamon Press, 1968.

[30] X. Fan, F. Forsberg, A. D. Smith, S. Schröder, S. Wagner, H. Rödjegård, A. C. Fischer, M. Östling, M. C. Lemme, and F. Niklaus, "Graphene ribbons with suspended masses as transducers in ultra-small nanoelectromechanical accelerometers," *Nature Electronics*, vol. 2, no. 9, pp. 394–404, 2019.

[31] M. Kodu, A. Berholts, T. Kahro, M. Kook, P. Ritslaid, H. Seemen, T. Avarmaa, H. Alles, and R. Jaaniso, "Graphene functionalised by laser-ablated V_2O_5 for a highly sensitive NH_3 sensor," *Beilstein journal of nanotechnology*, vol. 8, no. 1, pp. 571–578, 2017.

[32] A. D. Smith, K. Elgammal, X. Fan, M. C. Lemme, A. Delin, M. Råsander, L. Bergqvist, S. Schröder, A. C. Fischer, F. Niklaus, *et al.*, "Graphene-based CO_2 sensing and its cross-sensitivity with humidity," *RSC advances*, vol. 7, no. 36, pp. 22329–22339, 2017.

[33] A. Blaikie, D. Miller, and B. J. Alemán, "A fast and sensitive room-temperature graphene nanomechanical bolometer," *Nature communications*, vol. 10, no. 1, pp. 1–8, 2019.

[34] S. Wittmann, C. Glacer, S. Wagner, S. Pindl, and M. C. Lemme, "Graphene membranes for hall sensors and microphones integrated with cmos-compatible processes," *ACS Applied Nano Materials*, vol. 2, no. 8, pp. 5079–5085, 2019.

[35] G. Seo, G. Lee, M. J. Kim, S.-H. Baek, M. Choi, K. B. Ku, C.-S. Lee, S. Jun, D. Park, H. G. Kim, S.-J. Kim, J.-O. Lee, B. T. Kim, E. C. Park, and S. I. Kim, "Rapid detection of COVID-19 causative virus (SARS-CoV-2) in human nasopharyngeal swab specimens using field-effect transistor-based biosensor," *ACS nano*, vol. 14, no. 4, pp. 5135–5142, 2020.

[36] C. S. Lam, "A review of the recent development of mems and crystal oscillators and their impacts on the frequency control products industry," in *2008 IEEE Ultrasonics Symposium*, pp. 694–704, IEEE, 2008.

[37] D. J. Bell, T. J. Lu, N. A. Fleck, and S. M. Spearing, "Mems actuators and sensors: observations on their performance and selection for purpose," *Journal of Micromechanics and Microengineering*, vol. 15, no. 7, p. S153, 2005.

[38] R. C. Ruby, P. Bradley, Y. Oshmyansky, A. Chien, and J. D. Larson, "Thin film bulk wave acoustic resonators (fbar) for wireless applications," in *2001 IEEE Ultrasonics Symposium. Proceedings. An International Symposium (Cat. No. 01CH37263)*, vol. 1, pp. 813–821, IEEE, 2001.

[39] H. Du and R. Bogue, "Mems sensors: past, present and future," *Sensor Review*, 2007.

[40] M. C. Lemme, S. Wagner, K. Lee, X. Fan, G. J. Verbiest, S. Wittmann, S. Lukas, R. J. Dolleman, F. Niklaus, H. S. J. van der Zant, *et al.*, "Nanoelectromechanical sensors based on suspended 2d materials," *Research*, vol. 2020, 2020.

[41] X. Fan, F. Forsberg, A. D. Smith, S. Schröder, S. Wagner, M. Östling, M. C. Lemme, and F. Niklaus, "Suspended graphene membranes with attached silicon proof masses as piezoresistive nanoelectromechanical systems accelerometers," *Nano letters*, vol. 19, no. 10, pp. 6788–6799, 2019.

[42] I. Rosłoń, R. J. Dolleman, H. Licona, M. Lee, M. Šiškins, H. Lebius, L. Madauß, M. Schleberger, F. Alijani, H. S. J. van der Zant, *et al.*, "High-frequency gas effusion through nanopores in suspended graphene," *Nature communications*, vol. 11, no. 1, pp. 1–6, 2020.

[43] W. Yuan, A. Liu, L. Huang, C. Li, and G. Shi, "High-performance NO_2 sensors based on chemically modified graphene," *Advanced Materials*, vol. 25, no. 5, pp. 766–771, 2013.

[44] C. Chen, S. Rosenblatt, K. I. Bolotin, W. Kalb, P. Kim, I. Kymissis, H. L. Stormer, T. F. Heinz, and J. Hone, "Performance of monolayer graphene nanomechanical resonators with electrical readout," *Nature nanotechnology*, vol. 4, no. 12, pp. 861–867, 2009.

[45] T. Kuila, S. Bose, P. Khanra, A. K. Mishra, N. H. Kim, and J. H. Lee, "Recent advances in graphene-based biosensors," *Biosensors and bioelectronics*, vol. 26, no. 12, pp. 4637–4648, 2011.

[46] C. I. Justino, A. R. Gomes, A. C. Freitas, A. C. Duarte, and T. A. Rocha-Santos, "Graphene based sensors and biosensors," *TrAC Trends in Analytical Chemistry*, vol. 91, pp. 53–66, 2017.

[47] Y. Shao, J. Wang, H. Wu, J. Liu, I. A. Aksay, and Y. Lin, "Graphene based electrochemical sensors and biosensors: a review," *Electroanalysis: An International Journal Devoted to Fundamental and Practical Aspects of Electroanalysis*, vol. 22, no. 10, pp. 1027–1036, 2010.

[48] Y. Ohno, K. Maehashi, Y. Yamashiro, and K. Matsumoto, "Electrolyte-gated graphene field-effect transistors for detecting ph and protein adsorption," *Nano letters*, vol. 9, no. 9, pp. 3318–3322, 2009.

[49] Q. Zhou, J. Zheng, S. Onishi, M. F. Crommie, and A. K. Zettl, "Graphene electrostatic microphone and ultrasonic radio," *Proceedings of the National Academy of Sciences*, vol. 112, no. 29, pp. 8942–8946, 2015.

[50] D. Todorović, A. Matković, M. Milićević, D. Jovanović, R. Gajić, I. Salom, and M. Spasenović, "Multilayer graphene condenser microphone," *2D Materials*, vol. 2, no. 4, p. 045013, 2015.

[51] S. Wagner, C. Yim, N. McEvoy, S. Kataria, V. Yokaribas, A. Kuc, S. Pindl, C.-P. Fritzen, T. Heine, G. S. Duesberg, *et al.*, "Highly sensitive electromechanical piezoresistive pressure sensors based on large-area layered $PtSe_2$ films," *Nano letters*, vol. 18, no. 6, pp. 3738–3745, 2018.

[52] A. D. Smith, F. Niklaus, A. Paussa, S. Schröder, A. C. Fischer, M. Sterner, S. Wagner, S. Vaziri, F. Forsberg, D. Esseni, *et al.*, "Piezoresistive properties of suspended graphene membranes under uniaxial and biaxial strain in nanoelectromechanical pressure sensors," *ACS nano*, vol. 10, no. 11, pp. 9879–9886, 2016.

[53] R. J. Dolleman, S. J. Cartamil-Bueno, H. S. J. van der Zant, and P. G. Steeneken, "Graphene gas osmometers," *2D Materials*, vol. 4, no. 1, p. 011002, 2016.

[54] J. Romijn, S. Vollebregt, R. J. Dolleman, M. Singh, H. S. J. van der Zant, P. G. Steeneken, and P. M. Sarro, "A miniaturized low power pirani pressure sensor based on suspended graphene," in *2018 IEEE 13th Annual International Conference on Nano/Micro Engineered and Molecular Systems (NEMS)*, pp. 11–14, IEEE, 2018.

[55] C. Berger, R. Phillips, A. Centeno, A. Zurutuza, and A. Vijayaraghavan, "Capacitive pressure sensing with suspended graphene–polymer heterostructure membranes," *Nanoscale*, vol. 9, no. 44, pp. 17439–17449, 2017.

[56] D. Davidovikj, P. H. Scheepers, H. S. J. van Der Zant, and P. G. Steeneken, "Static capacitive pressure sensing using a single graphene drum," *ACS applied materials & interfaces*, vol. 9, no. 49, pp. 43205–43210, 2017.

[57] M. Šiškins, M. Lee, D. Wehenkel, R. van Rijn, T. W. de Jong, J. R. Renshof, B. C. Hopman, W. S. J. M. Peters, D. Davidovikj, H. S. J. van der Zant, *et al.*, "Sensitive capacitive pressure sensors based on graphene membrane arrays," *Microsystems & Nanoengineering*, vol. 6, no. 1, pp. 1–9, 2020.

[58] A. Steppke, L. Zhao, M. E. Barber, T. Scaffidi, F. Jerzembeck, H. Rosner, A. S. Gibbs, Y. Maeno, S. H. Simon, A. P. Mackenzie, *et al.*, "Strong peak in T_c of Sr_2RuO_4 under uniaxial pressure," *Science*, vol. 355, no. 6321, 2017.

[59] G. J. Verbiest, M. Goldsche, J. Sonntag, T. Khodkov, N. Driesch, D. Buca, and C. Stampfer, "Tunable coupling of two mechanical resonators by a graphene membrane," *arXiv preprint arXiv:2005.05358*, 2020.

[60] H. H. Pérez Garza, E. W. Kievit, G. F. Schneider, and U. Staufer, "Controlled, reversible, and nondestructive generation of uniaxial extreme strains (> 10%) in graphene," *Nano letters*, vol. 14, no. 7, pp. 4107–4113, 2014.

[61] S. Caneva, M. Hermans, M. Lee, A. García-Fuente, K. Watanabe, T. Taniguchi, C. Dekker, J. Ferrer, H. S. J. van der Zant, and P. Gehring, "A mechanically tunable quantum dot in a graphene break junction," *Nano letters*, vol. 20, no. 7, pp. 4924–4931, 2020.

[62] C. W. Hicks, D. O. Brodsky, E. A. Yelland, A. S. Gibbs, J. A. Bruin, M. E. Barber, S. D. Edkins, K. Nishimura, S. Yonezawa, Y. Maeno, *et al.*, "Strong increase of tc of Sr_2RuO_4 under both tensile and compressive strain," *Science*, vol. 344, no. 6181, pp. 283–285, 2014.

[63] S. S. Hong, M. Gu, M. Verma, V. Harbola, B. Y. Wang, D. Lu, A. Vailionis, Y. Hikita, R. Pentcheva, J. M. Rondinelli, *et al.*, "Extreme tensile strain states in $La_{0\cdot7}Ca_{0\cdot3}MnO_3$ membranes," *Science*, vol. 368, no. 6486, pp. 71–76, 2020.

[64] H. J. Conley, B. Wang, J. I. Ziegler, R. F. Haglund Jr, S. T. Pantelides, and K. I. Bolotin, "Bandgap engineering of strained monolayer and bilayer MoS_2," *Nano letters*, vol. 13, no. 8, pp. 3626–3630, 2013.

[65] D. Lloyd, X. Liu, J. W. Christopher, L. Cantley, A. Wadehra, B. L. Kim, B. B. Goldberg, A. K. Swan, and J. S. Bunch, "Band gap engineering with ultralarge biaxial strains in suspended monolayer MoS_2," *Nano letters*, vol. 16, no. 9, pp. 5836–5841, 2016.

[66] A. Castellanos-Gomez, R. Roldán, E. Cappelluti, M. Buscema, F. Guinea, H. S. J. van der Zant, and G. A. Steele, "Local strain engineering in atomically thin MoS_2," *Nano letters*, vol. 13, no. 11, pp. 5361–5366, 2013.

[67] C. Zhao, M. Hu, J. Qin, B. Xia, C. Liu, S. Wang, D. Guan, Y. Li, H. Zheng, J. Liu, *et al.*, "Strain tunable semimetal-topological-insulator transition in monolayer 1T'-WTe_2," *Physical Review Letters*, vol. 125, no. 4, p. 046801, 2020.

[68] N. Levy, S. A. Burke, K. L. Meaker, M. Panlasigui, A. Zettl, F. Guinea, A. H. C. Neto, and M. F. Crommie, "Strain-induced pseudo–magnetic fields greater than 300 tesla in graphene nanobubbles," *Science*, vol. 329, no. 5991, pp. 544–547, 2010.

[69] M. Uchida, T. Nomoto, M. Musashi, R. Arita, and M. Kawasaki, "Superconductivity in uniquely strained RuO_2 films," *Physical Review Letters*, vol. 125, no. 14, p. 147001, 2020.

[70] J. P. Ruf, H. Paik, N. J. Schreiber, H. P. Nair, L. Miao, J. K. Kawasaki, J. N. Nelson, B. D. Faeth, Y. Lee, B. H. Goodge, *et al.*, "Strain-stabilized superconductivity," *Nature Communications*, vol. 12, no. 1, pp. 1–8, 2021.

[71] N. H. Jo, L.-L. Wang, P. P. Orth, S. L. Bud'ko, and P. C. Canfield, "Magnetoelastoresistance in WTe_2: Exploring electronic structure and extremely large magnetoresistance under strain," *Proceedings of the National Academy of Sciences*, vol. 116, no. 51, pp. 25524–25529, 2019.

[72] Y. Xie, J. Lee, Y. Wang, and P. X.-L. Feng, "Straining and tuning atomic layer nanoelectromechanical resonators via comb-drive mems actuators," *Advanced Materials Technologies*, vol. 6, no. 2, p. 2000794, 2021.

[73] M. Goldsche, G. J. Verbiest, T. Khodkov, J. Sonntag, N. von den Driesch, D. Buca, and C. Stampfer, "Fabrication of comb-drive actuators for straining nanostructured suspended graphene," *Nanotechnology*, vol. 29, no. 37, p. 375301, 2018.

[74] L. Wang, A. Baumgartner, P. Makk, S. Zihlmann, B. S. Varghese, D. I. Indolese, K. Watanabe, T. Taniguchi, and C. Schönenberger, "Global strain-induced scalar potential in graphene devices," *arXiv preprint arXiv:2009.03035*, 2020.

[75] L. Wang, S. Zihlmann, A. Baumgartner, J. Overbeck, K. Watanabe, T. Taniguchi, P. Makk, and C. Schönenberger, "In situ strain tuning in hBN-encapsulated graphene electronic devices," *Nano letters*, vol. 19, no. 6, pp. 4097–4102, 2019.

[76] S. Caneva, P. Gehring, V. M. García-Suárez, A. García-Fuente, D. Stefani, I. J. Olavarria-Contreras, J. Ferrer, C. Dekker, and H. S. J. van der Zant, "Mechanically controlled quantum interference in graphene break junctions," *Nature nanotechnology*, vol. 13, no. 12, pp. 1126–1131, 2018.

[77] Y. Wang, C. Wang, S.-J. Liang, Z. Ma, K. Xu, X. Liu, L. Zhang, A. S. Admasu, S.-W. Cheong, L. Wang, *et al.*, "Strain-sensitive magnetization reversal of a van der waals magnet," *Advanced Materials*, vol. 32, no. 42, p. 2004533, 2020.

[78] M. Brahlek, A. S. Gupta, J. Lapano, J. Roth, H.-T. Zhang, L. Zhang, R. Haislmaier, and R. Engel-Herbert, "Frontiers in the growth of complex oxide thin films: past, present, and future of hybrid MBE," *Advanced Functional Materials*, vol. 28, no. 9, p. 1702772, 2018.

[79] A. Callaghan, C. W. Moeller, and R. Ward, "Magnetic interactions in ternary ruthenium oxides," *Inorganic Chemistry*, vol. 5, no. 9, pp. 1572–1576, 1966.

[80] N. Reyren, S. Thiel, A. Caviglia, L. F. Kourkoutis, G. Hammerl, C. Richter, C. W. Schneider, T. Kopp, A.-S. Rüetschi, D. Jaccard, *et al.*, "Superconducting interfaces between insulating oxides," *Science*, vol. 317, no. 5842, pp. 1196–1199, 2007.

[81] C. Liu, X. Yan, D. Jin, Y. Ma, H.-W. Hsiao, Y. Lin, T. M. Bretz-Sullivan, X. Zhou, J. Pearson, B. Fisher, *et al.*, "Two-dimensional superconductivity and anisotropic transport at $KTaO_3$ (111) interfaces," *Science*, vol. 371, no. 6530, pp. 716–721, 2021.

[82] C. Proust and L. Taillefer, "The remarkable underlying ground states of cuprate superconductors," *Annual Review of Condensed Matter Physics*, vol. 10, pp. 409–429, 2019.

[83] C. Randall, R. Newnham, and L. Cross, "History of the first ferroelectric oxide, $BaTiO_3$," *Materials Research Institute, The Pennsylvania State University, University Park, Pa, USA*, vol. 1, 2004.

[84] P. A. Lee, N. Nagaosa, and X.-G. Wen, "Doping a Mott insulator: Physics of high-temperature superconductivity," *Reviews of modern physics*, vol. 78, no. 1, p. 17, 2006.

[85] C. C. Tsuei and J. R. Kirtley, "Pairing symmetry in cuprate superconductors," *Reviews of Modern Physics*, vol. 72, no. 4, p. 969, 2000.

[86] Y. Lvovsky, E. W. Stautner, and T. Zhang, "Novel technologies and configurations of superconducting magnets for MRI," *Superconductor Science and Technology*, vol. 26, no. 9, p. 093001, 2013.

[87] H. Weinstock, *SQUID sensors: fundamentals, fabrication and applications*. Springer Science & Business Media, 2012.

[88] P. Muralt, "PZT thin films for microsensors and actuators: Where do we stand?," *IEEE transactions on ultrasonics, ferroelectrics, and frequency control*, vol. 47, no. 4, pp. 903–915, 2000.

[89] A. Bergen, R. Andersen, M. Bauer, H. Boy, M. Ter Brake, P. Brutsaert, C. Bührer, M. Dhallé, J. Hansen, H. Ten Kate, *et al.*, "Design and in-field testing of the world's first ReBCO rotor for a 3.6 MW wind generator," *Superconductor science and technology*, vol. 32, no. 12, p. 125006, 2019.

[90] J. Lloberas, A. Sumper, M. Sanmarti, and X. Granados, "A review of high temperature superconductors for offshore wind power synchronous generators," *Renewable and Sustainable Energy Reviews*, vol. 38, pp. 404–414, 2014.

[91] L. Bromberg, M. Tekula, L. A. El-Guebaly, R. Miller, A. Team, *et al.*, "Options for the use of high temperature superconductor in tokamak fusion reactor designs," *Fusion Engineering and Design*, vol. 54, no. 2, pp. 167–180, 2001.

[92] G. Mattoni, B. de Jong, N. Manca, M. Tomellini, and A. D. Caviglia, "Single-crystal pt-decorated WO_3 ultrathin films: a platform for sub-ppm hydrogen sensing at room temperature," *ACS applied nano materials*, vol. 1, no. 7, pp. 3446–3452, 2018.

[93] N. Manca, G. Mattoni, M. Pelassa, W. J. Venstra, H. S. van der Zant, and A. D. Caviglia, "Large tunability of strain in WO_3 single-crystal microresonators controlled by exposure to H_2 gas," *ACS applied materials & interfaces*, vol. 11, no. 47, pp. 44438–44443, 2019.

[94] X. Xu, Y. Pan, Y. Zhong, R. Ran, and Z. Shao, "Ruddlesden-popper perovskites in electrocatalysis," *Materials Horizons*, vol. 7, no. 10, pp. 2519–2565, 2020.

[95] Y. Yu, L. Ma, P. Cai, R. Zhong, C. Ye, J. Shen, G. D. Gu, X. H. Chen, and Y. Zhang, "High-temperature superconductivity in monolayer $Bi_2Sr_2CaCu_2o_{8+\delta}$," *Nature*, vol. 575, no. 7781, pp. 156–163, 2019.

[96] H. Guo, Y. Li, D. Urbina, B. Hu, R. Jin, T. Liu, D. Fobes, Z. Mao, E. W. Plummer, and J. Zhang, "Doping and dimensionality effects on the core-level spectra of layered ruthenates," *Physical Review B*, vol. 81, no. 15, p. 155121, 2010.

[97] A. G. Ricciardulli, S. Yang, J. H. Smet, and M. Saliba, "Emerging perovskite monolayers," *Nature Materials*, 2021.

[98] D. Lu, D. J. Baek, S. S. Hong, L. F. Kourkoutis, Y. Hikita, and H. Y. Hwang, "Synthesis of freestanding single-crystal perovskite films and heterostructures by etching of sacrificial water-soluble layers," *Nature materials*, vol. 15, no. 12, pp. 1255–1260, 2016.

[99] D. Ji, S. Cai, T. R. Paudel, H. Sun, C. Zhang, L. Han, Y. Wei, Y. Zang, M. Gu, Y. Zhang, *et al.*, "Freestanding crystalline oxide perovskites down to the monolayer limit," *Nature*, vol. 570, no. 7759, pp. 87–90, 2019.

2

2

Methods

Nano-fabrication is a critical yet often overlooked procedure in experimental condensed matter physics. It should be performed meticulously while sufficiently fast; it allows for creativity while the steps are repetitive; it is conceptually at a high level while being quite laborious; it is universally applicable while the exact parameters depend on the operator and the specific equipments used. In this chapter we discuss the nano-fabrication steps used in this thesis which can conceptually be reproduced in most nano-fabrication cleanrooms in the world. The details should be developed by the reader taking into account his/her equipments available.

2.1. Cavity devices

In this chapter, we will discuss the techniques through which we fabricate the suspended 2D membranes. First the nano-fabrication procedure used to fabricate the electrodes and cavities is laid out. Next various transfer methods of 2D materials are compared. Finally, the growth and release of free-standing complex oxides are discussed.

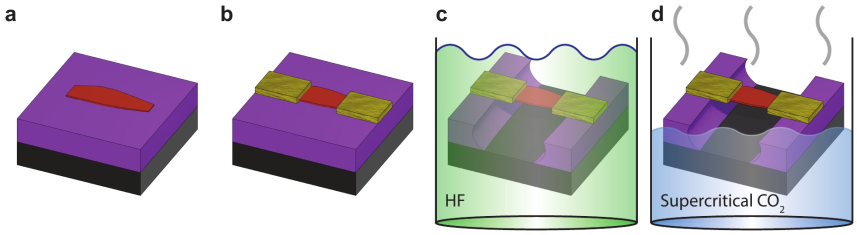

Figure 2.1: Illustration of the fabrication steps using HF to undercut the oxide. **a** Graphene is exfoliated onto SiO_2/Si. **b** Metal deposited as anchors and electrodes. **c** HF is used to remove the SiO_2 underneath the graphene. **d** Critical point drying used to remove liquids without collapsing the graphene.

It is an extremely challenging process to fabricate suspended structures out of 2D materials using HF to undercut the SiO_2/Si which releases the 2D membrane [1] (Fig. 2.1). In this process 2D materials are typically exfoliated on a pre-patterned SiO_2/Si with markers for alignment (Fig. 2.1a). Then, using lithography and deposition, electrodes are metallized on top of the 2D material to anchor and clamp it during the undercutting process and to use as probes during measurement (Fig. 2.1b). Next the 2D material is released from the substrate using HF to etch away the SiO_2. Finally, the sample is transferred to a solvent while still wet, and critical-point-dried to remove the sample from a liquid environment without the capillary forces collapsing the membrane to the cavity bottom (Fig. 2.1d). This process, although has shown to produce ultra-high mobility in graphene [1] is tedious and results in a low yield of devices. Furthermore, since metal deposition on top of 2D materials has shown to cause many problems such as strain [2] and degradation [3], and not every material can withstand the harsh HF treatment, this method, that is standard in MEMS to fabricate suspended structures, is therefore limited to only a few 2D materials.

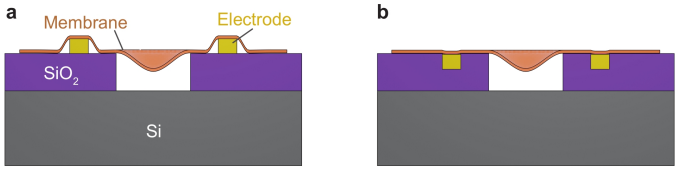

Figure 2.2: **a** Cross section of a device fabricated by directly evaporating on top of SiO_2/Si. **b** Cross section of a device fabricated embedding electrodes in the SiO_2/Si.

In this thesis we therefore use a different approach to make suspended 2D res-

onators. Scott-Bunch *et al.* [4] showed that graphene can be exfoliated directly on top of trenches and electrodes pre-defined on the substrate. This method, although more straight-forward, also has a low yield due to the randomness of the exfoliation process. We have taken this approach to pre-pattern the substrate and combined with it, a method to exfoliate and transfer the exfoliated flakes deterministically [5] which has resulted in a greater yield of devices with shorter fabrication times.

Pre-patterned devices presented in this thesis are made using nano-fabrication techniques such as e-beam lithography, reactive ion etching (RIE) and evaporation. One of the notable improvements in device design is that we pre-define the electrodes that are embedded into the oxide layer for easier transfer of 2D materials. As can be visualized in the illustration in Fig. 2.2a, when electrodes are defined on top of the SiO_2/Si substrate, the protrusion of the metal layer causes problems in adhesion. Due to the height of the electrodes, only the 2D flakes which can conform to the topography of the electrodes remain intact. The tenting effect seen near the electrodes are often where the 2D materials peel off from during the transfer process. This was the motivation for embedding the electrodes into the substrate. In Fig. 2.2b, we show a cross sectional illustration of a device with embedded contacts. There is notably less tenting effect and we have a higher yield of 2D materials transferred on top of the device area with these devices.

2.1.1. Lithography deposition and etching

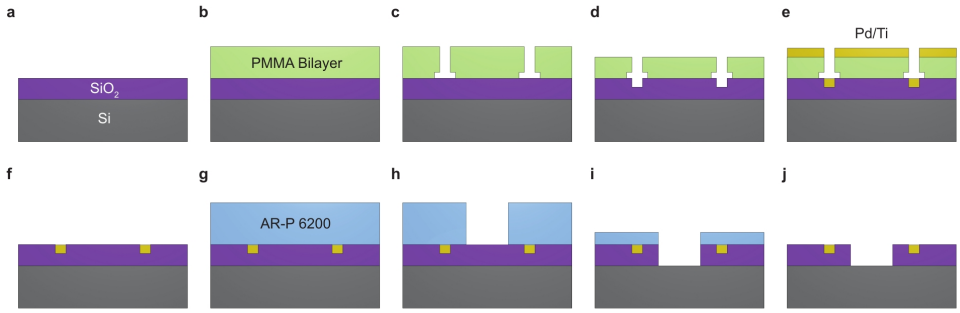

Figure 2.3: Illustration of the fabrication flow for the production of cavity devices with embedded electrodes. **a** LPCVD SiO_2/Si substrate is prepared. **b** PMMA bilayer is spin coated and baked. **c** Electrodes and markers are exposed. **d** Reactive ion etching (RIE) is used to anisotropically etch into the SiO_2/Si. **e** Pd/Ti is evaporated. **f** Lift off in PRS-3000, rinsed in deionized (DI) water and blown dry. **g** AR-P 6200 spin coated and baked. **h** Cavity layer is exposed and developed. **i** RIE is used to dry etch the cavity. **j** Remaining resist is removed in PRS-3000 overnight, rinsed in DI water, blown dry and plasma cleaned in a plasma asher.

The fabrication flow is illustrated in Fig. 2.3a-j. Our starting substrates are 4 inch wafers of dry low pressure chemical vapour deposition (LPCVD) SiO_2 grown on doped Si commercially available. These are spin coated with S1813 (for the protection of the high quality oxide during dicing) and diced, using a Disco dicer, into 19 mm × 19 mm substrates. The wafers are diced into smaller square wafers to allow faster device pattern updates between iterations. Nine samples of 5.5 mm × 5.5

mm fit into these square pieces of SiO_2/Si which are processed at once. Once the 19 mm × 19 mm wafers are cleaned in acetone and rinsed in isopropyl alcohol (Fig. 2.3a), positive e-beam resists are spin coated on top. For the process of the metallization of electrodes or contact pads, polymethyl methacrylate (PMMA) bilayers of 495 k/ 950 k are used (Fig. 2.3b). Thin 495 k layers are used on the bottom to ensure easier lift off and thick 950 k layers are used on the top to define the electrode pattern with high accuracy. The electrode patterns are exposed in the PMMA bilayer using Raith EBPG 5000+ at 100 kV and developed in a methyl isobutyl ketone (MIBK) : isopropyl alcohol (IPA) (3:1 by vol) mixture for 60 seconds, rinsed in pure IPA for 30 seconds and blow-dried (Fig. 2.3c). Using Sentech Etchlab 200, exposed SiO_2/Si is slightly etched in the electrode pattern (Fig. 2.3d). Quickly following the etching process, the electrode pattern is metallized using an e-beam evaporator (Fig. 2.3e). After deposition, metal coated PMMA layers are removed along with the excess metals in a warm bath of PRS-3000 over night (Fig. 2.3f). For the cavity layer, a thick positive e-beam resist is spin coated on top (Fig. 2.3g). AR-P 6200 is chosen due to its high dry etching resistance compared to PMMA. The cavity design is exposed using EBPG-5000+ again, and then developed in pentyl acetate for 60 seconds, MIBK : IPA (1:1) for 60 seconds, rinsed in pure IPA for 60 seconds and finally blow-dried (Fig. 2.3h). Next, Sentech Etchlab 200 is used to etch exposed SiO_2 all the way to the Si layer (Fig. 2.3i). Finally, the remnant resist is removed in a warm bath of PRS-3000, rinsed in DI water, blow-dried and plasma cleaned in a Tepla 300 oxygen plasma asher (Fig. 2.3j).

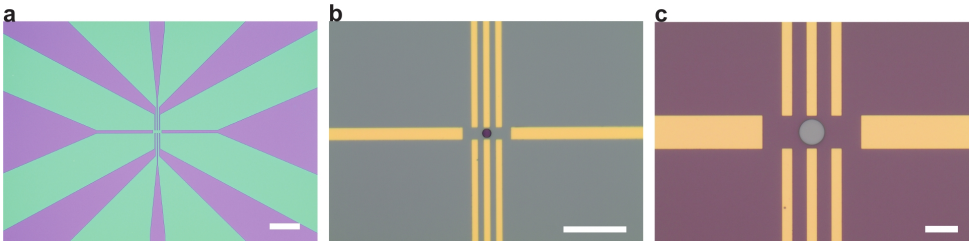

Figure 2.4: Optical image of the fabrication process. **a** Image of the device after e-beam lithography and development corresponding to illustration Fig. 2.3c. Scale bar: 100 µm. **b** Image of the device after the second e-beam lithography and development to define the cavity corresponding to illustration Fig. 2.3h. Scale bar: 20 µm. **c** Image of the finished device corresponding to illustration Fig. 2.3j. Scale bar: 10 µm.

Optical images of the device at various stages are shown in Fig. 2.4a-c. Figure 2.4a is an optical microscopy image after the first e-beam lithography and development step which defines the electrodes. The parts in green are the un-exposed bi-layer PMMA and the purple regions are where the exposed PMMA are removed by the development procedure and the underlying 285 nm SiO_2 is uncovered. This image corresponds to the illustration shown in Fig. 2.3c. Figure 2.4b shows an image after the second e-beam exposure and development. The areas in grey are the un-exposed AR-P 6200 and the circle in the center of the electrodes are where the AR-P 6200 resist is exposed and removed by the development procedure. This im-

age corresponds to the illustration shown in Fig. 2.3h. Figure 2.4c is an image of the finished device. The cavity is etched all the way through, leaving a flat grey cavity bottom of pure Si. This image corresponds to the illustration shown in Fig. 2.3j.

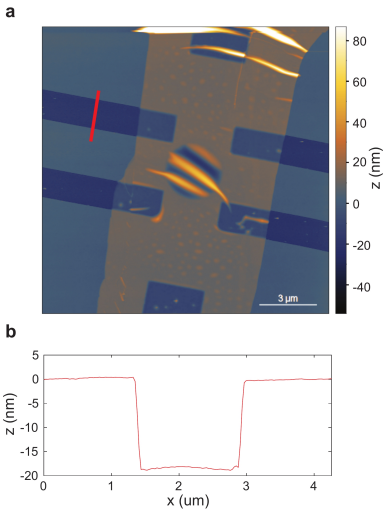

Figure 2.5: **a** Atomic force microscopy scan of a WTe_2 transferred on to a Hall bar with a cavity in the center. Red line is where the profile in **b** is taken. **b** Topographic profile of the embedded electrode.

Figure 2.5a shows an example atomic force microscopy (AFM) image of a device consisting of a flake of WTe_2 on a set of electrodes with a cavity in the center. Although the flake is not usable due to the wrinkles in the suspended area, this AFM image depicts how our typical devices look. In order to improve the ease of transfer, the electrodes composed of 10 nm Ti and 60 nm Pd are embedded into the SiO_2/Si which is etched first before deposition. Typical discrepancy between the top of the SiO_2 and the top of the electrodes are 5-20 nm. In Fig. 2.5b, a profile across one of the embedded electrodes corresponding to the red line in Fig. 2.5a is shown. For the dry transfer of 2D materials, having electrodes embedded in the substrate helps with the adhesion.

When a large sheet of CVD graphene is transferred, the height difference between the electrodes and the substrate does not play a significant role in the ease of the transfer. Therefore in Chapter 3 we simply evaporate the metal layer on top of the substrate without the etching step. In Chapter 4, we only use steps shown in Fig. 2.3g-j since electrodes are not needed. In Chapter 5, we used electrodes that are simply deposited on top of the substrate like in Fig. 2.2a. During the research of the work in Chapter 5 we noticed the difficulties in transferring 2D materials over the simply-evaporated electrodes and improved the fabrication process to include the embedding step (flow of Fig. 2.3) for the subsequent works in Chapter 6 and the outlook, Chapter 7.

2.2. 2D materials

Since the initial discovery of graphene using Scotch tape [6], many alternative methods have been developed to isolate 2D materials. Some of the top down processes include liquid phase exfoliation [7], plasma spraying [8], ball milling [9], strain engineered mechanical exfoliation [10] and reduction of graphene oxide [11]; and bottom up processes include chemical vapour deposition (CVD) [12], epitaxial growth [13, 14], and self assembly [15]. Of the listed methods, the most promising method for large scale production is the roll-to-roll CVD process [16], epitaxial growth on SiC [13] and liquid phase exfoliation [7], albeit the controversy on the quality of "graphene" produced in the industry using the liquid phase exfoliation technique [17].

In Chapter 3, we employ CVD grown double monolayer graphene on copper substrate transferred on top of devices using PMMA as a support layer. The growth and transfer of double layer graphene is performed by Applied Nano Layers BV. In Chapters 4-6, flakes of 2D materials mechanically exfoliated from bulk crystals are used for the proof of principle studies. We are aware that transfer-free methods of producing graphene based devices are under development [18, 19] and have shown promising results. Since this process combines graphene growth and CMOS integration without the need for manual transfer, it is attractive in the larger scale production and integration of graphene based devices.

Exfoliation and transfer of 2D materials have become a subfield of its own. There are a myriad of exfoliation and transfer techniques available in the literature now [20–23]. This is driven by the fact that even to this day, 15 years after the discovery of single layer graphene through mechanical exfoliation, "the Scotch tape" method is arguably still the best method to produce high quality graphene in a lab setting.

2.2.1. Deterministic visco-elastic transfer

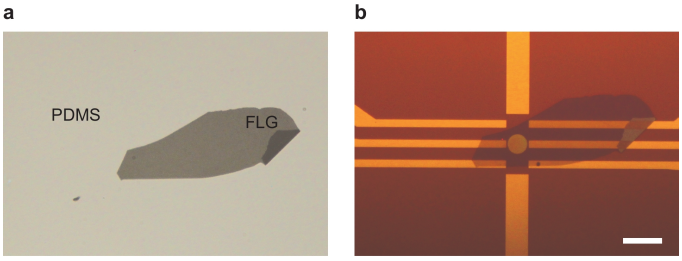

Figure 2.6: **a** Transmission optical microscopy image of few-layer-graphene (FLG) exfoliated onto polydimethyl siloxane (PDMS). **b** Reflection opical microscopy image of FLG transferred onto a circular cavity and a set of electrodes. Scalebar: 10 µm.

We have tested many transfer methods throughout the years, however, here we focus on only a few methods which are relevant for the projects in this dissertation. The first method we describe is the deterministic viscoelastic stamping method developed by Castellanos-Gomez *et al.* [5]. Instead of the commercial polydimethyl siloxane (PDMS) Castellanos-Gomez *et al.* used, we used home-made PDMS by

mixing Sylgard 184 base with the curing agent in a ratio of 10:1. After sufficient mixing, the mixture is degassed for an hour and left in room temperature for 48 hours to settle in a flat configuration and harden. We observe that these PDMS films are less sticky, cleaner, flatter and easier to leave down the flakes. However, the low adhesive property of the home made PDMS makes it more difficult to exfoliate monolayers of 2D materials. Therefore, we use the commercial PDMS when isolation of monolayers is compulsory and the home-made PDMS for the ease of transfer when multi-layers are sufficient. In Fig. 2.6, an example of the deterministic PDMS transfer process is shown. Figure 2.6a shows a transmission optical microscopy image of few-layer-graphene (FLG) exfoliated onto the PDMS (image inverted for the ease of visualization). Once an appropriate flake is identified on the PDMS, then it is inserted into a xyz stage for the deterministic transfer of the flake. For example, the flake is transferred onto a set of electrodes and a cavity as shown in Fig. 2.6b. This device is used for a piezoelectric actuator device shown in outlook, Chapter 7.

2.2.2. Polymer Pickup

Polymer assisted transfer of 2D materials has become ubiquitous in labs studying exfoliated 2D materials and their heterostructures. Typically, a PDMS film is used as a handling layer for a polymer layer which is coated on top. The polymer layers are either spin coated or draped on like a blanket over the PDMS layer. The polymers typically used for the transfers are polycarbonate (PC) [24] and polypropylene carbonate (PPC) [25]. These polymers are prepared by dissolving their pure solid pellets into anisole, chloroform or dichloromethane in a 6 % - 15 % w.t. solutions. Afterwards, they are drop cast on top of a coverglass and sandwiched with another cover glass. By sliding the two cover glasses past each other, individual cover glasses are coated with the polymer. Once these polymer coated cover glasses are lightly baked and cooled down, they are ready to be applied. In order to apply these films, a piece of Scotch tape is used as a handle. A hole is cut out in the center of the tape and this tape is applied onto the polymer coated cover glass. Then the tape can be peeled off along with the polymer film which can be draped over a PDMS block for the pick-up of 2D materials. In our case, we use small domes made of PDMS [26] to have better spatial control over the specific flake we wish to transfer and then apply a layer of either PC or PPC by draping it over the dome. In table 2.1 we compare the three techniques.

2.3. Complex oxides

Complex oxides unlike 2D materials do not have van der Waals gaps between the layers, so typically, complex oxides are not considered as exfoliatable materials. Some Ruddlesden-Popper phases of complex oxides such as Sr_2RuO_4 and layered superconductors such as YBCO are few examples where the crystals separate along preferential cleavage planes but these are difficult to exfoliate down to atomically thin limits. Figure 2.7 shows one of the thinnest flakes of Sr_2RuO_4 we managed to exfoliate as an example. Figure 2.7a-b show AFM of the flake, which is ap-

Polymer	bare flat PDMS	PPC/PDMS domes	PC/PDMSdomes
T_g	-	40 °C	147 °
Residues	Least	Invisible under optical microscope but visible under AFM & SEM	Thick puddles
Suspended Structure Compatible	Yes	Yes	PC removal problem
Monolayer Compatible	Yes but low yield	only via h-BN	Yes

Table 2.1: Table comparing various transfer methods.

proximately 300 nm thick. Devices are fabricated using this flake (Fig. 2.7c) and characterized in a flow cryostat (Fig. 2.7d-f). In this sample, the resistance vs. temperature (R-T, Fig. 2.7d) cannot resolve the full superconducting transition of Sr_2RuO_4 due to the temperature limitation of the flow-cryostat. The T_c of Sr_2RuO_4 is expected to be 1.3 K [27] which is near the limit of our cryostat. However, the current-voltage (I-V) characteristic and the differential resistance (dV/dI-I) taken at 1.4 K in Fig. 2.7e,f show signatures of the beginnings of a superconducting transition.

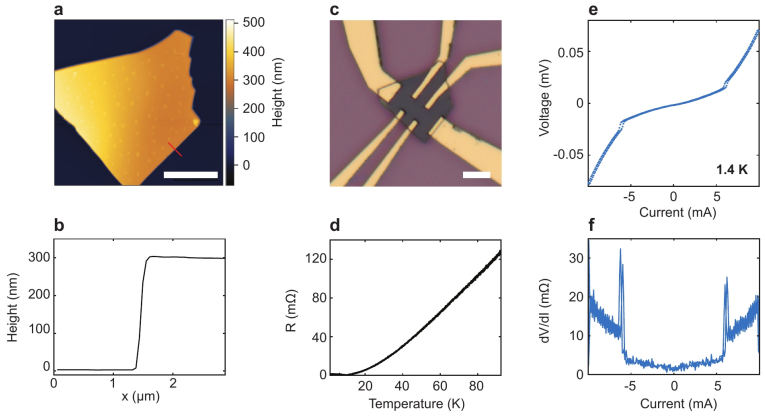

Figure 2.7: **a** AFM scan of a Sr_2RuO_4 flake. Scalebar: 4 µm. Red line indicates where a profile is taken. **b** Step height measurement of the edge of the flake indicated by the red line in **a**. **c** Optical microscopy image of a Hall bar device fabricated from the flake in **a**. Scale bar: 5 µm. **d** Four-probe resistance of device shown in **c** measured as a function of temperature. **e** Current-voltage relation measured at 1.4 K. **f** Differential resistance at 1.4 K. IV and dV/dI both show signs of the onset of superconductivity.

2.3.1. Free-standing complex oxides

Unlike 2D materials which consist of van der Waals gaps between the layers, complex oxides typically have chemical bonds between the unit cells, prohibiting their study in the ultra-thin, free-standing form. Emergence of interfacial effects such as polar discontinuities [33], inversion symmetry breaking [34] and epitaxial strain [35] are interesting phenomena, but at the same time, complicate the study of layer

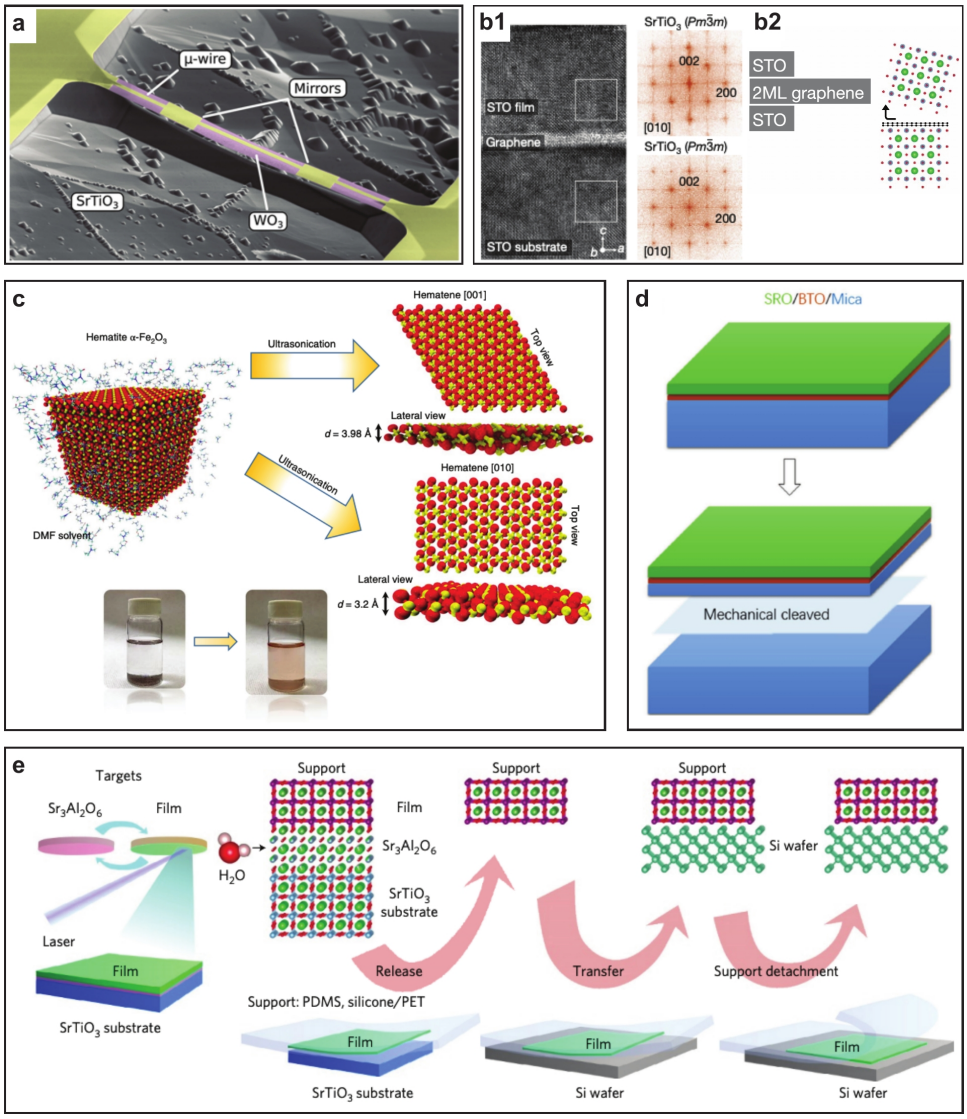

Figure 2.8: **a** False colored scanning electron microscope image of suspended WO_3 beam achieved by selectively etching away the substrate $SrTiO_3$ (figure adapted from [28]). **b1** Cross-sectional transmission electron microscopy image of crystalline $SrTiO_3$ grown on $SrTiO_3$ substrate with 2 layers of graphene as transparent buffer layer. **b2** Illustration of the cleaving process after growth (figure adapted from [29]). **c** Illustration of the liquid phase exfoliation of hematite from bulk crystals to its monolayer form using dimethylformamide (DMF) and sonication (figure adapted from [30]). **d** Illustration of the mechanical exfoliation of $SrRuO_3/BaTiO_3$ grown on layered mica substrate (figure adapted from [31]). **e** Illustration of pulsed laser deposition of the film-of-interest on a sacrificial water soluble layer $Sr_3Al_2O_6$ and release in water (figure adapted from [32]).

dependence of the physical properties of a material. It is only recent that free-standing single crystal complex oxides in their ultra-thin limit have been studied. For example, the coexistence of magnetism and superconductivity was discovered in Ca_2RuO_4 in the ultra-thin, strain-relaxed state [36]. In the bulk, Ca_2RuO_4 is a Mott insulator [37] which is correlated to the strain induced octahedral rotations. Nobukane *et al.* reported that when thinned down below a critical thickness, strain is reduced in Ca_2RuO_4 resulting in the relaxation of the octahedral tilt. In this ultra-thin strain relaxed state, Ca_2RuO_4 becomes a superconductor with a T_c of 64 K. Therefore, studying the free-standing form of complex oxides in the ultra thin limit is critical for the discovery of important states such as HTSC.

In recent years, many techniques to release epitaxially grown layers have been developed. Some of these techniques are illustrated in Fig. 2.8. Figure 2.8a shows a WO_3 micro bridge fabricated by selectively etching away the $SrTiO_3$ substrate [28]. This technique is often used in the release of 2D materials from SiO_2 substrates as well. This technique allows for the preservation of epitaxial strain, but is limited by the materials which are etch resistant to HF used to selectively etch away the substrate.

Figure 2.8b shows the growth of complex oxides on a transparent buffer layer which is later used to cleave the material grown on top [29]. In this case, two layers of graphene are used as a transparent barrier which the additional layers of $SrTiO_3$ ignore, thus growing in a crystalline fashion following the crystallinity of the substrate. This is a powerful technique which can cleanly release the entire over-layer with a size limited by the size of the graphene sheets and the growth technique. Unfortunately, this technique is limited to a few materials which grow well in vacuum because graphene quickly gets damaged at high temperatures in the presence of oxygen. Since high temperature and the presence of oxygen are common growth conditions of complex oxides, this technique is not universal to those materials which preferentially grow in high temperatures and oxygen pressures. Furthermore, transferring graphene twice and cleaving away the over-layer need specialization in both graphene growth as well as oxide growth.

Figure 2.8c shows an illustration of the liquid phase exfoliation process. This method is used to exfoliate hematite down to its monolayer [30] as well as Sr_2RuO_4 down to a few tens of nano meters [38]. Nobukane *et al.* also used a similar method to thin down Ca_2RuO_4 [36]. This is a simple and scalable technique, but - similar to the "graphene" produced in this manner [17] - lack reproducibility.

Figure 2.8d shows a method to mechanically exfoliate complex oxides from a layered mica substrate [31]. In this technique, the $BaTiO_3$ buffer layer along with the top-most layers of mica are not removed from the material of interest, $SrRuO_3$. Since $SrRuO_3$ in proximity to a ferroelectric such as $BaTiO_3$ is shown to host spin textures (skyrmions) and topological Hall effect [39] while with symmetric boundary conditions this is not observed [40], their findings do not fully represent the properties of free-standing $SrRuO_3$.

Finally, in Fig. 2.8e, a water-based release technique is illustrated. By growing a film of interest on top of a sacrificial buffer layer which is soluble in water, the film of interest can be released from the substrate by immersion in water [32]. The lat-

tice parameter of the sacrificial layer $Sr_3Al_2O_6$ can be tuned to facilitate the growth of a wide range of complex oxides by substitutional doping of Ca [41]. Using this technique, the suspension of a single unit cell of $SrTiO_3$ has been demonstrated [42]. In Chapter 7, this technique is employed for the study of free-standing $SrRuO_3$ and $BaTiO_3$ devices.

2.3.2. PLD growth

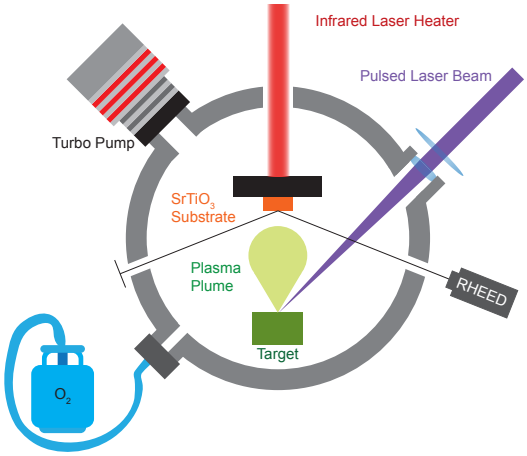

Figure 2.9: Illustration of the PLD chamber.

Recent advancements in releasing complex oxides from the growth substrate has allowed the study of 3D crystals in their atomically thin forms in the absence of epitaxial strain. As discussed in the previous section, thin films of complex oxides can be grown on a buffer layer which is later used to release the material of interest from the growth substrate. Unlike the mechanical exfoliation techniques (dry and in solvent) that rely on randomness, statistics and luck, deterministically growing a material of interest gives larger yield, better control of the number of layers and larger flakes of lateral dimensions.

There are mainly two methods of releasing an epitaxially grown 3D crystal completely from the substrate. The first method consists of a buffer layer which is also epitaxially grown and is itself a single crystal and later removing this layer by selective etching. Lu *et al.* reported such a technique where an epitaxial sacrificial layer $Sr_3Al_2O_6$ (SAO) is used in between the substrate and the material of interest as a buffer layer which is later removed by dissolving in water [32]. The second method consists of a transparent buffer layer which provides the crystalline footprint of the underlying substrate while later on be used as a weak link for the cleaving of the material grown on top. Kum *et al.* reported the cleaving of complex oxides by using double layer graphene as a transparent buffer layer [29]. Crystals grown on top of the double layer graphene were single crystalline, ignoring the graphene barrier. After growth, the van der Waals gap between the graphene layers provided a weak link for the epitaxially grown film to be easily cleaved away from the substrate. In

the outlook of this thesis, we show some preliminary work on studying the properties of free-standing complex oxides. We use the first technique by Lu *et al.* which involves growing single crystal SAO on top of TiO_2 terminated $SrTiO_3$ (STO) (001).

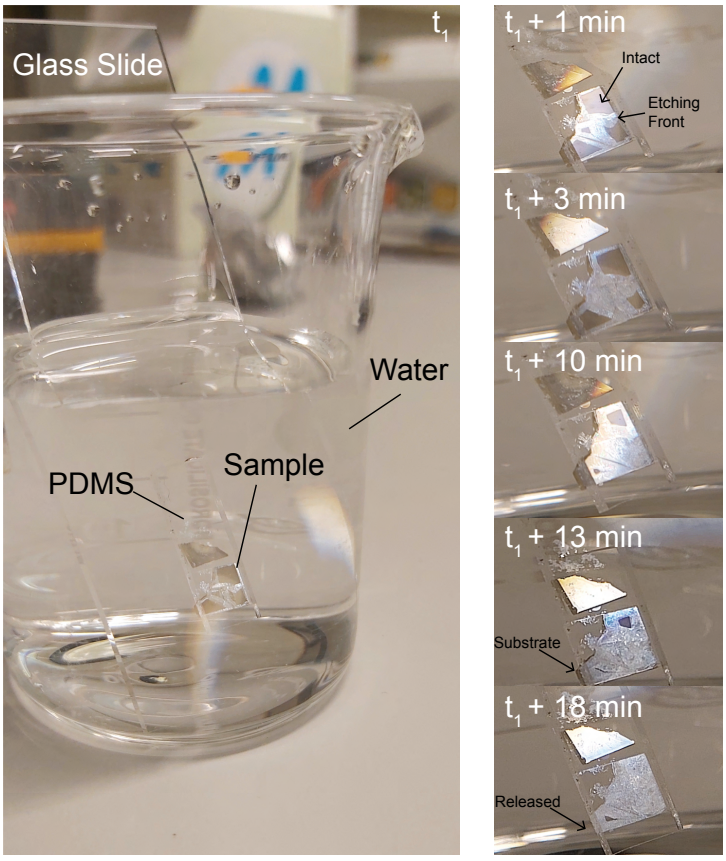

Figure 2.10: Releasing process of complex oxides in water. Left image shows how the sample is placed in a beaker filled with deionized water. Glass slide is used as a handle and PDMS as a support layer. Right panel of images show the progression of etching process. As time passes, the size of the dark area reduces. At t_1+18 min SAO is fully etched and the substrate detaches from the PDMS.

We grow the complex oxide films using pulsed laser deposition (PLD) which is depicted in Fig. 2.9. A chamber is pressure controlled using high purity O_2 and a turbo pump. An infra-red laser is used to heat the substrate from the back and a pulsed KrF excimer laser is used to deposit the films. The pulsed laser is exposed onto the target at a fixed frequency to create a repetition of plasma plume which travels within the pressure controlled chamber towards the substrate. The oxygen pressure controls the mean free path of the plume as well as the stoichiometry between the A and B atoms with respect to the O content. The temperature affects how mobile the atomic species are on top of the surface. During the growth process, reflection high energy electron diffraction (RHEED) is used to monitor the number

of unit cells and the quality of deposition.

Figure 2.10 shows images of the water etching process on a sample with multiple cracks, which illustrates the etching process. On the left, a glass slide partially submerged in a beaker half full of water is shown. The STO substrate is attached to a film of PDMS with the film side facing the PDMS and the PDMS film is attached to the glass slide. This image is taken a few minutes after the immersion at time equal to t_1. The right panel shows the images taken at 1-18 minutes after t_1. The etching process can be observed from the decreasing area of the dark region and increasing light areas propagating from the edges and the cracks. At $t = t_1 + 18$ min, the SAO film is etched away and the substrate detaches from the PDMS.

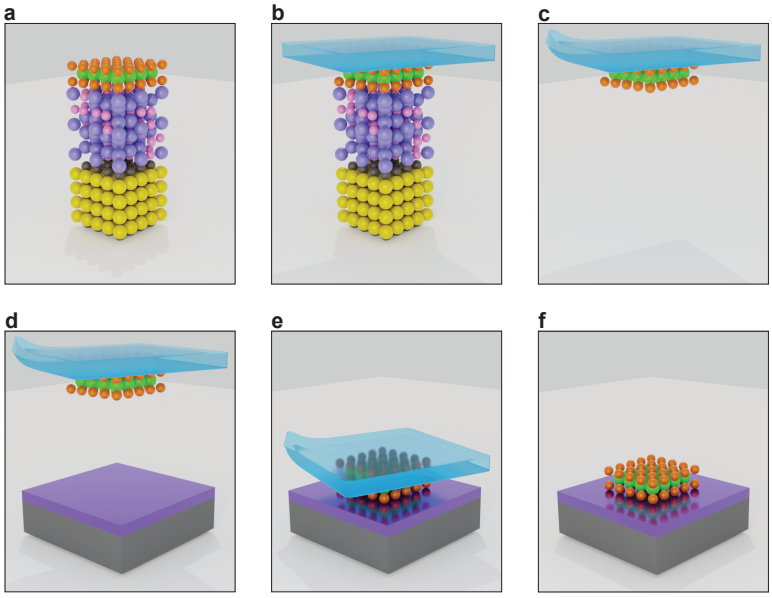

Figure 2.11: Illustration of the releasing process of complex oxides. **a** PLD grown ABO_3 (green & orange) layer on water soluble $Sr_3Al_2O_6$ (violet & pink) on $SrTiO_3$ substrate (yellow & grey). **b** PDMS is attached to the top. **c** Submerging in water releases the ABO_3 layer from the substrate.**d** Clean dummy SiO_2/Si is prepared.**e** Using the deterministic transfer process [5], the film is transferred onto a SiO_2/Si substrate. **f** PDMS is removed leaving the free-standing oxide film on SiO_2/Si.

Figure 2.11 shows the transfer procedure for the films grown on SAO/STO. Figure 2.11a shows a film of interest (green-orange) grown on SAO (purple-pink)/ STO (yellow-grey). A layer of PDMS is applied on the top of this stack as a support during the undercutting procedure (Fig. 2.11b). The sample covered with PDMS is submerged in water for more than 24 hours to ensure full dissolution of the SAO layer. Once the substrate is detached from the film, the PDMS/film is blow-dried (Fig. 2.11c). A dummy SiO_2/Si is used as an intermediate substrate for the characterization using X-ray diffraction (XRD) (Fig. 2.11d). Using the deterministic transfer setup [5], the film is brought in contact with the SiO_2/Si (Fig. 2.11e). Finally, the PDMS is peeled away leaving the film of free-standing complex oxide on

SiO_2/Si (Fig. 2.11f) ready for XRD. After XRD, adequate flakes are identified for the device fabrication and transferred from the dummy SiO_2/Si to a device using one of the polymer assisted transfer techniques discussed above.

References

[1] K. I. Bolotin, K. J. Sikes, Z. Jiang, M. Klima, G. Fudenberg, J. Hone, P. Kim, and H. Stormer, "Ultrahigh electron mobility in suspended graphene," *Solid state communications*, vol. 146, no. 9-10, pp. 351–355, 2008.

[2] A. De Sanctis, J. D. Mehew, S. Alkhalifa, F. Withers, M. F. Craciun, and S. Russo, "Strain-engineering of twist-angle in graphene/hBN superlattice devices," *Nano letters*, vol. 18, no. 12, pp. 7919–7926, 2018.

[3] Y. Liu, J. Guo, E. Zhu, L. Liao, S.-J. Lee, M. Ding, I. Shakir, V. Gambin, Y. Huang, and X. Duan, "Approaching the schottky-mott limit in van der waals metal-semiconductor junctions," *Nature*, vol. 557, no. 7707, pp. 696–700, 2018.

[4] J. S. Bunch, A. M. Van Der Zande, S. S. Verbridge, I. W. Frank, D. M. Tanenbaum, J. M. Parpia, H. G. Craighead, and P. L. McEuen, "Electromechanical resonators from graphene sheets," *Science*, vol. 315, no. 5811, pp. 490–493, 2007.

[5] A. Castellanos-Gomez, M. Buscema, R. Molenaar, V. Singh, L. Janssen, H. S. J. Van Der Zant, and G. A. Steele, "Deterministic transfer of two-dimensional materials by all-dry viscoelastic stamping," *2D Materials*, vol. 1, no. 1, p. 011002, 2014.

[6] K. S. Novoselov, A. K. Geim, S. V. Morozov, D. Jiang, Y. Zhang, S. V. Dubonos, I. V. Grigorieva, and A. A. Firsov, "Electric field effect in atomically thin carbon films," *science*, vol. 306, no. 5696, pp. 666–669, 2004.

[7] Y. Hernandez, V. Nicolosi, M. Lotya, F. M. Blighe, Z. Sun, S. De, I. McGovern, B. Holland, M. Byrne, Y. K. Gun'Ko, *et al.*, "High-yield production of graphene by liquid-phase exfoliation of graphite," *Nature nanotechnology*, vol. 3, no. 9, pp. 563–568, 2008.

[8] A. Islam, B. Mukherjee, K. K. Pandey, and A. K. Keshri, "Ultra-fast, chemical-free, mass production of high quality exfoliated graphene," *ACS nano*, vol. 15, no. 1, pp. 1775–1784, 2021.

[9] W. Zhao, M. Fang, F. Wu, H. Wu, L. Wang, and G. Chen, "Preparation of graphene by exfoliation of graphite using wet ball milling," *Journal of materials chemistry*, vol. 20, no. 28, pp. 5817–5819, 2010.

[10] J. Kim, H. Park, J. B. Hannon, S. W. Bedell, K. Fogel, D. K. Sadana, and C. Dimitrakopoulos, "Layer-resolved graphene transfer via engineered strain layers," *Science*, vol. 342, no. 6160, pp. 833–836, 2013.

[11] O. C. Compton and S. T. Nguyen, "Graphene oxide, highly reduced graphene oxide, and graphene: versatile building blocks for carbon-based materials," *small*, vol. 6, no. 6, pp. 711–723, 2010.

[12] X. Li, W. Cai, J. An, S. Kim, J. Nah, D. Yang, R. Piner, A. Velamakanni, I. Jung, E. Tutuc, *et al.*, "Large-area synthesis of high-quality and uniform graphene films on copper foils," *science*, vol. 324, no. 5932, pp. 1312–1314, 2009.

[13] K. V. Emtsev, A. Bostwick, K. Horn, J. Jobst, G. L. Kellogg, L. Ley, J. L. McChesney, T. Ohta, S. A. Reshanov, J. Röhrl, *et al.*, "Towards wafer-size graphene layers by atmospheric pressure graphitization of silicon carbide," *Nature materials*, vol. 8, no. 3, pp. 203–207, 2009.

[14] J.-H. Lee, E. K. Lee, W.-J. Joo, Y. Jang, B.-S. Kim, J. Y. Lim, S.-H. Choi, S. J. Ahn, J. R. Ahn, M.-H. Park, *et al.*, "Wafer-scale growth of single-crystal monolayer graphene on reusable hydrogen-terminated germanium," *Science*, vol. 344, no. 6181, pp. 286–289, 2014.

[15] O. Gröning, S. Wang, X. Yao, C. A. Pignedoli, G. B. Barin, C. Daniels, A. Cupo, V. Meunier, X. Feng, A. Narita, *et al.*, "Engineering of robust topological quantum phases in graphene nanoribbons," *Nature*, vol. 560, no. 7717, pp. 209–213, 2018.

[16] S. Bae, H. Kim, Y. Lee, X. Xu, J.-S. Park, Y. Zheng, J. Balakrishnan, T. Lei, H. R. Kim, Y. I. Song, *et al.*, "Roll-to-roll production of 30-inch graphene films for transparent electrodes," *Nature nanotechnology*, vol. 5, no. 8, p. 574, 2010.

[17] A. P. Kauling, A. T. Seefeldt, D. P. Pisoni, R. C. Pradeep, R. Bentini, R. V. Oliveira, K. S. Novoselov, and A. H. Castro Neto, "The worldwide graphene flake production," *Advanced Materials*, vol. 30, no. 44, p. 1803784, 2018.

[18] J. Romijn, S. Vollebregt, R. J. Dolleman, M. Singh, H. S. van der Zant, P. G. Steeneken, and P. M. Sarro, "A miniaturized low power pirani pressure sensor based on suspended graphene," in *2018 IEEE 13th Annual International Conference on Nano/Micro Engineered and Molecular Systems (NEMS)*, pp. 11–14, IEEE, 2018.

[19] F. Ricciardella, S. Vollebregt, B. Boshuizen, F. Danzl, I. Cesar, P. Spinelli, and P. M. Sarro, "Wafer-scale transfer-free process of multi-layered graphene grown by chemical vapor deposition," *Materials Research Express*, vol. 7, no. 3, p. 035001, 2020.

[20] M. Onodera, S. Masubuchi, R. Moriya, and T. Machida, "Assembly of van der waals heterostructures: exfoliation, searching, and stacking of 2d materials," *Japanese Journal of Applied Physics*, vol. 59, no. 1, p. 010101, 2020.

[21] R. Frisenda, E. Navarro-Moratalla, P. Gant, D. P. De Lara, P. Jarillo-Herrero, R. V. Gorbachev, and A. Castellanos-Gomez, "Recent progress in the assembly of nanodevices and van der waals heterostructures by deterministic placement of 2d materials," *Chemical Society Reviews*, vol. 47, no. 1, pp. 53–68, 2018.

[22] S. Fan, Q. A. Vu, M. D. Tran, S. Adhikari, and Y. H. Lee, "Transfer assembly for two-dimensional van der waals heterostructures," *2D Materials*, vol. 7, no. 2, p. 022005, 2020.

[23] X. Cao, C. Jiang, D. Tan, Q. Li, S. Bi, and J. Song, "Recent mechanical processing techniques of two-dimensional layered materials: a review," *Journal of Science: Advanced Materials and Devices*, 2021.

[24] P. Zomer, M. Guimarães, J. Brant, N. Tombros, and B. Van Wees, "Fast pick up technique for high quality heterostructures of bilayer graphene and hexagonal boron nitride," *Applied Physics Letters*, vol. 105, no. 1, p. 013101, 2014.

[25] F. Pizzocchero, L. Gammelgaard, B. S. Jessen, J. M. Caridad, L. Wang, J. Hone, P. Bøggild, and T. J. Booth, "The hot pick-up technique for batch assembly of van der waals heterostructures," *Nature communications*, vol. 7, no. 1, pp. 1–10, 2016.

[26] K. Kim, M. Yankowitz, B. Fallahazad, S. Kang, H. C. Movva, S. Huang, S. Larentis, C. M. Corbet, T. Taniguchi, K. Watanabe, *et al.*, "van der waals heterostructures with high accuracy rotational alignment," *Nano letters*, vol. 16, no. 3, pp. 1989–1995, 2016.

[27] A. P. Mackenzie and Y. Maeno, "The superconductivity of Sr_2RuO_4 and the physics of spin-triplet pairing," *Reviews of Modern Physics*, vol. 75, no. 2, p. 657, 2003.

[28] N. Manca, G. Mattoni, M. Pelassa, W. J. Venstra, H. S. van der Zant, and A. D. Caviglia, "Large tunability of strain in WO_3 single-crystal microresonators controlled by exposure to H_2 gas," *ACS applied materials & interfaces*, vol. 11, no. 47, pp. 44438–44443, 2019.

[29] H. S. Kum, H. Lee, S. Kim, S. Lindemann, W. Kong, K. Qiao, P. Chen, J. Irwin, J. H. Lee, S. Xie, *et al.*, "Heterogeneous integration of single-crystalline complex-oxide membranes," *Nature*, vol. 578, no. 7793, pp. 75–81, 2020.

[30] A. P. Balan, S. Radhakrishnan, C. F. Woellner, S. K. Sinha, L. Deng, C. de Los Reyes, B. M. Rao, M. Paulose, R. Neupane, A. Apte, *et al.*, "Exfoliation of a non-van der waals material from iron ore hematite," *Nature nanotechnology*, vol. 13, no. 7, pp. 602–609, 2018.

[31] J. Liu, Y. Feng, R. Tang, R. Zhao, J. Gao, D. Shi, and H. Yang, "Mechanically tunable magnetic properties of flexible $SrRuO_3$ epitaxial thin films on mica substrates," *Advanced Electronic Materials*, vol. 4, no. 4, p. 1700522, 2018.

[32] D. Lu, D. J. Baek, S. S. Hong, L. F. Kourkoutis, Y. Hikita, and H. Y. Hwang, "Synthesis of freestanding single-crystal perovskite films and heterostructures by etching of sacrificial water-soluble layers," *Nature materials*, vol. 15, no. 12, pp. 1255–1260, 2016.

[33] N. Nakagawa, H. Y. Hwang, and D. A. Muller, "Why some interfaces cannot be sharp," *Nature materials*, vol. 5, no. 3, pp. 204–209, 2006.

[34] J. Matsuno, N. Ogawa, K. Yasuda, F. Kagawa, W. Koshibae, N. Nagaosa, Y. Tokura, and M. Kawasaki, "Interface-driven topological hall effect in SrRuO$_3$-SrIrO$_3$ bilayer," *Science Advances*, vol. 2, no. 7, p. e1600304, 2016.

[35] M. Uchida, T. Nomoto, M. Musashi, R. Arita, and M. Kawasaki, "Superconductivity in uniquely strained RuO$_2$ films," *Physical Review Letters*, vol. 125, no. 14, p. 147001, 2020.

[36] H. Nobukane, K. Yanagihara, Y. Kunisada, Y. Ogasawara, K. Isono, K. Nomura, K. Tanahashi, T. Nomura, T. Akiyama, and S. Tanda, "Co-appearance of superconductivity and ferromagnetism in a Ca$_2$RuO$_4$ nanofilm crystal," *Scientific reports*, vol. 10, no. 1, pp. 1–10, 2020.

[37] D. Sutter, C. Fatuzzo, S. Moser, M. Kim, R. Fittipaldi, A. Vecchione, V. Granata, Y. Sassa, F. Cossalter, G. Gatti, *et al.*, "Hallmarks of Hunds coupling in the Mott insulator Ca$_2$RuO$_4$," *Nature communications*, vol. 8, no. 1, pp. 1–7, 2017.

[38] Y. Ying, N. Staley, Y. Xin, K. Sun, X. Cai, D. Fobes, T. Liu, Z. Mao, and Y. Liu, "Enhanced spin-triplet superconductivity near dislocations in Sr$_2$RuO$_4$," *Nature communications*, vol. 4, no. 1, pp. 1–7, 2013.

[39] L. Wang, Q. Feng, Y. Kim, R. Kim, K. H. Lee, S. D. Pollard, Y. J. Shin, H. Zhou, W. Peng, D. Lee, *et al.*, "Ferroelectrically tunable magnetic skyrmions in ultrathin oxide heterostructures," *Nature materials*, vol. 17, no. 12, pp. 1087–1094, 2018.

[40] D. J. Groenendijk, C. Autieri, T. C. van Thiel, W. Brzezicki, J. Hortensius, D. Afanasiev, N. Gauquelin, P. Barone, K. van den Bos, S. van Aert, *et al.*, "Berry phase engineering at oxide interfaces," *Physical Review Research*, vol. 2, no. 2, p. 023404, 2020.

[41] S. S. Hong, M. Gu, M. Verma, V. Harbola, B. Y. Wang, D. Lu, A. Vailionis, Y. Hikita, R. Pentcheva, J. M. Rondinelli, *et al.*, "Extreme tensile strain states in La$_{0\cdot7}$Ca$_{0\cdot3}$MnO$_3$ membranes," *Science*, vol. 368, no. 6486, pp. 71–76, 2020.

[42] D. Ji, S. Cai, T. R. Paudel, H. Sun, C. Zhang, L. Han, Y. Wei, Y. Zang, M. Gu, Y. Zhang, *et al.*, "Freestanding crystalline oxide perovskites down to the monolayer limit," *Nature*, vol. 570, no. 7759, pp. 87–90, 2019.

3

3

Sensitive capacitive pressure sensors based on graphene membrane arrays

The high flexibility, impermeability and strength of graphene membranes are key properties that can enable the next generation of nanomechanical sensors. However, for capacitive pressure sensors the sensitivity offered by a single suspended graphene membrane is too small to compete with commercial sensors. Here, we realize highly sensitive capacitive pressure sensors consisting of arrays of nearly ten thousand small, freestanding double-layer graphene membranes. We fabricate large arrays of small diameter membranes using a procedure that maintains the superior material and mechanical properties of graphene, even after high-temperature anneals. These sensors are readout using a low cost battery-powered circuit board, with a responsivity of up to 47.8 *aF* $Pa^{-1}mm^{-2}$*, thereby outperforming commercial sensors.*

Parts of this chapter have been published in Microsystems & Nanoengineering **6**, 102 (2020) by M. Šiškins, **M. Lee**, D. Wehenkel, R. van Rijn, T. W. de Jong, J. R. Renshof, B. C. Hopman, W. S. J. M. Peters, D. Davidovikj, H. S. J. van der Zant, and P. G. Steeneken.

3.1. Introduction

Graphene grown by chemical vapour deposition (CVD) is a strong candidate for realizing next-generation sensor devices [1]. Its hermeticity [2–4], and superior mechanical [5–7] and electrical [8] properties, have enabled various types of gas pressure sensors. In most conventional pressure sensors, the pressure is determined from the deflection of a membrane due to the pressure difference between ambient gas and gas in a hermetically sealed reference cavity. There are different ways to readout the deflection of the membrane and thereby quantify the pressure difference. In capacitive graphene pressure sensors, the deflection is readout by measuring the capacitance between the graphene membrane and a reference electrode [9–12]. As the pressure induced deflection increases the mechanical stress and tension in the membrane, it can be measured using the piezoresistive effect [13–15] and can also be probed via the mechanical resonance frequency [2, 3, 16]. In contrast, graphene squeeze-film pressure sensors [17] and Pirani pressure sensors [18] do not require a hermetic reference cavity and operate at small deflection, which can be beneficial for their operation range.

Resonant sensors are conceptually attractive because they potentially offer both gas sensing [19, 20] and pressure sensing [2, 17] functionality within a single device. However, accurate readout of resonance frequencies with low-power electronics is challenging, requires elimination of mass loading and can not be easily scaled up to many devices in parallel. In piezoresistive and Pirani sensors, it is a challenge to eliminate non-pressure related effects of the surrounding gas on the graphene resistance. In contrast, capacitive pressure sensors have the advantage that the membrane capacitance is rather insensitive to gas induced changes in its mass and electrical resistance, and thus depends mainly on geometry and membrane deflection. However, it was found that a single graphene membrane with a diameter of 5 μm has a too small responsivity (< 0.1 aF Pa^{-1}) to be competitive with commercial sensors [12].

In this work, we counter this drawback by creating arrays with a large number of membranes connected in parallel to increase the responsivity [12]. We present few-atom thick pressure sensors that can compete with commercial capacitive pressure sensors using arrays of nearly 10000 double-layer graphene (DLG) membranes. We optimize the design of the sensor elements, the chip layout and the readout electronics to attain a handheld, low-cost, battery-powered electrical readout circuit capable of detecting pressure changes via the static deflection of graphene nanodrums.

3.2. Materials and Methods

3.2.1. Chip design and graphene transfer

Simulations [12] show that to achieve the commercially competitive sensitivity, an array of around 10000 circular graphene drums is needed, each with a diameter of 5 micron. When the drums are placed on a hexagonal grid with a pitch of 10 micron between their centers, they fit on a 1×1 mm^2 chip as shown in Fig. 3.1a. To fabricate this design, Ti/Au electrodes (5 nm/60 nm), for contacting the graphene

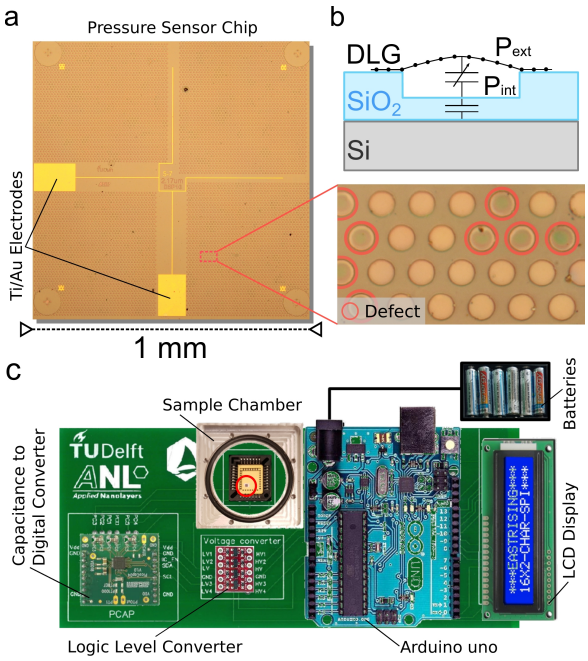

Figure 3.1: Pressure sensor and readout circuitry. (a) Optical image of the sensor chip with 10000 circular holes, a DLG/PMMA membrane and Ti/Au electrodes. Close-up image shows the difference in contrast between intact and defect drums with red circles indicating collapsed membranes. (b) Schematic device cross-section and capacitive pressure readout principle. (c) Read-out circuitry PCB board with the elements labeled. The total size of the PCB board is 6.9×17.5 cm^2. The red circle indicates the pressure sensor chip.

top electrode, are patterned on a silicon chip with a 285 nm SiO_2 layer. Then the pattern of circular holes with a depth of 240 nm is reactive ion etched into the SiO_2. As shown in the cross-section in Fig. 3.1b, the cavity depth of the holes is less than the SiO_2 layer thickness to prevent the graphene from touching the silicon bottom electrode, and thereby creating an electrical short-circuit between the electrodes, when one of the membranes collapses. As a last step the graphene is transferred over the cavities. We use two layers of graphene and small membrane diameter to improve the yield [21] and the mechanical strength [7, 22]. Since the probability that 2 pore defects align is low, the impermeability of DLG is also much higher than that of single layer graphene [3].

To fabricate the double layer graphene (DLG), two sheets of CVD graphene are synthesized and then stacked on top of each other maintaining a pristine quality interface between the sheets. Using Polymethyl Methacrylate (PMMA) as a support layer of 800 nm thickness, DLG is suspended over the pre-patterned circular holes in the SiO_2/Si chip with Ti/Au electrodes (Fig. 3.1a). DLG was produced and transferred in ambient pressure by Applied Nanolayers. From the differences in contrast between suspended, broken and collapsed drums [21, 23] we estimate that the dry transfer technique results in a yield of 95 – 99% of freely suspended DLG/PMMA

membranes. The red circles in the inset of Fig. 3.1a indicate defect drums in a damaged region of the sample and show this difference in contrast.

3.2.2. Sensor readout circuit board

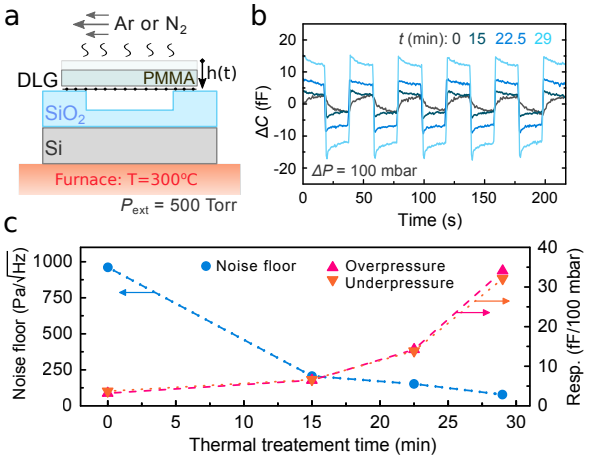

Figure 3.2: Thermal removal of the polymer and its effect on the capacitive response of the sensor. (a) Schematic explanation of the thermal annealing principle that reduces the PMMA thickness $h(t)$. (b) Change in capacitance of a single chip as a function of measurement in response to time dependent pressure changes, ΔP, for samples that have been annealed for different times t (line colors corresponds to color of the corresponding anneal times indicated in the legend). The gas pressure is changed at a rate of 175.4 mbar s^{-1}. (c) Responsivity and noise floor extracted from the data in (b) calculated using equation (3.1).

The graphene capacitive pressure sensor responds to the difference established between the internal pressure of the reference cavity, P_{int} and the external pressure of the environment, P_{ext}. This pressure difference results in a deflection of the atomically thin membrane and a corresponding change in capacitance [12] of the drum, ΔC as schematically depicted in Fig. 3.1b. We wedge bond a 25 μm AlSi 1% wire to Ti/Au pads on a chip for electrical contact to graphene and use a conductive silver-paste to contact the Si substrate. The response of the graphene capacitive pressure sensor is high enough to be read-out by chip-scale commercial electronic components as is demonstrated using the battery-powered circuit shown in Fig. 3.1c. Here, the sample under test is kept in a small on-board vacuum chamber that allows local control over the external gas pressure while preventing the pressure to affect electrical read-out elements. A commercial capacitance to digital converter (AMS PCap04) is then used to record and digitize the capacitance of the sample measured at a peak-to-peak voltage $V_{\text{pp}} = 1.5$ V with a hundred of charge and discharge cycles of 5.73 ms each. After voltage level adjustment by a logic level converter, an Arduino Uno board converts the measured capacitance into pressure using a predetermined calibration curve and displays it on an LCD screen. The circuit board is capable of measuring a change in the chip's capacitance down to ~10 aF on top of a background capacitance of a few tens of picofarads.

3.2.3. Effect of PMMA removal

After chip fabrication and transfer, the PMMA transfer polymer still covers the DLG sheets. In a number of previous studies protective polymer layers were used to support the graphene to increase the yield, mechanical performance, hermeticity and durability of the devices, in both suspended [10, 24] and touch-mode operation [11]. However, the bending rigidity of the polymer layers reduces the deflection and responsivity of the membranes and sensor. To improve the sensor performance we therefore gradually remove the transfer polymer by annealing it in dry gas [25–28], as shown in Fig. 3.2. PMMA removal mechanisms are mostly related to removing pendant functional groups in the polymer at high temperatures [25, 27]. However, this can trigger the reaction between the graphene and the carbon by-products from the residual polymer and produce amorphous carbon [25, 26]. Lower temperatures of the process and an atmosphere of inert gas, like argon, are needed to prevent the production of amorphous carbon and to maintain a good quality of graphene during the thermal annealing [26].

The sample is put inside a furnace and left at a pressure of 500 Torr with a constant flow of 0.5 SLPM of an inert dry gas (Ar or N_2) at a temperature of 300°C as schematically depicted in Fig. 3.2a. We found no notable difference between the use of Ar or N_2 gas flow in terms of the end quality of DLG layers or PMMA removal rate. The average thickness of the transfer PMMA reduces with time at an estimated rate of ~ 27 nm/minute with only minor residues left on and in-between the graphene layers. For some samples, small regions of local PMMA residue accumulation are still present after the annealing procedure. They accumulate on the surface of a DLG layer that has a thickness of 1.4–2.2 nm, as measured by tapping mode atomic force microscopy (AFM) (see Supplementary Fig. 1). The PMMA thickness reduction by thermal treatment is found to substantially improve the responsivity of the sensors. Figure 3.2b shows the capacitance change ΔC of a single chip to external pressure changes between 1000 and 900 mbar with a period of 40 seconds as measured after 0, 15, 22.5 and 29 minutes of annealing. Figure 3.2c shows that by following the thermal anneal procedure, an increase in responsivity of almost an order of magnitude was achieved for this particular sample, while in the best case an increase in responsivity of nearly two orders of magnitude was observed after a 30 minute continuous thermal anneal treatment. Further annealing the sample for longer times does not significantly affect the capacitance response (see Supplementary Fig. 2). The detection noise floor also decreases substantially as a result of the process. The noise floor, NF, in Pa/$\sqrt{\text{Hz}}$ is defined as:

$$NF = \frac{C_{\text{RMS}}}{\frac{dC}{dP}\sqrt{f_{\text{meas}}}}, \tag{3.1}$$

where C_{RMS} is the root mean squared (RMS) noise in the capacitance measurement, $\frac{dC}{dP}$ the responsivity of the sensor and $f_{\text{meas}} = 1.745$ Hz, the frequency at which the measurements are acquired. The decrease in NF as shown in Fig. 3.2c qualitatively follows from the equation (3.1) considering the measured increase in responsivity.

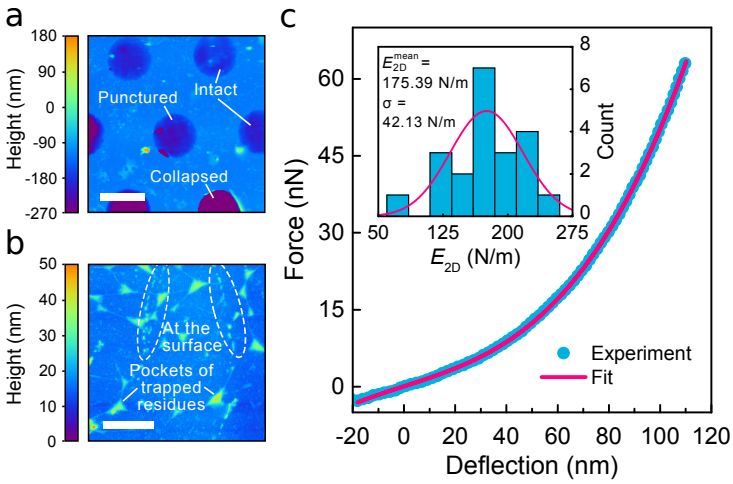

Figure 3.3: Atomic force microscopy (AFM) characterisation of membranes. (a) AFM tapping mode image of DLG drums. State of the drum is labeled. Scale bar: 5 μm. (b) AFM tapping mode image of a supported region of DLG. Residue types are indicated. Scale bar: 1 μm. (c) Force versus membrane deflection curve. Experimental data (blue dots) are fit by the membrane model of equation (3.2). Inset: statistics over 21 membranes with corresponding mean values for the extracted two-dimensional Young's modulus, E_{2D}, with a mean pre-tension $n_0 = 0.04 \pm 0.02$ N/m.

3.3. Results and Discussion

3.3.1. Sample characterization

After thermal treatment for 30 minutes at 300°C, we inspect the samples for damage. In Fig. 3.3a a tapping mode Atomic Force Microscopy (AFM) image of the sample is shown. Three types of drums can be distinguished visually: intact, ruptured and collapsed drums. Collapsed drums are in contact with the bottom of the cavity and probably do not significantly contribute to the response [11] because they are predominantly damaged and thus not airtight. The ruptured drums are also expected to leak fast [17] and therefore have a negligible contribution to the static capacitance response to gradual pressure changes. Intact drums, however, show a full coverage of the cavity. These drums can hermetically seal the cavity with a constant internal pressure exploiting the extremely low permeability of graphene [2–4], although in part of these membranes small pores can be present that are too small to be visually detected. As shown in the AFM measurements in Fig. 3.3b, after the anneal, a substantial number of residues are observed on and below the DLG. The residues form pockets and are also observed in the suspended regions of the device, which suggests that part of the residues is trapped in-between the graphene layers, where they cannot be easily removed [29].

During the fabrication, the capability of graphene to withstand high strains [5, 6, 30] facilitates damage-free transfer, while the thickness of only a few atoms favours higher membrane deflections and thus higher responsivity to pressure changes of the sensor. In order to test the elasticity and mechanical properties of the drums after thermal treatment, we use force-indention AFM to apply a point-force in

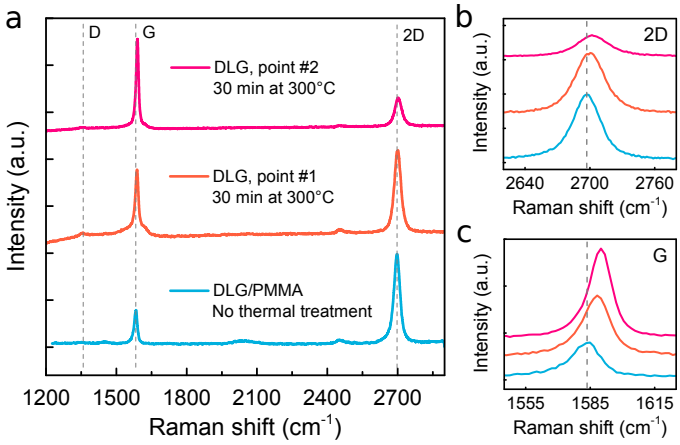

Figure 3.4: Raman spectroscopy of supported DLG. (a) Raman spectra of the DLG/PMMA layer before and after the polymer removal. (b) Close-up of a blue-shift in the 2D peak and (c) the G peaks of graphene.

the centre of a single membrane while measuring its deflection [5]. The applied force, F, is proportional to the stiffness of a cantilever k_c and its deflection Δz_c as $F = k_c \Delta z_c$. We use two cantilevers of $k_c = 1.25 \pm 0.12$ N/m and 1.48 ± 0.05 for two separate sets of measurements in two distant places on the chip. We record a force versus membrane deflection curve at the centre of each drum, as depicted in Fig. 3.3c, and fit it to a model for point deflection of a circular membrane [5, 31]:

$$F = n_0 \pi \delta + E_{2D} R q^3 \left(\frac{\delta}{R}\right)^3, \tag{3.2}$$

where n_0 is the pre-tension, E_{2D} the two dimensional Young's modulus of the layer, $\nu = 0.16$ the Poisson's ratio [7], δ the resulting deflection, R the radius and $q = 1/\left(1.05 - 0.15\nu - 0.16\nu^2\right)$ a geometrical factor [5, 31]. We use the two dimensional Young's modulus, $E_{2D} = E_{3D} h$ for the stacked DLG sheet since the thickness, h, of the layer after the thermal treatment is not well defined. Such an effective quasi-2D Young's modulus provides a more realistic estimate for the mechanical elasticity of the layer and can be directly compared to that of a pristine single layer graphene [5]. In the inset of Fig. 3.3c, the statistics over 21 different drums are shown that yield a mean value of $E_{2D} = 175$ N/m. This is substantially lower than reported values for both exfoliated and pristine CVD single-layer graphene [5, 7], but comparable to other CVD graphene membranes [24, 30, 32, 33], high-quality oxidized graphene sheets [34, 35] and other 2D materials like single-layer MoS_2 [31].

We also examined the sheets of DLG by using Raman spectroscopy, as displayed in Fig. 3.4. Figure 3.4a shows Raman spectra of DLG acquired before the removal of the PMMA layer (blue line) and after the processing at an elevated temperature (orange and magenta line). Before the thermal treatment, the Raman spectrum of DLG is reasonably homogeneous across the chip, showing a Lorenzian-shaped 2D peak of graphene and a well-defined G peak [36]. Full width at half maximum

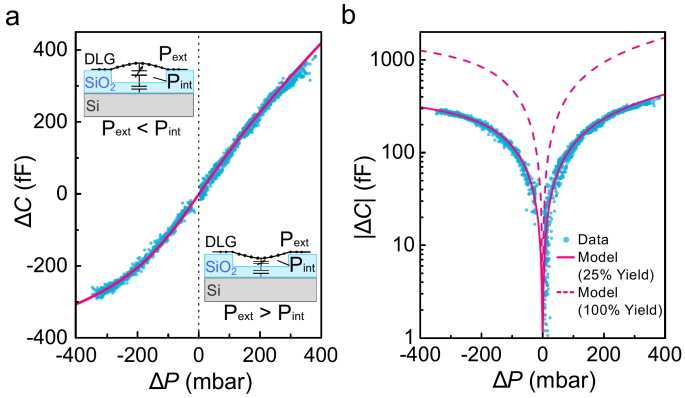

Figure 3.5: Capacitance-pressure curves of the DLG pressure sensor. (a) Measured capacitance-pressure curve (blue points); solid magenta line is a fit of equation (3.5) to the data with P_{int} = 0.933 bar, N/N_{tot}=0.25, E_{2D}=175 N/m and n_0 = 0.45 N/m. Insets: schematic images of the effect of membrane deflection. (b) Comparison, on log-scale, of the measured data (blue points) to the model with 100% (magenta dashed line) and 25% (solid magenta line) yield of the hermetic drums using the 2D Young's modulus from Fig. 3.3. All data is acquired during a continuous measurement within a total time of 1 hour at $P_{\text{ext}} \neq P_{\text{int}}$ with a maximal rate of change of the gas pressure of 3.3 mbar s^{-1}.

(FWHM) of the 2D peak is around ~ 30 cm^{-1} and a high intensity ratio of 2D to G peaks resemble typical features of pristine graphene [36]. In the case of DLG, this indicates that the two layers in the stack are well decoupled and/or have on average a twist-angle [37] larger than 15°. After processing at a high temperature, the width of the 2D peak remains the same (see Fig. 3.4b) while the ratio between 2D to G peaks changes drastically depending on the chosen location of the measurement on the chip (see Fig. 3.4a, orange and magenta lines). Also, a notable blue-shift of both 2D and G peaks is observed, as shown in Fig. 3.4b,c. These observations are attributed to a substantial difference in twist-angle across the DLG sheet [37] as well as local changes in strain as a result of annealing of the graphene layers [38].

We also note the almost complete absence of the D peak in all Raman spectra as shown in Fig. 3.4a, indicating a very low amount of defects in the stacked graphene layers even after exposure to high temperatures [39]. This result is in agreement with the outstanding high-temperature stability of graphene when encapsulated by protective layers [40, 41], and provides evidence that damage, caused by the removal of polymer from suspended graphene, is minimal [25–28].

3.3.2. Analysis of the sensor response

A pressure difference ΔP results in a deflection δ of a circular graphene membrane with radius R, given by:

$$\Delta P = \frac{4n_0}{R^2}\delta + \frac{8E_{2D}}{3R^4(1-\nu)}\delta^3, \tag{3.3}$$

where the graphene membrane takes the shape of the section of a sphere [12, 42]. Since the pressure inside the reference cavity is about $P_{\text{int}} \approx 1$ bar (the pressure during transfer), at $P_{\text{ext}} = 1$ bar atmospheric pressure $\Delta P \approx 0$ and according to equa-

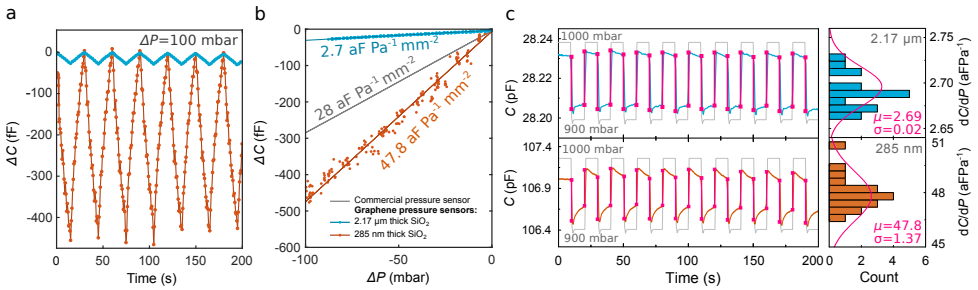

Figure 3.6: Comparison of different capacitive pressure sensors. (a) Triangular pressure wave applied to two graphene sensors with 285 nm and 2.17 μm of oxide thickness showing the measured change in capacitance. The gas pressure is changed at a rate of 6.25 mbar s^{-1}.(b) Responsivity of the chips from (a) at small ΔP and the comparison to a commercial capacitive pressure sensor (Murata SCB10H). (c) Analysis of the responsivity of the chips as determined from periodic pressure steps between 1000 and 900 mbar. The gas pressure is changed at a rate of 175.4 mbar s^{-1}. Panels on the left: Blue line - measured capacitance of a graphene sensor with $t_{SiO_2} = 2.17$ μm. Orange line - measured capacitance of a sensor with $t_{SiO_2} = 285$ nm. Thin grey line - applied time-dependent pressure profile. Magenta lines - extracted capacitance response of the sensors. Panels on the right: statistics over a number of cycles for both oxide thicknesses. Magenta lines - fit to a normal distribution with corresponding mean values μ and standard deviations σ in aF Pa^{-1} indicated.

tion (3.3) the sensors are expected to have a linear response at small $\Delta\delta$. However, at larger deflections nonlinear mechanical and capacitance effects start to result in non-linearities in the capacitance $C_d(\Delta P)$ curve that can be calculated using the parallel-plate approximation [12] as:

$$C_d(\Delta P) = 2\pi\epsilon_0 \int_0^R \frac{r}{g_0 - \delta(\Delta P)\left(1 - \frac{r^2}{R^2}\right)} \mathrm{d}r, \tag{3.4}$$

where ϵ_0 is the vacuum permittivity, g_0 the gap size between the membrane and bottom electrode for $\Delta P = 0$. The contribution of quantum capacitance of graphene is small [43, 44] and is neglected. The total capacitance change of the sensor can be modeled from equation (3.3) and (3.4) as:

$$\Delta C_{total} = N \times \Delta C_d(\Delta P), \tag{3.5}$$

where N is the number of intact, hermetic drums after both fabrication and thermal treatment. We experimentally test if equations (3.4) and (3.5) can model the graphene pressure sensor by applying both substantial negative and positive pressure differences while measuring its capacitance. Figure 3.5a shows the response of the same sensor that was characterized in Figs. 3.3 and 3.4.

The maximal responsivity of the sensor is achieved near ambient pressure in the linear regime, while a notable nonlinear response occurs for $|\Delta P| > 200$ mbar. A number of design factors, such as the drum diameter, the number of drums and the pitch between the drums influence the sensor performance [12]. Importantly, the pressure dependence of ΔC can be well reproduced by the model of equation (3.5) using a Young's modulus of $E_{2D} = 175$ N/m, estimated by an AFM probe for this

particular sample, and a pre-tension $n_0 = 0.45$ N/m as shown by the magenta line in Fig. 3.5a. The model follows the measurement closely when we use a fitted value of N/N_{tot}=0.25 as shown in Fig. 3.5b (solid magenta line), where $N_{\text{tot}} \approx 10000$ is the total number of drums. This indicates that the yield of intact hermetic drums is 25%, and suggests that a large number of drums that look visually intact do not remain hermetic after polymer removal. The theoretical maximum response at a perfect yield of 100% is also shown (dashed magenta line).

Many other factors can influence the responsivity. Since the device capacitance has a strong dependence on the distance between the plates of the pressure sensor, the cavity depth has a large influence on the performance of the sensor. In Fig. 3.6 we demonstrate the performance of two of the best samples with a SiO_2 thickness of 285 nm and 2.17 μm respectively. Both chips have circular holes with a depth of 240 nm fabricated as described previously. Figure 3.6a shows the triangular wave response of both 285 nm (orange line) and 2.17 μm (blue line) chips. As shown in Fig. 3.6b, the difference in responsivity for the two oxide thicknesses as a function of pressure can be more than an order of magnitude. Using equation (3.1), we calculate the noise floor to be 34.2 Pa/$\sqrt{\text{Hz}}$ for the 285 nm thick SiO_2 sample and 43.4 Pa/$\sqrt{\text{Hz}}$ for the 2.17 μm one. The measured responsivity of the 285 nm gap device is significantly higher than that of the 2.17 μm one, in qualitative accordance with the equation (3.1).

There is a notable scatter in the measured capacitance values as seen in Fig. 3.6b that is attributed to the effect of gas escaping the cavities for part of the drums, thus causing $|\Delta P|$ to decrease with time. It has been reported before that when graphene is suspended over a SiO_2/Si cavity, it does not always form a perfect hermetic seal[2, 3]. As recently shown by Lee, *et al.*, most of the gas permeation in graphene drums occurs along the van der Waals interface between the 2D material and the substrate [2]. As a result of the contribution of this effect, an exponential decrease of C with time is visible in Fig. 3.6c, in response to periodic pressure steps of $\Delta P = 100$ mbar. However, if a good graphene crystallinity is preserved over large areas, the mean path that the gas needs to travel to escape the cavities becomes large, and this will increase the flow resistance of the gas channel and the permeation time constant [2, 20]. This condition seems to be achieved across part of the sample, because no significant hysteresis was observed during the slow pressure sweeps (> 10 minutes per sweep) in Fig. 3.5a and b, suggesting that of the order of 25 % of the drums maintain a constant internal pressure P_{int} for $\Delta P \neq 0$, as supported by the fits in Fig. 3.5a and b.

Optimization of all parameters is required to achieve the best sensor performance for detecting very small pressure differences over an extended range of pressure. DLG pressure sensors show reproducible operation over a pressure range of 65 – 138 kPa (see Fig. 3.5a). In terms of responsivity our best sensor with 285 nm of SiO_2 oxide (orange dots in Fig. 3.6a and b), with a responsivity of 47.8 aF $\text{Pa}^{-1}\text{mm}^{-2}$ over the range of 90 – 100 kPa, already outperforms the commercially available state-of-the-art Murata SCB10H sensor with a responsivity of 28 aF $\text{Pa}^{-1}\text{mm}^{-2}$ in the same range, as shown in Fig. 3.6b. This is comparably larger than what was previously achieved with capacitive sensors based on atomically thin 2D membranes

[9, 12], yet competitive with a thicker suspended graphene-covered 140 nm PMMA sheets [10] with a reported responsivity of 123 aF $Pa^{-1}mm^{-2}$ over 0–80 kPa, using an area of 210 μm^2 of tightly-packed hexagonal membranes. However, if yields close to 100% and hermetic sealing of all drums is realized and the pre-tension is lowered down to ~ 0.04 N/m, the presented graphene-based 2D devices are expected to achieve a theoretical maximum responsivity of ~ 450 aF $Pa^{-1}mm^{-2}$ near ambient pressure of 90 – 100 kPa. Further design improvement might even be possible if the gap is reduced, the unsuspended area is minimised and the packing density of the membranes is increased. Using three or five layers of stacked graphene instead of two might help to improve the hermetic sealing issue but would result in a lower sensitivity (see Supplementary Fig. 3). Increasing the diameter of drums, on the other hand, could compensate this and produce an increase in responsivity (see Supplementary Fig. 4), however, also decrease the yield [21]. Eventually, also the temperature-related effects on capacitance need to be excluded by combining the pressure sensor with a temperature sensor and using appropriate calibration.

3.4. Conclusions

Where previous studies had addressed part of the challenges related to realizing portable graphene gas pressure sensors, like the pressure sensitivity, impermeability to gasses and electrical readout, here we bridged these studies by constructing a portable, battery powered functional graphene pressure sensor that outperforms commercial devices. Using off-the-shelf systems for electronic readout and data processing, we enable capacitive readout of a 1×1 mm^2 array of DLG graphene pressure sensors. We realize sensor chips with a high yield of suspended membranes, resulting in a sensor responsivity of 47.8 aF $Pa^{-1}mm^{-2}$. We demonstrate that thermal treatment is an effective measure for controllable thickness reduction of the support polymer layer, that leads to a significant performance improvement because the thin 2D material membranes are much more flexible than with the support polymer. It is anticipated that further design and fabrication improvements and better control over the device yield can increase the responsivity by a factor 10, thus enabling improvements in applications like indoor navigation, altitude monitoring and activity monitoring, and can enable new applications like presence detection.

Appendix.

A. Annealed polymer

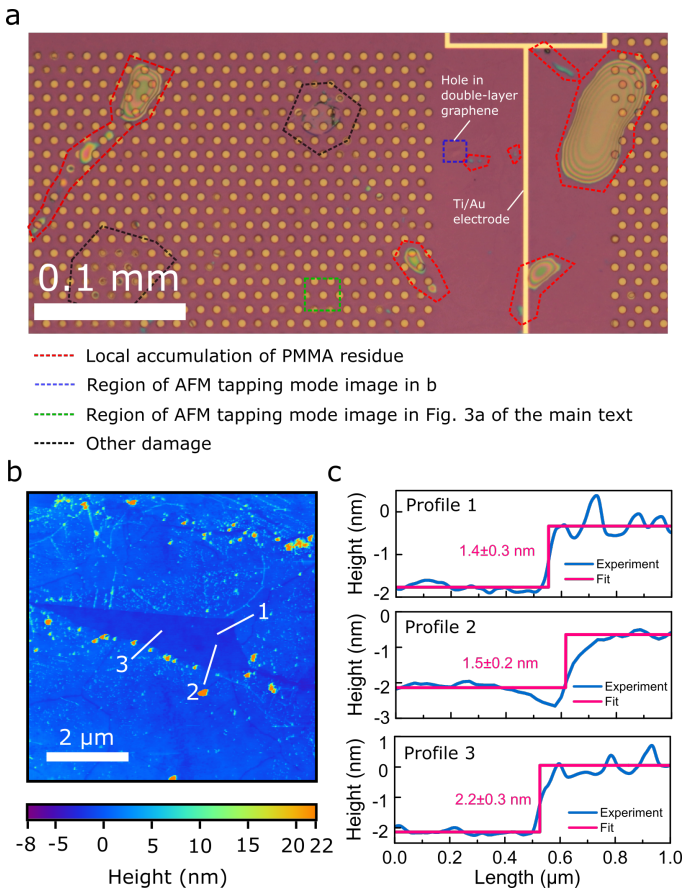

Figure A.1: Detailed characterization of annealed double-layer graphene in a region where PMMA residues were observed. (a) Optical image of a thermally annealed graphene sample with a 285 nm thickness of SiO_2, results of which are also presented in Fig. 3 of the main text. (b) Tapping mode AFM image of the area indicated with a dashed blue line in (a). Numbered white lines indicate corresponding height profiles in (c). The extracted thickness of DLG is indicated for each case.

B. Simulations of capacitance

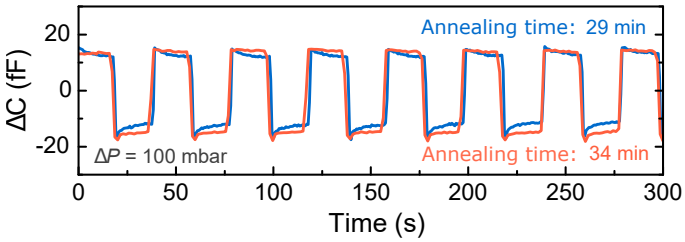

Figure A.2: Capacitance response of a DLG sample to pressure step-changes after thermal annealing. Coloured lines - change in capacitance of a single chip as a function of measurement time in response to ΔP, annealed for a time indicated in the legend.

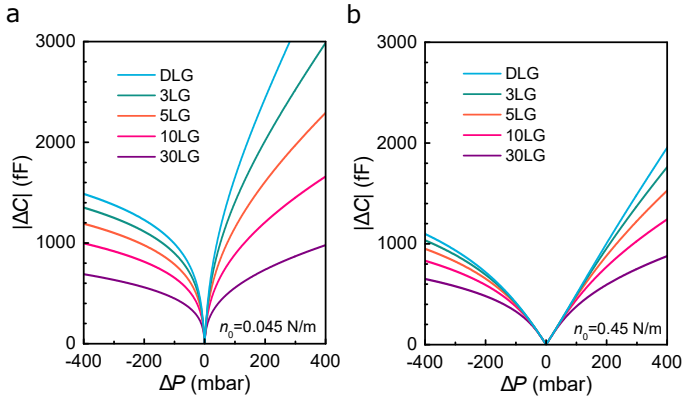

Figure B.1: Simulated capacitance-pressure curves of the graphene pressure sensor with a different number of layers and pre-tension of (a) 0.045 N/m and (b) 0.45 N/m.

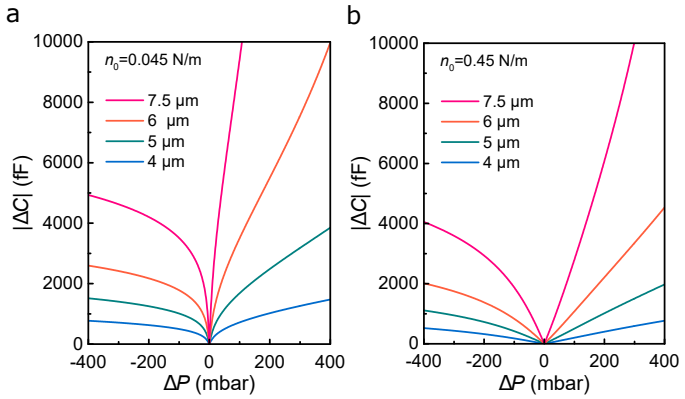

Figure B.2: Simulated capacitance-pressure curves of the graphene pressure sensor with a different diameter of drums and pre-tension of (a) 0.045 N/m and (b) 0.45 N/m.

References

[1] A. Zurutuza and C. Marinelli, "Challenges and opportunities in graphene commercialization," *Nature Nanotech.*, vol. 9, pp. 730–734, Oct. 2014.

[2] M. Lee, D. Davidovikj, B. Sajadi, M. Šiškins, F. Alijani, H. S. J. van der Zant, and P. G. Steeneken, "Sealing graphene nanodrums," *Nano Lett.*, vol. 19, pp. 5313–5318, July 2019.

[3] J. S. Bunch, S. S. Verbridge, J. S. Alden, A. M. van der Zande, J. M. Parpia, H. G. Craighead, and P. L. McEuen, "Impermeable atomic membranes from graphene sheets," *Nano Lett.*, vol. 8, pp. 2458–2462, Aug. 2008.

[4] P. Sun, Q. Yang, W. Kuang, Y. V. Stebunov, W. Xiong, J. Yu, R. R. Nair, M. I. Katsnelson, S. Yuan, I. V. Grigorieva, M. Lozada-Hidalgo, F. Wang, and A. K. Geim, "How permeable is the impermeable graphene?," 2020. Preprint at https://arxiv.org/abs/1912.09220.

[5] C. Lee, X. Wei, J. W. Kysar, and J. Hone, "Measurement of the elastic properties and intrinsic strength of monolayer graphene," *Science*, vol. 321, pp. 385–388, July 2008.

[6] T. Cui, S. Mukherjee, P. M. Sudeep, G. Colas, F. Najafi, J. Tam, P. M. Ajayan, C. V. Singh, Y. Sun, and T. Filleter, "Fatigue of graphene," *Nature Mater.*, Jan. 2020.

[7] G.-H. Lee, R. C. Cooper, S. J. An, S. Lee, A. van der Zande, N. Petrone, A. G. Hammerberg, C. Lee, B. Crawford, W. Oliver, J. W. Kysar, and J. Hone, "High-strength chemical-vapor-deposited graphene and grain boundaries," *Science*, vol. 340, pp. 1073–1076, May 2013.

[8] J.-H. Chen, C. Jang, S. Xiao, M. Ishigami, and M. S. Fuhrer, "Intrinsic and extrinsic performance limits of graphene devices on SiO_2," *Nature Nanotech.*, vol. 3, pp. 206–209, Mar. 2008.

[9] Y.-M. Chen, S.-M. He, C.-H. Huang, C.-C. Huang, W.-P. Shih, C.-L. Chu, J. Kong, J. Li, and C.-Y. Su, "Ultra-large suspended graphene as a highly elastic membrane for capacitive pressure sensors," *Nanoscale*, vol. 8, no. 6, pp. 3555–3564, 2016.

[10] C. Berger, R. Phillips, A. Centeno, A. Zurutuza, and A. Vijayaraghavan, "Capacitive pressure sensing with suspended graphene–polymer heterostructure membranes," *Nanoscale*, vol. 9, no. 44, pp. 17439–17449, 2017.

[11] C. Berger, R. Phillips, I. Pasternak, J. Sobieski, W. Strupinski, and A. Vijayaraghavan, "Touch-mode capacitive pressure sensor with graphene-polymer heterostructure membrane," *2D Mater.*, vol. 5, p. 015025, Nov. 2017.

[12] D. Davidovikj, P. H. Scheepers, H. S. J. van der Zant, and P. G. Steeneken, "Static capacitive pressure sensing using a single graphene drum," *ACS Appl. Mater. Interfaces*, vol. 9, pp. 43205–43210, Nov. 2017.

[13] S.-E. Zhu, M. K. Ghatkesar, C. Zhang, and G. C. A. M. Janssen, "Graphene based piezoresistive pressure sensor," *Appl. Phys. Lett.*, vol. 102, p. 161904, Apr. 2013.

[14] A. D. Smith, F. Niklaus, A. Paussa, S. Vaziri, A. C. Fischer, M. Sterner, F. Forsberg, A. Delin, D. Esseni, P. Palestri, M. Östling, and M. C. Lemme, "Electromechanical piezoresistive sensing in suspended graphene membranes," *Nano Lett.*, vol. 13, pp. 3237–3242, June 2013.

[15] A. D. Smith, F. Niklaus, A. Paussa, S. Schröder, A. C. Fischer, M. Sterner, S. Wagner, S. Vaziri, F. Forsberg, D. Esseni, M. Östling, and M. C. Lemme, "Piezoresistive properties of suspended graphene membranes under uniaxial and biaxial strain in nanoelectromechanical pressure sensors," *ACS Nano*, vol. 10, pp. 9879–9886, Nov. 2016.

[16] R. N. Patel, J. P. Mathew, A. Borah, and M. M. Deshmukh, "Low tension graphene drums for electromechanical pressure sensing," *2D Mater.*, vol. 3, p. 011003, Jan. 2016.

[17] R. J. Dolleman, D. Davidovikj, S. J. Cartamil-Bueno, H. S. J. van der Zant, and P. G. Steeneken, "Graphene squeeze-film pressure sensors," *Nano Lett.*, vol. 16, pp. 568–571, Dec. 2015.

[18] J. Romijn, S. Vollebregt, R. J. Dolleman, M. Singh, H. S. van der Zant, P. G. Steeneken, and P. M. Sarro, "A miniaturized low power pirani pressure sensor based on suspended graphene," in *2018 IEEE 13th Annual International Conference on Nano/Micro Engineered and Molecular Systems (NEMS)*, IEEE, Apr. 2018.

[19] I. E. Rosłoń, R. J. Dolleman, H. Licona, M. Lee, M. Šiškins, H. Lebius, L. Madauß, M. Schleberger, F. Alijani, H. S. van der Zant, and P. G. Steeneken, "Graphene effusion-based gas sensor," 2020. Preprint at https://arxiv.org/abs/2001.09509v1.

[20] R. J. Dolleman, S. J. Cartamil-Bueno, H. S. J. van der Zant, and P. G. Steeneken, "Graphene gas osmometers," *2D Mater.*, vol. 4, p. 011002, Oct. 2016.

[21] S. J. Cartamil-Bueno, A. Centeno, A. Zurutuza, P. G. Steeneken, H. S. J. van der Zant, and S. Houri, "Very large scale characterization of graphene mechanical devices using a colorimetry technique," *Nanoscale*, vol. 9, no. 22, pp. 7559–7564, 2017.

[22] R. A. Barton, B. Ilic, A. M. van der Zande, W. S. Whitney, P. L. McEuen, J. M. Parpia, and H. G. Craighead, "High, size-dependent quality factor in an array of graphene mechanical resonators," *Nano Lett.*, vol. 11, pp. 1232–1236, Mar. 2011.

[23] S. J. Cartamil-Bueno, P. G. Steeneken, A. Centeno, A. Zurutuza, H. S. J. van der Zant, and S. Houri, "Colorimetry technique for scalable characterization of suspended graphene," *Nano Lett.*, vol. 16, pp. 6792–6796, Oct. 2016.

[24] C. N. Berger, M. Dirschka, and A. Vijayaraghavan, "Ultra-thin graphene–polymer heterostructure membranes," *Nanoscale*, vol. 8, no. 41, pp. 17928–17939, 2016.

[25] Y.-C. Lin, C.-C. Lu, C.-H. Yeh, C. Jin, K. Suenaga, and P.-W. Chiu, "Graphene annealing: How clean can it be?," *Nano Lett.*, vol. 12, pp. 414–419, Dec. 2011.

[26] Y. Ahn, J. Kim, S. Ganorkar, Y.-H. Kim, and S.-I. Kim, "Thermal annealing of graphene to remove polymer residues," *Mater. Express*, vol. 6, pp. 69–76, Feb. 2016.

[27] L.-W. Huang, C.-K. Chang, F.-C. Chien, K.-H. Chen, P. Chen, F.-R. Chen, and C.-S. Chang, "Characterization of the cleaning process on a transferred graphene," *J. Vac. Sci. Technol.*, vol. 32, p. 050601, Sept. 2014.

[28] L. Gammelgaard, J. M. Caridad, A. Cagliani, D. M. A. Mackenzie, D. H. Petersen, T. J. Booth, and P. Bøggild, "Graphene transport properties upon exposure to PMMA processing and heat treatments," *2D Mater.*, vol. 1, p. 035005, Nov. 2014.

[29] A. Jain, P. Bharadwaj, S. Heeg, M. Parzefall, T. Taniguchi, K. Watanabe, and L. Novotny, "Minimizing residues and strain in 2D materials transferred from PDMS," *Nanotechnology*, vol. 29, p. 265203, May 2018.

[30] C. S. Ruiz-Vargas, H. L. Zhuang, P. Y. Huang, A. M. van der Zande, S. Garg, P. L. McEuen, D. A. Muller, R. G. Hennig, and J. Park, "Softened elastic response and unzipping in chemical vapor deposition graphene membranes," *Nano Lett.*, vol. 11, pp. 2259–2263, June 2011.

[31] A. Castellanos-Gomez, M. Poot, G. A. Steele, H. S. J. van der Zant, N. Agraït, and G. Rubio-Bollinger, "Elastic properties of freely suspended MoS_2 nanosheets," *Adv. Mater.*, vol. 24, pp. 772–775, Jan. 2012.

[32] R. J. Nicholl, H. J. Conley, N. V. Lavrik, I. Vlassiouk, Y. S. Puzyrev, V. P. Sreenivas, S. T. Pantelides, and K. I. Bolotin, "The effect of intrinsic crumpling on the mechanics of free-standing graphene," *Nat. Commun.*, vol. 6, Nov. 2015.

[33] Z. Li, I. A. Kinloch, R. J. Young, K. S. Novoselov, G. Anagnostopoulos, J. Parthenios, C. Galiotis, K. Papagelis, C.-Y. Lu, and L. Britnell, "Deformation of wrinkled graphene," *ACS Nano*, vol. 9, pp. 3917–3925, Mar. 2015.

[34] J. W. Suk, R. D. Piner, J. An, and R. S. Ruoff, "Mechanical properties of monolayer graphene oxide," *ACS Nano*, vol. 4, pp. 6557–6564, Oct. 2010.

[35] C. Gómez-Navarro, M. Burghard, and K. Kern, "Elastic properties of chemically derived single graphene sheets," *Nano Lett.*, vol. 8, pp. 2045–2049, July 2008.

[36] A. C. Ferrari, "Raman spectroscopy of graphene and graphite: Disorder, electron–phonon coupling, doping and nonadiabatic effects," *Solid State Commun.*, vol. 143, pp. 47–57, July 2007.

[37] K. Kim, S. Coh, L. Z. Tan, W. Regan, J. M. Yuk, E. Chatterjee, M. F. Crommie, M. L. Cohen, S. G. Louie, and A. Zettl, "Raman spectroscopy study of rotated double-layer graphene: Misorientation-angle dependence of electronic structure," *Phys. Rev. Lett.*, vol. 108, June 2012.

[38] Z. H. Ni, H. M. Wang, Y. Ma, J. Kasim, Y. H. Wu, and Z. X. Shen, "Tunable stress and controlled thickness modification in graphene by annealing," *ACS Nano*, vol. 2, pp. 1033–1039, May 2008.

[39] A. Eckmann, A. Felten, A. Mishchenko, L. Britnell, R. Krupke, K. S. Novoselov, and C. Casiraghi, "Probing the nature of defects in graphene by raman spectroscopy," *Nano Lett.*, vol. 12, pp. 3925–3930, July 2012.

[40] M. Šiškins, C. Mullan, S.-K. Son, J. Yin, K. Watanabe, T. Taniguchi, D. Ghazaryan, K. S. Novoselov, and A. Mishchenko, "High-temperature electronic devices enabled by hBN-encapsulated graphene," *Appl. Phys. Lett.*, vol. 114, p. 123104, Mar. 2019.

[41] S.-K. Son, M. Šiškins, C. Mullan, J. Yin, V. G. Kravets, A. Kozikov, S. Ozdemir, M. Alhazmi, M. Holwill, K. Watanabe, T. Taniguchi, D. Ghazaryan, K. S. Novoselov, V. I. Fal'ko, and A. Mishchenko, "Graphene hot-electron light bulb: incandescence from hBN-encapsulated graphene in air," *2D Mater.*, vol. 5, p. 011006, Nov. 2017.

[42] J. S. Bunch, *Mechanical and electrical properties of graphene sheets*. Cornell University Ithaca, NY, 2008.

[43] L. A. Ponomarenko, R. Yang, R. V. Gorbachev, P. Blake, A. S. Mayorov, K. S. Novoselov, M. I. Katsnelson, and A. K. Geim, "Density of states and zero landau level probed through capacitance of graphene," *Phys. Rev. Lett.*, vol. 105, Sept. 2010.

[44] J. Xia, F. Chen, J. Li, and N. Tao, "Measurement of the quantum capacitance of graphene," *Nature Nanotech.*, vol. 4, pp. 505–509, July 2009.

4

4

Sealing graphene nanodrums

Despite theoretical predictions that graphene should be impermeable to all gases, practical experiments on sealed graphene nanodrums show small leak rates. Thus far, the exact mechanism for this permeation has remained unclear, because different potential leakage pathways have not been studied separately. In this chapter, we demonstrate a sealing method that consists of depositing SiO_2 across the edge of suspended multilayer graphene flakes using electron beam induced deposition. By sealing, leakage along the graphene-SiO_2 interface is blocked, which is observed to result in a reduction in permeation rate by a factor of 10^4. The experiments thus demonstrate that gas flow along the graphene-SiO_2 interface tends to dominate the leak rate in unsealed graphene nanodrums. Moreover, the presented sealing method enables the study of intrinsic gas leakage through graphene membranes and can enable hermetic graphene membranes for pressure sensing applications.

Parts of this chapter have been published in Nano letters **19**, 8 (2019) [ ] by M. Lee, D. Davidovikj, B. Sajadi, M. ŠiŠkins, F. Alijani, H. S. J. van der Zant, and P. G. Steeneken.

4.1. Introduction

In the past decade, there has been a growing interest into the use of 2D materials as ultrathin membranes for separation and filtration of gases and ionic solutions. In particular, graphene has been at the focus of these studies because of its exceptional mechanical strength [2] and its impermeability to ions [3] and gases [4].

However, in previous studies of gas permeability of 2D materials, small leak rates of unknown origin have been observed even in the absence of defects or pores [4–11], making it difficult to determine the intrinsic gas permeability of the graphene membrane or its pores. This inherent gas leakage also hinders the application of graphene membranes in ultrasensitive pressure sensors because these sensors require a hermetically sealed cavity that contains a fixed amount of reference gas [4, 5, 7, 10, 12, 13].

In this chapter, we show that the leak rates of graphene cavities can be significantly reduced by depositing glass (SiO_2) across the edges of an exfoliated multilayered-graphene (MLG) flake using an electron beam induced deposition (EBID) technique. Device fabrication and sealing methodology are described and leak rate measurements using resonance frequency analysis are presented. By comparing leak rates of sealed and unsealed cavities, the effectiveness of the sealing method is assessed and the dominant pathway for gas leakage into graphene cavities is identified. This work thus presents strong evidence that gas permeation along the graphene-SiO_2 interface is the dominant leakage pathway, and provides a route towards eliminating this leakage.

4.2. Gas Leakage Pathways

Although gas leak rates into and out of graphene sealed cavities have been investigated in several studies [4, 8, 14, 15], the leakage pathway and mechanism by which gas permeates into the cavity is still under debate. Fig. 4.1a schematically illustrates the three potential leakage pathways along which gas leakage can occur [4]: 1. through the graphene, 2. through the SiO_2 and 3. along the graphene-substrate interface.

Although gas leakage through chemical vapour deposition (CVD) grown graphene (see path 1 in Fig. 4.1a) has been reported to occur [14, 16, 17], it is probable that this leakage is not so much an intrinsic property of pristine graphene, but is due to imperfections and defects in the CVD grown graphene. Evidence that leakage through crystalline graphene (or its defects) is not the dominant leakage pathway, was provided by experiments on exfoliated natural graphene flakes of different thicknesses [4]. These experiments demonstrated a thickness independent leak rate, whereas according to Fick's first law the permeation rate is expected to be inversely proportional to thickness, and, in case permeation is mediated by a small number of pores/imperfections, an even stronger thickness dependence is expected. This experiment therefore excluded path 1 as a dominant leakage pathway.

By gas dependent measurements, it was observed that the leakage rate for He gas was much higher than for other gases [4]. Since SiO_2 is known to be perme-

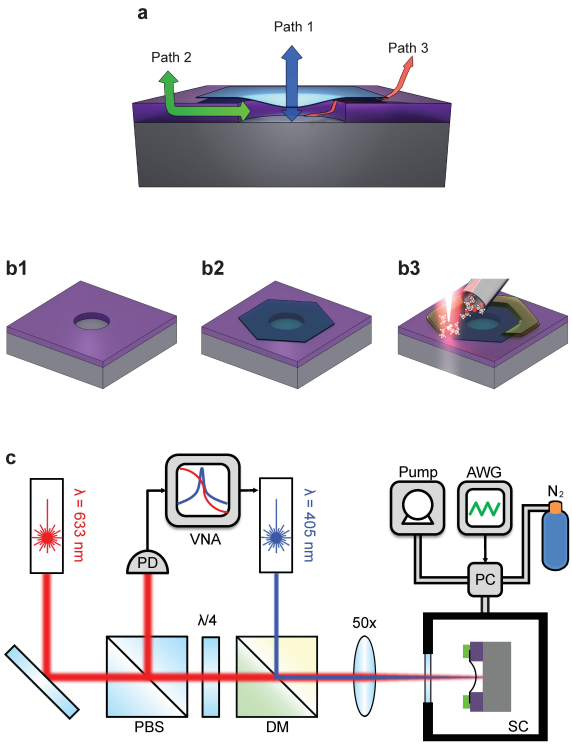

Figure 4.1: **a** Illustration showing the three possible leakage pathways through which gases can leak. Blue: Path 1, through the defects in graphene. Green: Path 2, through the oxide. Red: Path 3, along the interface between graphene and the substrate. **b** Schematic showing the sealing procedure. **b1** Cavity is etched into a SiO_2/Si substrate using standard e-beam lithography followed by reactive ion etching. **b2** Multi-layer graphene (MLG) is deterministically transferred onto the cavity. **b3** Electron beam is scanned over the edge of MLG-SiO_2 interface while gas injection system (GIS) introduces tetraethyl orthosilicate (TEOS), resulting in local deposition of SiO_2. **c** Schematic of the interferometry setup. Sample is mounted in a sample chamber (SC) where the pressure is regulated by the pressure controller (PC) and the arbitrary waveform generator (AWG). A modulated blue laser with wavelength of 405 nm optothermally heats the suspended membrane. Intensity modulations in the reflected red laser light (λ = 633 nm), caused by the graphene motion, are measured by the photodiode (PD) and sent to the vector network analyzer (VNA). PBS: Polarized Beam Splitter, DM: Dichroic Mirror.

able for He [18], it was hypothesized that for all types of gases, leakage into the cavity was dominated by permeation through the SiO_2 substrate (see path 2 in Fig. 4.1a)[4]. However, there was no method available to distinguish between permeation of gas along the interface between graphene and SiO_2 substrate (see path 3 in Fig. 4.1a) and permeation through the substrate itself. Based on these observations, leakage along the SiO_2-graphene interface, can therefore not be ruled out. By studying permeation rates before and after sealing the interface between graphene and SiO_2 (see path 3 in Fig. 4.1a) we aim to identify whether path 2 or path 3 is the dominant leakage pathway.

4.3. Sealing Method

In order to investigate these gas leakage pathways, circular cavities with a depth of 285 nm and diameters of 5 μm and 10 μm are fabricated in a 285 nm thick SiO_2 layer, grown by dry oxidation of a silicon (100) wafer (Fig. 4.1b1). Subsequently, MLG flakes are exfoliated from naturally occurring bulk graphite and suspended over the cavities by a dry transfer method [19] (Fig. 4.1b2). We use MLG exfoliated from naturally occurring bulk graphite with thicknesses ranging from 2 layers to 8 nm to ensure that the permeation we observe is not due to the permeation through the defects along pathway 1.

After initial characterization of the unsealed graphene drums, we seal the cavities to prevent external gas from entering the interface between graphene and SiO_2 (Fig. 1b3). For this purpose we developed a sealing method for locally covering the edge of the graphene flake by an additional SiO_2 layer using EBID of tetraethyl orthosilicate (TEOS) (discussed in more detail in the Methods section).

4.4. Experimental Setup

To test the hermeticity of the graphene drums, we used the suspended graphene drum as a differential pressure sensor [4, 5, 12, 13]. When a pressure difference is present across suspended graphene, tension is induced in the material that causes a change in the resonance frequency. To measure the resonance frequency of our devices, we use the laser interferometry setup shown in Fig. 4.1c.

A modulated blue laser diode (λ= 405 nm) is used to optothermally actuate the MLG membrane. The motion of the graphene membrane is detected using a red He-Ne laser with wavelength, λ= 633 nm. The motion of the suspended graphene modulates the reflected red laser intensity via its position dependent absorption of the standing light wave [20]. This modulated light is collected at the photodiode (PD) and read by the vector network analyzer (VNA). The pressure P_{ext} inside the sample chamber (SC) is controlled by the output from the arbitrary waveform generator (AWG) that drives the pressure controller (PC). The PC then regulates the pressure inside the SC with a vacuum pump and a gas supply (N_2 or He).

4.5. Hermeticity Tests of Graphene Cavities

Fig. 4.2 shows measurements of the pressure response of device 1 in N_2 atmosphere before (Fig. 4.2 a-c) and after sealing (Fig. 4.2 d-e). We observe significant changes in the fundamental resonance frequency f_{res}, of more than 30 MHz, as chamber pressure is varied from 0 to 1000 mbar. Fig. 4.2b shows the time-dependent resonance frequency in response to a triangular pressure waveform with a period of 1000 seconds. Before sealing, the resonance frequency exhibits hysteresis (Fig. 4.2b), which is attributed to leakage, that causes P_{int} to vary in time, thus resulting in different pressure $\Delta P = P_{ext} - P_{int}$ across the membrane at the same value of P_{ext}. In Fig. 4.2c the same device is exposed to pressure steps of 50 mbar. Each step in pressure results in a sudden increase in frequency followed by an exponential decay that is attributed to gas leakage. By fitting, an average leakage time constant $\tau = 31 \pm 4$ seconds is found for N_2 (see supplementary information S1).

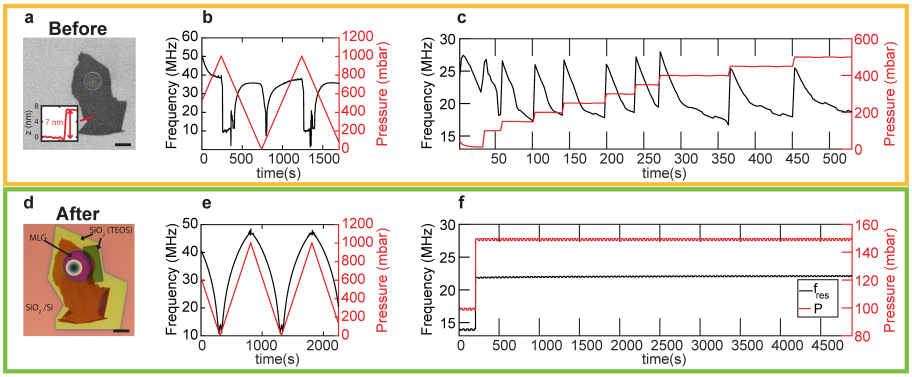

Figure 4.2: Top row: device 1 and its experimental data before sealing. Bottom row: device 1 and its experimental data after sealing. **a** SEM image of the device before sealing. Inset: AFM profile showing the step height of the MLG flake. **b** Fundamental resonance frequency (black) of the non-sealed graphene resonator while the chamber pressure (red) is swept in triangular waveform with period of 1000 seconds. **c** Fundamental resonance frequency (black) of the sealed graphene resonator after 50 mbar step increases in chamber pressure (red). **d** Optical image of the device after sealing. Due to a slight drift in the e-beam during the EBID process, the deposition was off-centered which left some part of the MLG edge exposed. In order to correct this and fully cover all the edges, a second EBID step was necessary which resulted in two layers of SiO_2 in some areas (yellow: first layer, green: second layer). **e** Same procedure as in **b** after sealing. **f** Resonance frequency shift in response to a single 50 mbar step pressure increase.

These measurements are repeated on the same device after sealing the edges of the MLG flake by TEOS (Fig. 4.2d). After covering the edges, hysteresis is eliminated (Fig. 4.2e) and the resonance frequency closely and reproducibly follows the applied pressure changes in P_{ext}. Furthermore, no apparent decay in the resonance frequency is observed after a 50 mbar pressure step as shown in Fig. 4.2f. This shows that the cavity is hermetically sealed or at least that the permeation is greatly suppressed. The absence of hysteresis in Fig. 4.2e and the absence of a frequency decay in Fig. 4.2f indicates that after sealing, the internal pressure P_{int} inside the cavity is thus constant within our measurement accuracy, enabled by the leak-tight seal between graphene and the EBID deposited SiO_2.

4.6. Pressure Sensing with Sealed Graphene Drums

Sealing of the graphene drum allows a more accurate study of the performance of the device as a pressure sensor. We first analyse the pressure response, and subsequently determine its precision as a pressure sensor. Fig. 4.3a-c shows the frequency, responsivity and Q-factor of device 1 as a function of external pressure. Once the cavity is sealed, the pressure difference between the outside and inside of the cavity greatly affects the tension of the membrane which affects the resonance frequency. If the pressure inside is higher, the membrane deflects upward (pressure regime highlighted in pink), which causes the membrane to stretch and the tension to increase. If the pressures outside and inside the cavity are equal,

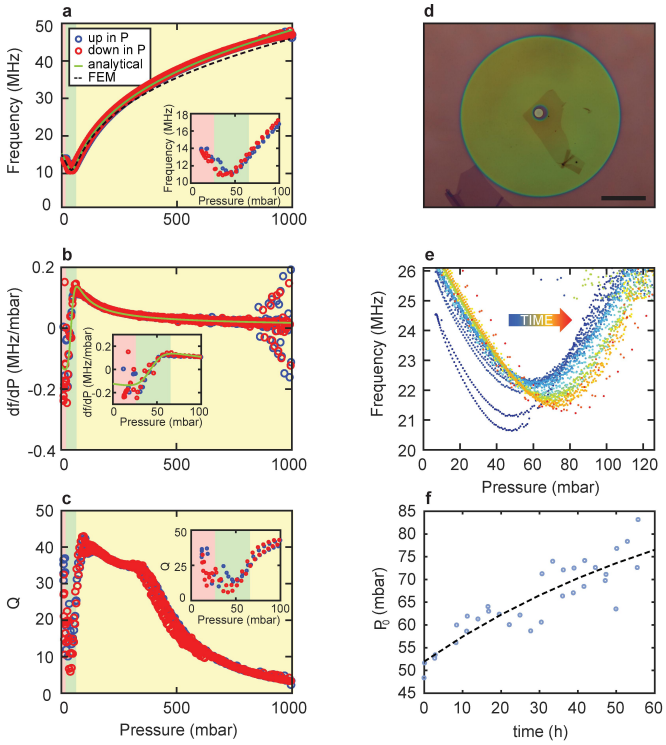

Figure 4.3: **a** Pressure P_{ext} dependence of the resonance frequency of device 1 shown in Fig 4.2. Plotted in red and blue circles are the pressure response of the resonance frequency while increasing and decreasing pressure, respectively. The analytical fit, based on the resonance frequency of a pressurized circular membrane is plotted in green. The fit parameters, E, n_0 and P_0 extracted from the analytical model are used in a FEM simulation (dashed black line). Inset: zoom-in near the minimum. **b** Differential responsivity (df/dP) plotted in red and blue circles and derivative of the analytical solution from **a** plotted in green. Inset: zoom-in near P_0. **c** Q-factor as a function of pressure. Inset: zoom-in near the minimum. **d** Optical image of a sealed device (device 2) which consists of only 2 layers of graphene. Scalebar: 25 µm. **e** Plots similar to **a** are measured continuously over 55.7 hours using triangular pressure sweeps with a period of 10000 s. **f** P_0 is traced over 55.7 hours and fitted to an exponential resulting in a time constant of $\tau_{sealed} = 2.88 \times 10^5$ seconds.

the membrane is flat (regime in green) and the membrane has minimum tension. Finally, if the pressure outside is larger, the membrane deflects downward (regime in yellow) which causes the membrane to stretch, resulting in higher tension in the membrane. The resonance frequency (Fig. 4.3a) and Q-factor (Fig. 4.3c) show minima near $P_{ext} = 42$ mbar, indicative of $P_{int} \simeq 42$ mbar.

In order to relate the pressure dependence of the observed resonance frequencies to the properties of the graphene, we employ a theoretical model to fit the experimental data. The analytical expression for the deflection of a circular mem-

brane subjected to a uniformly distributed pressure across the membrane ΔP is

$$\Delta P = \frac{3.61 n_0}{a^2} x_s + \frac{2.094 E h}{a^4} x_s^3, \tag{4.1}$$

where x_s is the static deflection at the center of the drum, h the thickness, a the radius of the drum, n_0 the pre-tension and E the Young's modulus (see supplementary information S2 for derivation).

After determining the deflection x_s from Eq. 4.1, we calculate the fundamental resonance frequency of a tensioned circular drum with respect to static deflection x_s caused by uniform external load of ΔP using [21]

$$f_{res} = \frac{1}{2\pi} \sqrt{\frac{k_1 + 3 k_3 x_s^2}{m}}, \tag{4.2}$$

where $k_1 = 4.8967 n_0$ the linear spring constant, $k_3 = \frac{2.8398 E h}{a^2}$ the third order spring constant, $m = 0.8467 \rho a^2 h$ the modal mass [21], and ρ the density of the membrane (see supplementary information S2 for derivation).

Fig. 4.3a shows a comparison of experimental data (red and blue circles) and fitted curves based on Eq. 4.2 and finite element method (FEM) simulations. To obtain these curves, we first extract the pre-tension n_0 in the membrane. In order to find n_0 in the membrane, we consider the case where the resonance frequency is minimum ($\Delta P \simeq 0$). The minimum in the frequency, $f_{res,min} = 10.9$ MHz, corresponds to the membrane in the flat ($x_s = 0$) configuration. Using this pre-tension, the thickness $h = 7$ nm determined from AFM, and the density of graphite $\rho = 2300$ kg/m^3, we fit Eq. 4.2 to the data resulting in a cavity pressure of $P_{ext}(f = f_{min}) = P_0 = 41.7 \pm 0.6$ mbar and Young's modulus of $E = 137.4 \pm 0.7$ GPa. In the discussion section, potential causes for the low value of the experimentally extracted Young's modulus are analyzed. With the same parameters, we numerically simulate the pressure response of a circular membrane to obtain the FEM simulations shown in Fig. 4.3a. The effect of the membrane deflection on P_{int} and the effect of squeeze film damping on the resonance frequency are relatively small (estimated systematic error less than 5%), and are therefore not included in the simulation. The FEM results are also plotted in Fig. 4.3 as dashed lines and are in close agreement with the measurements and Eq. 4.2.

It is notable that the pressure dependence of the resonance frequenecy in these devices is very large [4]. At P_0, the frequency of the relaxed graphene membrane is 10.9 MHz and when the pressure difference is at a maximum, the resonance frequency of the strained graphene membrane is 48.4 MHz. Using the measured $f(P_{ext})$, we can estimate the responsivity of the sealed pressure sensor. Over the full range from $P_{ext} = P_0$ to 1000 mbar, we find an average responsivity of 39.2 kHz/mbar whereas the maximum differential responsivity can be as high as 136 kHz/mbar (Fig. 4.3b). Compared to the graphene based squeeze-film pressure sensor previously reported [12], which was already 45 times more sensitive than the state of the art MEMS squeeze film pressure sensors, this sealed pressure sensor is a factor of 15 more responsive, demonstrating the potential of fully sealed membranes of 2D materials for pressure sensing applications.

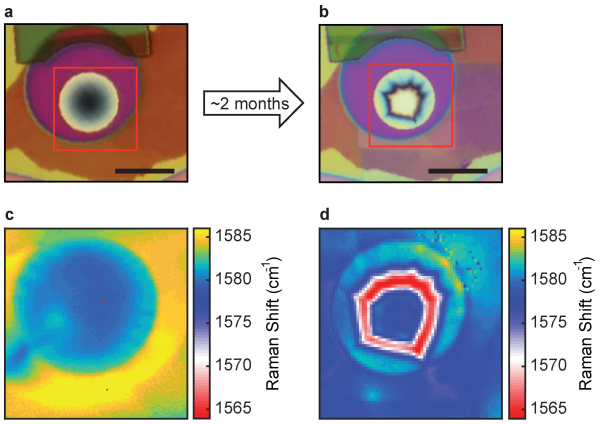

Figure 4.4: Raman mapping study of a sealed graphene drum (device 1) before and after ~2 months in ambient conditions. **a** Optical image of the sealed device with area under Raman study highlighted in red. **b** Optical image of the same drum after ~2 months in ambient conditions. Scale bars are 10 µm **c** Raman mapping of the sealed drum; the G peak is used for mapping. Surrounding the bulged down membrane (under tensile strain) are regions of compressive strain, evidenced by the unusually high G peak position. **d** Raman mapping of the sealed drum after ~2 months of being in ambient conditions. Areas surrounding the drum are relaxed and the center of the membrane touches the cavity bottom.

4.7. Long Term Stability

We study the long term stability of resonance frequency of the devices, because stability is essential for pressure sensing applications. In Fig. 4.3d-f we show measurement results on a sealed device, with a duration of 55.7 hours. The measured device, device 2 shown in Fig. 4.3d, is the thinnest device we fabricated, being only 2 layers thick (see supplementary information S3). This device had a leakage time constant of 26 ± 3 seconds before sealing (see supplementary information S4) which is considerably shorter than those observed in other works [4, 9]. After sealing, the fundamental resonance frequency was measured continuously while P_{ext} was swept from 0 to 1000 mbar in a triangular waveform with a period of 10000 seconds. We determined the pressure at minimum frequency (P_0) for each sweep during the whole experiment (Fig. 4.3e). Thus we observed P_0 increasing from 48.3 mbar to 83.1 mbar in 55.7 hours (Fig. 4.3f). The time constant as obtained from an exponential fit is 2.88×10^5 seconds (~ 80 hours), which is a factor of 1.11×10^4 longer than the leakage time constant before sealing.

When He is used, we observe a decay time-constant $\tau \simeq 72.2$ seconds of the resonance frequency after sealing with TEOS, which is much shorter than that for N_2 gas (see supplementary information S5). The sealing procedure only reduces the leak rate by a factor 10 for He gas. This lower effectivity of the sealing procedure can be attributed to leakage of He through TEOS and thermal oxide, since He gas is known to be able to diffuse through SiO_2 layers [18].

4.8. Discussion

Eventually the goal of any sealing procedure is to reach a situation where the graphene cavity is leak-tight for many years. However, judging from Fig.4.3f, it can be seen that the internal pressure P_0 is slowly increasing as a function of time, which could be an indication of slow gas leakage into the membrane over periods of hours. Alternatively, the increase of pressure inside the membrane might also result from another effect. If the membrane is slowly slipping and sagging into the cavity, the enclosed volume of gas would slowly decrease as a function of time. For a fixed temperature and amount of gas molecules, the product of pressure and volume $P_{int}V_{int}$ is constant according to Boyle's law, and therefore such a decrease in volume would be accompanied by an increase in pressure. So two hypotheses might account for the observed increase in pressure: gas leakage and sagging of the membrane resulting in cavity volume reduction. To verify which of these hypotheses can account for the observed pressure increase in Fig.4.3f, we carried out microscopy and Raman studies on the membranes at the start and end of the experiment.

Sealing is performed in a high vacuum SEM environment for a period of ~ 1 hour, which results in a near-vacuum state inside the sealed cavity. After sealing, when the sealed device is exposed to the atmospheric pressure, the large pressure difference causes the membrane to bulge down. The resulting curvature of the membrane is clearly visible, as an optical contrast [11] difference between the center and the edges of the drum, as shown in the optical microscope image in Fig. 4.4a, that is taken within 10 minutes after EBID. The curvature of the membrane is also verified in an AFM scan of a similarly sealed device (see supplementary information S6). When the device is exposed to the overpressure for a prolonged time (about 2 months) the bulged down membrane eventually adheres to the bottom of the cavity as evidenced by the optical microscopy image in Fig. 4.4b. Raman mapping has been employed to study the changes in the lateral strain distribution due to the membrane collapsing. A Raman map shown in Fig. 4.4c indicates that the suspended part of the graphene is initially under tensile strain, as evidenced by the lower value of the G-peak Raman wavenumbers (see supplementary information S7) [22]. The regions surrounding this tensile membrane exhibits comparably lower strain. However, after 2 months of constant overpressure, the Raman wavenumbers in the surrounding region are shifted downwards (Fig. 4.4d), indicating higher tensile stress, and the membrane adhered to the bottom of the cavity.

The collapsing of the membrane on the cavity bottom supports the second of the two hypotheses listed above because if there were small pinholes or defects, through which gas leaks at small rates, then over time, P_{int} and P_{ext} would equilibrate and the initially downward bulged membrane would become flat. However, we are observing that the membrane collapsed to the cavity bottom and that the MLG in the nearby region became more strained. A potential explanation for the observed sagging of the graphene membrane is that the high, pressure induced, tensile strain in the suspended graphene pulls the layer, such that it slides into the cavity until it touches the bottom of the cavity. During this motion the strain distribution in the MLG can change and the graphene edge might also slowly move with respect to the TEOS. Another effect that might play a role is that creep may

be occurring in the graphene, either due to dislocation motion, or due to mutual slipping of graphene layers with respect to each other in the MLG. The increase in pressure $P_{int} = P_0$ in Fig. 4.3f can thus be at least partly, but maybe even completely attributed to the volume reduction due to sagging.

The obtained value of the Young's modulus from the fit is so much lower than the well-established literature value of around $E = 1$ TPa, that we suspect that the assumptions underlying the continuum model are not adequately capturing the true membrane physics. Potential causes for this discrepancy include wrinkles (observed around the edge of the membrane as can be seen from Raman measurements in Fig. 4.4c & d), material residues from the transfer or sealing method, and non-perfect clamping of the edge of the membrane causing elastic sliding of the suspended part of the membrane near the edge. This last effect seems especially likely considering the observation of the collapse of the membrane under prolonged exposure to high pressures in Fig. 4.4b. The resulting value for the Young's modulus from the fit in Fig. 4.3a is therefore not an accurate representation of the actual material properties, rather shall be seen as an equivalent property representing a continuum mechanics model that fits the observed physics.

4.9. Conclusions

In this work, we demonstrate that the N_2 leakage rate can be drastically reduced (by a factor $> 10^4$) by sealing the edge of graphene with TEOS. Since leakage through the thermal oxide would not be significantly blocked by the TEOS, we can also conclude from these results that the dominant leakage pathway is along the interface between graphene and SiO_2. From long-term hermeticity tests it is found that the internal pressure inside the graphene sealed cavity does still increase in time. Although small leakage might still play a role, sagging of the membrane is also identified as a potential contributor for pressure increase and eventual device failure due to membrane collapse. By presenting a sealing method for graphene membranes, the current work sets steps towards improved permeability characterization of 2D materials and towards new sensors based on impermeable ultrathin membranes.

Appendix.

A. Leakage time constant of N_2 before sealing

In this section, the average leakage time constant of device 1 in N_2 atmosphere before performing the seal is extracted from the experimental data shown in Fig. 2c of the main text.

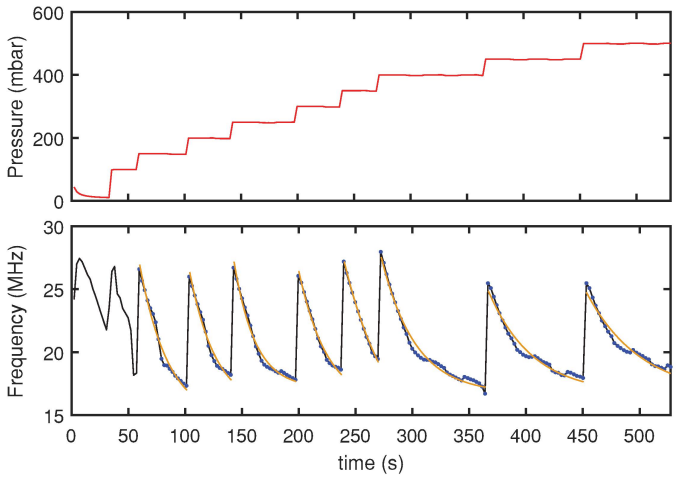

Figure A.1: Top row: Sample chamber pressure (P_{ext}) varied in 50 mbar steps. Bottom row: Resonance frequency of the graphene membrane (black). The parts of the data which are used to fit to the exponential decay are blue dots and the fits orange. First two decays were omitted due to abnormal decay profile.

Fig. A.1 is the graph shown in Fig. 2c of the main text where the resonance frequency of device 1 is measured while increasing the P_{ext} in 50 mbar steps. The decay curves in orange are fitted to $f(t) = ae^{-t/\tau} + c$ where τ is the leakage time constant. Individual time constants are listed and averaged in A.1. Before sealing, the average leakage time constant of N_2 into the cavity is 31 ± 4 seconds.

B. Derivation of analytical expression

In this section, the Eq. 1 and 2 from the main text are derived.

Using von Kármán membrane theory and Lagrangian approach, one can obtain the following differential equation governing the motion $x(t)$ of a circular membrane [23]:

$$m\ddot{x} + k_1 x + k_3 x^3 = p \tag{4.3}$$

in which

$$m = 0.8467\rho a^2 h, \tag{4.4a}$$

$$k_1 = 4.8967 n_0, \tag{4.4b}$$

$$k_3 = \frac{2.8398Eh}{a^2}, \tag{4.4c}$$

	τ (s)
curve 1	omitted
curve 2	omitted
curve 3	25.42
curve 4	23.47
curve 5	18.64
curve 6	25.53
curve 7	41.88
curve 8	29.80
curve 9	38.92
curve 10	48.18
Mean	31.47

Table A.1: Leakage time constants τ extracted from Fig. A.1 and their mean

$$p = 1.3567 \Delta P a^2, \tag{4.4d}$$

where E is the Young's modulus, h is the thickness and a is the radius of the membrane; derived while assuming $\nu = 0.16$ as the Poisson's ratio of graphene [8]. Moreover, ΔP is the uniform distribution of pressure acting on the membrane.

In order to find the natural frequency about the static deflection, we split the solution to the static x_s and dynamic $x_d(t)$ components as [21]

$$x = x_s + x_d(t). \tag{4.5}$$

We can now obtain the static deflection due to ΔP by solving the following algebraic equation:

$$k_1 x_s + k_3 x_s^3 = p. \tag{4.6}$$

The linearized equation of motion around the statically deflected configuration can then be obtained as

$$m\ddot{x_d} + k_1 x_d + 3k_3 x_s^2 x_d = 0, \tag{4.7}$$

which gives the following linearized fundamental frequency (Hz):

$$f = \frac{1}{2\pi}\sqrt{\frac{\left(4.897 n_0 + \frac{8.519 E h x_s^2}{a^2}\right)}{0.8467 \rho a^2 h}}, \tag{4.8}$$

where x_s is the real solution of Eq.4.6.

C. Time constant before and after the seal

In this section, we discuss the effectiveness of the seal by comparing the decay time constant in the fundamental resonance frequency before the seal with the decay time constant associated with the increase in the P_0 after the seal.

Device 2 of the main text before sealing is shown in Fig. C.1a. As seen in Fig. C.1b and c, the fundamental resonance frequency decayed after sudden increase in pressure before the sealing is performed. Similar to S1, the decay curves (orange)

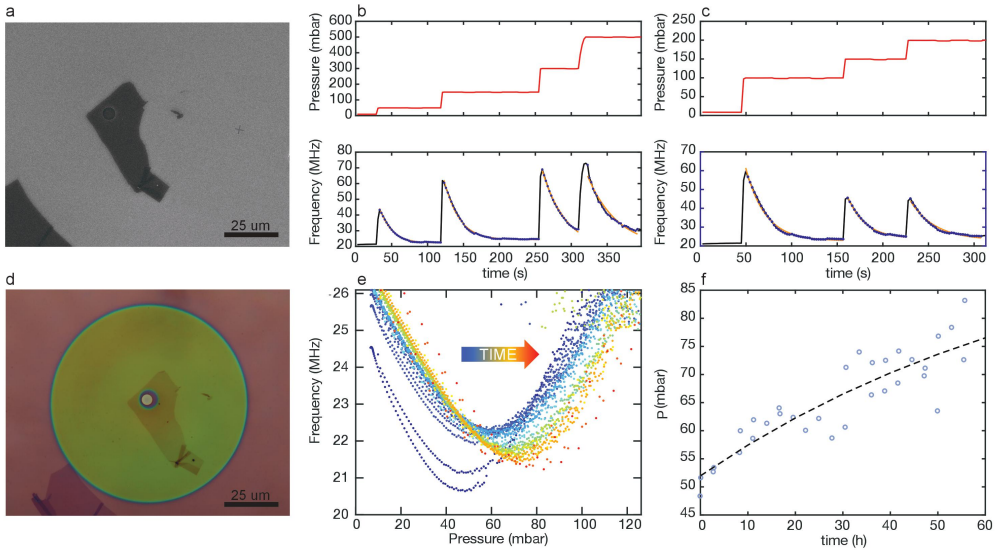

Figure C.1: **a** SEM image of device 2 before sealing. **b& c** Pressure step response of the unsealed membrane in N_2. Pressure steps are plotted in red, the resonance frequency in black, data used to fit exponential function in blue dots and fit results in orange. Decay time constant extracted is $\tau = 26 \pm 3$ seconds. **d** Optical image of device 2 after sealing. **e** Sealed drum measured over 55.7 hours. Over time, the minimum in the resonance frequency shifts higher. **f** Progression of the minimum in the frequency fitted to exponential decay function. P_0 increases from 48.3 mbar to 83.1 mbar in 55.7 hours.

in Fig. C.1b and c are fitted to $f(t) = ae^{-t/\tau} + c$ where τ is the leakage time constant, and listed in Table C.2. Before sealing, the average leakage time constant of N_2 into the cavity is 26 ± 3 seconds.

The image of device 2 after sealing is shown in Fig. C.1d where the green circular shape is the electron beam induced deposition of SiO_2 using tetraethyl orthosilicate as the precursor. When measuring a pressure step response of a sealed drum, as done in Fig. 2f of the main text, it is very difficult to fit a decay function to a nearly straight line. Therefore we swept P_{ext} while measuring the resonance frequency continuously for 55.7 hours to monitor the cavity pressure P_0. The progression of the minimum in the fundamental resonance frequency is shown in Fig. C.1. The position of the minima are then plotted with respect to time in Fig. C.1f and fitted to an exponential function. Resulting time constant is $\tau_{sealed} = 2.88 \times 10^5$ seconds which is a factor of 1.11×10^4 greater than the leakage time constant $\bar{\tau} = 25.9$ seconds before sealing.

D. Raman spectrum of sealed membrane

In this section, we discuss the Raman spectroscopy of a sealed membrane and its implications in the strain of the suspended graphene. Raman spectroscopy has been employed to study the effect of overpressure. In the sealed cavity in Fig. D.1, $P_0 = 44$ mbar of gas is present. The Raman spectroscopy is performed in ambi-

	τ (s)
curve b1	16.94
curve b2	20.39
curve b3	34.26
curve b4	41.96
curve c1	21.40
curve c2	19.18
curve c3	27.16
Mean	25.90

Table C.2: Leakage time constants τ extracted from Fig. C.1 and their mean.

ent conditions which means that the membrane is bulged down due large pressure difference across the membrane. This results in added strain which can be read by checking the change in the position of the G peak and the 2D peak Raman numbers. Fig. D.1b and c shows the red shifting of both of the peaks due to strain induced in the membrane. In Fig. D.1, the G peak and 2D peaks are mapped.

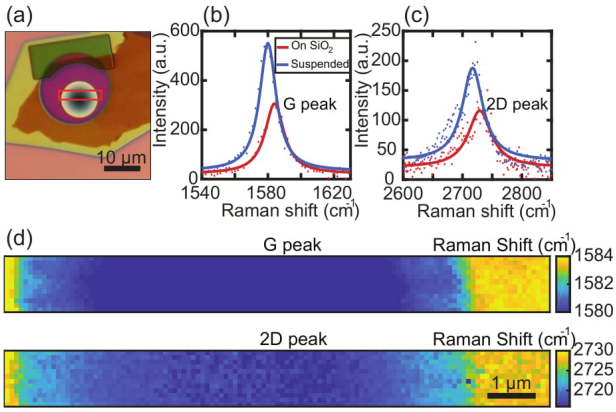

Figure D.1: **a** Optical image of the sealed graphene pressure sensor with the area used for Raman Mapping shown in red. Scale bar is 10 μm. **b** Comparison of the G peak between suspended region and a supported region of graphene. **c** Comparison of the 2D peak between suspended and supported region of graphene. Both $2D_1$ and $2D_2$ are fitted to a single Lorentzian for simplicity. Red shifting of both G and 2D peaks suggests strain present in the suspended region. **d** Raman map of the red boxed region in **a** showing both G peak and 2D peak.

E. Leakage time constant of He before and after sealing

In this section we compare the leakage time constant of He before and after sealing. Since the permeation of He through SiO_2 is well known, we expect the seal, which consists of electron beam induced deposition of SiO_2, to be less effective for He than N_2.

Pressure response in the resonance frequency of the sample is measured in He

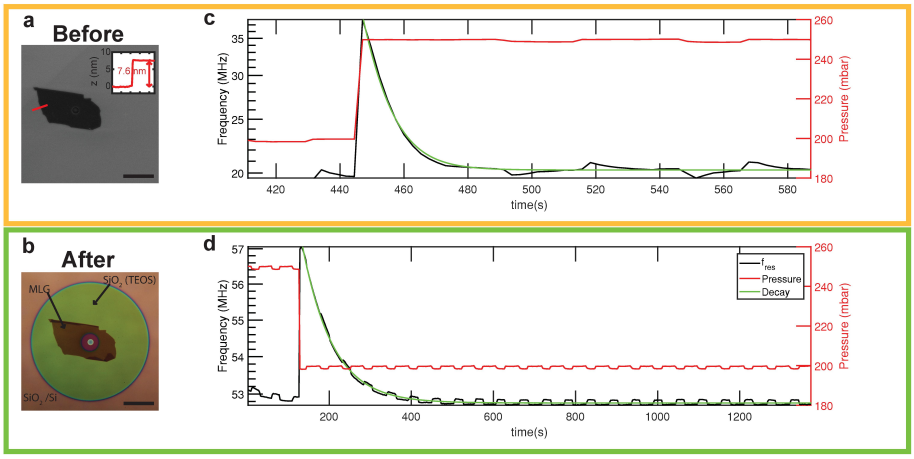

Figure E.1: Top row: image and experimental data of device 3 before sealing. Bottom row: image and experimental data of device 3 after sealing. **a** SEM image of device 3 before sealing. Inset: AFM profile showing the step height of the MLG flake. **b** Optical image of the device after sealing. **c & d** Fundamental frequency (black) of the graphene resonator after a 50 mbar step in chamber pressure (red) for **c** unsealed and **d** sealed MLG drum with exponential decay (green) fitted .

before (Fig. E.1a) and after the sealing (Fig. E.1b). The sample prior to sealing is put into the sample chamber where the air is flushed out and replaced with He. Then the resonance frequency is measured following a pressure step of 50 mbar differences in He. As shown in Fig. E.1c, there is a sharp transition immediately after the pressure step and a decay in the resonance frequency. The decay is fitted to an exponential decay which reveals that the leakage time constant is $\tau = 7.8$ seconds. Same experiment has been performed after the sealing in Fig. E.1d. The leakage time constant extracted from the decay profile is $\tau = 72.2$ seconds, which is almost 10 times larger than before sealing.

References

[1] M. Lee, D. Davidovikj, B. Sajadi, M. Šiškins, F. Alijani, H. S. van der Zant, and P. G. Steeneken, "Sealing graphene nanodrums," *Nano letters*, vol. 19, no. 8, pp. 5313–5318, 2019.

[2] C. Lee, X. Wei, J. W. Kysar, and J. Hone, "Measurement of the elastic properties and intrinsic strength of monolayer graphene," *science*, vol. 321, no. 5887, pp. 385–388, 2008.

[3] V. Berry, "Impermeability of graphene and its applications," *Carbon*, vol. 62, pp. 1–10, 2013.

[4] J. S. Bunch, S. S. Verbridge, J. S. Alden, A. M. Van Der Zande, J. M. Parpia, H. G. Craighead, and P. L. McEuen, "Impermeable atomic membranes from graphene sheets," *Nano letters*, vol. 8, no. 8, pp. 2458–2462, 2008.

[5] D. Davidovikj, P. H. Scheepers, H. S. van der Zant, and P. G. Steeneken, "Static capacitive pressure sensing using a single graphene drum," *ACS applied materials & interfaces*, vol. 9, no. 49, pp. 43205–43210, 2017.

[6] D. Davidovikj, D. Bouwmeester, H. S. van der Zant, and P. G. Steeneken, "Graphene gas pumps," *2D Materials*, vol. 5, no. 3, p. 031009, 2018.

[7] J. Lee, Z. Wang, K. He, J. Shan, and P. X.-L. Feng, "Air damping of atomically thin mos2 nanomechanical resonators," *Applied Physics Letters*, vol. 105, no. 2, p. 023104, 2014.

[8] S. P. Koenig, L. Wang, J. Pellegrino, and J. S. Bunch, "Selective molecular sieving through porous graphene," *Nature nanotechnology*, vol. 7, no. 11, p. 728, 2012.

[9] D. Lloyd, X. Liu, J. W. Christopher, L. Cantley, A. Wadehra, B. L. Kim, B. B. Goldberg, A. K. Swan, and J. S. Bunch, "Band gap engineering with ultralarge biaxial strains in suspended monolayer mos2," *Nano letters*, vol. 16, no. 9, pp. 5836–5841, 2016.

[10] A. Smith, F. Niklaus, A. Paussa, S. Vaziri, A. C. Fischer, M. Sterner, F. Forsberg, A. Delin, D. Esseni, P. Palestri, M. Östling, and M. C. Lemme, "Electromechanical piezoresistive sensing in suspended graphene membranes," *Nano letters*, vol. 13, no. 7, pp. 3237–3242, 2013.

[11] S. J. Cartamil-Bueno, P. G. Steeneken, A. Centeno, A. Zurutuza, H. S. van der Zant, and S. Houri, "Colorimetry technique for scalable characterization of suspended graphene," *Nano letters*, vol. 16, no. 11, pp. 6792–6796, 2016.

[12] R. J. Dolleman, D. Davidovikj, S. J. Cartamil-Bueno, H. S. van der Zant, and P. G. Steeneken, "Graphene squeeze-film pressure sensors," *Nano letters*, vol. 16, no. 1, pp. 568–571, 2015.

[13] A. D. Smith, F. Niklaus, A. Paussa, S. Schröder, A. C. Fischer, M. Sterner, S. Wagner, S. Vaziri, F. Forsberg, D. Esseni, M. Östling, and M. C. Lemme, "Piezoresistive properties of suspended graphene membranes under uniaxial and biaxial strain in nanoelectromechanical pressure sensors," *ACS nano*, vol. 10, no. 11, pp. 9879–9886, 2016.

[14] M. S. Boutilier, C. Sun, S. C. O'Hern, H. Au, N. G. Hadjiconstantinou, and R. Karnik, "Implications of permeation through intrinsic defects in graphene on the design of defect-tolerant membranes for gas separation," *Acs Nano*, vol. 8, no. 1, pp. 841–849, 2014.

[15] S. P. Koenig, N. G. Boddeti, M. L. Dunn, and J. S. Bunch, "Ultrastrong adhesion of graphene membranes," *Nature nanotechnology*, vol. 6, no. 9, p. 543, 2011.

[16] S. Huang, M. Dakhchoune, W. Luo, E. Oveisi, G. He, M. Rezaei, J. Zhao, D. T. Alexander, A. Züttel, M. S. Strano, and K. Varoon Agrawal, "Single-layer graphene membranes by crack-free transfer for gas mixture separation," *Nature communications*, vol. 9, 2018.

[17] L. Huang, M. Zhang, C. Li, and G. Shi, "Graphene-based membranes for molecular separation," *The journal of physical chemistry letters*, vol. 6, no. 14, pp. 2806–2815, 2015.

[18] W. Perkins and D. Begeal, "Diffusion and permeation of he, ne, ar, kr, and d2 through silicon oxide thin films," *The Journal of Chemical Physics*, vol. 54, no. 4, pp. 1683–1694, 1971.

[19] A. Castellanos-Gomez, M. Buscema, R. Molenaar, V. Singh, L. Janssen, H. S. Van Der Zant, and G. A. Steele, "Deterministic transfer of two-dimensional materials by all-dry viscoelastic stamping," *2D Materials*, vol. 1, no. 1, p. 011002, 2014.

[20] D. Davidovikj, J. J. Slim, S. J. Cartamil-Bueno, H. S. van der Zant, P. G. Steeneken, and W. J. Venstra, "Visualizing the motion of graphene nanodrums," *Nano letters*, vol. 16, no. 4, pp. 2768–2773, 2016.

[21] B. Sajadi, F. Alijani, D. Davidovikj, J. Goosen, P. G. Steeneken, and F. van Keulen, "Experimental characterization of graphene by electrostatic resonance frequency tuning," *Journal of Applied Physics*, vol. 122, no. 23, p. 234302, 2017.

[22] M. A. Bissett, M. Tsuji, and H. Ago, "Strain engineering the properties of graphene and other two-dimensional crystals," *Physical Chemistry Chemical Physics*, vol. 16, no. 23, pp. 11124–11138, 2014.

[23] D. Davidovikj, F. Alijani, S. J. Cartamil-Bueno, H. Zant, M. Amabili, and P. G. Steeneken, "Nonlinear dynamic characterization of two-dimensional materials," *Nature Communications*, vol. 8, no. 1, p. 1253, 2017.

5

5

Magnetic and electronic phase transitions probed by nanomechanical resonators

The reduced dimensionality of two-dimensional (2D) materials results in characteristic types of magnetically and electronically ordered phases. However, only few methods are available to study this order, in particular in ultrathin insulating antiferromagnets that couple weakly to magnetic and electronic probes. Here, we demonstrate that phase transitions in thin membranes of 2D antiferromagnetic $FePS_3$, $MnPS_3$ and $NiPS_3$ can be probed mechanically via the temperature-dependent resonance frequency and quality factor. The observed relation between mechanical motion and antiferromagnetic order is shown to be mediated by the specific heat and reveals a strong dependence of the Néel temperature of $FePS_3$ on electrostatically induced strain. The methodology is not restricted to magnetic order, as we demonstrate by probing an electronic charge-density-wave phase in 2H-TaS_2. It thus offers the potential to characterize phase transitions in a wide variety of materials, including those that are antiferromagnetic, insulating or so thin that conventional bulk characterization methods become unsuitable.

Parts of this chapter have been published in Nature Communications **11**, 2698 (2020) by M. ŠiŠkins, **M. Lee**, S. Mañas-Valero, E. Coronado, Y. M. Blanter, H. S. J. van der Zant, and P. G. Steeneken.

5.1. Introduction

Nanomechanical resonators made of two-dimensional (2D) materials offer interesting pathways for realizing high-performance devices [1, 2]. Unique functionalities and phenomena emerge when combining nanomechanics with the types of magnetic and electronic phases that have recently been uncovered in 2D materials like magic-angle induced phase transitions [3, 4], 2D Ising antiferromagnets [5] and ferromagnetism in 2D atomic layers [6, 7] and heterostructures [8]. Only a few methods are available to study these phases in 2D materials [5–9]. A universal method to characterize phase transitions in bulk crystals is via anomalies in the specific heat, that are present at the transition temperature according to Landau's theory [10]. However, specific heat is difficult to measure in thin micron-sized samples with a mass of less than a picogram [11, 12].

We demonstrate that these phases are strongly coupled to mechanical motion: the temperature dependent resonance frequency and quality factor of multilayer 2D material membranes show anomalies near the phase transition temperature. Although coupling between mechanical and electronic/magnetic degrees of freedom might not seem obvious, the intuitive picture behind this coupling is that changes in the electronic/magnetic order and entropy in a material are reflected in its specific heat, which in turn results in variations in the thermal expansion coefficient that affect the tension and resonance frequency. As the specific heat near a phase transition is expected to exhibit a discontinuity [10], the temperature dependent resonance frequency of a suspended membrane can thus be used to probe this transition.

The coupling of mechanical degrees of freedom to magnetic and electronic order is attributed to thermodynamic relations. Nanomechanical resonators, therefore, offer the potential to characterize phase transitions and realize device concepts in a wide variety of systems, not restricted only to van der Waals materials but including those that are ultrathin, antiferromagnetic or insulating [8]. Here, we use nanomechanical motion to investigate magnetic order in membranes of semiconducting $FePS_3$, $NiPS_3$ and insulating $MnPS_3$ - antiferromagnetic members of the transition-metal phosphor trisulphides (MPS_3) [13], and subsequently discuss results on metallic 2H-TaS_2, which exhibits a transition to a charge density wave state [14].

5.2. Results

5.2.1. Antiferromagnetic mechanical resonators.

$FePS_3$ is an Ising-type antiferromagnet with a Néel temperature in bulk in the range of $T_N \sim 118 - 123$ K [5, 13, 16], exhibiting a distinct feature in its specific heat near T_N [16]. Ionic layers in $FePS_3$ are stacked in van der Waals planes, that can be exfoliated to thin the crystal down with atomic precision [5]. Using mechanical exfoliation and all-dry viscoelastic stamping [17], we transfer thin flakes of $FePS_3$ over circular cavities etched in an oxidised Si wafer, to form membranes (see the inset in Fig. 5.1a). Suspended $FePS_3$ devices with thicknesses ranging from 8 to 45 nm are placed in a cryostat and cooled down to a temperature of 4 K. The resonance fre-

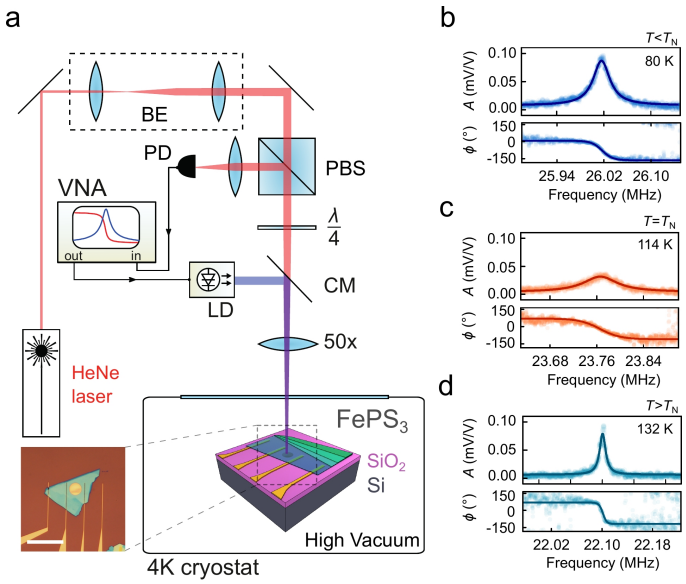

Figure 5.1: Characterisation of mechanical resonances in a thin antiferromagnetic $FePS_3$ membrane. (a) Laser interferometry setup. Red interferometric detection laser: $\lambda_{red} = 632$ nm. Blue actuation laser diode: $\lambda_{blue} = 405$ nm. VNA - Vector Network Analyzer, CM - Cold Mirror, PBS - Polarizing Beam Splitter, PD - Photodiode, LD - Laser Diode. Inset: optical image of a $FePS_3$ membrane, including electrodes introducing an option for electrostatic control of strain in the membrane. Flake thickness: 45.2 ± 0.6 nm; membrane diameter: $d = 10$ μm. Scale bar: 30 μm. (b-d) Amplitude (A) and phase (ϕ) of the fundamental resonance at three different temperatures for the device shown in (a). Filled dots - measured data; solid lines - fit of the mechanical resonance used to determine f_0 and Q [15].

quency of the nanodrums is then characterized using a laser interferometry technique [15] (see Fig. 5.1a and Methods).

The resonance frequency of the fundamental membrane mode, $f_0(T)$, is measured in the temperature range from 4 to 200 K. Typical resonances are shown in Fig. 5.1b-d in the antiferromagnetic phase (80 K), near the transition (114 K) and in the paramagnetic phase (132 K), respectively. Figure 5.2a shows $f_0(T)$ of the same $FePS_3$ membrane (solid blue curve). Near the phase transition, significant changes in amplitude, resonance frequency and quality factor are observed.

5.2.2. Resonance and specific heat.

To analyze the data further, we first analyze the relation between f_0 and the specific heat. The decrease in resonance frequency with increasing temperature in Fig. 5.2a is indicative of a reduction in strain due to thermal expansion of the membrane. The observed changes can be understood by considering the resonance frequency of a bi-axially tensile strained circular membrane:

$$f_0(T) = \frac{2.4048}{\pi d}\sqrt{\frac{E}{\rho}\frac{\epsilon(T)}{(1-\nu)}}, \tag{5.1}$$

where E is the Young's modulus of the material, ν its Poisson's ratio, ρ its mass density, $\epsilon(T)$ the strain and T the temperature. The linear thermal expansion coefficient of the membrane, $\alpha_{\mathrm{L}}(T)$, and silicon substrate, $\alpha_{\mathrm{Si}}(T)$, are related to the strain in the membrane [18] as $\frac{\mathrm{d}\epsilon(T)}{\mathrm{d}T} \approx -(\alpha_{\mathrm{L}}(T) - \alpha_{\mathrm{Si}}(T))$, using the approximation $\alpha_{\mathrm{SiO_2}} \ll \alpha_{\mathrm{Si}}$ (see Supplementary Note 1). By combining the given expression for $\frac{\mathrm{d}\epsilon(T)}{\mathrm{d}T}$ with equation (5.1) and by using the thermodynamic relation $\alpha_{\mathrm{L}}(T) = \gamma c_{\mathrm{v}}(T)/(3KV_{\mathrm{M}})$ [19] between $\alpha_{\mathrm{L}}(T)$ and the specific heat (molar heat capacity) at constant volume, $c_{\mathrm{v}}(T)$, we obtain:

$$c_{\mathrm{v}}(T) = 3\alpha_{\mathrm{L}}(T)\frac{KV_{\mathrm{M}}}{\gamma} = 3\left(\alpha_{\mathrm{Si}} - \frac{1}{\mu^2}\frac{\mathrm{d}[f_0^2(T)]}{\mathrm{d}T}\right)\frac{KV_{\mathrm{M}}}{\gamma}. \tag{5.2}$$

Here, K is the bulk modulus, γ the Grüneisen parameter, $V_{\mathrm{M}} = M/\rho$ the molar volume of the membrane and $\mu = \frac{2.4048}{\pi d}\sqrt{\frac{E}{\rho(1-\nu)}}$, that are assumed to be only weakly temperature dependent. The small effect of non-constant volume ($\nu \neq 0.5$) on c_{v} is neglected.

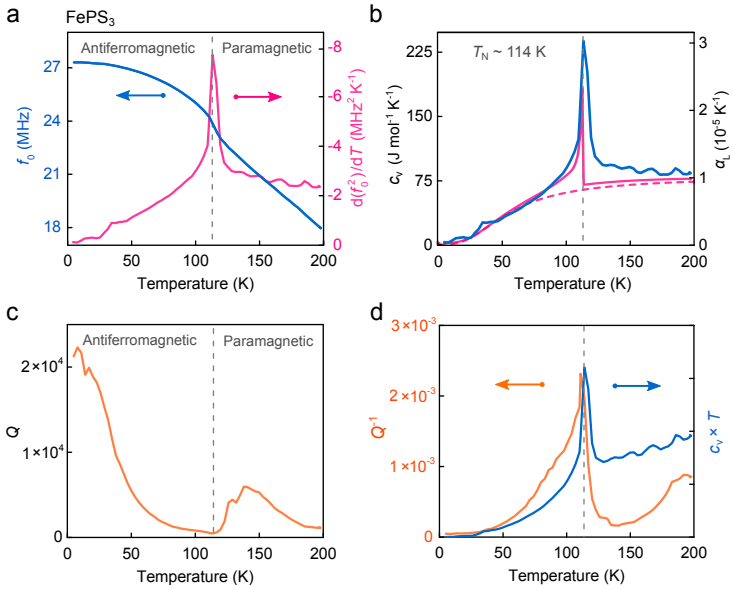

Figure 5.2: Mechanical and thermal properties properties of a $FePS_3$ resonator with membrane thickness of 45.2 ± 0.6 nm. In all panels, dashed vertical lines indicate the detected transition temperature, $T_{\mathrm{N}} = 114 \pm 3$ K as determined from the peak in the temperature derivative of f_0^2. (a) Solid blue line - measured resonance frequency as a function of temperature. Solid magenta line - temperature derivative of f_0^2. (b) Solid blue line - experimentally derived specific heat and corresponding thermal expansion coefficient. Solid magenta line - the theoretical calculation of the magnetic specific heat as reported in Takano et al. [16] added to the phononic specific heat from Debye model (dashed magenta line) with a Debye temperature of $\Theta_{\mathrm{D}} = 236$ K [16]. (c) Mechanical quality factor $Q(T)$ of the membrane fundamental resonance. (d) Solid orange line - measured mechanical damping $Q^{-1}(T)$ as a function temperature. Solid blue line - normalized $c_{\mathrm{v}}(T)\,T$ term [20, 21] (see supplementary equation (14)), with $c_{\mathrm{v}}(T)$ taken from (b).

We use the equation (5.2) to analyze $f_0(T)$ and compare it to the calculated spe-

cific heat for $FePS_3$ from literature [16]. In doing so, we estimate the Grüneisen parameter following the Belomestnykh–Tesleva relation $\gamma \approx \frac{3}{2}\left(\frac{1+\nu}{2-3\nu}\right)$ [19, 22]. This is an approximation to Leont'ev's formula [23], which is a good estimation of γ for bulk isotropic crystalline solids within ~ 10% of uncertainty [19]. Furthermore, we use literature values for the elastic parameters of $FePS_3$ as obtained from first-principles theoretical calculations [24] to derive $E = 103$ GPa, $\nu = 0.304$ and $\rho = 3375$ kg m^{-3} (see Supplementary Note 2).

5.2.3. Detecting phase transitions.

In Fig. 5.2a, the steepest part of the negative slope of $f_0(T)$ (solid blue curve) leads to a large peak in $\frac{\mathrm{d}(f_0^2(T))}{\mathrm{d}T}$ (solid magenta curve) near 114 K, the temperature which we define as T_N and indicate by the vertical dashed lines. In Fig. 5.2b the specific heat curve of $FePS_3$ (blue solid line) as estimated from the data in Fig. 5.2a and equation (5.2) is displayed. The results are compared to a theoretical model for the specific heat of $FePS_3$ (magenta solid line in Fig. 5.2b), which is the sum of a phononic contribution from the Debye model (magenta dashed line) and a magnetic contribution as calculated by Takano et al. [16]. It is noted that other, e.g. electronic contributions to $c_\mathrm{v}(T)$ are small and can be neglected in this comparison, as is supported by experiments on the specific heat in bulk $FePS_3$ crystals [16]. The close correspondence in Fig. 5.2b between the experimental and theoretical data for $c_\mathrm{v}(T)$ supports the applicability of equation (5.2). It also indicates that changes in the Young's modulus near the phase transition, that can be of the order of a couple of percent [25, 26], are insignificant and that it is the anomaly in c_v of $FePS_3$ which produces the observed changes in resonance frequency and the large peak in $\frac{\mathrm{d}(f_0^2)}{\mathrm{d}T}$ visible in Fig. 5.2a.

5.2.4. Effect of strain.

The abrupt change in $c_\mathrm{v}(T)$ of the membrane can be understood from Landau's theory of phase transitions [10]. To illustrate this, we consider a simplified model for an antiferromagnetic system, like $FePS_3$, with free energy, F, which includes a strain-dependent magnetostriction contribution (see Supplementary Note 3). Near the transition temperature and in the absence of a magnetic field it holds that:

$$F = F_0 + [a(T - T_\mathrm{N}) + \zeta(\epsilon)]L_z^2 + BL_z^4. \tag{5.3}$$

Here, a and B are phenomenological positive constants, L_z is the order parameter in the out-of-plane direction and $\zeta(\epsilon) = \eta_{ij}\epsilon_{ij}$, a strain-dependent parameter with η_{ij} a material-dependent tensor, that includes the strain and distance dependent magnetic exchange interactions between neighbouring magnetic moments. By minimizing equation (5.3) with respect to L_z, the equilibrium free energy, F_min, and order parameter are obtained (see Supplementary Note 3). Two important observations can be made. Firstly, strain shifts the transition temperature according to:

$$T_\mathrm{N}^*(\epsilon) = T_\mathrm{N} - \frac{\zeta(\epsilon)}{a}, \tag{5.4}$$

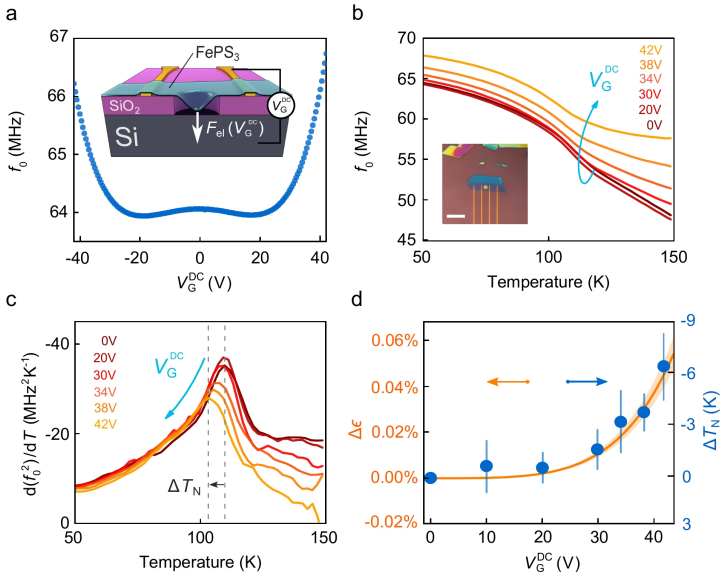

Figure 5.3: Resonance frequency and transition temperature tuning with a gate voltage. (a) Resonance frequency as a function of gate voltage at 50 K. Inset - schematics of the electrostatic tuning principle. (b) Resonance frequency as a function of temperature for six different voltages. Inset: optical image of the sample, $t = 8 \pm 0.5$ nm. Scale bar: 16 μm. (c) Derivative of f_0^2 as a function of gate voltage and temperature. Blue arrow, line colors and legend indicate the values of V_G^{DC}. Dashed grey lines indicate the decrease in transition temperature $\Delta T_N = T_N^*(V_G^{DC}) - T_N(0\,V)$ with increasing V_G^{DC}. (d) Blue solid dots - shift in T_N as a function of V_G^{DC} extracted from the peak position in (c). Vertical blue bars - error bar in ΔT_N estimated from determining the peak position in (c) within 2% accuracy in the measured maximum. Orange solid line - model of electrostatically induced strain $\Delta\epsilon$ as a function of V_G^{DC} (see Supplementary Note 5).

where T_N^* is the Néel temperature, below which free energy minima F_{min} with finite order ($L_z \neq 0$) appear. Secondly, since close to the transition the specific heat follows $c_v(T) = -T\frac{\partial^2 F_{min}}{\partial T^2}$, this general model predicts a discontinuity in c_v of magnitude $T_N^* \frac{a^2}{2B}$ at the transition temperature T_N^*, in accordance with the experimental jump in $c_v(T)$ and $\frac{d(f_0^2(T))}{dT}$ observed in Fig. 5.2a and b.

5.2.5. Temperature dependent Q-factor.

We now analyze the quality factor data shown in Fig. 5.2c,d. Just above T_N, the quality factor of the resonance (Fig. 5.2c) shows a significant increase as the temperature is increased from 114 to 140 K. The observed minimum in the quality factor near the phase transition, suggests that dissipation in the material is linked to the thermodynamics and can be related to thermoelastic damping. We model the thermoelastic damping according to Zener [20] and Lifshitz-Roukes [21] that report dissipation of the form $Q^{-1} = \beta c_v(T)\,T$, where β is the thermomechanical term (see Supplementary Note 4). Since we have obtained an estimate of $c_v(T)$ from the

resonance frequency analysis (Fig. 5.2b), we use this relation to compare the experimental dissipation $Q^{-1}(T)$ (orange solid line) to a curve proportional to $c_v(T)\,T$ (blue solid line) in Fig. 5.2d. Both the measured dissipation and the thermoelastic term display a peak near $T_N \sim 114$ K. The close qualitative correspondence between the two quantities is an indication that the thermoelastic damping related term indeed can account for the temperature dependence of $Q(T)$ near the phase transition. We note that the temperature dependent dissipation in thin membranes is still not well understood, and that more intricate effects might play a role in the observed temperature dependence.

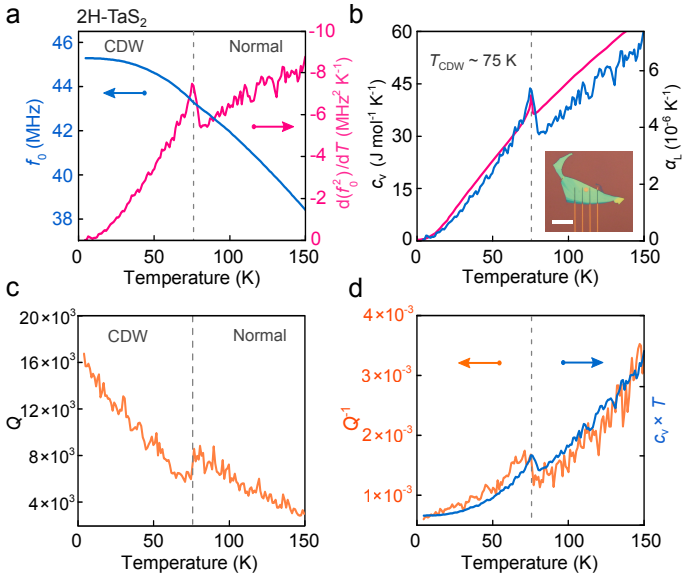

Figure 5.4: Mechanical properties of a 2H-TaS_2 resonator with membrane thickness of 31.2 ± 0.6 nm and $d = 4$ μm. Dashed vertical line in all 4 panels indicates the detected T_{CDW}, that is defined by the peak in $\frac{d(f_0^2(T))}{dT}$. (a) Solid blue line - resonance frequency as a function of temperature. Solid magenta line - temperature derivative of f_0^2. (b) Solid blue line - experimentally derived c_v and thermal expansion coefficient as a function of temperature (see Supplementary Note 6). Solid magenta line - specific heat of bulk 2H-TaS_2 as reported in Abdel-Hafiez et al. [14]. Inset: optical image of the sample. Scale bar: 20 μm. (c) Quality factor $Q(T)$ as a function of temperature. (d) Solid orange line - measured mechanical damping $Q^{-1}(T)$ as a function of temperature. Solid blue line - curve proportional to the term $c_v(T)\,T$ [20, 21] (see supplementary equation (14)), with $c_v(T)$ taken from the experimental data in (b).

5.2.6. Electrostatic strain.

Equation (5.4) predicts that the transition temperature is strain-dependent due to the distance dependent interaction coefficient $\zeta(\epsilon)$ between magnetic moments. To verify this effect, we use an 8 ± 0.5 nm thin sample of $FePS_3$ suspended over a cavity of 4 μm in diameter. A gate voltage V_G^{DC} is applied between the flake and the doped bottom Si substrate to introduce an electrostatic force that pulls the membrane down and thus strains it (see Supplementary Fig. 4 and 5). As shown in

Fig. 5.3a, the resonance frequency of the membrane follows a W-shaped curve as a function of gate voltage. This is due to two counteracting effects [27]: at small gate voltages capacitive softening of the membrane occurs, while at higher voltages the membrane tension increases due to the applied electrostatic force, which causes the resonance frequency to increase.

Figure 5.3b shows $f_0(T)$ for six different gate voltages. The shift of the point of steepest slope of $f_0(T)$ with increasing V_G^{DC} is well visible in Fig. 5.3b and even more clear in Fig. 5.3c, where the peak in $\frac{d(f_0^2)}{dT}$ shifts 6 K downward by electrostatic force induced strain. The observed reduction in T_N^* as determined by the peak position in $\frac{d(f_0^2)}{dT}$ qualitatively agrees with the presented model and its strain dependence from equation (5.4), as shown in Fig. 5.3d indicative of a reduced coupling of magnetic moments with increasing distance between them due to tensile strain.

5.3. Discussion

Since the coupling between specific heat and the order parameter in materials is of a general thermodynamic nature, the presented methodology is applicable to a wide variety of materials provided that elastic properties of the material and Grüneisen parameter are weakly temperature dependent, the substrate satisfies the condition $\alpha_{substrate} \ll \alpha_{material}$ and that the frequency shifts and changes in Q are large enough to be resolved. We further demonstrate the method by detecting magnetic phase transitions in $NiPS_3$ and $MnPS_3$. Compared to $FePS_3$, the effect of the phase transitions in $MnPS_3$ and $NiPS_3$ on the resonances is more gradual (see Supplementary Fig. 2) with both materials showing broader maxima in $\frac{d(f_0^2(T))}{dT}$ near their T_N at 76 K and 151 K, respectively, which is consistent with measurements of bulk crystals [13, 16].

In order to demonstrate the detection of an electronic phase transition, we now discuss results for 2H-TaS_2 that in bulk exhibits a charge density wave (CDW) transition at $T_{CDW} \sim 77$ K [14]. Figure 5.4a shows a transition-related anomaly in both $f_0(T)$ (solid blue line) and the temperature derivative of $f_0^2(T)$ (solid magenta line) that peaks at 75 ± 3 K. We convert $\frac{d(f_0^2(T))}{dT}$ to the corresponding $c_v(T)$ using the same approach as discussed before (see Supplementary Note 6). Figure 5.4b shows a downward step in the specific heat at 75 K (solid blue line), indicative of a phase transition from the CDW to the disordered high-temperature state [10, 28] with a close quantitative correspondence to c_v measured in a bulk crystal [14] (drawn magenta line). This anomaly occurs near the electrically determined phase transition temperature of ~ 77 K on the same flake (see Supplementary Fig. 6c) and is also consistent with the CDW transition temperature previously reported in 2H-TaS_2 [14]. The Q-factor also shows a local minimum with a drop next to the transition temperature (see Fig. 5.4c). As discussed before [20, 21], $Q^{-1}(T)$ is expected to follow the same trend as $c_v(T)\,T$. Both quantities are displayed in Fig. 5.4d and indeed show a good qualitative correspondence.

In conclusion, we have demonstrated that there exist a strong coupling between mechanical motion and order in ultrathin membranes of 2D materials. An ana-

lytical equation for the relation between the specific heat of the material and the temperature dependent resonance frequency is derived and shown to be in good agreement with experimental results. Since the materials are utilized in a suspended state, substrate effects on the electronic and magnetic properties of the thin materials are excluded. The technique is not only appealing for the characterisation of ultrathin membranes of antiferromagnetic and insulating materials that are difficult to characterize otherwise, but also for the development of device concepts exploiting the unique properties of the materials involved. It is anticipated that it can be applied to a large range of van der Waals materials [8, 9], 2D ferromagnets [29], thin 2D complex oxide sheets [30, 31] and organic antiferromagnets [32].

5.4. Methods

5.4.1. Sample fabrication

To realize electrical contact to the samples for electrostatic experiments, Ti/Au electrodes are pre-patterned by a lift-off technique. Cavities are defined by reactive ion etching of circular holes with a diameter of $4-10$ μm in oxidized doped silicon wafers with an SiO_2 thickness of 285 nm. Flakes of van der Waals crystals are exfoliated from high quality synthetically grown crystals with known stoichiometry (see Supplementary Note 7). All flakes are transferred on a pre-patterned chip by an all-dry viscoelastic stamping directly after exfoliation. Subsequently, samples are kept in an oxygen free environment to avoid degradation. In total, data on measurements of three $FePS_3$, one 2H-TaS_2, one $NiPS_3$ and one $MnPS_3$ devices is presented in this manuscript.

5.4.2. Controlled measurement environment

The samples are mounted on a piezo-based xy nanopositioning stage inside a chamber of a closed-cycle cryostat with optical access. A closed feedback loop controlled local sample heater is used to perform temperature sweeps at a rate of ~ 5 K per minute, while keeping the pressure in the chamber below 10^{-6} mbar. During the data acquisition temperature is kept constant with ~ 10 mK stability.

5.4.3. Laser interferometry

A blue diode laser ($\lambda = 405$ nm), which is power-modulated by a Vector Network Analyzer (VNA), is used to excite the membrane and optothermally drive it into motion. Displacements are detected by focusing a red He-Ne laser beam ($\lambda = 632$ nm) on the cavity formed by the membrane and Si substrate. The reflected light, which is modulated by the position-dependent membrane motion, is recorded by a photodiode and processed by a phase-sensitive VNA. All measurements are performed at incident laser powers of $P_{\mathrm{red}} < 10$ μW and $P_{\mathrm{blue}} < 0.6$ μW. It is checked for all membranes that the resonance frequency changes due to laser heating are insignificant. Laser spot size is on the order of ~ 1 μm. The uncertainty in measured transition temperatures is estimated from determining the peak position in $-\frac{\mathrm{d}(f_0^2(T))}{\mathrm{d}T}$ within 2% accuracy in the measured maximum. Information about the

reproducibility of measurements is available in Supplementary Note 8.

5.4.4. Atomic Force Microscopy

AFM inspections to determine sample thickness are performed in tapping mode on a Bruker Dimension FastScan AFM. We use cantilevers with spring constants of $k = 30 - 40$ N m^{-1}. Error bars on reported thickness values are determined by measuring three to five profile scans of the same flake.

Appendix.

A. Fundamental resonance frequency of a circular plate and membrane

In this section we analyze in more detail the resonance frequency of the $FePS_3$ resonators and show that near the phase transition they are close to the membrane limit. The fundamental resonance frequency of the mechanical resonator, f_0, in the crossover membrane-plate regime can be approximated as [15, 33]:

$$f_0(T) \approx \sqrt{f_{\text{membrane}}^2 + f_{\text{plate}}^2} = \sqrt{\left(\frac{2.4048}{\pi d}\right)^2 \frac{E}{\rho}\frac{\epsilon(T)}{(1-\nu)} + \left(\frac{10.21\,t}{\pi d^2}\right)^2 \frac{E}{3\rho\left(1-\nu^2\right)}}, \tag{5.5}$$

where d is the diameter of the membrane, E the Young's modulus, $\epsilon(T)$ the strain, ν the Poisson's ratio, t the thickness, ρ the mass density and T the temperature. The resonance frequency of the fundamental mode of a circular resonator is thickness dependent. For plate resonators $f_{\text{plate}} \propto t$, as expected for small and linear deflection [15, 33, 34]. For membranes, however, f_0 is dominated by the biaxial tension N:

$$f_{\text{membrane}} = \frac{2.4048}{\pi d}\sqrt{\frac{N}{\rho t}}. \tag{5.6}$$

Supplementary equation (5.6) yields $f_{\text{membrane}} \propto t^{-0.5}$ for thin resonators. When the membrane is subjected to temperature changes, the total tension is dominated by thermal strains $\epsilon_{\text{r}}^{\text{th}}$. Thermal strains are of dilatational nature and do not cause any shear, thus, these can be written as: $\epsilon_{\text{r}}^{\text{th}} = \alpha\Delta T$, where α is the thermal expansion coefficient. In-plane radial thermal strain is then related to tension according to the Hooke's law as $N = N_0 + Et\epsilon_{\text{r}}^{\text{th}}/(1-\nu)$, where N_0 the intrinsic pre-tension introduced during the fabrication process. Thus, supplementary equation (5.5) is used to determine if the membranes under study are in the plate or in the membrane limit at a given temperature, as shown in Supplementary Fig. A.1a,b.

The relative contribution of the plate term to the frequency of the resonator is largest at room temperature because the membrane tension is the lowest. As shown in Supplementary Fig. A.1a at $T = 300$ K and $N_0 = 0.1$ N m^{-1}, thicker $FePS_3$ samples ($t > 40$ nm) behave as circular plates. However, as shown in Supplementary Fig. A.1b, in proximity of the transition temperature ($T \approx 114$ K) due to temperature-induced strain $\epsilon(T)$ (see supplementary equation (5.5)), the resonator behaves close to the membrane limit over a thickness range from zero to 60 nm.

The total strain in the membrane is estimated using $\epsilon(T) = \epsilon_0 - \int_{300\text{K}}^{T}(\alpha_{\text{material}}(T) - \alpha_{\text{Si}}(T))\text{d}T$, where ϵ_0 is the intrinsic pre-strain at $T = 300$ K [18, 35]. Because $\alpha_{SiO_2} \ll \alpha_{\text{Si}}$ [36, 37], the effect of the thin SiO_2 layer can be neglected. As shown in Supplementary Fig. A.1c, the thermal expansion coefficient of the silicon substrate (solid magenta line) is small compared to that of $FePS_3$. Therefore, the total strain in the membrane will mainly build up due to α_{FePS_3}, and this term dominates the change in resonance frequency, $f_0(T)$ as depicted in Supplementary Fig. A.1d.

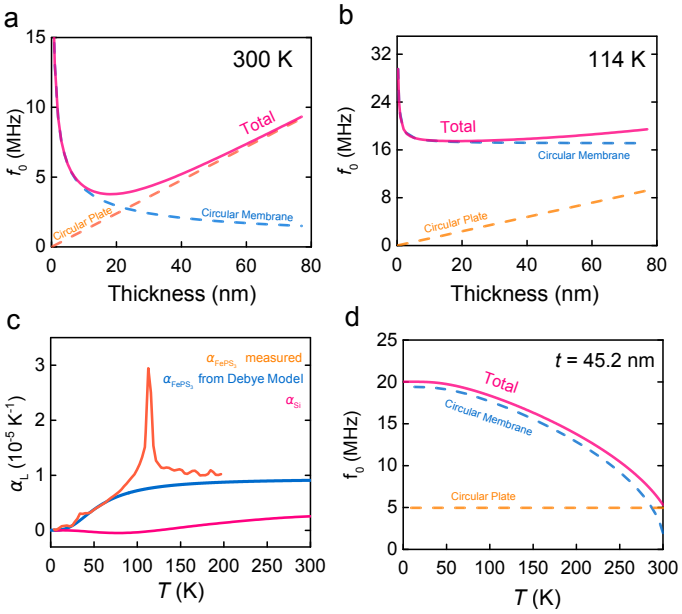

Figure A.1: Resonance frequency of a $FePS_3$ resonator as a function of thickness for (a) 300 K and (b) 114 K. (c) Comparison of thermal expansion coefficients of $FePS_3$ as measured (solid orange line) and as predicted from the Debye model (solid blue line) to that of the Si substrate (solid magenta line). (d) Calculated resonance frequency of a $FePS_3$ membrane using supplementary equation (5.5) with a diameter of 10 μm taking into account the thermal expansion coefficient of $FePS_3$ as predicted by the Debye model.

B. Mechanical resonances and specific heat of MPS_3 (M=Fe, Ni, Mn)

In addition to $FePS_3$, we measure $MnPS_3$ and $NiPS_3$ membranes with a 10 μm diameter and thicknesses of 31.8 ± 1.2 and 35.7 ± 1.1 nm, respectively. Comparative study of these is particularly interesting since $FePS_3$ is an Ising antiferromagnet, while the other two are Heisenberg ($MnPS_3$) and XY ($NiPS_3$) antiferromagnets. The resonance peak of the fundamental membrane mode, $f_0(T)$, as well as the Q-factor is measured from $4-200$ K using the procedure described in the main text. We note that the resonance frequency and quality factor are related via causality: $f(T) = f_0(T)\sqrt{1-\frac{1}{4Q(T)^2}}$. However, for a quantitative change in the Q-factor next to the phase transition in samples presented in Fig. 2c of the main text and Supplementary Fig. B.1, we expect the effect on $f_0(T)$ to be of the order of kHz, which is insignificant compared to the change in frequency up to ~ 2 MHz.

At the phase transition, significant changes in both the resonance frequency (Supplementary Fig. B.1a) and quality factor (Supplementary Fig. B.1b) of the $MnPS_3$ membrane are observed. Supplementary figure B.1a shows the resonance frequency (solid blue line) and the corresponding $\frac{d(f_0^2)}{dT}$ (solid magenta line) with a peak that occurs at a temperature similar to the transition temperature from the antiferromagnetic phase (< 78 K) to the paramagnetic phase (> 78 K) in the bulk material

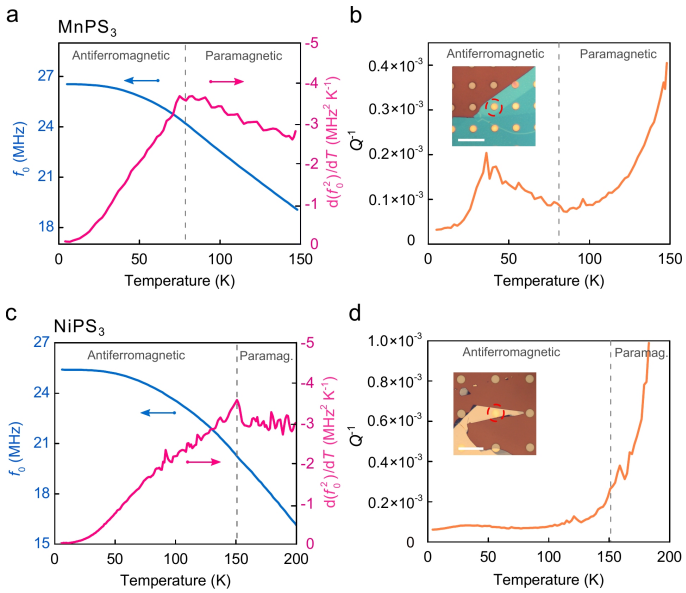

Figure B.1: Mechanical properties of $MnPS_3$ and $NiPS_3$ membranes. Dashed vertical lines indicate transition temperatures, T_N. (a) Solid blue line - Measured resonance frequency of $MnPS_3$ membrane as a function of temperature. Solid magenta line - Temperature derivative of f_0^2. (b) Measured mechanical damping (Q^{-1}) as a function temperature. Inset: Optical image of the sample, $t = 32.3 \pm 0.4$ nm. Scale bar: 40 μm. (c) Solid blue line - Measured resonance frequency of $NiPS_3$ membrane as a function of temperature. Solid magenta line - Temperature derivative of f_0^2. (b) Measured mechanical damping (Q^{-1}) as a function temperature. Inset: Optical image of the sample, $t = 35.7 \pm 0.5$ nm. Scale bar: 30 μm.

[16] and is thus attributed as T_N. The temperature dependence of $d(f_0^2)/dT$ shows a broad hump with a smeared peak at T_N, which resembles the temperature dependent specific heat $c_v(T)$ of this material in bulk form [16]. Supplementary figure B.1b shows the mechanical dissipation, Q^{-1}, that exhibits a local minimum close to T_N as well as a local maximum at $T \sim 36$ K. In Supplementary Fig. B.1c the resonance frequency of the $NiPS_3$ membrane (solid blue line) is shown with the corresponding $\frac{d(f_0^2)}{dT}$ (solid magenta line). A small peak is noticeable in $\frac{d(f_0^2)}{dT}$ near bulk $T_N \sim 155$ K indicating the phase transition [38]. However, as shown in Supplementary Fig. B.1d, no significant anomalies in the Q-factor were observed in the case of $NiPS_3$. Compared to $FePS_3$, the effect of the phase transitions in $MnPS_3$ and $NiPS_3$ on the resonances is more gradual (Supplementary Fig. B.1a-d). Both materials show a peak in $\frac{d(f_0^2)}{dT}$ at the T_N, but their dissipation does not show a clear jump at T_N like in the case of $FePS_3$.

We also calculated the corresponding temperature dependent specific heat $c_v(T)$ for the three MPS_3 samples. Following the methodology described in the main text, we estimate the Grüneisen parameter following the Belomestnykh–Tesleva relation [22, 39]: $\gamma \approx \frac{3}{2}\left(\frac{1+\nu}{2-3\nu}\right)$. We use reported values for monolayers of $FePS_3$ ($C_{11} = 72.7$ N m^{-1}, $C_{12} = 22.1$ N m^{-1} and $\rho_{2D} = 2.16 \times 10^{-6}$ kg m^{-2}), $MnPS_3$ ($C_{11} = 61.7$

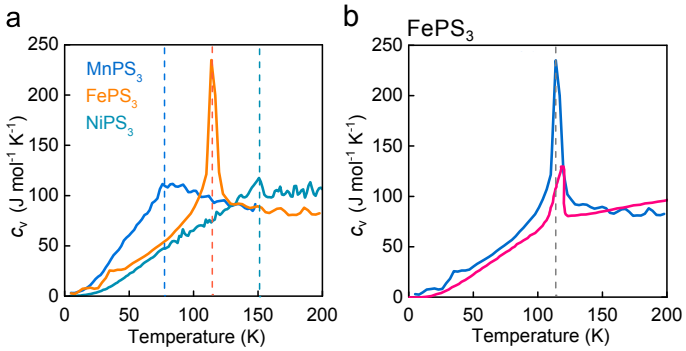

Figure B.2: Estimated specific heat (c_v) for (a) MPS_3 (M=Fe, Mn, Ni) membranes of $t = 45.2 \pm 0.6$ nm, 31.8 ± 1.2 nm and 35.7 ± 1.1 nm, respectively. Dashed lines indicate the corresponding transition temperatures (T_N): $T_N = 76 \pm 5$ K for $MnPS_3$, $T_N = 114 \pm 3$ K for $FePS_3$ and $T_N = 151 \pm 5$ K for $NiPS_3$. (b) Specific heat of ultrathin $FePS_3$ membrane compared to that of its bulk form. Solid blue line - measured c_v of the $FePS_3$ ultrathin membrane. Solid magenta line - c_v reported by Takano et al. [16] for a bulk crystal.

5

N m^{-1}, $C_{12} = 20.2$ N m^{-1} and $\rho_{2D} = 2.00 \times 10^{-6}$ kg m^{-2}) and $NiPS_3$ ($C_{11} = 87.0$ N m^{-1}, $C_{12} = 23.1$ N m^{-1} and $\rho_{2D} = 2.15 \times 10^{-6}$ kg m^{-2}) as obtained from first-principles calculations [24, 40]. We convert these to three-dimentional Young's modulus E, mass density ρ and Poisson's ratio ν using $E = \frac{C_{11}^2 - C_{12}^2}{C_{11}} \frac{1}{t}$, $\rho = \frac{\rho_{2D}}{t}$ and $\nu = \frac{C_{12}}{C_{11}}$, assuming the interlayer distance for the compounds to be $t_{FePS_3} = 0.64$ nm, $t_{MnPS_3} = 0.65$ nm and $t_{NiPS_3} = 0.64$ nm as determined from Supplementary Fig. G.1a-c. The resulting values are $E = 103$ GPa, $\nu = 0.304$ and $\rho = 3375$ kg m^{-3} for $FePS_3$, $E = 85$ GPa, $\nu = 0.327$ and $\rho = 3076$ kg m^{-3} for $MnPS_3$ and $E = 126$ GPa, $\nu = 0.265$ and $\rho = 3359$ kg m^{-3} for $NiPS_3$.

In Supplementary Fig. B.2a the specific heat for the three MPS_3 are displayed, as determined from the data in Supplementary Fig. B.1a,c, and Fig. 2a using equation (2) from the main text. Detected temperatures are indicated by dashed lines and found to be $T_N = 76 \pm 5$ K for $MnPS_3$, $T_N = 114 \pm 3$ K for $FePS_3$ and $T_N = 151 \pm 5$ K for $NiPS_3$, which are in agreement with experiments in bulk crystals of MPS_3 [13, 16]. As shown in Supplementary Fig. B.2b, for $FePS_3$ we obtain a good correspondence to bulk literature values [16] (solid magenta curve) without fitting parameters. The transition related peak in c_v, however, is more pronounced in the case of the ultrathin membrane (solid blue curve) than in the bulk.

C. Entropy in a suspended antiferromagnet

A uniaxial antiferromagnet with two antiparallel magnetic sub-lattices close to the phase transition can be modeled by the Landau theory of phase transitions [10, 41]. In this theory, the vector order parameter L is defined as the difference between the magnetizations of the two sublattices, M_1 and M_2 (thus, the antiferromagnetic vector $L = M_1 - M_2$). This order parameter is zero in the paramagnetic phase and is finite in the antiferromagnetic phase. The magnetization, M, is the sum of both magnetizations ($M = M_1 + M_2$) and equals to zero in the absence of an external magnetic

field, H.

For a uniaxial crystal antiferromagnet, the transition temperature is commonly known as Néel temperature, T_N, but, as conveyed by Landau et al. [10, 41], it is also referred to as the antiferromagnetic Curie temperature and denoted as T_c. Note that further we will consider the Néel temperature, denoted as T_N, as the temperature where the transition from a paramagnetic to an antiferromagnetic phase takes place. Near T_N, L is small and the free energy, F, can be expanded in terms of L and H, since the magnetization is only non-zero when an external field H is present (i.e. a spin-flop transition). Following Landau formalism and considering z-axis as the main axis of symmetry, we write (see e.g. Ref. [10]):

$$F = F_0 + AL^2 + BL^4 + D\,(\mathrm{H}\cdot\mathrm{L})^2 + D'H^2L^2 - \frac{1}{2}\chi_p H^2 + \frac{1}{2}\beta\left(L_x^2 + L_y^2\right) - \frac{1}{2}\mu_M\left(H_x^2 + H_y^2\right) - \frac{H^2}{8\pi}\,, \tag{5.7}$$

where $A = a(T - T_N)$, D, D', a and B are phenomenological positive constants which are taken temperature independent, χ_p the isotropic susceptibility for $T > T_N$, β the index that describes the temperature dependence of the spontaneous magnetization below T_N ($\beta > 0$ for L directed out-of-plane) and μ_M the magnetic susceptibility in the paramagnetic phase. The minimization of supplementary equation (5.7), where the vector L is along the z-axis (thus, $L_x = L_y = 0$ and $\beta > 0$) and in the absence of field ($H = 0$), gives $L_x = L_y = 0$ and $L_z = 0$ for $T > T_N$ (paramagnetic phase) and $L_z = \sqrt{a(T_N - T)/(2B)}$ for $T < T_N$ (antiferromagnetic phase).

Now we introduce strain. For an easy-axis antiferromagnet near T_N with the vector L along the z-axis and in the absence of field, we can write supplementary equation (5.7) as:

$$F = F_0 + AL^2 + BL^4 + \frac{1}{2}\beta\left(L_x^2 + L_y^2\right) + \zeta L_z^2 + \zeta_x L_x^2 + \zeta_y L_y^2\,, \tag{5.8}$$

where the last three added terms describe the magnetostriction effects, i.e., the coupling of magnetic moments to strain; the coefficients ζ, $\zeta_{x,y}$ are linear combinations of the components of the strain tensor. We assume that the strain is determined by the deformation of the membrane, and that the back-action exerted by the magnetization on the strain is negligible. In that case, for the calculation of the order parameter, ζ and $\zeta_{x,y}$ can be treated as temperature-independent constants. We also assume that $|\zeta|, |\zeta_{x,y}| \ll \beta$, so that even the strained antiferromagnet exhibits an easy-axis. The minimization of supplementary equation (5.8) gives $L_x = L_y = 0$, leading to a free energy which only depends on L_z,

$$F = F_0 + [a\,(T - T_N) + \zeta]\,L_z^2 + BL_z^4. \tag{5.9}$$

The first observation is that the magnetostriction effects shift the antiferromagnetic phase transition point. Indeed, the phase transition occurs at the temperature T_N^* at which the coefficient multiplying L_z^2 in supplementary equation (5.9) vanishes. This gives $T_N^* = T_N - \zeta/a$ (which is equation (4) in the main text).

Second, we calculate the behavior of the specific heat close to the phase transition. Minimizing supplementary equation (5.9) with respect to L_z, we find the

equilibrium free energy, $F_{\min} = F_0 - a^2(T - T_N^*)^2/(4B)$ in the antiferromagnetic phase, where F_0 is the free energy of the paramagnetic phase. We proceed by calculating the entropy $S_{\min} = -\partial F_{\min}/\partial T$,

$$S_{\min} - S_0 = \begin{cases} -a^2(T_N^* - T)/(2B) & T < T_N^* \\ 0 & T > T_N^* \end{cases}, \tag{5.10}$$

where $S_0 = -\partial F_0/\partial T$ is the entropy of the paramagnet with S_0 the non-magnetic contribution to the entropy. Since the renormalized transition temperature T_N^* is strain-dependent, the entropy of the antiferromagnet contains an additional (as compared to the paramagnetic phase) strain-dependent term. The specific heat near T_N^*, $c_{v,\min} = T\partial S_{\min}/\partial T$, reads

$$c_{v,\min} - c_{v,0} = \begin{cases} T_N^* a^2/(2B) & T < T_N^* \\ 0 & T > T_N^* \end{cases}, \tag{5.11}$$

where $c_{v,0}$ is the non-magnetic contribution to the specific heat. This derivation shows, in line with Landau theory [10, 41], that the specific heat has a jump at the transition temperature, T_N^*.

5

D. Dissipation and thermoelastic damping in vibrating membranes

For a membrane in motion the dissipation Q^{-1} is defined as the ratio of the energy lost per cycle to 2π times the stored energy. The total dissipation in a membrane is given by the sum of all contributing dissipation mechanisms [42]:

$$Q^{-1} = Q^{-1}_{\text{medium}} + Q^{-1}_{\text{clamping}} + Q^{-1}_{\text{intrinsic}} + Q^{-1}_{\text{other}}. \tag{5.12}$$

Q^{-1}_{medium} is related to losses due to the interaction with a fluid medium or gas and can thus be neglected in high vacuum. Q^{-1}_{clamping} is related to the transfer of mechanical energy to the anchoring substrate, which has a small temperature dependence [42]. $Q^{-1}_{\text{intrinsic}}$ quantifies all intrinsic damping mechanisms of the material, such as thermoelastic damping, internal and surface friction, and phonon-phonon interaction loss. Q^{-1}_{other} relates all other possible damping mechanisms, such as electrical charge damping and magneto-motive damping. In this section we focus on deriving the expression for the thermoelastic damping. Further derivation in this section follows Zener's standard linear solid model [20, 43].

The dissipation is equal to the ratio between the imaginary and real parts of the complex elastic modulus $E^*(\omega) = E'(\omega) + iE''(\omega)$:

$$Q^{-1} = \frac{E''}{E'}. \tag{5.13}$$

For a standard linear solid with a single relaxation mechanism, real and imaginary parts of the complex elastic modulus are given by:

$$E'(\omega) = E_r + (E_u - E_r)\frac{\omega^2\tau^2}{1+(\omega\tau)^2},\ E''(\omega) = (E_u - E_r)\frac{\omega\tau}{1+(\omega\tau)^2}, \tag{5.14}$$

where ω is the resonance eigenfrequency, τ the thermal relaxation time, E_r and E_u are the relaxed (or isothermal) and unrelaxed (or adiabatic) Young's moduli, respectively (see Ref. [42, 43] for more details). From supplementary equation (5.13), the dissipation is then:

$$Q^{-1} = (E_u - E_r)\frac{\omega\tau}{E_r + E_u(\omega\tau)^2} \approx \frac{E_u - E_r}{E_r}\frac{\omega\tau}{1+(\omega\tau)^2}, \tag{5.15}$$

for $(E_u - E_r) \ll E_r \approx E_u$. For a standard thermoelastic solid and in the case of thermoelastic damping Q^{-1}_{TED}, supplementary equation (5.15) can be rewritten as [20, 21, 43]:

$$Q^{-1}_{TED} = \frac{E_u - E_r}{E_r}\beta = \frac{E\alpha^2 T}{c_v}\beta, \tag{5.16}$$

where α is the thermal expansion coefficient, c_v the specific heat and β the thermomechanical parameter, that in Zener's model is $\beta_Z = \frac{\omega\tau}{1+(\omega\tau)^2}$. The exact expression for thermoelastic damping and its relation to the thermal properties of solids was found by Lifshitz and Roukes [21] with $\beta_{LR} = \frac{6}{\xi^2} - \frac{6}{\xi^3}\frac{\sinh(\xi)+\sin(\xi)}{\cosh(\xi)+\cos(\xi)}$, where $\xi = \frac{\pi}{\sqrt{2}}\sqrt{\omega\tau}$. Under the assumption that the temperature dependence of $\omega\tau$ is small, supplementary equation (5.16) can be written as:

$$Q^{-1}_{TED} \propto \frac{E\alpha^2 T}{c_v}. \tag{5.17}$$

The close correspondence between this expression and the data in Fig. 2d and 4d in the main text indicates that this assumption is reasonable.
As could be noted from equation (2) in the main text and assuming the elastic properties of the material and its Grüneisen parameter to have a negligible temperature dependence at low temperatures, the thermoelastic damping Q^{-1}_{TED} is related to the frequency f_0 of the resonator as:

$$Q^{-1}_{TED}(T) \propto \frac{E\alpha^2(T)T}{c_v(T)} \propto c_v(T)\,T \propto -T\frac{\mathrm{d}[f_0^2(T)]}{\mathrm{d}T}, \tag{5.18}$$

where we use $\alpha(T) \propto c_v(T)$ and $c_v(T) \propto \frac{\mathrm{d}[f_0^2(T)]}{\mathrm{d}T}$ according to equation (2) in the main text. Therefore, in accordance with our observations in the main text, an anomaly (a jump) in the specific heat at the transition temperature will be visible in both $\frac{\mathrm{d}[f_0^2(T)]}{\mathrm{d}T}$ and $Q^{-1}(T)$ if the thermoelastic damping is the dominating dissipation mechanism.

E. Electric field induced strain in a circular $FePS_3$ membrane

A constant electrostatic load is applied to the circular membrane with a radius a (see Supplementary Fig. E.1). This results in a uniform curvature R with a maximum deflection δ.
In this system, the electrostatic load is balanced by the total tension N_{total}:

$$\frac{\varepsilon_0 (V_G^{DC})^2}{2(g_0-\delta)^2}\pi R^2 = 2\pi N_{total} R, \tag{5.19}$$

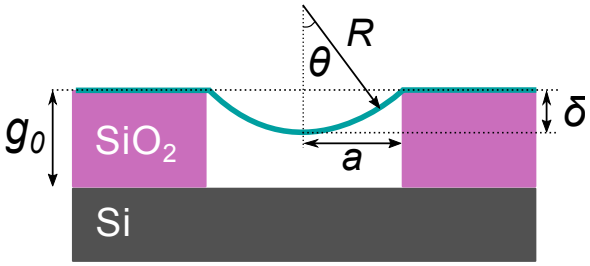

Figure E.1: Schematic of the membrane deformation, cross-section view.

where ε_0 is the vacuum permittivity, V_G^{DC} the applied voltage, g_0 the gap size between the membrane and the bottom silicon plate. For small deflections the radius of curvature can be approximated as:

$$R \approx \frac{a^2}{2\delta}, \tag{5.20}$$

so that the tension N_{total} becomes:

$$N_{\text{total}} = \frac{\varepsilon_0 (V_G^{DC})^2}{2(g_0-\delta)^2}\frac{a^2}{4\delta}. \tag{5.21}$$

The radial strain in such a membrane can be estimated from the arc length [44, 45]:

$$\epsilon = \frac{R\theta - a}{a} \approx \frac{a^2}{6R^2}. \tag{5.22}$$

Combining this result with supplementary equation (5.20) yields:

$$\epsilon \approx \frac{2\delta^2}{3a^2}. \tag{5.23}$$

From Hooke's law and including supplementary equation (5.23), one can write the strain due to deformation as:

$$N = \frac{Et}{1-\nu}\epsilon = \frac{2Et\delta^2}{3a^2(1-\nu)}, \tag{5.24}$$

Therefore, the total tension in the membrane, including the thermal expansion induced tension $N_0(T)$ at a certain temperature T, can be written as:

$$N_{\text{total}} = N_0(T) + N = N_0(T) + \frac{2Et\delta^2}{3a^2(1-\nu)} = \frac{\varepsilon_0 (V_G^{DC})^2}{2(g_0-\delta)^2}\frac{a^2}{4\delta}, \tag{5.25}$$

which also can be rewritten as:

$$V_G^{DC} = \sqrt{\frac{2(g_0-\delta)^2}{\varepsilon_0}\left(\frac{4\delta N_0(T)}{a^2} + \frac{8Et\delta^3}{3a^4(1-\nu)}\right)}. \tag{5.26}$$

As shown in Supplementary Fig. E.2a, supplementary equation (5.26) in combination with (5.23) and (5.5) fits the experimental data well and is used to provide an an estimate of the electrostatically induced strain in the membrane (see Supplementary Fig. E.2b).

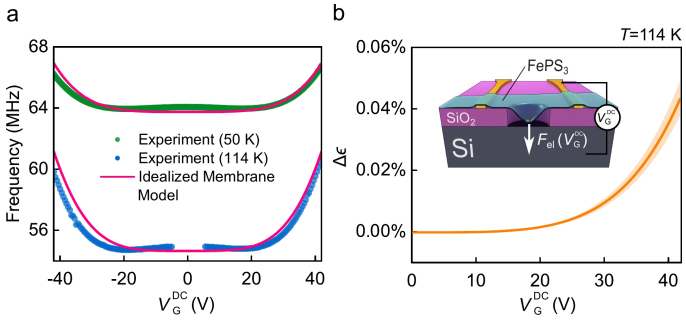

Figure E.2: (a) Idealized electrostatically strained membrane model for $N_0 = 0.01$ N m^{-1}, $g_0 = 285$ nm, $a = 2$ μm, $t = 8$ nm, $E = 103$ GPa and $\nu = 0.304$; superimposed with corresponding experimental data. (b) Estimate of added radial strain at $T = 114$ K. The shaded orange region represents an estimated uncertainty from the accuracy in determining the temperature induced strain (±0.015%) at $T = 114$ K. Inset - schematics of the experiment.

F. Mechanical resonances and specific heat of 2H-TaS_2 near the charge density wave transition

For 2H-TaS_2 resonance frequency measurements were performed on a $d = 4$ μm drum made of a 31 nm thin flake (see Supplementary Fig. F.1a, solid blue line). As shown by the solid green line in Supplementary Fig. F.1a, the specific heat-related temperature derivative of f_0^2 reveals a clear peak at $T_{CDW} \sim 75$ K. We convert the measured $\frac{d(f_0^2)}{dT}$ to the specific heat using the methodology described in the main text. We use reported values of $E_{2D} = 87$ N m^{-1} and $\nu = 0.27$ for a monolayer of 1H-TaS_2 obtained from molecular dynamics simulations [46] and mass density $\rho = 6110$ kg m^{-3}. We find the corresponding $E = E_{2D}/t = 149$ GPa, taking the interlayer spacing $t = 0.58$ nm. The estimated specific heat of the 2H-TaS_2 membrane is depicted in Supplementary Fig. F.1b (solid blue line). The four-probe resistance was measured on the same flake to confirm the existence of a CDW transition using a conventional electronic based method as shown in Supplementary Fig. F.1c. The expected characteristic kink in the resistance is visible at ~ 77 K, consistent with the CDW transition temperature previously reported in 2H-TaS_2 [14].

G. Crystal growth and characterization

The crystal growth of MPS_3 (M = Mn, Fe, Ni) was performed following a typical solid state reaction. Powders of Mn (> 99.9%, from Sigma-Aldrich), Fe (99.998%, from Alfa-Aesar), Ni (99.99%, from Sigma-Aldrich), P (> 99.99%, from Sigma-Aldrich) and S (99.998%, from Sigma-Aldrich) were mixed in a stoichiometric ratio, pressed into a pellet and sealed in an evacuated quartz ampoule ($P \sim 5 \times 10^{-5}$ mbar, length = 25 cm, internal diameter = 1.5 cm) and heated from room temperature to 400 °C at 1.1 °C per minute. Then, the temperature was kept constant for twenty days and slowly cooled down (0.07 °C per minute).

For obtaining large crystals, 4 mmol of the previous material was mixed with I_2 as a transport agent ($[I_2] \sim 5$ mg cm^{-3}) in an evacuated quartz ampoule ($P \sim 5 \times 10^{-5}$

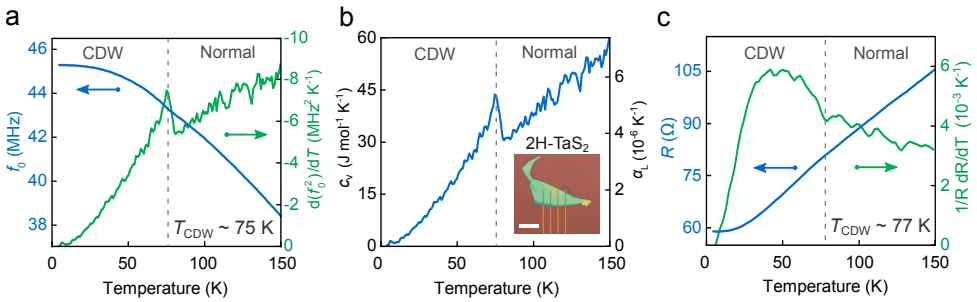

Figure F.1: Mechanical properties of a 2H-TaS_2 resonator with membrane thickness of 31.2 ± 0.6 nm. Dashed vertical lines in the panels indicate the transition temperature, T_{CDW}. (a) Solid blue line - resonance frequency as a function of temperature. Solid green line - temperature derivative of f_0^2. (b) Solid blue line - estimated specific heat (c_v) and thermal expansion coefficient (α_L). Inset: optical image of the sample. Scale bar: 20 μm. (c) Solid blue line - four-point resistance of the same sample. Solid green line - $\frac{1}{R}\frac{dR}{dT}$ plot showing the CDW related feature at T_{CDW}.

5

mbar, length = 50 cm, internal diameter = 1.5 cm). The quartz tube was placed inside a three-zone furnace with the material in the leftmost zone. The other two zones were heated up in 24 h from room temperature to 650 °C and kept at that temperature for one day. After this, the leftmost side was heated up to 700 °C in 3 h and a gradient of 700 °C/650 °C/675 °C was established in the three-zone furnace. Then the temperature was kept constant for 28 days and cooled down naturally. As shown in Supplementary Fig. G.1, with this process we could obtain crystals with a length up to several centimeters. The obtained crystals were analyzed by ICP-OES (Inductively Coupled Plasma - Optical Emission Spectrometry) and powder X-ray diffraction. The relative weights of elements obtained are summarized in Supplementary table 1. The refinement of the X-ray diffraction pattern (Supplementary Fig. G.1) revealed a monoclinic base-centered crystal system with C12/m1 space group and a unit cell determined by $\alpha = \gamma = 90°$ and $\beta = 107.33(1)°$ ($MnPS_3$), $\beta = 107.13(1)°$ ($FePS_3$), $\beta = 106.945(9)°$ ($NiPS_3$), and $a = 6.077(7)$ Å, $b = 10.55(2)$ Å and $c = 6.805(9)$ Å for $MnPS_3$, $a = 5.939(6)$ Å, $b = 10.296(3)$ Å and $c = 6.716(3)$ Å for $FePS_3$ and $a = 5.815(4)$ Å, $b = 10.087(5)$ Å and $c = 6.627(4)$ Å for $NiPS_3$. The obtained results are in accordance with the ones reported in the literature [47].

The crystal growth and characterization of 2H-TaS_2 was performed as already reported in earlier works [48, 49].

H. Reproducibility of measurements

In order to assess reproducibility of the measured effect between the samples, we show the Q^{-1} data for the $FePS_3$ sample from Fig. 2 of the main text (Drum 1) compared with the data for one additional sample (Drum 2) in Supplementary Fig. H.1.

We choose the sample parameters (i.e., thickness, t, and drum diameter, d) to be similar for a fair comparison. The features related to phase transition in both frequency (Supplementary Fig. H.1b) and quality factor (Supplementary Fig. H.1c) are present in both cases. The drum 2, however, has a higher pre-stress accumu-

Element		Obtained (%)	Expected (%)
$MnPS_3$	**Mn**	28.0 ± 1.0	30.2
	P	12 ± 1	17.0
	S	49 ± 2	52.8
$FePS_3$	**Fe**	30.0 ± 1.0	30.5
	P	15.7 ± 0.5	16.9
	S	51 ± 2	52.6
$NiPS_3$	**Ni**	30.0 ± 1.0	31.6
	P	15.7 ± 0.5	16.6
	S	53 ± 2	51.8

Table G.1: Experimental and expected relative weights analyzed by inductively coupled plasma - optical emission spectrometry (ICP-OES) for the different MPS_3 crystals (M = Mn, Fe and Ni).

lated in a result of the fabrication, which is concluded from a notable frequency mismatch in Supplementary Fig. H.1a. Some variation in T_N of around $2-3$ K can be noted between the samples in Supplementary Fig. H.1b, which we attribute to the pre-strain variation in a result of fabrication since, as we report in Fig. 3 of the main text, T_N^* of $FePS_3$ is very sensitive to strain. In Supplementary figure H.2, the Q^{-1} terms from Supplementary Fig. H.1c are displayed and compared to $c_v \times T$ terms for both drums. We note that the position of the peak for Q^{-1} and $c_v \times T$ corresponds to each other up to the resolution of the measurement.

The results for $FePS_3$ are also well reproducible within a single device (Drum 2) with no hysteresis observed in both frequency and Q-factor for multiple temperature sweeps, as shown in Supplementary Fig. H.3.

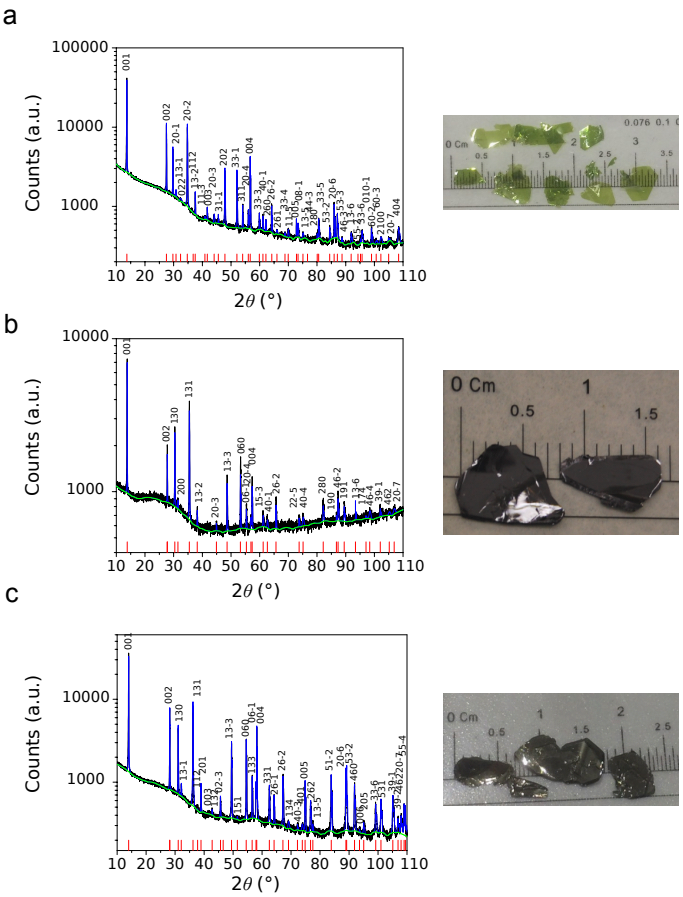

Figure G.1: XRPD experimental patterns (black) and corresponding fits (peaks in blue and background in green) for MPS_3 (M = Mn, Fe and Ni) crystals. For clarity, the peaks have been marked by red lines. (a) Left: Pattern of $MnPS_3$. Right: Photography of a $MnPS_3$ crystal. The fit gives as a result: a = 6.077(7) Å, b = 10.55(2) Å and c = 6.805(9) Å, $\alpha = \gamma = 90°$ and $\beta = 107.33(1)°$, monoclinic C face center crystal system with C12/m1 space group, $\chi^2 = 5.8 \times 10^{-5}$. (b) Left: Pattern of $FePS_3$. Right: Photography of a $FePS_3$ crystal. The fit gives as a result: $a = 5.939(6)$ Å, $b = 10.296(3)$ Å and $c = 6.716(3)$ Å, $\alpha = \gamma = 90°$ and $\beta = 107.13(1)°$, monoclinic C face center crystal system with C12/m1 space group, $\chi^2 = 1.5 \times 10^{-6}$. (c) Left: Pattern of $NiPS_3$. Right: Photography of a $NiPS_3$ crystal. The fit gives as a result: $a = 5.815(4)$ Å, $b = 10.087(5)$ Å and $c = 6.627(4)$ Å, $\alpha = \gamma = 90°$ and $\beta = 106.945(9)°$, monoclinic C face center crystal system with C12/m1 space group, $\chi^2 = 1.1 \times 10^{-5}$.

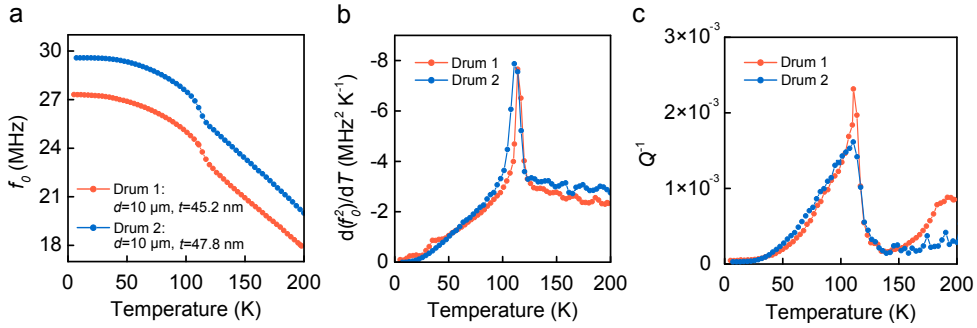

Figure H.1: Mechanical properties of a $FePS_3$ resonators with membrane thicknesses indicated in a legend. (a) Resonance frequency as a function of temperature. (b) Temperature derivative of f_0^2 for both samples. (c) Measured mechanical damping Q^{-1} as a function temperature.

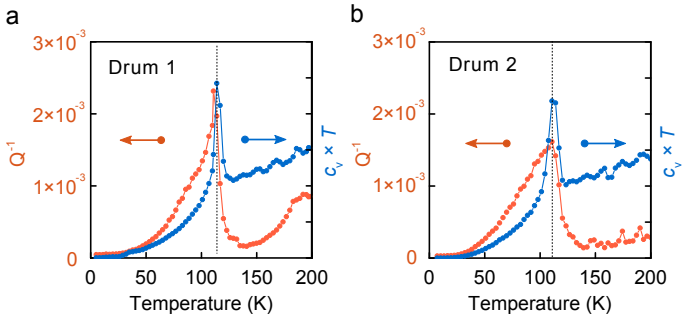

Figure H.2: Measured mechanical damping $Q^{-1}(T)$ as a function temperature in filled orange dots in both panels for samples form Supplementary Fig. H.1. Filled blue dots in both panels - normalized $c_V(T)$ T term (see Supplementary Note 4).

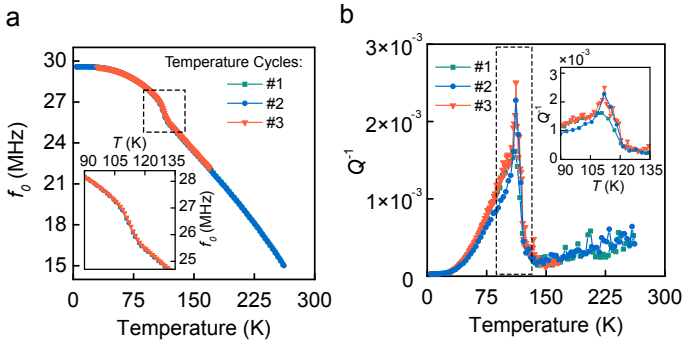

Figure H.3: Multiple temperature cycles for Drum 2 from Supplementary Fig. H.1. (a) Filled dots - resonance frequency as a function of temperature. Inset: a close-up of the region indicated with dashed line box. (b) Filled dots - measured mechanical damping Q^{-1} as a function temperature. Inset: a close-up of the region indicated with dashed line box.

References

[1] C. Chen, S. Rosenblatt, K. I. Bolotin, W. Kalb, P. Kim, I. Kymissis, H. L. Stormer, T. F. Heinz, and J. Hone, "Performance of monolayer graphene nanomechanical resonators with electrical readout," *Nature nanotechnology*, vol. 4, no. 12, pp. 861–867, 2009.

[2] C. Chen, S. Lee, V. V. Deshpande, G.-H. Lee, M. Lekas, K. Shepard, and J. Hone, "Graphene mechanical oscillators with tunable frequency," *Nature nanotechnology*, vol. 8, no. 12, pp. 923–927, 2013.

[3] Y. Cao, V. Fatemi, S. Fang, K. Watanabe, T. Taniguchi, E. Kaxiras, and P. Jarillo-Herrero, "Unconventional superconductivity in magic-angle graphene superlattices," *Nature*, vol. 556, no. 7699, pp. 43–50, 2018.

[4] A. L. Sharpe, E. J. Fox, A. W. Barnard, J. Finney, K. Watanabe, T. Taniguchi, M. Kastner, and D. Goldhaber-Gordon, "Emergent ferromagnetism near three-quarters filling in twisted bilayer graphene," *Science*, vol. 365, no. 6453, pp. 605–608, 2019.

[5] J.-U. Lee, S. Lee, J. H. Ryoo, S. Kang, T. Y. Kim, P. Kim, C.-H. Park, J.-G. Park, and H. Cheong, "Ising-type magnetic ordering in atomically thin feps3," *Nano letters*, vol. 16, no. 12, pp. 7433–7438, 2016.

[6] B. Huang, G. Clark, E. Navarro-Moratalla, D. R. Klein, R. Cheng, K. L. Seyler, D. Zhong, E. Schmidgall, M. A. McGuire, D. H. Cobden, *et al.*, "Layer-dependent ferromagnetism in a van der waals crystal down to the monolayer limit," *Nature*, vol. 546, no. 7657, pp. 270–273, 2017.

[7] C. Gong, L. Li, Z. Li, H. Ji, A. Stern, Y. Xia, T. Cao, W. Bao, C. Wang, Y. Wang, *et al.*, "Discovery of intrinsic ferromagnetism in two-dimensional van der waals crystals," *Nature*, vol. 546, no. 7657, pp. 265–269, 2017.

[8] M. Gibertini, M. Koperski, A. Morpurgo, and K. Novoselov, "Magnetic 2d materials and heterostructures," *Nature nanotechnology*, vol. 14, no. 5, pp. 408–419, 2019.

[9] K. Novoselov, o. A. Mishchenko, o. A. Carvalho, and A. C. Neto, "2d materials and van der waals heterostructures," *Science*, vol. 353, no. 6298, 2016.

[10] L. D. Landau, L. P. Pitaevskii, and E. M. Lifshitz, *Electrodynamics of continuous media*, vol. 8. New York: Butterworth, 2 ed., 1984.

[11] N. Morell, S. Tepsic, A. Reserbat-Plantey, A. Cepellotti, M. Manca, I. Epstein, A. Isacsson, X. Marie, F. Mauri, and A. Bachtold, "Optomechanical measurement of thermal transport in two-dimensional mose2 lattices," *Nano letters*, vol. 19, no. 5, pp. 3143–3150, 2019.

[12] R. J. Dolleman, D. Lloyd, M. Lee, J. S. Bunch, H. S. Van Der Zant, and P. G. Steeneken, "Transient thermal characterization of suspended monolayer mos 2," *Physical Review Materials*, vol. 2, no. 11, p. 114008, 2018.

[13] P. A. Joy and S. Vasudevan, "Magnetism in the layered transition-metal thiophosphates MPS_3 (M=Mn, Fe, and Ni)," *Phys. Rev. B*, vol. 46, pp. 5425–5433, Sept. 1992.

[14] M. Abdel-Hafiez, X.-M. Zhao, A. A. Kordyuk, Y.-W. Fang, B. Pan, Z. He, C.-G. Duan, J. Zhao, and X.-J. Chen, "Enhancement of superconductivity under pressure and the magnetic phase diagram of tantalum disulfide single crystals," *Sci. Rep.*, vol. 6, Aug. 2016.

[15] A. Castellanos-Gomez, R. van Leeuwen, M. Buscema, H. S. J. van der Zant, G. A. Steele, and W. J. Venstra, "Single-layer MoS_2 mechanical resonators," *Adv. Mater.*, vol. 25, pp. 6719–6723, Oct. 2013.

[16] Y. Takano, N. Arai, A. Arai, Y. Takahashi, K. Takase, and K. Sekizawa, "Magnetic properties and specific heat of MPS_3 (M=Mn, Fe, Zn)," *J. Magn. Magn. Mater.*, vol. 272-276, pp. E593–E595, May 2004.

[17] A. Castellanos-Gomez, M. Buscema, R. Molenaar, V. Singh, L. Janssen, H. S. Van Der Zant, and G. A. Steele, "Deterministic transfer of two-dimensional materials by all-dry viscoelastic stamping," *2D Materials*, vol. 1, no. 1, p. 011002, 2014.

[18] N. Morell, A. Reserbat-Plantey, I. Tsioutsios, K. G. Schädler, F. Dubin, F. H. L. Koppens, and A. Bachtold, "High quality factor mechanical resonators based on WSe_2 monolayers," *Nano Lett.*, vol. 16, pp. 5102–5108, Aug. 2016.

[19] D. Sanditov and V. Belomestnykh, "Relation between the parameters of the elasticity theory and averaged bulk modulus of solids," *Technical Physics*, vol. 56, no. 11, pp. 1619–1623, 2011.

[20] C. Zener, "Internal friction in solids. I. Theory of internal friction in reeds," *Phys. Rev.*, vol. 52, pp. 230–235, Aug. 1937.

[21] R. Lifshitz and M. L. Roukes, "Thermoelastic damping in micro- and nanomechanical systems," *Phys. Rev. B*, vol. 61, pp. 5600–5609, Feb. 2000.

[22] V. N. Belomestnykh and E. P. Tesleva, "Interrelation between anharmonicity and lateral strain in quasi-isotropic polycrystalline solids," *Tech. Phys.*, vol. 49, pp. 1098–1100, Aug. 2004.

[23] K. Leont'ev, "On connection between elastic and thermal properties of substances," *Akusticheskij Zhurnal*, vol. 27, pp. 554–561, 1981.

[24] A. Hashemi, H.-P. Komsa, M. Puska, and A. V. Krasheninnikov, "Vibrational properties of metal phosphorus trichalcogenides from first-principles calculations," *J. Phys. Chem. C*, vol. 121, pp. 27207–27217, Nov. 2017.

[25] M. Barmatz, L. Testardi, and F. Di Salvo, "Elasticity measurements in the layered dichalcogenides ta se 2 and nb se 2," *Physical Review B*, vol. 12, no. 10, p. 4367, 1975.

[26] S. Sengupta, H. S. Solanki, V. Singh, S. Dhara, and M. M. Deshmukh, "Electromechanical resonators as probes of the charge density wave transition at the nanoscale in nbse 2," *Physical Review B*, vol. 82, no. 15, p. 155432, 2010.

[27] J. Lee, Z. Wang, K. He, R. Yang, J. Shan, and P. X.-L. Feng, "Electrically tunable single-and few-layer mos2 nanoelectromechanical systems with broad dynamic range," *Science advances*, vol. 4, no. 3, p. eaao6653, 2018.

[28] M. Saint-Paul and P. Monceau, "Survey of the thermodynamic properties of the charge density wave systems," *Advances in Condensed Matter Physics*, vol. 2019, 2019.

[29] S. Jiang, H. Xie, J. Shan, and K. F. Mak, "Two-dimensional magnetic nanoelectromechanical resonators," *arXiv preprint arXiv:2001.03153*, 2020.

[30] D. Ji, S. Cai, T. R. Paudel, H. Sun, C. Zhang, L. Han, Y. Wei, Y. Zang, M. Gu, Y. Zhang, *et al.*, "Freestanding crystalline oxide perovskites down to the monolayer limit," *Nature*, vol. 570, no. 7759, pp. 87–90, 2019.

[31] D. Davidovikj, D. J. Groenendijk, A. M. R. Monteiro, A. Dijkhoff, D. Afanasiev, M. Šiškins, M. Lee, Y. Huang, E. van Heumen, H. van der Zant, *et al.*, "Ultrathin complex oxide nanomechanical resonators," *Communications Physics*, vol. 3, no. 1, pp. 1–6, 2020.

[32] J. López-Cabrelles, S. Mañas-Valero, I. J. Vitórica-Yrezábal, P. Bereciartua, J. Rodríguez-Velamazán, J. C. Waerenborgh, B. J. Vieira, D. Davidovikj, P. Steeneken, H. Van der Zant, *et al.*, "Isoreticular two-dimensional magnetic coordination polymers prepared through pre-synthetic ligand functionalization," *Nature chemistry*, vol. 10, no. 10, pp. 1001–1007, 2018.

[33] T. Wah, "Vibration of circular plates," *J. Acoust. Soc. Am.*, vol. 34, pp. 275–281, Mar. 1962.

[34] S. Timoshenko, D. H. Young, and W. Weaver, *Vibration Problems in Engineering*. New York: Wiley, 4 ed., 1974.

[35] V. Singh, S. Sengupta, H. S. Solanki, R. Dhall, A. Allain, S. Dhara, P. Pant, and M. M. Deshmukh, "Probing thermal expansion of graphene and modal dispersion at low-temperature using graphene nanoelectromechanical systems resonators," *Nanotechnology*, vol. 21, p. 165204, Mar. 2010.

[36] G. White, J. Birch, and M. H. Manghnani, "Thermal properties of sodium silicate glasses at low temperatures," *J. Non-Cryst. Solids*, vol. 23, pp. 99–110, Jan. 1977.

[37] K. G. Lyon, G. L. Salinger, C. A. Swenson, and G. K. White, "Linear thermal expansion measurements on silicon from 6 to 340 K," *J. Appl. Phys.*, vol. 48, pp. 865–868, Mar. 1977.

[38] K. Kim, S. Y. Lim, J.-U. Lee, S. Lee, T. Y. Kim, K. Park, G. S. Jeon, C.-H. Park, J.-G. Park, and H. Cheong, "Suppression of magnetic ordering in XXZ-type antiferromagnetic monolayer $NiPS_3$," *Nat. Commun.*, vol. 10, Jan. 2019.

[39] D. S. Sanditov, A. A. Mashanov, M. V. Darmaev, B. D. Sanditov, and V. V. Mantatov, "Grüneisen parameter and elastic constants of crystals and vitreous bodies," *Russ. Phys. J.*, vol. 52, pp. 221–230, Mar. 2009.

[40] X. Zhang, X. Zhao, D. Wu, Y. Jing, and Z. Zhou, "$MnPSe_3$ monolayer: A promising 2D visible-light photohydrolytic catalyst with high carrier mobility," *Adv. Sci.*, vol. 3, p. 1600062, Apr. 2016.

[41] L. D. Landau, "On the theory of phase transitions," *Zh. Eksp. Teor. Fiz.*, vol. 7, pp. 19–32, 1937. [*Ukr. J. Phys.* **53**, 25 (2008)].

[42] S. Schmid, L. G. Villanueva, and M. L. Roukes, *Fundamentals of Nanomechanical Resonators*. Springer International Publishing, 2016.

[43] C. Zener, "Internal friction in solids II. General theory of thermoelastic internal friction," *Phys. Rev.*, vol. 53, pp. 90–99, Jan. 1938.

[44] M. K. Small and W. Nix, "Analysis of the accuracy of the bulge test in determining the mechanical properties of thin films," *J. Mater. Res. Technol.*, vol. 7, pp. 1553–1563, June 1992.

[45] P. Weber, J. Güttinger, I. Tsioutsios, D. E. Chang, and A. Bachtold, "Coupling graphene mechanical resonators to superconducting microwave cavities," *Nano Lett.*, vol. 14, pp. 2854–2860, Apr. 2014.

[46] J.-W. Jiang and Y.-P. Zhou, "Parameterization of Stillinger-Weber potential for two-dimensional atomic crystals," in *Handbook of Stillinger-Weber Potential Parameters for Two-Dimensional Atomic Crystals*, IntechOpen, 2017.

[47] G. Ouvrard, R. Brec, and J. Rouxel, "Structural determination of some MPS_3 layered phases (M = Mn, Fe, Co, Ni and Cd)," *Mater. Res. Bull.*, vol. 20, pp. 1181–1189, Oct. 1985.

[48] E. Pinilla-Cienfuegos, S. Mañas-Valero, E. Navarro-Moratalla, S. Tatay, A. Forment-Aliaga, and E. Coronado, "Local oxidation nanolithography on metallic transition metal dichalcogenides surfaces," *Appl. Sci.*, vol. 6, p. 250, Sept. 2016.

[49] E. Navarro-Moratalla, J. O. Island, S. Mañas-Valero, E. Pinilla-Cienfuegos, A. Castellanos-Gomez, J. Quereda, G. Rubio-Bollinger, L. Chirolli, J. A. Silva-Guillén, N. Agraït, G. A. Steele, F. Guinea, H. S. J. van der Zant, and E. Coronado, "Enhanced superconductivity in atomically thin TaS_2," *Nat. Commun.*, vol. 7, Mar. 2016.

6

6

Study of charge density waves in suspended 2H-TaS_2 and 2H-$TaSe_2$

The charge density wave (CDW) state in van der Waals systems shows interesting scaling phenomena as the number of layers can significantly affect the CDW transition temperature, T_{CDW}. However, it is often difficult to use conventional methods to study the phase transition in these systems due to their small size and sensitivity to degradation. Degradation is an important parameter which has been shown to greatly influence the superconductivity in layered systems. Since the CDW state competes with the onset of superconductivity, it is expected that T_{CDW} will also be affected by the degradation. Here, we probe the CDW phase transition by the mechanical resonances of suspended 2H-TaS_2 and 2H-$TaSe_2$ membranes and study the effect of disorder on the CDW state. Pristine flakes show the transition near the reported values of 75 K and 122 K respectively. We then study the effect of degradation on 2H-TaS_2 which displays an enhancement of T_{CDW} up to 129 K after degradation in ambient air. Finally, we study a sample with local degradation and observe that multiple phase transitions occur at 87 K, 103 K and 118 K with a hysteresis in temperature in the same membrane. The observed spatial variations in the Raman spectra suggest that variations in crystal structure cause domains with different transition temperatures which could result in the hysteresis. This work shows the potential of using nanomechanical resonance to characterize the CDW in suspended 2D materials and demonstrate that degradation can have a large effect on transition temperatures.

Parts of this chapter have been published in APL **19**, 193105 by **M. Lee***, M. ŠiŠkins*, S. Mañas-Valero, E. Coronado, P. G. Steeneken, and H. S. J. van der Zant.

6.1. Introduction

The charge density wave (CDW) state in van der Waals (vdW) materials has recently become a resurgent area of research. Archetypal systems such as 2H-$NbSe_2$, 2H-TaS_2 and 2H-$TaSe_2$ have been under study since the 1970s [1–14]. However, recent works on surprising and unexpected layer dependence and degradation effects on superconductivity (SC) and CDW in these systems have revived interest in studying their phase transitions. For example, the superconducting transition temperature, T_{SC} of 2H-$NbSe_2$ is suppressed from 7.2 K in the bulk to 3 K in the monolayer limit while the CDW transition temperature, T_{CDW} is increased[15] from 33 K to 145 K. More surprisingly, 2H-TaS_2 has a T_{SC} of 0.6 K in the bulk which increases to 3 K in a monolayer [16, 17] and a T_{CDW} of 75 K which also increases to 140 K [18]. Similar scaling is seen for T_{SC} in 2H-$TaSe_2$[19]. Furthermore, degradation of the crystal in air has shown to enhance the superconductivity in 2H-TaS_2 [20] which is in stark contrast to other air-sensitive vdW superconductors which lose their superconductivity upon degradation [21–24]. It is an ongoing challenge to clarify these contradicting layer dependencies and degradation effects in order to shine light on the competition between CDW and SC in these materials.

The CDW transition, like other first and second order phase transitions, can be described by Landau's theory of phase transitions [25] where the emergence of charge order gives rise to a sudden change in the specific heat. Using the specific heat anomaly to probe the phase transition is already established in several systems [6, 26–30]. However, the traditional methods of probing the specific heat are nearly impossible to apply on ultrathin exfoliated 2D material flakes. Recent works on using the nanomechanical resonance to extract various phase transitions including structural, magnetic and electronic phase transitions [31–34] have shown to be an interesting alternative.

In this work, we study the CDW transitions of suspended 2H-TaS_2 and 2H-$TaSe_2$ flakes by tracking the temperature dependence of their nanomechanical resonance frequency. The resonance frequency of suspended pristine 2H-TaS_2 and 2H-$TaSe_2$ flakes show an anomaly at the phase transition temperatures of 75 K and 122 K respectively. We then employ this technique as a probe to study the effect of degradation on the T_{CDW} of 2H-TaS_2. Flakes of 2H-TaS_2 show greatly enhanced T_{CDW} after being exposed to ambient conditions for prolonged durations. Furthermore, we induce local disorder in a region of a suspended part of the membrane which causes varying degrees of disorder across the flake as observed in Raman spectroscopy. In this sample, multiple transitions appear with a hysteretic switching behavior pointing towards the existence of domains with varying T_{CDW}.

6.2. Results

6.2.1. Measurement setup and device

The interferometry setup and the sample are described in Fig. 6.1. Figure 6.1(a) shows an illustration of the interferometry setup. The intensity of the blue diode laser (λ_{Blue} = 405 nm) is modulated by the vector network analyzer (VNA) which optothermally excites the membrane into motion. Simultaneously, a continuous

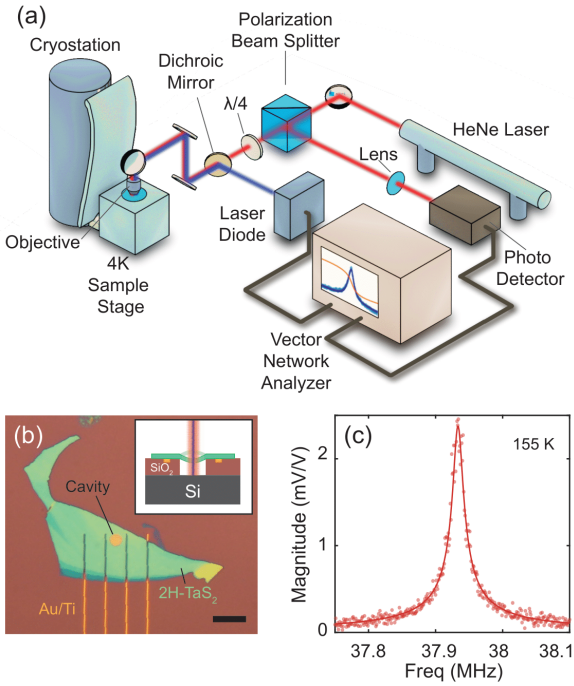

Figure 6.1: Interferometry setup, device geometry and basic characterization of a 2H-TaS_2 membrane. **(a)** Illustration of the laser interferometry setup. Blue diode laser is used to optothermally actuate the membrane while the He-Ne red laser is used to read out its motion. **(b)** Optical image of device 1 composed of a 2H-TaS_2 flake of thickness t = 31.2±0.6 nm transferred onto pre-defined electrodes surrounding a cavity. Scale bar: 10 µm. Inset: Illustration of the cross-section of a device. **(c)** Example frequency responses of device 1 at 155 K.

He-Ne laser (λ_{Red} = 632 nm) is used to read out the movement of the membrane. The interference signal is collected by the photodetector which is read out by the VNA. The sample is situated in a 4 K dry cryostat at high vacuum with a heater beneath the sample to control the temperature.

Devices are fabricated by deterministically stamping [35] 2H-TaS_2 and 2H-$TaSe_2$ flakes on top of electrodes metallized by evaporation and circular cavities etched into SiO_2/Si by reactive ion etching. The suspended membrane is in a drum geometry with a rigid Si back mirror. High-quality 2H-TaS_2 and 2H-$TaSe_2$ flakes are exfoliated from synthetically grown bulk crystals [17, 36]. Detailed description of the setup and the fabrication processes can be found in S.I.

An optical image of device 1 is shown in Fig. 6.1(b), the cross-sectional illustration is in the inset and its typical frequency response at 155 K near the fundamental resonance frequency in Fig. 6.1(c). The data is collected at every temperature once stabilized to within 10 mK from the set-point and fitted to a simple harmonic oscillator model. The fundamental resonance frequency $f_0(T)$, extracted from such sweeps is plotted in frequency vs. temperature plots in subsequent figures.

6.2.2. Specific heat anomaly at the CDW transition

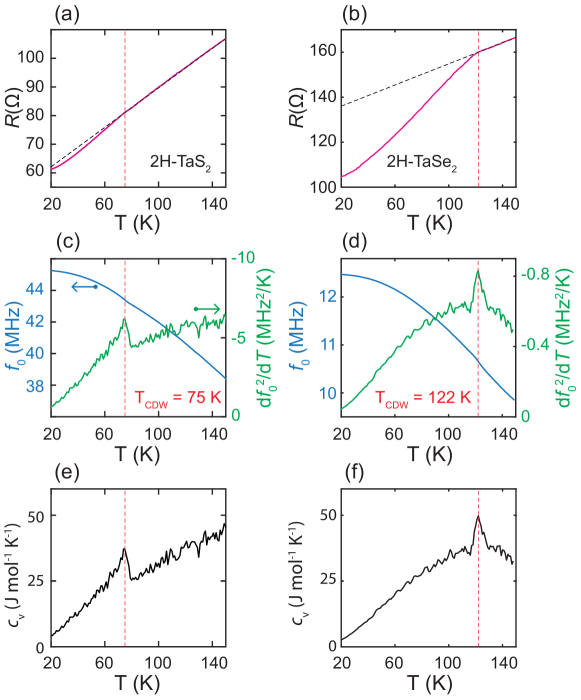

Figure 6.2: Electrical and mechanical characterization of a pristine 2H-TaS_2 (left column, device 1) and 2H-$TaSe_2$ (right column, device 2) membrane. The data from device 1 is also used in Ref. [31]. Dashed red lines indicate the CDW transition temperature determined from the peak of $\frac{d[f_0^2(T)]}{dT}$. **(a-b)** Four-probe resistance as a function of temperature (pink). Dashed straight black lines are plotted as visual aid. **(c-d)** Resonance frequency f_0 (left y-axis, blue) and $\frac{d[f_0^2(T)]}{dT}$ (right y-axis, green). **(e-f)** Specific heat extracted from (c-d) using Eq. 6.4.

In this section, we introduce the lambda type anomaly in the specific heat due to the normal - CDW phase transition, as described by Landau-Lifshitz [25, 31, 37]. The Landau free energy can be written for CDW transitions as:

$$F = F_0 + a(T - T_{\mathrm{CDW}})Q^2 + BQ^4 \tag{6.1}$$

where F_0 is the temperature dependent free energy of the normal state, Q is the order parameter and a and B are phenomenological positive constants. Minimizing the above equation with respect to Q (i.e. $\partial F/\partial Q = 0$), gives the CDW order parameter:

$$Q = \sqrt{\frac{-a(T - T_{\mathrm{CDW}})}{2B}}, \tag{6.2}$$

and a minimum free energy $F_{\mathrm{min}} = F_0 - \frac{a^2}{4B}(T - T_{\mathrm{CDW}})^2$. Using the relation for the specific heat at constant pressure, $c_{\mathrm{p}}(T) = -T\left[\frac{\partial^2 F}{\partial T^2}\right]_{\mathrm{p}}$ and by substituting the ex-

pression for $F_{\min}$ into Eq. 6.1, the magnitude of the jump in the specific heat at the phase transition can be derived as $\Delta c_p = \frac{a^2 T_{CDW}}{2B}$. To find the relationship between the membrane resonance frequency and $c_p(T)$ we note that the fundamental resonance frequency of a circular membrane under thermal strain can be described by:

$$f_0(T) = \frac{2.4048}{\pi d}\sqrt{\frac{E}{\rho}\frac{\epsilon(T)}{(1-\nu)}} \tag{6.3}$$

where d is the membrane diameter, E the Young's modulus, ρ the density, $\epsilon(T)$ the temperature dependent biaxial strain, and ν Poisson's ratio.

The thermal strain accumulated in the membrane is a result of the difference in the linear thermal expansion coefficient of the membrane α_L and that of the substrate α_{Si}. It can be expressed as: $\frac{d\epsilon(T)}{dT} \simeq -(\alpha_L(T) - \alpha_{Si}(T))$ assuming that the thermal expansion coefficient of SiO_2 is negligible in comparison to Si [38, 39]. Using the thermodynamic relation between the thermal expansion coefficient and the specific heat: $\alpha_L(T) = \gamma c_v(T)/(3KV_M)$, and the above-mentioned thermal strain relation, we arrive at an expression:

$$c_v(T) = 3\left(\alpha_{si} - \frac{1}{\mu^2}\frac{d[f_0^2(T)]}{dT}\right)\frac{KV_M}{\gamma}, \tag{6.4}$$

where $c_v(T)$ is the specific heat of the membrane at constant volume, $K = \frac{E}{3(1-2\nu)}$ the bulk modulus, γ the Grüneisen parameter, $V_M = M/\rho$ the molar volume of the membrane and $\mu = \frac{2.4048}{\pi d}\sqrt{\frac{E}{\rho(1-\nu)}}$ a constant. We note that the Young's modulus E is also slightly temperature dependent and exhibits an anomaly at the phase transition. However, this change is on the order of a percent throughout the temperature range of our experiment [40]. We therefore approximate it as a constant and assume the thermal strain to be dominant in determining the frequency changes [31]. Since $c_v \simeq c_p$ in solids, Eq. 6.4 directly relates the mechanical resonance of the membrane to the specific heat derived using the Landau free energy (Eq. 6.1). Through this relation we can extract the specific heat from the temperature derivative of f_0^2 and thus the T_{CDW} from determining the discontinuity in the specific heat. Detailed discussion on this relation can be found in Ref.[31] and the supplementary materials B.

6.2.3. Phase transition in pristine samples

Temperature dependent mechanical and electrical responses of pristine flakes of 2H-TaS_2 (left column, device 1, thickness, t = 31.2 ± 0.6 nm, d = 4 µm) and 2H-$TaSe_2$ (right column, device 2, t = 23.3 ± 0.5 nm , d = 10 µm, device not shown) are shown in Fig. 6.2. Figure 6.2(a-b) show the four-probe resistance (left y-axis, pink). Dashed black lines are plotted as a visual guide to highlight the deviation of the resistance data from the linear drop. The kink below which the resistance drop deviates from the dashed black line is the CDW transition temperature universally seen in other CDW systems [41]. This can also be seen in the $\frac{dR}{dT}$ as the temperature at which the slope changes. The CDW transition temperatures for 2H-TaS_2

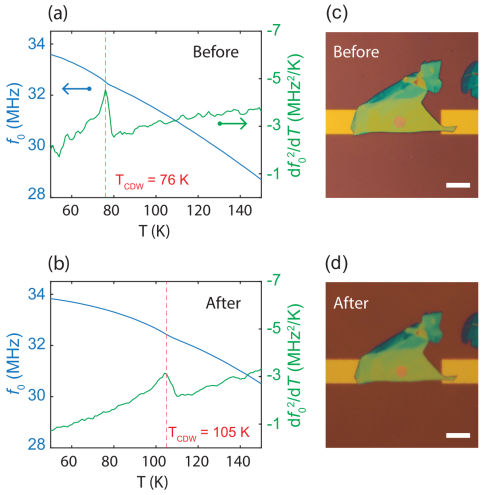

Figure 6.3: Enhancement of the T_{CDW} from the pristine state to the degraded state in device 3. f_0 (blue, left y-axis) and $\frac{d[f_0^2(T)]}{dT}$ (green, right y-axis) measured **(a)** immediately following fabrication and **(b)** after exposure to ambient conditions for several hours. Optical image of the device **(c)** immediately after fabrication and **(d)** after measurements of (a-b). Scale bar: 10 µm. The dashed red line corresponds to the T_{CDW}.

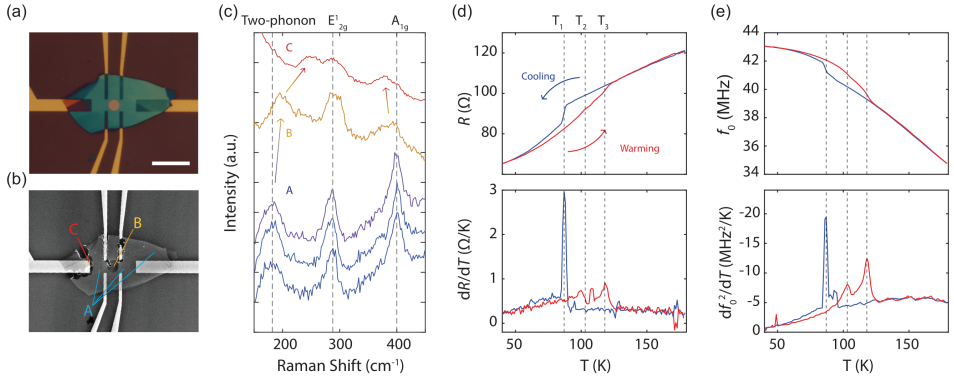

Figure 6.4: Raman, electrical and mechanical characterizations of device 4 showing competing transitions of CDW with enhanced T_{CDW}. **(a)** Optical image of device 4 immediately after the fabrication. Scale bar: 10 µm. **(b)** SEM of device 4 after measurement. Labels A, B and C indicate the positions where Raman spectroscopy data were acquired from. **(c)** Raman spectroscopy data at A, B and C. Dashed lines indicate the position of two-phonon mode, E^1_{2g} and A_{1g}. **(d)** Two point resistance as a function of temperature (top) and its derivative (bottom). **(e)** Resonance frequency f_0, as a function of temperature (top) and $\frac{d[f_0^2(T)]}{dT}$ (bottom). In both (d) and (e), the blue lines indicate measurements taken while cooling down and red lines indicate measurements taken while warming up as indicated by the arrows in (d). The dashed lines indicate the positions of new transition temperatures T_1 = 87 K, T_2 = 103 K, T_3 = 118 K.

and 2H-$TaSe_2$ by analysing the $\frac{dR}{dT}$ are 77 K and 122 K respectively and are in good agreement with the values in literature [3].

On the same membranes, the resonance frequency f_0 extracted by fitting a simple harmonic oscillator function to the resonance peak such as in Fig. 6.1(c) are plotted against temperature in Fig. 6.2(c-d) in blue (left y axis). There is a monotonic increase in the resonance frequency as the sample temperature is lowered, arising from the difference in the thermal expansion coefficient between the membrane and the substrate thus increasing the tension of the resonator. The temperature derivative of f_0^2 are plotted in green in Fig. 6.2(c-d) (right y axis). Since $c_v \propto \frac{d[f_0^2(T)]}{dT}$ from Eq. 6.4, the phase transition temperature T_{CDW} can be determined as the temperature where the peak in $\frac{d[f_0^2(T)]}{dT}$ is observed. The T_{CDW} of 2H-TaS_2 and 2H-$TaSe_2$ extracted from Fig. 6.2(c-d) are 75 K and 122 K respectively, and are in good agreement with the values from the transport data as well as the literature values [3]. Therefore, this method can be a complementary tool to the transport technique to probe the phase transition in CDW materials which show subtle changes in the slope of the resistance. In the subsequent sections, the T_{CDW}'s are extracted by finding the peak position of the anomaly in $\frac{d[f_0^2(T)]}{dT}$ vs. T.

The $c_v(T)$ can be estimated from the same data by including the material parameters into Eq. 6.4. The reported material parameters for 2H-TaS_2 are $E = E_{2D}/t = 149$ GPa [42] assuming an interlayer spacing $t = 0.58$ nm, $\nu = 0.27$ [42] and $\rho = 6110$ kg/m^3. The parameters for 2H-$TaSe_2$ are $E = 120$ GPa [40], $\nu \sim 0.2$ [43] and $\rho = 8660$ kg/m^3. The Grüneisen parameters can be estimated as $\gamma \simeq \frac{3}{2}(\frac{1+\nu}{2-3\nu})$ [44]. Finally, the temperature dependent thermal expansion coefficient of single crystalline Si is used as experimentally measured in Ref. [45]. Using these parameters, the $\frac{d[f_0^2(T)]}{dT}$ data in Fig. 6.2(c-d) are converted to c_v and plotted in Fig. 6.2(e-f).

6.2.4. Enhancement of transition temperature by degradation

For the remainder of the study, we focus on the effect of degradation on the CDW transition, specifically in 2H-TaS_2. We first use the above-mentioned technique to probe the phase transition temperature in 2H-TaS_2 before and after prolonged exposure to air. Degradation is often accompanied by changes in the material properties such as doping [20], Poisson's ratio [46], Young's modulus [47], dimensions [48] and density[49]. Therefore, in the following, we extract the transition temperatures from $\frac{d[f_0^2(T)]}{dT}$ plots and refrain from showing c_v in order to circumvent any errors in c_v arising from using wrong material parameters in Eq. 6.4.

To study degradation effects on the CDW transition temperature, device 3 ($t = 53.3 \pm 0.7$ nm, $d = 5$ µm) is measured before and after exposure to ambient conditions. In the first measurement, it is cooled down immediately following fabrication. Figure 6.3(a) shows f_0 (blue) as well as the temperature derivative of f_0^2 (green). As expected, the CDW transition occurs at $T_{CDW} = 76$ K (dashed red line) which is in good agreement with device 1 and literature values [3]. After the first cool down, the sample is removed from the cryostat and is exposed to air for several hours.

In the second cool down a remarkable 29 K enhancement of the T_{CDW} is observed. As shown in Fig. 6.3(b), the anomaly in $\frac{d[f_0^2(T)]}{dT}$ occurs at 105 K instead of 76 K. Several additional samples of air-degraded 2H-TaS_2 have been measured, one of which showed an even higher T_{CDW} of 129 K (see supplementary material C). In contrast to the drastic change in the T_{CDW}, no observable changes in the optical microscopy images before and after could be identified. Figure 6.3(c) is an image of device 3 immediately after the stamping process whereas Fig. 6.3(d) is the image taken after the second round of measurements.

6.2.5. Hysteresis and multiple phase transitions

We have also fabricated and measured several different samples of 2H-TaS_2 drums with disorder induced by laser induced oxidation [50] and focused ion beam (FIB) induced milling [51] to intentionally degrade the suspended flakes. Neither of these samples with different forms of disorder showed the CDW transition (see supplementary material D). However, in device 4, an electrostatic discharge across two electrodes adjacent to the suspended membrane caused a severe degradation of the membrane between the two electrodes. Figure 6.4(a) shows an image of the device immediately after fabrication showing no signs of damage. In Fig. 6.4(b), a scanning electron microscopy (SEM) image is shown of the device after the measurements are taken. It shows that the discharge caused severe damage to the the top electrodes as well as a small part of the membrane. The areas labeled A, B and C are the locations where the Raman spectroscopy data in Fig. 6.4(c) are taken. Raman spectroscopy is performed at room temperature in ambient conditions.

The blue Raman spectra shown in Fig. 6.4(c) are taken from the areas surrounding the drum and show the spectra comparable to literature [17, 52]. The three characteristic peaks of 2H-TaS_2 are plotted in dashed grey lines at 180 cm^{-1}, 286 cm^{-1} and 400 cm^{-1} corresponding to the two-phonon mode, the in-plane E^1_{2g} mode and out-of-plane A_{1g} mode respectively [4]. The yellow line in Fig. 6.4(c) is the Raman spectrum taken directly on the drum and shows slight red shifting of the two-phonon mode. The red line is the spectrum taken from the area with the most damage observed. This spectrum shows the most severely red shifted two-phonon mode as well as slightly blue shifted A_{1g} mode as indicated by the arrows.

Figure 6.4(d) shows the two-probe resistance - measured across the two wide electrodes far left and right of the cavity - of this device measured as a function of temperature (top) and its temperature derivative (bottom). The mechanical resonance of the membrane as a function of temperature (top) as well as $\frac{d[f_0]^2}{dT}$ (bottom) are plotted in Fig. 6.4(e). In both resistance and mechanics measurements, more than one phase transition accompanied by a hysteretic behavior in the temperature sweeps are observed. The red lines correspond to the measurements performed while warming up and the blue lines to the measurements performed while cooling down. There are three distinct peaks in the $\frac{d[f_0^2(T)]}{dT}$ at T_1 = 87 K, T_2 = 103 K and T_3 = 118 K. Between the lowest transition temperature and the highest, both the resistance and the mechanical resonance show hysteretic behavior of split branches in the R-T and the f_0-T data. Even though the effective area probed via transport and

nanomechanics are not identical, similar behaviors are observed in both R-T and f_0-T suggesting that the degraded area has a significant contribution to the resistance as well as the mechanics. This experiment has been repeated multiple times to rule out measurement artifacts but nonetheless, the hysteresis was present every time.

6.3. Discussion & Conclusion

We believe that both the thickness and degradation are playing a role in our observation of enhanced T_{CDW} in Fig. 6.3&6.4. The study by Bekaert et al. [20] on the "healing" of the sulphur vacancies by oxygen, demonstrated that the electron phonon coupling could be enhanced by 80%, thus increasing the T_{SC}. Also, Zhang et al. recently reported the persistence of the CDW up to 140 K in the monolayer[18]. The increase of T_{CDW} upto 129 K in our air degraded sample could be an indication of partial amorphization of the multilayer sample which reduces the effective thickness of the crystal from bulk towards an intermediate, few-effective-layers.

The two-phonon mode shown in Fig. 6.4(c) represents a second order scattering process where an electron scatters to create a pair of phonons with opposite momenta near the CDW wave vector q_{CDW} [3]. Softening of the two-phonon peaks below T_{CDW} in many 2H-MX_2 systems has been observed and used to characterize the CDW [4, 52–56]. Typically the position of the two-phonon mode shifts down with decreasing temperature and the peak disappears as it reaches the CDW state. This is a direct result of the phonon dispersion renormalization due to the Kohn anomaly forming at T_{CDW}. The fact that we see differences in the two-phonon mode and the out of plane A_{1g} mode in the degraded areas is indicative of local changes in the phonon branches and the chemical bond lengths caused by degradation. Controlled systematic Raman study of degradation dynamics should be conducted to correlate the changes in the chemical bonds to the phonon dispersion relation and the T_{CDW}.

The enhancement of the T_{CDW} from the nominal 75 K up to 118 K in Fig. 6.4 may be due to a degradation similar to the one observed in Fig. 6.3 but is attributed in this case to the discharge which caused the flake and the electrodes to be damaged. The absence of the peaks at 103 K and 118 K in the downward sweep and at 87 K in the upward sweep may be an indication of competition between various domains with different transition temperatures. This picture is further supported by the the difference in the Raman spectra taken at room temperature in various areas of the same flake.

In conclusion, we studied the CDW transitions in the archetypal vdW systems 2H-TaS_2 and 2H-$TaSe_2$, by using the resonance frequency of suspended membranes. The temperature dependence of the resonance frequency can be translated into the specific heat which shows an anomaly at the phase transition temperature. We showed that degradation can irreversibly change the CDW transition temperature from the nominal value of T_{CDW} = 75 K to as high as 129 K. Furthermore, we studied a suspended drum with partial local disorder which showed multiple transition temperatures as well as a hysteresis loop. In this work, we have demonstrated that nanomechanical resonance is a powerful tool to study the CDW transitions in ul-

trathin suspended vdW materials complementary to the temperature dependent electronic transport.

Appendix.

A. Methods

Prepatterend SiO_2/Si

Dry thermal oxide of 285 nm, grown on highly doped (Si++) silicon is used as the substrate. Using standard e-beam lithography (EBL), electrodes are patterned into a PMMA 495 k - 950 k bilayer. After development, exposed SiO_2 areas are briefly dry etched using CHF_3 and Ar plasma in an anisotropic reactive ion etcher (RIE) such that 100 nm of the 285 nm SiO_2 is removed. Using an e-beam evaporator, 5 nm Ti and 95 nm Au are evaporated in the etched structure, embedding the electrodes into the SiO_2. The wafer is submerged in acetone for lift off and rinsed in isopropanol. In the second step, circular cavities are defined using EBL and AR-P 6200 resist. After development, exposed SiO_2 areas are dry etched completely down to the Si using RIE. AR-P 6200 is stripped in PRS-3000 and the sample is plasma cleaned in an O_2 barrel asher prior to stamping.

Transfer of 2H-TaS_2 and 2H-$TaSe_2$

The exfoliation and transfer of multi-layer 2H-TaS_2 and 2H-$TaSe_2$ flakes is done using PDMS transfer method [35]. First, PDMS is made by mixing Sylgard 184 base with the curing agent in a 10:1 ratio by mass and desiccating to remove pockets of gas. The mixture is left to cure for at least 48 hours before use. Using magic tape, 2H-TaS_2 and 2H-TaS_2 are exfoliated onto the PDMS. Flakes of tens of nanometers in thickness - confirmed by the optical contrast - are identified and transferred onto the set of electrodes and cavity in SiO_2/Si.

Laser interferometry

Sample is mounted on a heater stage which is cooled down to 4 K using a dry cryostat with optical access to the sample space. An AC signal sent from the vector network analyzer (VNA) drives the intensity of the blue diode laser (λ_{blue} = 405 nm). The laser is focused on the center of the membrane which is optothermally driven into motion. The motion of the membrane across the optical field of a second laser (continuous red laser of λ_{red} = 632 nm) causes an interference with the red light reflected from the Si cavity bottom and is collected at the photodetector and read by the VNA in a homodyne fashion.

R vs. T measurement

Temperature dependence of the sample resistance is performed using a Keysight B2902A precision source measure unit. At every temperature, current-voltage trace is measured while current biasing and the resistance is extracted by fitting a linear slope.

Raman spectroscopy and SEM

Raman spectroscopy is performed at room temperature using a Renishaw InVia system with a 514 nm green excitation laser. 0.5% of 50 mW is used for the collection of the Raman data. Scanning electron microscopy (SEM) is performed using a FEI Helios G4 CX system at 20 kV acceleration voltage.

B. Derivation of the change in specific heat

In this section, we derive the Landau-Lifshitz [25, 31, 37] expression for the charge density wave (CDW) order parameter, minimum free energy and the change in the specific heat Δc_v at the transition temperature T_{CDW}. The Landau free energy is written as:

$$F = F_0 + a(T - T_{CDW})Q^2 + BQ^4 \tag{6.5}$$

where F_0 is the temperature dependent free energy of the normal state, Q is the order parameter and a and B are phenomenological positive constants. Minimizing the free energy (Eq. 6.5) with respect to Q by setting the derivative equal to zero, we get $0 = 2a(T - T_{CDW})Q + 4BQ^3$ so that $Q^2 = \frac{-a(T-T_{CDW})}{2B}$, which can be written as:

$$Q = \sqrt{\frac{-a(T - T_{CDW})}{2B}}. \tag{6.6}$$

Using Eq. 6.5 and Eq. 6.6, the equilibrium free energy F_{min} equals:

$$F_{min} = F_0 - \frac{a^2(T - T_{CDW})^2}{4B}.$$

We can now calculate the entropy, $S = -\partial F/\partial T$ as

$$S_{min} = -\frac{\partial F_{min}}{\partial T} = \frac{a^2(T - T_{CDW})}{B}.$$

The difference in entropy above and below the transition temperature is:

$$S_{min} - S_0 = \begin{cases} \frac{a^2(T-T_{CDW})}{2B} & T < T_{CDW}, \\ 0 & T > T_{CDW}, \end{cases} \tag{6.7}$$

where S_0 is the entropy of the normal state.

From Eq. 6.7, the specific heat at constant pressure by $c_p = T\left[\frac{\partial S}{\partial T}\right]_p$ can be found by subtracting the specific heat of the normal state. The difference in the specific heat caused by the phase transition is thus:

$$\Delta c_p = c_{p,min} - c_{p0} = \begin{cases} \frac{a^2}{2B} & T < T_{CDW}, \\ 0 & T > T_{CDW}. \end{cases} \tag{6.8}$$

Since the specific heat at constant volume c_v is comparable to c_p (i.e. $c_v \simeq c_p$) in incompressible solids we can relate Eq. 6.8 to Eq. 6.4 of the main text. This change in c_v is basically the height of the anomaly - commonly refered to as the "lambda anomaly" due to its shape - visible in the c_v vs temperature plots in the main text Fig. 6.2(e-f). Compared to the data in Ref. [31], an improved analysis method is used to analyze the data shown in Fig. 6.2 of main text which may cause slight differences in the magnitude of the c_v in these plots with respect to the original plots. The transition temperature values remain unaffected.

C. Additional sets of measurements on degradation

In this section, we show additional measurements performed on multiple flakes of air degraded 2H-TaS_2 stamped on two separate substrates (A and B).

Two flakes on substrate A

Two devices (A1 and A2) of 2H-TaS_2 on substrate A are prepared separately by cleaving freshly from the bulk crystal. The two flakes are stamped on the same substrate at relatively the same time and therefore have been exposed to the ambient conditions for nearly the same amount of time; the time exposed to the ambient is a few hours.

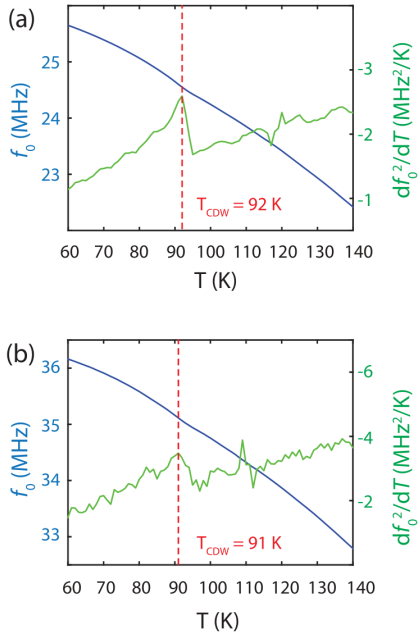

Figure C.1: Measurements of two flakes on substrate A. The resonance frequencies f_0 are plotted in blue (left y-axis) and its temperature derivative $\frac{d[f_0^2]}{dT}$ in green (right y-axis) **(a)** Device A1, showing the T_{CDW} = 92 K. **(b)**. Device A2 on the same substrate as device A1, showing the T_{CDW} = 91 K.

Figure C.1(a-b) show the resonance frequencies f_0 in blue (left y-axis) and $\frac{d[f_0^2]}{dT}$ in green (right y-axis) of sample A1 and A2. Both flakes on substrate A show a similar T_{CDW} of 92 K and 91 K as determined from the peaks of $\frac{d[f_0^2]}{dT}$. This demonstrates that degradation globally affected both samples on the substrate.

Two flakes on substrate B

A similar procedure was applied to two devices (B1 and B2) on substrate B. As shown in Fig. C.2, CDW transitions occur at much higher temperatures of 126 K and 129 K.

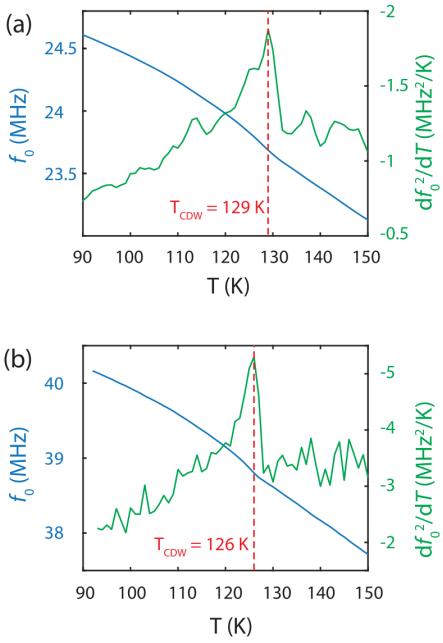

Figure C.2: Measurements of two flakes on substrate B. The resonance frequencies f_0 are plotted in blue (left y-axis) and its temperature derivative $\frac{d[f_0^2]}{dT}$ in green (right y-axis) **(a)** Device B1, showing the T_{CDW} = 129 K. **(b)**. Device B2, showing the T_{CDW} = 126 K.

The observation that the respective flakes on A and B show the same trend in the increased T_{CDW}, indicates that the enhancement in CDW transition temperature is caused by an external factor such as air and humidity, rather than fluctuation in the flake quality. As far as we could observe, there were no differences in the sample preparation between samples on A and B. We suspect that the temperature and humidity variation of the day may have played a role.

D. Other methods of inducing disorder

In this section, we explore two alternative methods of inducing disorder: laser induced oxidation performed similarly to Ref. [50] on a flake stamped on substrate C and focused ion beam (FIB) induced milling performed similarly to Ref. [51, 57, 58] on a flake stamped on substrate D.

Laser induced oxidation on a flake on substrate C

We use the method previously reported by Cartamil et al.[50] who induced oxidation and recrystallization in their 2H-$TaSe_2$ membrane by shining high intensity laser on the membrane. We use the same protocol in our suspended 2H-TaS_2 flake stamped on substrate C. The optical image of the sample is displayed in Fig. D.1 (a-b). Figure D.1(a) shows the image of the flake before laser irradiation and (b)

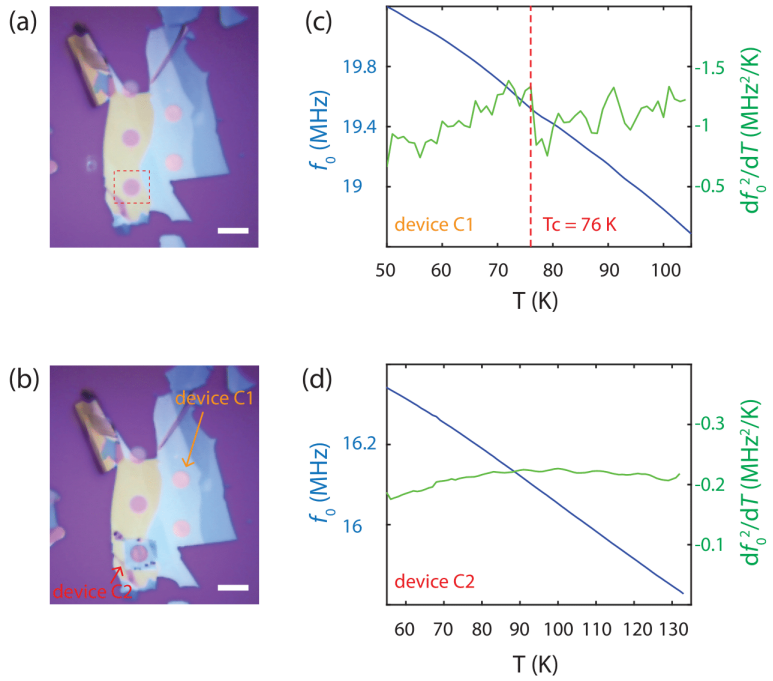

Figure D.1: Optical image of a 2H-TaS_2 flake on sample C **(a)** before high intensity laser irradiation and **(b)** after. The dotted red box in (a) indicates the area before the laser irradiation occurred. The square of discoloration can be seen in (b). Scale bars: 10 µm. **(c)** Measurement of f_0 (blue, left y-axis) and $\frac{d[f_0^2]}{dT}$ (green, right y-axis) of the drum labelled "device C1". It displays the expected CDW transition of T_{CDW} = 76 K. **(d)** f_0 (blue, left y-axis) and $\frac{d[f_0^2]}{dT}$ (green, right y-axis) of the drum labelled "device C2". The data shows no signs of a phase transition.

after irradiation. The dotted red square is the region where the laser is rastered. As can be seen by the color changes in Fig. D.1(b), there is an optically observable degradation on the drum labelled "device C2". To compare with the pristine state, we performed measurements on the drum labelled "device C1" which is of the same flake but hasn't been irradiated by the laser.

Figure D.1(c-d) plots f_0 (blue, left y-axis) and $\frac{d[f_0^2]}{dT}$ (green, right y-axis) of drums labelled "device C1" and "device C2". The dotted red line in Fig. D.1(c) indicates T_{CDW} = 76 K which is in agreement with literature values of T_{CDW} in pristine bulk 2H-TaS_2 [3]. Thus the mechanical response of C1 displays an un-altered CDW transition in 2H-TaS_2. Figure D.1(d) shows the same type of data but taken from C2 which has been irradiated with a high intensity laser. There are no clear signs of T_{CDW}, at least in the temperature ranges we took the data from.

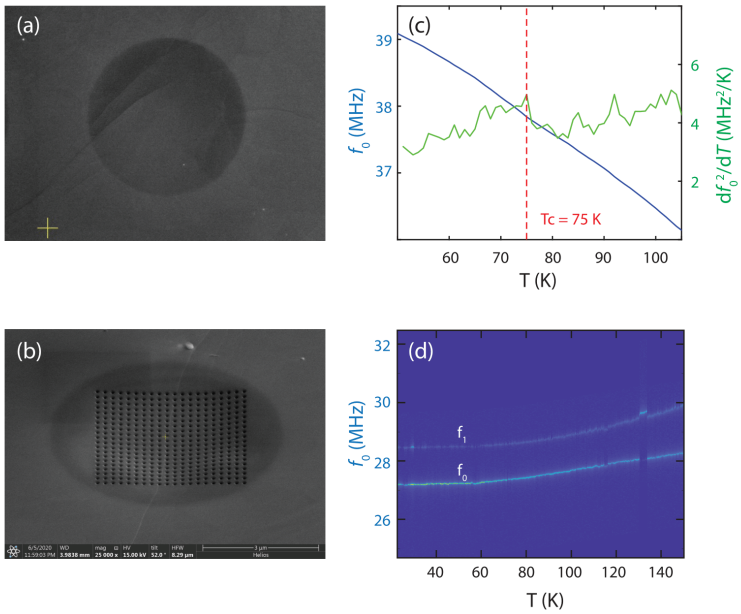

Figure D.2: **(a)** Scanning electron microscopy (SEM) image of a pristine 2H-TaS_2 drum (device D1).**(b)** SEM image taken at an angle of 52°, of a drum with 400 pores (device D2) milled by focused ion beam (FIB).**(c)** Measurement of f_0 (blue, left y-axis) and $\frac{d[f_0^2]}{dT}$ (green, right y-axis). Dotted red line indicates the T_{CDW} of 75 K. **(d)** Measurement of the fundamental frequency, f_0 and the first harmonic, f_1 represented in a heat map.

Focused ion beam induced disorder on a flake on substrate D

In Fig. D.2(a-b), we show scanning electron microscopy (SEM) images of 2H-TaS_2 flakes stamped on substrate D. Fig. D.2(a) is a SEM image of a pristine flake which has not been irradiated with the Ga+ beam (device D1). Therefore, it can be seen that in the f_0 data and $\frac{d[f_0^2]}{dT}$ data of Fig. D.2(c), there is a CDW transition at 75 K as expected.

Figure D.2(b) shows a SEM image of a device (device D2) irradiated with Ga+ ions in a pattern of 20 x 20 array of 50 nm pores that are 200 nm apart. The the fundamental mode and the second mode of this FIB irradiated device are plotted in Fig. D.2(d) in a heat map. As can be seen from the plot, it is striking that the resonance frquencies do not increase with lowering temperature as we have observed in the other devices. The resonance frequency of this device decreases as the temperature decreases, which signifies that the membrane perhaps has a thermal expansion coefficient with a negative sign possibly arising from the structure [59]. Furthermore, as in the case of the laser irradiated sample in the previous section, there is no observable phase transition in this sample in the range of temperatures we investigated.

References

[1] J. A. Wilson, F. Di Salvo, and S. Mahajan, "Charge-density waves and superlattices in the metallic layered transition metal dichalcogenides," *Advances in Physics*, vol. 24, no. 2, pp. 117–201, 1975.

[2] J. C. Tsang, J. E. Smith Jr, and M. W. Shafer, "Raman spectroscopy of soft modes at the charge-density-wave phase transition in 2H-$NbSe_2$," *Physical Review Letters*, vol. 37, no. 21, 1976.

[3] S. Sugai, "Lattice vibrations in the charge-density-wave states of layered transition metal dichalcogenides," *Physica Status Solidi. B, Basic Research*, vol. 129, no. 1, pp. 13–39, 1985.

[4] S. Sugai, K. Murase, S. Uchida, and S. Tanaka, "Studies of lattice dynamics in 2H-TaS_2 by Raman scattering," *Solid State Communications*, vol. 40, no. 4, pp. 399–401, 1981.

[5] J. M. E. Harper, T. H. Geballe, and F. J. Di Salvo, "Heat capacity of 2H-$NbSe_2$ at the charge density wave transition," *Physics Letters A*, vol. 54, no. 1, 1975.

[6] R. A. Craven and S. F. Meyer, "Specific heat and resistivity near the charge-density-wave phase transitions in 2H-$TaSe_2$ and 2H-TaS_2," *Physical Review B*, vol. 16, no. 10, 1977.

[7] R. Delaplace, P. Molinie, and D. Jerome, "On the pressure dependence of a charge density wave state in 2H-TaS_2," *Journal de Physique Lettres*, vol. 37, no. 1, 1976.

[8] T. M. Rice and G. K. Scott, "New mechanism for a charge density wave instability," *Physical Review Letters*, vol. 35, no. 120, 1975.

[9] G. Campagnoli, A. Gustinetti, A. Stella, and E. Tosatti, "Plasmon behavior at the charge density wave onset in 2H-$TaSe_2$," *Physical Review B*, vol. 20, no. 2217, 1979.

[10] E. F. Steigmeier, G. Harbeke, H. Auderset, and F. J. Di Salvo, "Softening of charge density wave excitations at the superstructure transition in 2H-$TaSe_2$," *Solid State Communications*, vol. 20, no. 7, 1976.

[11] J. C. Tsang, J. E. J. Smith, M. W. Shafer, and S. F. Meyer, "Raman spectroscopy of the charge-density-wave state in 1T-and 2H-$TaSe_2$," *Physical Review B*, vol. 16, no. 4239, 1977.

[12] W. L. McMillan, "Theory of discommensurations and the commensurate-incommensurate charge-density-wave phase transition," *Physical Review B*, vol. 14, no. 1496, 1976.

[13] D. E. Moncton, J. D. Axe, and F. J. Di Salvo, "Neutron scattering study of the charge density wave transitions in 2H-$TaSe_2$ and 2H-$NbSe_2$," *Physical Review B*, vol. 16, no. 801, 1977.

[14] J. A. Wilson, "Questions concerning the form taken by the charge density wave and the accompanying periodic structural distortions in 2H-$TaSe_2$ and closely related materials," *Physical Review B*, vol. 17, no. 3880, 1978.

[15] X. Xi, L. Zhao, Z. Wang, H. Berger, L. Forró, J. Shan, and K. F. Mak, "Strongly enhanced charge-density-wave order in monolayer $NbSe_2$," *Nature nanotechnology*, vol. 10, no. 9, pp. 765–769, 2015.

[16] C. Sergio, M. R. Sinko, D. P. Gopalan, N. Sivadas, K. L. Seyler, K. Watanabe, T. Taniguchi, A. W. Tsen, X. Xu, D. Xiao, and B. M. Hunt, "Tuning ising superconductivity with layer and spin–orbit coupling in two-dimensional transition-metal dichalcogenides," *Nature Communications*, vol. 9, no. 1, pp. 1–8, 2018.

[17] E. Navarro-Moratalla, J. O. Island, S. Manas-Valero, E. Pinilla-Cienfuegos, A. Castellanos-Gomez, J. Quereda, G. Rubio-Bollinger, L. Chirolli, J. A. Silva-Guillén, N. Agraït, G. A. Steele, F. Guinea, H. S. J. van der Zant, and E. Coronado, "Enhanced superconductivity in atomically thin TaS_2," *Nature Communications*, vol. 7, no. 1, pp. 1–7, 2016.

[18] D. Zhang, Y. Wu, Y.-H. Su, M.-C. Hsu, C. Ó Coileáin, J. Cho, M. Choi, B. S. Chun, Y. Guo, C.-R. Chang, and H.-C. Wu, "Charge density waves and degenerate modes in exfoliated monolayer 2H-TaS_2," *IUCrJ*, vol. 7, no. 5, 2020.

[19] Y. Wu, J. He, J. Liu, H. Xing, Z. Mao, and Y. Liu, "Dimensional reduction and ionic gating induced enhancement of superconductivity in atomically thin crystals of 2H-$TaSe_2$," *Nanotechnology*, vol. 30, no. 3, p. 035702, 2018.

[20] J. Bekaert, E. Khestanova, D. G. Hopkinson, J. Birkbeck, N. Clark, M. Zhu, D. A. Bandurin, R. Gorbachev, S. Fairclough, Y. Zou, M. Hamer, D. J. Terry, J. J. P. Peters, A. M. Sanchez, B. Partoens, S. J. Haigh, V. Milošević, Milorad, and V. Grigorieva, Irina, "Enhanced superconductivity in few-layer TaS_2 due to healing by oxygenation," *Nano Letters*, vol. 20, no. 5, pp. 3808–3818, 2020.

[21] R. Yang, W. Luo, S. Chi, D. Bonn, and G. M. Xia, "The stability of exfolicated FeSe nanosheets during in-air device fabrication processes," *IEEE Transactions on Nanotechnology*, vol. 18, pp. 37–41, 2018.

[22] K. S. Novoselov, D. Jiang, F. Schedin, T. J. Booth, V. V. Khotkevich, S. V. Morozov, and A. K. Geim, "Two-dimensional atomic crystals," *Proceedings of the National Academy of Sciences*, vol. 102, no. 30, pp. 10451–10453, 2005.

[23] L. J. Sandilands, A. A. Reijnders, A. H. Su, V. Baydina, Z. Xu, A. Yang, G. Gu, T. Pedersen, F. Borondics, and K. S. Burch, "Origin of the insulating state in exfoliated high-T_c two-dimensional atomic crystals," *Physical Review B*, vol. 90, no. 8, p. 081402, 2014.

[24] Y. Yu, L. Ma, P. Cai, R. Zhong, C. Ye, J. Shen, G. D. Gu, X. H. Chen, and Y. Zhang, "High-temperature superconductivity in monolayer bi 2 sr 2 cacu 2 o 8+ δ," *Nature*, vol. 575, no. 7781, pp. 156–163, 2019.

[25] L. D. Landau and E. M. Lifshitz, *Course of theoretical physics. Vol. 5: Statistical physics.*, vol. 5. Pergamon Press, 1968.

[26] E. B. Nyeanchi, D. F. Brewer, T. E. Hargreaves, A. L. Thomson, C. Liezhao, and C. Zhao-Jia, "The specific heat of BSCCO (2201) single crystal at low temperatures," *Physica C: Superconductivity*, vol. 235, 1994.

[27] Y. Takano, N. Arai, A. Arai, Y. Takahashi, K. Takase, and K. Sekizawa, "Magnetic prperties and specific heat of MPS_3 (M = Mn, Fe, Zn)," *Journal of magnetism and magnetic materials*, vol. 272-276, 2004.

[28] L. R. Testardi, "Elastic modulus, thermal expansion and specific heat at a phase transition," *Physical Review B*, vol. 12, no. 3849, 1975.

[29] J. W. Loram, J. L. Tallon, and W. Y. Liang, "Absence of gross static inhomogeneity in cuprate superconductors," *Physical Review B*, vol. 69, no. 060602, 2004.

[30] S. V. Grabovsky, I. V. Shnaidshtein, M. Takesada, A. Onodera, and B. A. Strukov, "Calorimetric study of ferroelectric $BaTiO_3$ in cubic phase," *Journal of Advanced Dielectrics*, vol. 3, no. 4, 2013.

[31] M. Šiškins, M. Lee, S. Mañas-Valero, E. Coronado, Y. M. Blanter, H. S. van der Zant, and P. G. Steeneken, "Magnetic and electronic phase transitions probed by nanomechanical resonators," *Nature Communications*, vol. 11, no. 1, pp. 1–7, 2020.

[32] D. Davidovikj, D. J. Groenendijk, A. M. R. Monteiro, A. Dijkhoff, D. Afanasiev, M. Šiškins, M. Lee, Y. Huang, E. van Heumen, H. S. J. van der Zant, A. D. Caviglia, and P. G. Steeneken, "Ultrathin complex oxide nanomechanical resonators," *Communications Physics*, vol. 3, no. 1, pp. 1–6, 2020.

[33] S. Jiang, H. Xie, J. Shan, and K. F. Mak, "Exchange magnetostriction in two-dimensional antiferromagnets," *Nature Materials*, vol. 19, no. 12, pp. 1295–1299, 2020.

[34] S. Sengupta, H. S. Solanki, V. Singh, S. Dhara, and M. M. Deshmukh, "Electromechanical resonators as probes of the charge density wave transition at the nanoscale in $NbSe_2$," *Physical Review B*, vol. 82, no. 15, p. 155432, 2010.

[35] A. Castellanos-Gomez, M. Buscema, R. Molenaar, V. Singh, L. Janssen, H. S. Van Der Zant, and G. A. Steele, "Deterministic transfer of two-dimensional materials by all-dry viscoelastic stamping," *2D Materials*, vol. 1, no. 1, p. 011002, 2014.

[36] D. C. Freitas, P. Rodière, M. R. Osorio, E. Navarro-Moratalla, N. M. Nemes, V. G. Tissen, L. Cario, E. Coronado, M. García-Hernández, S. Vieira, M. Núñez Regueiro, and H. Suderow, "Strong enhancement of superconductivity at high pressures within the charge-density-wave states of 2H-TaS_2 and 2H-$TaSe_2$," *Physical Review B*, vol. 93, no. 18, p. 184512, 2016.

[37] M. Saint-Paul and P. Monceau, "Survey of the thermodynamic properties of the charge density wave systems," *Advances in Condensed Matter Physics*, vol. 2019, 2019.

[38] G. K. White, J. A. Birch, and M. H. Manghnani, "Thermal properties of sodium silicate glasses at low temperatures," *Journal of Non-Crystalline Solids*, vol. 23, no. 1, pp. 99–110, 1977.

[39] K. G. Lyon, G. L. Salinger, C. A. Swenson, and G. K. White, "Linear thermal expansion measurements on silicon from 6 to 340 K," *Journal of Applied Physics*, vol. 48, no. 3, pp. 865–868, 1977.

[40] M. Barmatz, L. R. Testardi, and F. J. Di Salvo, "Elasticity measurements in the layered dichalcogenides $TaSe_2$ and $NbSe_2$.," *Physical Review B*, vol. 12, no. 10, 1975.

[41] D. Lin, S. Li, J. Wen, H. Berger, L. Forró, H. Zhou, S. Jia, T. Taniguchi, K. Watanabe, X. Xi, and M. S. Bahramy, "Patterns and driving forces of dimensionality-dependent charge density waves in 2H-type transition metal dichalcogenides," *Nature Communications*, vol. 11, no. 1, 2020.

[42] J. W. Jiang and Y. P. Zhou, "Parameterization of stillinger-weber potential for two-dimensional atomic crystals.," *arxiv*, 2017.

[43] J. Kang, S. Tongay, J. Zhou, J. Li, and J. Wu, "Band offsets and heterostructures of two-dimensional semiconductors," *Applied Physics Letters*, vol. 102, no. 1, 2013.

[44] D. S. Sanditov and V. N. Belomestnykh, "Relation between the parameters of the elasticity theory and averaged bulk modulus of solids," *Technical Physics*, vol. 56, no. 11, 2011.

[45] T. Middelmann, A. Walkov, G. Bartl, and R. Schödel, "Thermal expansion coefficient of single-crystal silicon from 7 K to 293 K," *Physical Review B*, vol. 92, no. 17, p. 174113, 2015.

[46] F. Hao, X. Liao, M. Li, H. Xiao, and X. Chen, "Oxidation-induced negative Poisson's ratio of phosphorene.," *Journal of Physics: Condensed Matter*, vol. 30, no. 31, 2018.

[47] A. Falin, M. Holwill, H. Lv, W. Gan, J. Cheng, R. Zhang, D. Qian, M. R. Barnett, E. J. Santos, K. S. Novoselov, and T. Tao, "Mechanical properties of atomically thin tungsten dichalcogenides: WS_2, WSe_2, and WTe_2," *ACS nano*, 2021.

[48] Q. Li, Q. Zhou, L. Shi, Q. Chen, and J. Wang, "Recent advances in oxidation and degradation mechanisms of ultrathin 2D materials under ambient conditions and their passivation strategies," *Journal of Materials Chemistry A*, vol. 7, no. 9, 2019.

[49] M. T. Lavik, T. M. Medved, and G. D. Moore, "Oxidation characteristics of MoS_2 and other solid lubricants," *ASLE Transactions*, vol. 11, no. 1, 1968.

[50] S. J. Cartamil-Bueno, P. G. Steeneken, F. D. Tichelaar, E. Navarro-Moratalla, W. J. Venstra, R. van Leeuwen, E. Coronado, H. S. van der Zant, G. A. Steele, and A. Castellanos-Gomez, "High-quality-factor tantalum oxide nanomechanical resonators by laser oxidation of $TaSe_2$," *Nano Research*, vol. 8, no. 9, pp. 2842–2849, 2015.

[51] I. E. Rosłoń, R. J. Dolleman, H. Licona, M. Lee, M. Šiškins, H. Lebius, L. Madauß, M. Schleberger, F. Alijani, H. S. J. van der Zant, and P. G. Steeneken, "High-frequency gas effusion through nanopores in suspended graphene," *Nature Communications*, vol. 11, no. 1, pp. 1–6, 2020.

[52] K. Zhang, Z.-Y. Cao, and X.-J. Chen, "Effects of charge-density-wave phase transition on electrical transport and Raman spectra in 2H-tantalum disulfide," *Applied Physics Letters*, vol. 114, no. 14, p. 141901, 2019.

[53] P. Hajiyev, C. Cong, C. Qiu, and T. Yu, "Contrast and Raman spectroscopy study of single-and few-layered charge density wave material: 2H-$TaSe_2$," *Scientific reports*, vol. 3, no. 1, pp. 1–6, 2013.

[54] J. Joshi, H. M. Hill, S. Chowdhury, C. D. Malliakas, F. Tavazza, U. Chatterjee, A. R. H. Walker, and P. M. Vora, "Short-range charge density wave order in 2H-TaS_2," *Physical Review B*, vol. 99, no. 24, p. 245144, 2019.

[55] J. Pandey and A. Soni, "Electron-phonon interactions and two-phonon modes associated with charge density wave in single crystalline 1T-VSe_2," *Physical Review Research*, vol. 2, no. 3, p. 033118, 2020.

[56] M. Klein, "Theory of two-phonon Raman scattering in transition metals and compounds," *Physical Review B*, vol. 24, no. 8, p. 4208, 1981.

[57] E. Mykkänen, A. Bera, J. S. Lehtinen, A. Ronzani, K. Kohopää, T. Hönigl-Decrinis, R. Shaikhaidarov, S. Graaf, J. Govenius, and M. Prunnila, "Enhancement of superconductivity by amorphizing molybdenum silicide films using a focused ion beam. nanomaterials," *Nanomaterials*, vol. 10, no. 5, p. 950, 2020.

[58] K. Celebi, J. Buchheim, R. M. Wyss, A. Droudian, P. Gasser, I. Shorubalko, J. I. Kye, C. Lee, and H. G. Park, "Ultimate permeation across atomically thin porous graphene," *Science*, vol. 344, no. 6181, pp. 289–292, 2014.

[59] L. Cabras, M. Brun, and D. Misseroni, "Micro-structured medium with large isotropic negative thermal expansion," *Proceedings of the Royal Society A*, vol. 475, no. 2232, p. 20190468, 2019.

7

7

Outlook

In this chapter, we present some of the exciting on-going research that is not yet published at the time of writing this dissertation. First, a new class of quasi 2D materials - free-standing complex oxides - is characterized using magnetotransport. Next we test the viability of using these complex oxides for realizing self-sealing pressure sensors. Then we interface a ferroelectric complex oxide, $BaTiO_3$ with graphene in a van der Waals heterostructure to create an ultra-thin piezoelectric actuator. Finally we end with a transport study, demonstrating the gate-independence of the superconductivity of microbridges fabricated from single crystal van der Waals superconductor 2H-TaS_2.

7.1. Introduction

We have mainly dealt with van der Waals materials in the body of this dissertation, however recent developments in growing and releasing epitaxial complex oxides by using a water soluble buffer layer $Sr_3Al_2O_6$ [1], have allowed the study of free-standing complex oxides close to the atomically thin limit, similar to 2D materials [1–3]. Complex oxides in their ultra-thin free-standing form are mechanically robust [4] withstanding large strains up to 8% [5, 6], flexible enough to allow large curvatures [7] and have already been demonstrated as viable nanomechanical resonators [8, 9]. Furthermore, wafer scale production methods for single crystalline complex oxides are being developed [10] which makes them more attractive for large scale CMOS compatible fabrications. This outlook chapter contains preliminary results from currently on-going projects that deal with this new family of quasi 2D materials made from single crystalline free-standing complex oxides which are released from their growth substrate.

7.2. Transport of Suspended Complex Oxides

In this section, some preliminary results on the mechanical and transport properties of free-standing complex oxides are presented. Device geometry similar to the ones presented in Chapters 5 and 6, are used, but instead of exfoliating van der Waals materials from bulk crystals, we grow the complex oxide layers using pulsed laser deposition (PLD) and release the layers from the growth substrate by etching away the water soluble buffer layer. A KrF excimer laser of λ = 248 nm is pulsed at 1 Hz onto the target creating a plume of plasma while a crystalline substrate is positioned in front of the plume and heated to a fixed temperature. A 30 kV electron gun is used to monitor the growth in-situ for the reflection high energy electron diffraction (RHEED). Electrons diffracted off of the surface of the substrate at a grazing angle is collected at the detector and monitored throughout the growth process.

First, water soluble complex oxide $Sr_3Al_2O_6$ (SAO) layers are grown layer-by-layer on top of TiO_2 terminated single crystal $SrTiO_3$ (001) substrates. Then on top of this SAO film, the material of interest is grown on top. After growth, the sample is annealed in high oxygen partial pressure for an hour and submerged in water to release the material of interest from the growth substrate. A commercially available polydimethyl siloxane (PDMS) film is attached to the top of the material of interest during the immersion in water as support. After the SAO is fully etched away, the $SrTiO_3$ (STO) substrate is detached from the film and the film/PDMS is removed from the DI bath and blown dry. Using the deterministic transfer method, the film is temporarily transferred to a dummy substrate for X-ray diffraction characterization. The release process is illustrated in Figs. 2.10&2.11.

7.2.1. Magnetotransport in suspended, curved $SrRuO_3$

Ruddlesden-Popper phases of $Sr_{n+1}Ru_nO_{3n+1}$ are an interesting class of materials which shows rich variations of electronic ground states. Sr_2RuO_4 (n = 1) is a superconductor below 1.3 K as briefly shown in Chapter 2 Fig. 2.7. Interestingly,

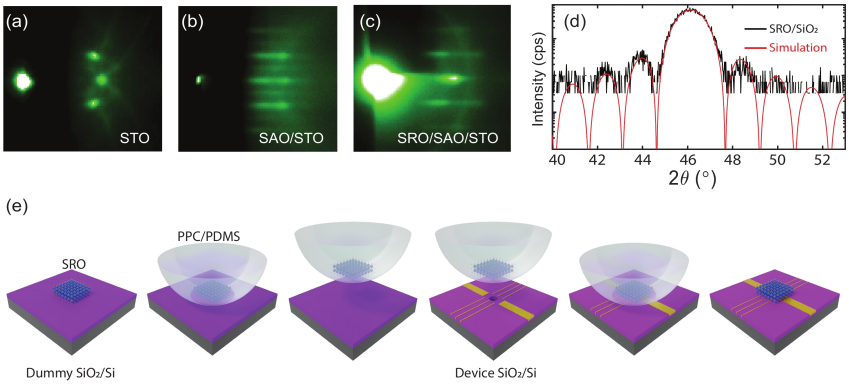

Figure 7.1: Reflection high energy electron diffraction (RHEED) images of (a) $SrTiO_3$ (STO) substrate, (b) $Sr_3Al_2O_6$ (SAO) grown on STO and (c) $SrRuO_3$ grown on SAO/STO. (d) X-Ray diffraction (black) of exfoliated SRO stamped on SiO_2/Si and the simulation(red). The c axis lattice parameter extracted from the simulation is 3.931 Å and the thickness of 16 unit cells.(e) Illustration of the fabrication procedure. From left to right: SRO flakes on SiO_2/Si are prepared by viscoelastic stamping method [11] after growth and subsequent water etching.

it is the only *p*-wave superconductor that has been through rigorous experimental examinations [12–16]. $Sr_3Ru_2O_7$ (n = 2) on the other hand is a metamagnetic metal with a nematic electronic liquid phase in the presence of a magnetic field [17]. The perovskite phase of the strontium ruthenate (n = ∞), $SrRuO_3$ (SRO) is an itinerant ferromagnet. From the first synthesis in 1959 [18] to the discovery of its ferromagnetism in 1966[19], SRO was mainly employed as a metallic contact material for other complex oxide compounds. However, recent controversy over the presence of skyrmions in bare epitaxial SRO [20–23] and interface engineered SRO [24, 25] have attracted great interest from the community. In this work, we study the anomalous Hall effect (AHE) in free-standing SRO in the absence of substrate or interface effects while tuning the geometric deformation in-situ.

Figure 7.1(a-c) show the RHEED pattern of the STO substrate, SAO grown on STO and SRO on SAO/STO respectively, demonstrating crystalline flat growth of both SAO and SRO layers. After growth, the sample is annealed in 300 mbar O_2 at 550 °C to reduce the amount of oxygen vacancies in the film. Once the sample is ready and removed from the PLD chamber, commercially available PDMS film (gel-Pak®) is attached to the sample and submerged under deionized (DI) water for 24 hours. After the SAO layer is dissolved away and the SRO film is released, the SRO film on PDMS is removed from water and gently blown dry. Using the deterministic transfer process [11], the film of SRO is transferred onto a dummy SiO_2/Si chip for the X-ray diffraction (XRD) analysis.

XRD is performed using Bruker D8 discover. Figure 7.1(d) shows the 2θ scan of the film on SiO_2. Finite sized oscillation can be observed on both sides of the SRO (002) peak near 46 ° demonstrating the high crystallinity of the film even after water etching and stamping process. XRD simulation which showed the best fit to

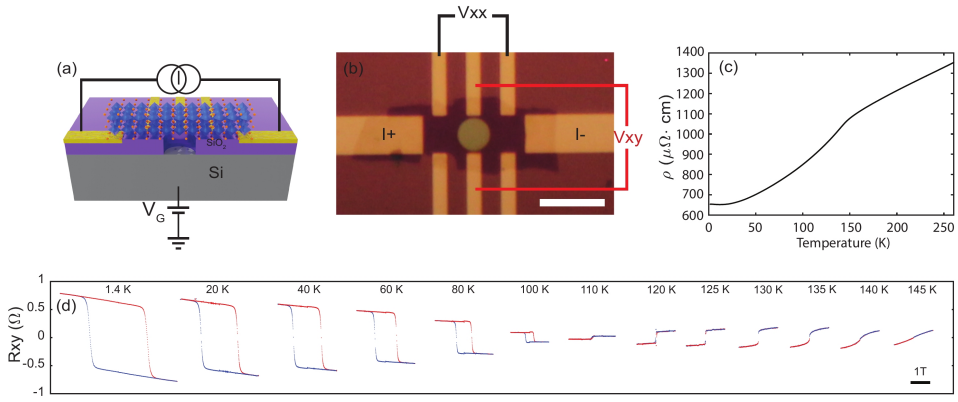

Figure 7.2: (a) Illustration of the cross section of the device. (b) Optical microscopy image of the device. Scalebar corresponds to 10 µm. (c) Resistivity as a function of temperature as the sample is cooled down. (d) Antisymmetrized Hall resistance across various temperatures from 1.4 K to 145 K. The curves in red are measured while ramping up the field and blue while ramping down.

the data is plotted in red on top of the data. A c-axis lattice parameter of 3.931 Å which agrees well with the literature values of the bulk SRO [26] and a thickness of 16 unit cells are used for the simulation. After XRD characterization, flakes of adequate sizes are identified and transferred from the dummy substrate to the pre-patterned SiO_2/Si device. Polymer (polypropylene carbonate on PDMS) based pick up technique as shown in Fig. 7.1(e) is used to transfer the flakes [27, 28].

As can be seen in the cross sectional illustration in Fig. 7.2(a), pre-patterned devices consist of electrodes in a Hall-bar pattern with a circular cavity etched in the center. Gate voltage is applied to the Si substrate to electrostatically pull on the flake as previously demonstrated in Chapter 5. Figure 7.2(b) shows an optical microscopy image of the SRO flake stamped on a Hall-bar with a cavity in the center. This sample is cooled down in an Oxford He flow cryostat and its temperature dependent resistivity is plotted in 7.2(c). This resistivity is an estimated resistivity taking into account the geometry of the Hall probes, not the irregularly shaped flake. The resistivity shows a Fermi liquid behavior from the kink at 150 K (the paramagnet to ferromagnet transition) and all the way down to the base temperature of 1.4 K. Anomalous Hall loops are measured at various temperatures from 1.4 K to 145 K as shown in Fig. 7.2(d) and are showing typical behaviors of epitaxial SRO with symmetric boundary conditions [21]. The anomalous Hall loops can be understood by the combination of the classical Hall effect which linearly depends on the external field H, and the anomalous Hall component which is related to the magnetization M. This can be written as

$$\rho_{xy} = \mu_0(R_H H + R_A M), \tag{7.1}$$

where R_H and R_A are the classical and anomalous Hall coefficients. At low temperatures, the overall slope of the Hall loop is negative meaning that electrons

dominate the conduction. This later flips sign at higher temperatures above 110 K where the holes start to dominate the conduction.

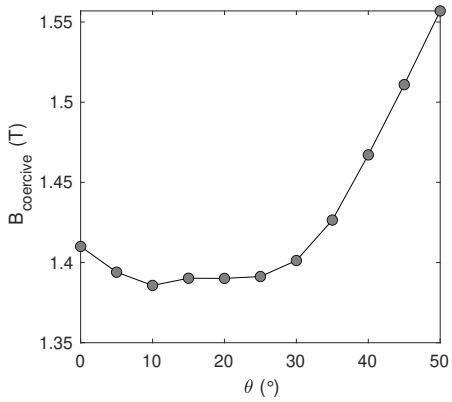

Figure 7.3: Angle dependence of the coercive field.

SRO has a nearly perpendicular magnetization in the ultra-thin limit [29] and transitions to nearly 45° in the bulk [30]. In order to extract the magnetic easy axis, we have performed the Hall measurements as a function of angle and plotted the coercive field in Fig. 7.3. As expected, our 16 unit cell SRO which is in between the ultra thin limit and the bulk, has a minimum coercive field between 0° and 45° with respect to the normal. The angle in which the coercive field is minimum is the easy axis, which in our case is estimated to be ~ 20 °.

After the device is characterized in the flat configuration, gate voltage is used to create tensile stress and a curvature in the suspended part of the flake. Using the Hall probes facing directly across the cavity as seen in Fig. 7.2(b), the effect of geometric deformation on the anomalous Hall effect is studied. We applied 0 V to 25 V and measured the Hall loop. As can be seen in Fig. 7.4(a), the coercive field is slightly reduced. The change in the coercive field with respect to the flat configuration is plotted in Fig. 7.4(b) which shows that there is a general trend towards reduction in the coercive field at higher voltages. However, the change is not monotonic which raises the question whether this is due to strain or geometric deformations.

The anisotropy field for strained SRO can be estimated as [31]

$$\Delta H_A = \frac{3\lambda_{100}}{\mu_0 M_S}(c_{11} - c_{12})\left(1 + \frac{2c_{11}}{c_{12}}\right)\epsilon, \tag{7.2}$$

where ϵ the strain, λ_{100} is the magnetostriction coefficient, $\mu_0 M_S \simeq 0.3$ T the saturation magnetization and c_{11} = 252 GPa and c_{12} = 132 GPa the elastic moduli. Using equations 5.26 and 5.23 and using Young's modulus of 180 GPa, Poisson's ratio of 0.344 [32], thickness of 6.3 nm and radius of 2.5 µm, the strain applied to the SRO at the maximum gate voltage of 30 V can be extracted. The strain added

to the membrane due to 30 V back gate is 0.1 %. This added strain is equivalent to the change in the anisotropic field of 1.01 T which is obtained from using Eq. 7.2.

It is worth noting that the volume reduction analysis by Kiyama *et al.* [33] simply converted to a linear thermal expansion coefficient results in an estimated 5×10^{-5} K^{-1} throughout 300 K to 150 K and remains constant below the phase transition temperature. The constant unit cell volume of SRO arises from the "invar effect" also seen in several magnetic alloys including $Fe_{0.64}Ni_{0.36}$ which has nearly zero thermal expansion coefficient in the ferromagnetic state[34, 35]. The thermal strain accumulated due to the thermal expansion coefficient of SRO is then arising mostly in the range of 300 K to 150 K. The thermal strain we estimate from using the analysis in Chapter 5 results in 0.75 %.

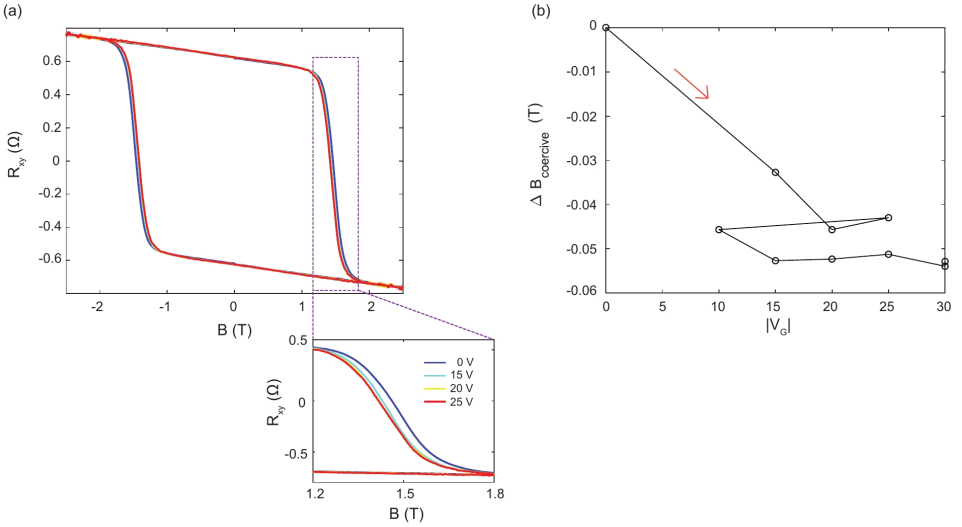

Figure 7.4: (a) Anomalous Hall hysteresis as a function of gate voltages. The figure below is a zoom-in near the positive coercive fields. (b) The difference in the coercive field across various V_G with respect to the coercive field at V_G = 0 V.

Additional experiments have been performed on another SRO flake of 55 unit cells prepared in the same growth and release procedure. Shown in Fig. 7.5 are the anomalous Hall loops at V_G of 0 V (red) and 40 V (blue). Similar reduction in the coercive field is observed.

The origin of the reduction in the coercive field in the absence of the reduction in the anomalous Hall amplitude requires careful analysis through additional analytical calculations and/or magnetic simulations. This tunability can be attributed to electrostatic strain and/or geometric curvature. At the time of writing this dissertation, we are considering the geometric curvature as a main contributor. Below are our rationale behind this hypothesis.

1. We can rule out field effect affecting the transport properties. Since SRO is a high carrier density system, we expect the field from Si to be efficiently screened

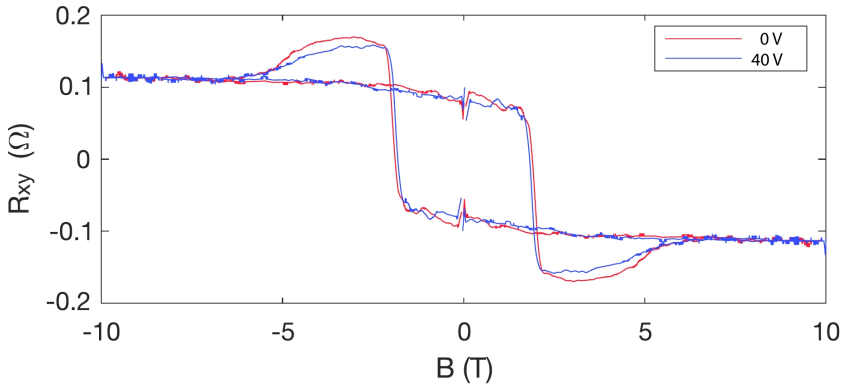

Figure 7.5: Anomalous Hall measurements of a 55 unit cell SRO at V_G of 0 V (red) and 40 V (blue). Measurements are performed at 1.4 K.

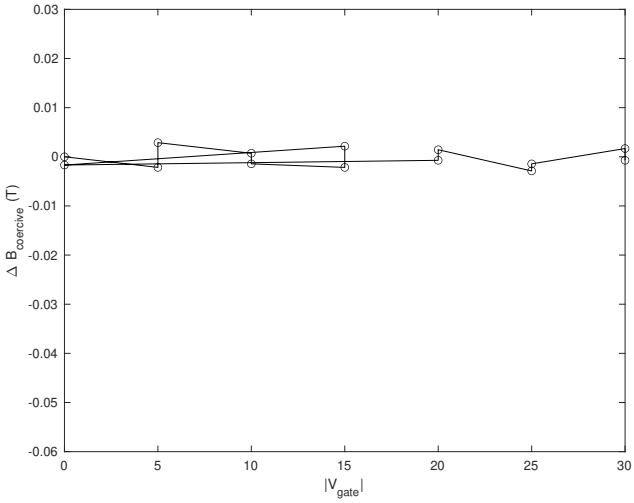

Figure 7.6: Anomalous Hall loop measured across the supported part of the sample showing no gate dependence.

within the first few Å. As can be seen in Fig. 7.6, the Hall probes measuring across the supported part of the Hall bar is unaffected by the gate voltage.

2. In Fig. 7.4(b), we show that the tunability is non-monotonic. We swept up to 25 V and decreased to 10 V and observed that the coercive field remains nearly constant. This is reminiscent of creep seen in suspended van der Waals materials similar to Fig. 4.3e where the membrane sagged due to exposure to large external pressures for a long time.

3. Since SRO has a relatively small magnetostriction, large strains are needed to

observe significant changes in the anomalous Hall loops. However, in both epitaxial strain as well as uni-axial bending experiments both the coercive field as well as the anomalous Hall amplitudes were affected simultaneously [36, 37]. Since strain affects the magnetic moments and thus the overall magnetization, it is expected that the ρ_{xy} in Eq. 7.1 is also affected. Since we do not observe the change in the anomalous Hall amplitudes and we only tune the coercive field, it is more likely that the coercive field is affected by the geometric curvature. Since the easy axis is $\sim 20\,^{\circ}$ from the perpendicular, we suspect that curvature may help position the easy axis of a part of the suspended film in line with the external field.

Due to these reasons above, we suspect that the curvature has a bigger contribution to the coercive field tuning rather than the electrostatic strain.

7.2.2. Strain tuning the MIT transition in $NdNiO_3$

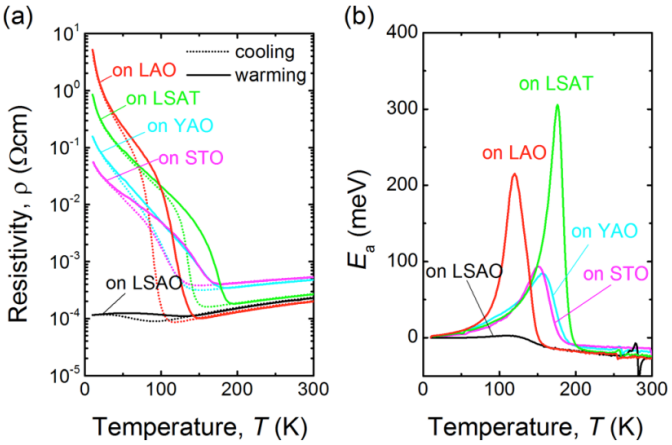

Figure 7.7: Temperature dependence of resistivity (a) and activation energy (b) of NNO films deposited on various substrates. Figure adapted from Ref. [38]

Materials with larger sensitivity to strain are easier to analyse. In order to distinguish the effect of curvature and strain, a non-magnetic material that is susceptible to strain should be used as an idealized system to characterize the strain dependence of the electronic properties. One such material is $NdNiO_3$ (NNO). As shown in Fig. 7.7, NNO has a metal to insulator transition (MIT) which can be greatly tuned by strain. Although it has already been explored using epitaxial strain, thanks to the advent of the release technique, we may be able to continuously tune the electronic properties of suspended NNO in-situ through strain by applying voltages to the Si back gate.

7.3. New sealing methods

In Chapter 4 we identified the gas leakage pathways in graphene drums and developed a sealing technique to hermetically seal off the graphene drum. Although

the improvement in the leakage time constant of 4 orders of magnitude is impressive, there are critical disadvantages to the technique discussed which includes the question of scalability and the large deflection at 1 bar - the preferred base pressure of consumer pressure sensors. As an alternative, we consider self-sealing free-standing complex oxide perovskites as a nearly 2D membrane for pressure sensing MEMS applications. In this work, we use free-standing $SrRuO_3$ (SRO) and $SrTiO_3$ (STO) suspended over SiO_2/Si cavities to make pressure sensors and demonstrate a simple, CMOS compatible sealing technique which does not require additional fabrication steps. The sealing consists of annealing the devices above 300 °C in ambient conditions for as short as 15 minutes. Pressure dependence of the resonance frequency is measured to extract the gas permeation time constant. By comparing the permeation time constant of the pressure sensor devices before and after annealing, we show that the hermeticity improves by a factor of more than 10^3. Comparable devices fabricated on Si_3N_4/Si cavities do not show this enhancement of the hermeticity which suggests that the improved interface between the complex oxide and the substrate is mediated by the oxygen vacancies in the complex oxides drawing out the oxygen in the substrate creating a chemical bond. The SRO film shown in Fig. 7.1 is used for this work as well as a 82 nm thick free-standing STO prepared in a similar way.

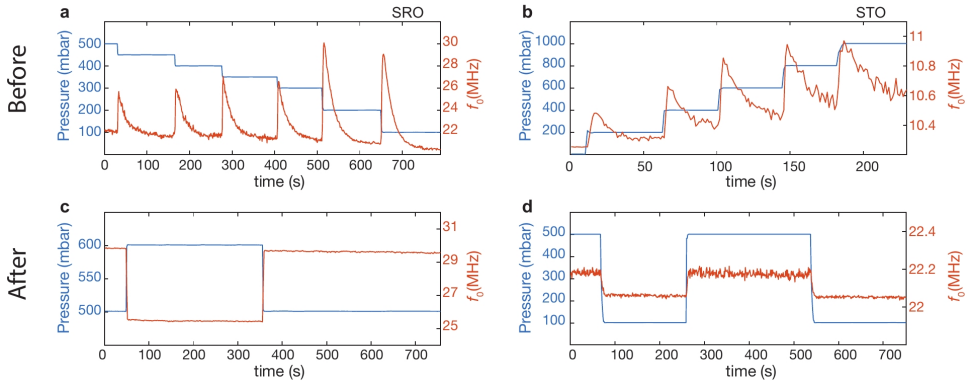

Figure 7.8: Pressure response of the resonance frequency before (**a**&**b**) and after (**c**&**d**) annealing. Left column shows the behavior of a 16 unit cell SRO device and the right column shows the behavior of 218 unit cell STO device. The external pressure controlled by the pressure controller is plotted in blue on the left y-axes and the resonance frequency is plotted in orange on the right y-axes.

The pressure dependence of the resonance frequency of SRO and STO devices in their freshly fabricated state are shown in Fig. 7.8a&b. The setup shown in Fig. 4.1(c) is used for these measurements. The chamber pressures plotted in blue (left y-axis) are adjusted in step-wise fashion while the resonance frequencies plotted in orange (right y-axis) are traced. In both SRO and STO devices before the sealing procedure, sudden increase in the resonance frequencies followed by exponential decay of time constant τ are observed. This behavior suggests that the membranes are tensioned due to the change in the pressure difference in and outside of the

cavity which then quickly relaxes due to the equilibration of the pressures inside and out, enabled by the permeation of the gases. In SRO and STO, the average permeation time constant τ is on the order of 21 seconds and 14 seconds respectively, which are extracted by fitting exponential functions to the decays shown in Fig. 7.8a,b.

Same procedure was performed after the samples are annealed in ambient conditions. The data from SRO sample shown in Fig. 7.8c is after 1 hour of annealing in 300 °C. It can be observed that the sudden spike in the resonance frequency followed by a fast decay are not observed but rather very long drift in the resonance frequency can be seen. By fitting an exponential decay to the slow reduction in the resonance frequency, we achieve a τ of 1.1×10^4 seconds. Similar behavior is observed in the STO device after annealing for 15 minutes at 400 °C. As shown in Fig. 7.8d, no observable decays in the resonance frequencies are present and there are small drifts. Fitting this data to an exponential decay results in $\tau = 1.2 \times 10^5$ seconds, but these values may not be reliable due to the low goodness-of-fit caused by the flatness of the data.

We believe that the mechanism in which the complex oxides bind with the SiO_2 underneath is mediated by the dangling bonds at the bottom surface of complex oxide flakes. The interaction of $SrTiO_3$ and SiO_2 has been investigated by Yong *et al.* [39] who report the formation of additional chemical species at the interface, namely $TiSi_2$ and/or $SrSiO_3$.

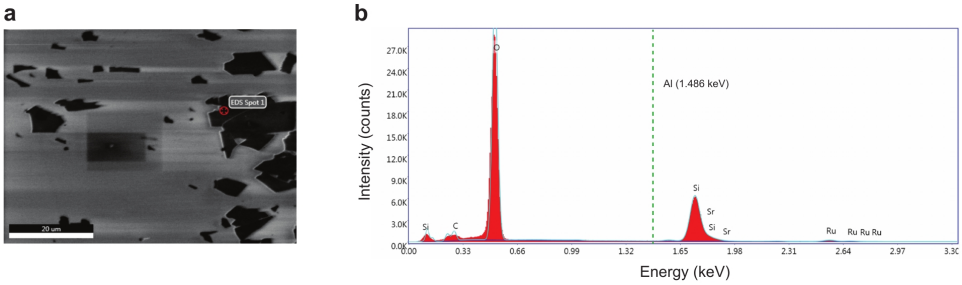

Figure 7.9: **a** Scanning electron microscopy (SEM) image of SRO stamped on a dummy SiO_2/Si. The position in which energy dispersive X-ray spectrum (EDX) is taken from is highlighted with a marker. **b** EDX elemental analysis on a SRO flake showing the constituents of SRO and the substrate. Al peak at 1.486 keV (green dashed line) is not observable which suggests the absence of SAO.

An alternative hypothesis for the binding mechanism is the remnant SAO which may be present due to partial etching in water. Remnant SAO layers which are not completely etched away may provide reactive dangling bonds underneath the SRO and STO flakes, that can readily bind to the SiO_2. In order to eliminate this hypothesis, we have performed energy dispersive X-ray spectroscopy (EDX) of the flakes (Fig. 7.9) and atomic force microscopy (AFM) topography analysis of the STO substrate after the release of the layers (not shown here). Due to the absence of the Al peak in the EDX as well as the stepping terraces observed in the AFM of the substrate, we can say that the hypothesis of the improved bonding occurring due to the residual SAO layer is highly unlikely.

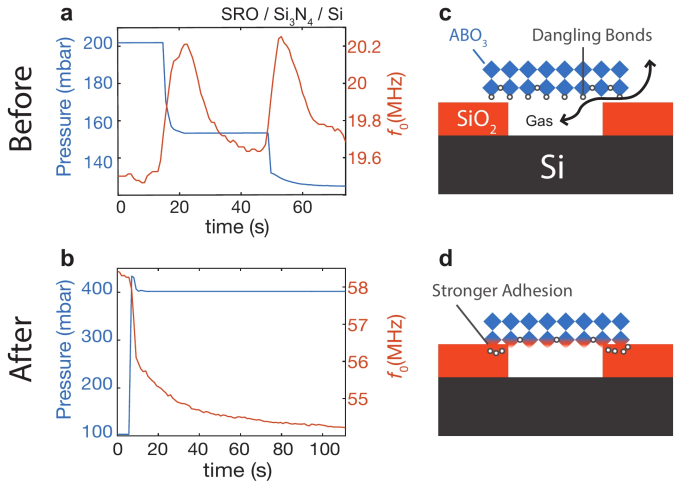

Figure 7.10: Annealing experiment performed on a SRO membrane stamped on 350 nm LPCVD Si_3N_4/Si. Pressure (left y-axis, blue) response of the resonance frequency (right y-axis, orange) of SRO membrane **a** before annealing and **b** after annealing. Possible mechanism of the bonding is illustrated in **c**&**d**. **c** Before annealing, there are dangling bonds at the bottom of the SRO flake. The van der Waals gap between the SRO and the SiO_2 allows for gases to pass through. **d** After annealing, the vacancies bond with the oxygen from the substrate leading to a stronger bond to form at the interface.

In order to further support the hypothesis that the bonding is mediated by the oxygen vacancies, we have fabricated additional samples on substrates that are oxygen free. By performing an identical experiment on cavity substrates fabricated from Si_3N_4/Si we are able to check if similar improvements in the permeation time constant can be observed in oxygen-free, nitride based substrates as well. Figure 7.10a&b show the pressure response of the resonance frequency of a SRO sample on Si_3N_4/Si before and after annealing. Large increase in the resonance frequency can be seen but improvements in the leakage time constants are not significant (6 seconds before to 22 seconds after). Figure 7.10c&d show illustrations of the hypothetical bonding mechanism. Further experiments are needed to indisputably conclude on the microscopic mechanism.

One potential method to support or refute the mechanism is by measuring the acoustic impedance at the boundary before and after annealing. Ultra-fast acoustic impedance measurements can be used to observe the properties at the interface of two different materials [40]. If the flake is weakly bound to the substrate in the non-annealed state, then there should be a refection at the interface of the flake and the substrate arising due to the large impedance mismatch. If chemical bonds form at the interface after annealing, then the acoustic impedance mismatch between the complex oxide and SiO_2 should be reduced, allowing for higher transmission of the acoustic waves. Finally, samples annealed at higher temperatures and lower pressures similar to the parameters in [39] should be investigated to check for the possibilities of ultimate hermeticity by promoting more robust chemical bonds.

Although graphene holds immense potential as the material for next-generation

pressure sensors, it has multiple disadvantages that are intrinsic to the van der Waals nature of the material. **1.** In order for graphene to reach the market, a pinhole-free method of fabricating graphene based capacitive sensors need to be developed and perfected, and additional measures need to be taken to seal the interface between graphene and the substrate. **2.** If one of those drums rupture or if there is a leak somewhere, then all of the remaining drums become obsolete because that opening can leak gases through the entire device via the interface. **3.** Most deposition processes take place in high vacuum, which means that the cavities will be sealed with vacuum beneath the graphene. This limits the working range with the highest sensitivity to be near vacuum which is a very small niche market.

We believe that there are three alternatives to address the above problems. **1.** If a free-standing complex oxide is used and the above-mentioned annealing protocol is developed (i.e. by optimizing the oxygen vacancy or annealing temperature) then individual drums can be sealed off in ambient pressures. This lets the remaining drums to still function as a pressure sensor. **2.** With clever fabrication and growth techniques, other 3D materials may be able to bond to a substrate using chemical or bonding procedures. **3.** Graphene squeeze film sensors can be used with intentional venting holes [41].

7.4. Piezoelectric actuation with van der Waals - complex oxide heterostructures

Complex oxides and van der Waals (vdW) materials together encompass a wide spectrum of ground states such as superconductivity, magnetism, and ferroelectricity. However, it is difficult to interface the two classes of materials to study the emergent phenomena due to the 3D nature of epitaxially grown complex oxides and 2D nature of exfoliated van der Waals materials. Studies so far have used $SrTiO_3$ as a substrate to study the electron transport in 2D materials [42–44] or graphene as a transparent interlayer for the growth of complex oxides [3, 45]. In this work, we combine $BaTiO_3$ (BTO) in a vdW heterostructure with graphene as electrodes to piezoelectrically excite the heterostructure into motion. Free standing BTO is prepared by epitaxially growing it on a water soluble SAO layer. Once released, vdW assembly techniques are used to create a capacitor geometry of graphene - BTO - graphene suspended over a cavity in SiO_2/Si. We investigate the differences in the driving mechanism by optothermally, electrostatically and piezoelectrically driving the system into motion. When electrostatically driven, the system reduces in resonance frequency due to capacitive softening. The forward and backward traces in the DC offset overlap as expected in an electrostatically driven system. However, when piezoelectrically driven, we observe a hysteresis in the forward sweep in comparison to the backward sweep indicative of ferroelectric polarization switching. We further investigate this in the resonance frequency, Q factor, and phase which all show the hysteretic behavior.

First, free-standing BTO is prepared in the same way as the previous sections. Figure 7.11a-c show the RHEED patterns of the STO (001) growth substrate, SAO/STO

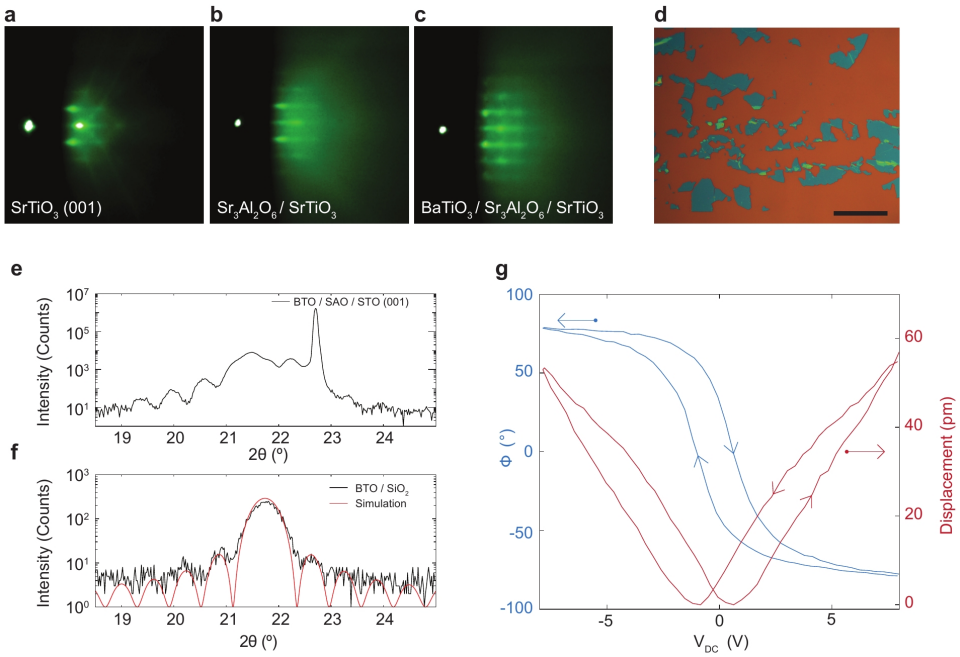

Figure 7.11: Growth and characterization of bare $BaTiO_3$ (BTO) film. Reflection high energy electron diffraction (RHEED) pattern of **a** the $SrTiO_3$ (STO) substrate, **b** sacrificial layer $Sr_3Al_2O_6$ (SAO) on STO and **c** BTO on SAO on STO. **d** Optical image of the film transferred onto SiO_2/Si. Scalebar: 50 µm. **e** X-ray diffraction (XRD) spectrum of BTO/SAO/STO before the releasing process. **f** XRD of bare BTO transferred onto SiO_2/Si. Lattice spacing of 4.085 Å and thickness of 36 unit cells are used to plot the simulation in red. **g** Phase (left y-axis, blue) and displacement (right y-axis, red) data from piezoresponse force microscopy (PFM).

and BTO/SAO/STO. The growth of BTO becomes more 3D towards the end as can be seen by Fig. 7.11c. After growth, XRD is performed to check the crystallinity of the grown layers (Fig. 7.11e). The films are then released from the substrate and deterministically stamped on a dummy SiO_2/Si as shown in Fig. 7.11d. XRD is performed again on this substrate in order to extract the c-axis parameter as well as the thickness of the BTO alone. A lattice constant of 4.085 Å which agrees well with the literature value of the bulk BTO and a thickness of 36 unit cells is used to simulate the curve plotted in red (Fig. 7.11f). Then using the polypropylene carbonate (PPC) based transfer technique [27], individual flakes are deposited on a prepatterned substrate with gold electrodes for the characterization using piezoresponse force microscopy (PFM).

Asylum Cypher AFM with a MFMV metal coated cantilever is used for the PFM measurements. An AC actuation with a DC bias is applied to the tip while the bottom gold electrode is grounded. The resulting bias dependence of the PFM data is shown in Fig. 7.11g. The ferroelectric switching can be observed in both the displacement (right y-axis, red) as well as the phase (left y-axis, blue). The hysteresis occurs with a coercive field of about 1 V.

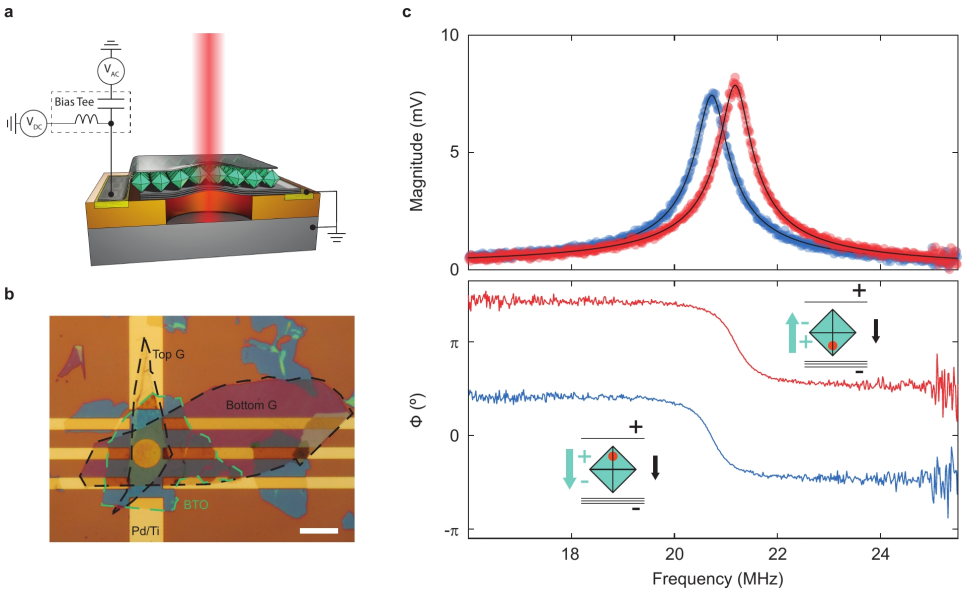

Figure 7.12: Measurement setup and device. **a** Cross-sectional illustration of the graphene-BTO-graphene heterostructure device. Driving signal is applied to the top graphene while the bottom graphene and Si are grounded. **b** Optical image of device 1 with top and bottom graphene highlighted with dashed black outlines and BTO highlighted with a dashed green outline. Scalebar: 10 µm. **c** Magnitude (top) and phase (bottom) of the device in parallel polarization state (blue) and anti-parallel polarization state (red). Both signals are taken at V_{DC} = 0 V.

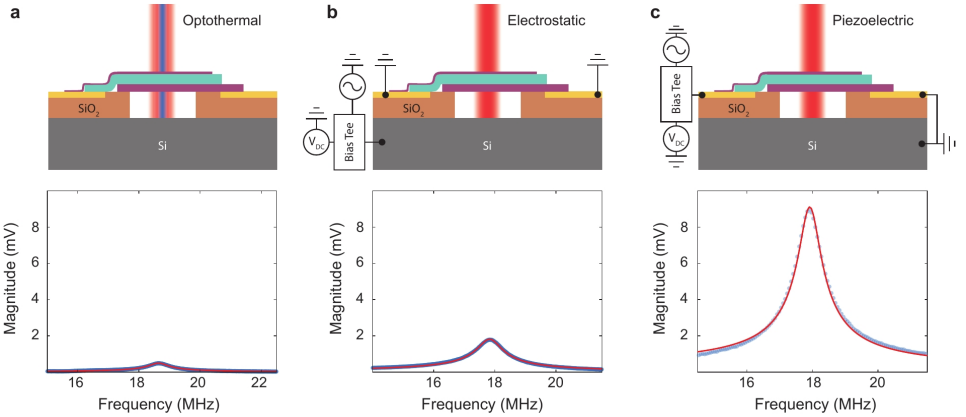

Figure 7.13: Comparison between different actuation methods. Top row: Illustration of the actuation methods. Bottom row: Resonance peaks measured using the respective actuation methods at -10 dBm. **a** Optothermal actuation using intensity modulated blue laser. **b** Electrostatic actuation using bottom Si. **c** Piezoelectric actuation with excitation voltage sent to the top graphene. Data points are plotted in blue and the simple harmonic oscillator fit in red.

The device is fabricated on SiO_2/Si substrates with pre-patterned electrodes and cavities. Electrodes are defined by e-beam lithography followed by a short reactive ion etching then metallization using the e-beam evaporation of Ti/Pd. The heterostructure is fabricated by transferring individual layers on top of the pre-patterned device area. First, the bottom graphene layer is transferred using the deterministic PDMS transfer method [11]. Next, a BTO flake of adequate size is transferred from the dummy SiO_2/Si to the device area on top of the bottom graphene using the polymer assisted pick-up technique [27, 28]. Finally, the PDMS technique is employed again to transfer the top graphene layer. A cross-sectional illustration is shown in Fig. 7.12a. The thickness of the bottom layer graphene (16 nm) is chosen such that the thickness exceeds the electron screen length of 1.2 nm [46] to efficiently screen the electric field originating at the top graphene from the Si. Figure 7.12b shows an optical microscopy image of a device with black dashed lines highlighting the outline of the graphene layers and a green dashed line highlighting the outline of the BTO flake. Figure 7.12c shows the resonance peaks (top) and the phase (bottom) of the heterostructure at V_{DC} = 0 V after poling the BTO first by driving the V_{DC} to the extrema. The curves in blue are when the actuation is in parallel to the polarization of the BTO and the curves in red are when the actuation is anti-parallel to the polarization. This can be observed clearly in the phase offset of π between the red and blue curves, providing evidence that the actuation is of piezoelectric and not of electrostatic nature.

We use three different methods to actuate the heterostructure. In addition to the optothermal actuation used in previous chapters, here we also added a way to electrically actuate the device. The output of the vector network analyser (VNA) can be used to modulate the blue diode laser intensity (Fig. 7.13a), or connected directly to the sample to electrically actuate the sample. By using a Bias Tee, we are also able to add a DC offset to the AC signal. This can be connected to the bottom silicon to drive the heterostructure electrostatically (Fig. 7.13b) or to the top graphene to drive the heterostructure piezoelectrically (Fig. 7.13c). The red laser interferometry is used in all three methods to measure the vibration of the membrane.

Using identical output power of -10 dBm to actuate the sample, we compare the magnitude of the resonance peaks in Fig. 7.13a-c (bottom row). The magnitude of the resonance peak is related to the actuation efficiency as well as the amplitude of the resonance [47]. Although it is difficult to quantify the amplitude, we can conclude by looking at peak heights in Fig. 7.13a-c (bottom row) that the piezoelectric actuation is more efficient than the electrostatic actuation in this sample at V_{DC} = 0 V. The efficiency of optothermally driven systems is difficult to compare with electrically driven systems due to the reflective losses at every optical component.

Next we compare the DC bias response of the sample when electrostatically driven vs. piezoelectrically driven. The left column of Fig. 7.14 shows the resonance frequency f_0, phase ϕ, the Q factor and the magnitude in the piezoelectrically driven state and the right column of Fig. 7.14 shows those of electrostatically driven state. The data plotted in blue are collected while ramping down the DC bias and the data plotted in red are collected while increasing the DC bias. In all of f_0,

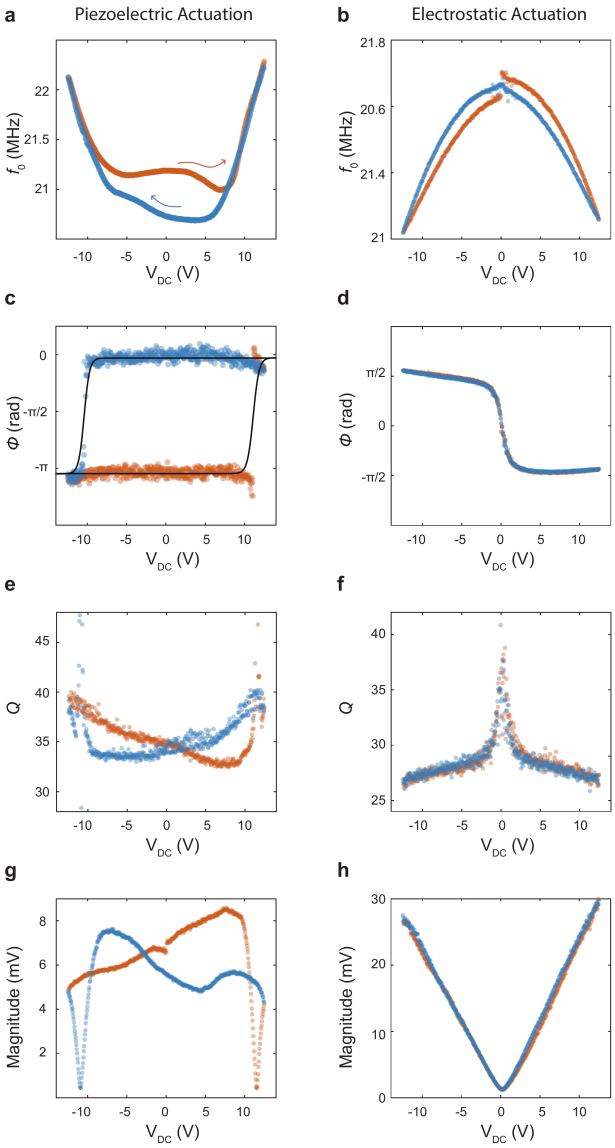

Figure 7.14: Comparison between piezoelectric actuation (left column) and electrostatic actuation (right column) of device 1. **a&b** Resonance frequency, **c&d** phase, **e&f** Q factor, and **g&h** magnitude as a function of the DC bias. The blue data points are collected while reducing the DC bias and the red data points are collected while increasing the DC bias.

ϕ, Q and magnitude, the measurements show hysteretic behaviors. In stark contrast, the sample, when electrostatically driven, shows no signs of hysteresis. The deviation in the start and the finish of Fig. 7.14b is due to the drift in the resonance frequency due to creep. Furthermore, the sign of curvature of the f_0 in Fig. 7.14a

compared to Fig. 7.14b shows that in the piezoelectrically driven case, the strain is accumulated at high DC biases similar to the quadratic strain-voltage relation in electrostrictively strained systems. The negative curvature of the electrostatically driven sample in Fig. 7.14b signifies that the resonance frequency is reduced due to capacitive softening, a phenomenon often observed in 2D resonators with large pre-tensions[48].

In Fig. 7.14c&d we compare the phases of the device when piezoelectrically and electrostatically driven. In Fig. 7.14d, we observe that the forward trace overlaps with the backward trace. In contrast, the phase from piezoelectrically driven case in Fig. 7.14c shows that the forward is 180 ° out of phase until the switching field. A similar phenomenon is observed in the backward trace. The backward trace is in phase until the negative switching field. The out-of-phase trace can be visualized with a DC offset anti-parallel to the polarization of the ferroelectric domain and the in-phase trace with the DC offset parallel to the polarization of the ferroelectric domain. When the DC offset exceeds the coercive field of ~11 V, then the DC voltage flips the ferroelectric domain, forcing the domains to align parallel to it.

In Fig. 7.14e, we observe the minima in Q of both the forward and backward traces just before the coercive fields. Then at the transition, the resonance becomes difficult to analyse due to the significant reduction in the magnitude as can be seen in Fig. 7.14g. In the electrostatically driven case, the Q factor is reduced at higher V_{DC} similar to the electrostatically actuated MoS_2 resonator by Lee *et al.* [48] (Fig. 7.14f). The reduction in the Q factor at larger DC offsets can be understood by the increase in the dissipation through circulating currents induced by the applied gate voltages.

Finally, Figs. 7.14g&h show the magnitudes of piezoelectrically driven and electrostatically driven sample. The magnitude when electrostatically driven (Fig. 7.14h), shows linear dispersion from 0 V with overlapping upward and downward traces. The linear behavior of the magnitude vs. V_{DC} can be understood by [48]

$$F = \frac{1}{2}\frac{\partial C_{DC}}{\partial z}(V_{DC}^2 + 2V_{DC}V_{AC}\cos(\omega t) + V_{AC}^2\cos^2(\omega t)), \tag{7.3}$$

where F is the force applied by the applied voltages, $\frac{\partial C_{DC}}{\partial z}$ change in the capacitance due to change in the z position of the membrane and $V_{AC}\cos(\omega t)$ the AC drive signal from the VNA. Therefore the magnitude follows $F \propto V_{\mathrm{DC}}$ at the frequency $f = \omega/2\pi$ for $V_{\mathrm{DC}} > V_{\mathrm{AC}}$. Fig. 7.14g show the magnitude of the piezoelectrically driven membrane as a function of DC bias. Coercive fields are shown as minima in both negative and positive DC voltages. The overall DC voltage dependence of the magnitude plotted in Fig. 7.14g should be dependent on the strength of the piezoelectric constants d_{33} (in the actuation direction) and d_{31} (in-plane of the membrane). The qualitative resemblance between the PFM data and the mechanics data can be more easily observed in device 2. Figure 7.15 shows the DC voltage dependence of the magnitude from device 2. It can be observed that the overall shape of the magnitude data extracted from the mechanics looks strikingly similar to the PFM data - also replotted on the same figure.

It is worth noting that the coercive field measured using PFM (0.98 V) of bare

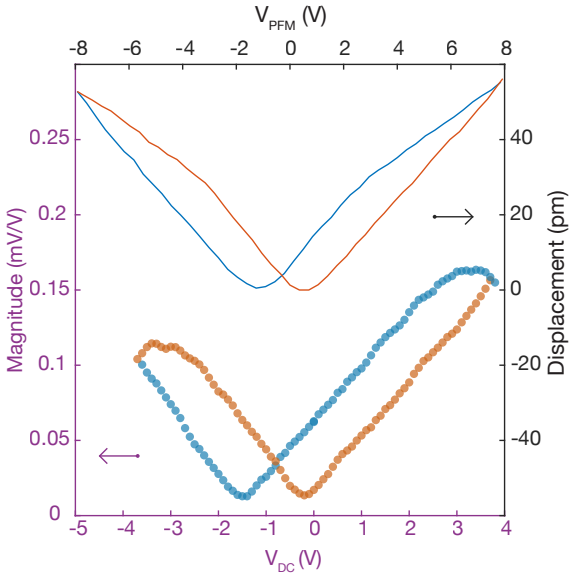

Figure 7.15: Magnitude (left y-axis) data from device 2 compared to the PFM data (right y-axis). Plots in blue are measured while decreasing the DC voltages and in orange are measured while increasing.

flake and using mechanics of device 1 (10.7 V) are different by a factor of ~10. The apparent difference in the coercive field most likely arises from PPC residues left over from the transfer process. Unlike traditional capacitors formed by sandwiching BTO in SRO electrodes, graphene-BTO-graphene have van der Waals interfaces with residues or air pockets in between, which can give a "tenting" effect, acting as capacitors in series due to the potentially large gap [49]. Since capacitors in series result in a reduced total capacitance (i.e. $1/C_{tot} = 1/C_{g-BTO} + 1/C_{BTO} + 1/C_{BTO-g}$), this tenting effect can reduce the effective voltage drop across the BTO thus increasing the apparent coercive field in the capacitor geometry used for the mechanics measurements. In device 2, we observe a coercive field that is comparable to the PFM data. This suggests that the interface between graphene and BTO in device 2 is much cleaner. It is worth noting that in the fabrication of device 2, the top interface has been effectively "cleaned" prior to the transfer of the final graphene layer. After the transfer of the BTO layer, many unsuccessful attempts have been made to transfer the top layer of graphene. We speculate that the polymer residues on top of the BTO flake may have been picked up by the graphene layers, each time an unsuccessful attempt had been made.

Other potential culprits behind the inconsistent coercive fields to consider are the inhomogeneity of the ferroelectric properties and the formation of "dead layers" in ferroelectric materials. In PFM measurements, the cantilever tip probes local properties of very small areas of few tens of nanometres [50]. If it happens to land in an area of a weakly ferroelectric or passive domains, then it will show smaller apparent coercive fields [51]. Alternative explanation is in the formation

of a "dead layer" at the interface of the ferroelectric and the metallic electrode. Although the origin and the existence of the dead layer is under debate [52–54], similar effects can be expected in our devices due to the nature of the BTO-graphene interface.

The displacement data plotted in Fig. 7.15 can be explained by [55]

$$S_{33}^{tot} = Q_{33}P_3^2 + 2Q_{33}\epsilon_{33}P_3E_3 + Q_{33}\epsilon_{33}^2E_3^2, \tag{7.4}$$

where S_{33}^{tot} is the total strain along the z direction with an external electric field E_3 pointed in the same direction, Q_{33} the corresponding electrostriction coefficient, ϵ_{33} the dielectric constant and P_3 the polarization. The first term in the above equation is due to the ferroelectricity, second is due to the piezoelectricity ($S \sim E_3$) and the third due to electrostriction ($S \sim E_3^2$) and in a ferroelectric material, the first two terms dominate. Therefore, the voltage dependence of the displacement shows the minima at the coercive field (i.e. $P_3 = 0$) and linearly increases away from it. Since the magnitude of the harmonic oscillator fit from the mechanics data also plotted in Fig. 7.15 qualitatively looks similar to the displacement data from the PFM measurements, we believe that the magnitude of the resonance is also linearly related to Eq. 7.4.

Proper modelling and analysis of the measurement data are needed to understand the behavior of this ultra-thin actuator operating in the membrane mode. Unlike the film bulk acoustic resonators (FBAR) used in high frequency filtering in 5G telecommunication applications, our membrane is not purely operated in the breathing mode, but in bending mode, resulting in lower resonance frequencies. In conventional FBAR resonators made of ~1 µm sputtered polycrystalline piezoelectrics, the electric field is applied in the out-of-plane direction, and the bulk acoustic wave is dominated by the breathing mode due to its geometry. Therefore, the acoustic wave can be assumed to depend purely on one of the piezoelectric constants, d_{33}. In our system, we observe the motion of the piezoelectric resonator in the membrane regime where the resonance frequency is mostly defined by the pretension and diameter of the cavity. We believe that the model should consist of the electric field applied in the out-of-plane direction somehow exciting an expansion in the in-plane direction which is associated with the d_{31} term of the piezoelectric tensor.

This works is, to the best of our knowledge, the first demonstration of a van der Waals heterostructure device composed of 2D materials and free-standing complex oxides. We expect further studies to include piezoelectric generation using acoustic, electronic or optothermal actuation as the source of excitation. Furthermore, if the interferometry constraint is relieved by exploring electrical actuation and detection using S_{11} or S_{21} parameters of a VNA, then the size limitations of this device can be lifted and the device can be further reduced. Reduction in the device size will push the frequency range to the breathing mode in the high GHz microwave frequencies, which is attractive for applications in next generation mobile technologies. As shown in Fig. 7.16, our device is among the thinnest reported in literature. Tanifuji *et al.* report one the thinnest piezoelectric resonator devices composed of 30 nm thick AlN and electrodes of 40 nm total thickness [56]. They

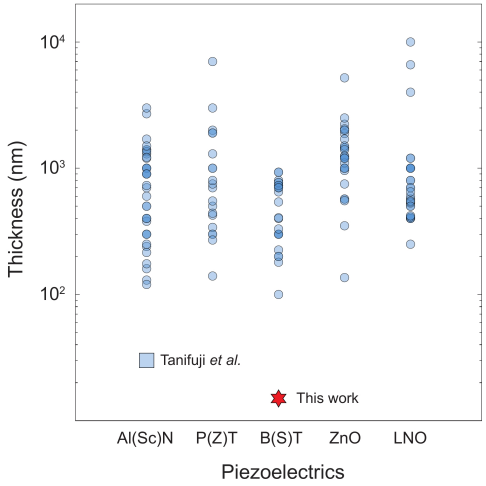

Figure 7.16: Thicknesses and ferro/piezoelectric materials of several thin ferro/piezoelectric resonators reported in literature.

have successfully fabricated the devices and anticipate the resonance frequency to be $f_{\text{breathing}} \sim 50$ GHz from calculations but have not reported any experimental results on the resonance. Since $f_{\text{breathing}} \simeq c_{\text{acoustic}}/2t$ where c_{acoustic} is the speed of sound along the actuation direction and t the thickness of the piezoelectric material, we can estimate the resonance frequency of our heterostructure in the breathing mode $f_{\text{breathing}}$, which is typically the mode of operation in thin film bulk acoustic resonators (FBAR). Assuming $c_{\text{acoustic}} = 6300$ m/s in BTO [57] we expect a resonance frequency of ~ 210 GHz.

7.5. Monolithic van der Waals microbridge and gate independence of TaS_2

In this section we show the experimental characterization of monolithic single crystal van der Waals superconducting micro-bridge devices. Recent works by De Simoni *et al.* showed unconventional field tunability in fully metallic superconductors [58]. By gating microbridges made of sputtered polycrystalline Ti, they were able to completely suppress the critical current. Field effect in their device has been shown to manifest up to a few µm. Field tunability has been shown in many dilute superconductors including LAO/STO [59], twisted bilayer graphene [60] and WTe_2 [61] however, it has long been thought to have negligible effect in fully metallic high carrier density superconductors. From the ultra short Thomas-Fermi screening length and the theory of superconductivity by London, we expect all of the electric field to be screened at the surface of the superconductor and the electric field to have no effect on the critical current in a high density system. Therefore, recent works on field tuning of the critical current I_c by pinching-off the high density superconducting nano-bridge is a promising platform for future quantum electronics

[58, 62–65].

In this work, we investigate the side-gate dependence of the critical current I_c in monolithic nano-bridge devices made from a single crystal van der Waals superconductor, 2H-TaS_2. The current - voltage ($I-V$) and the differential resistance (dV/dI) characteristics of the devices are first measured in a magnetic field without applying the gate. Rich features in the $I-V$ and dV/dI suggest that at intermediate fields below H_{c2}, the bridges become dissipative, effectively becoming S-n-S junctions caused by small hot spots in the nano-bridges. We then apply large side gate voltages at various magnetic fields H_{c2}, in attempts to pinch off the superconductivity completely. However, the I_c does not show any dependence on the side gate voltages in all three devices. We therefore hypothesize that the crystallinity of the nano-bridge plays a big role in the field susceptibility of the superconductivity in such systems. Our observation provides an insight into the complicated microscopic origin of the field tunability of superconducting nano-bridge systems.

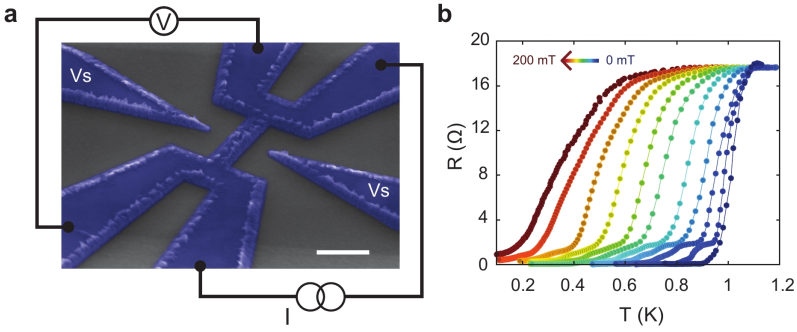

Figure 7.17: **a** False colored scanning electron microscopy image of the device. The hBN/TaS_2 device is colored in blue. Scalebar: 1 um. False coloration credit: E. J. S. van Thiel. **b** Four-probe resistance as a function of temperature measured at perpendicular magnetic fields ranging from 0 to 200 mT.

2H-TaS_2 has an interesting scaling behavior with the number of layers. While other van der Waals superconductors such as 2H-$NbSe_2$ and FeSe show reduction in T_c when thinned down [66, 67], 2H-TaS_2 shows the highest T_c in the monolayer limit [68]. Since the coherence length ξ scales inversely with the T_c, we have chosen to work with 2H-TaS_2 in the bulk limit. Bulk 2H-TaS_2 has a coherence length of $\xi \simeq$ 50 nm [68] which is on the same order as Ti measured by De Simoni *et al.* [58].

Devices similar to the polycrystalline Ti sample characterized by De Simoni *et al.* are fabricated from 2H-TaS_2 flakes exfoliated from bulk single crystals. Using deterministic transfer [11], three devices consisting of 2H-TaS_2 flakes covered by hexagonal boron nitride (hBN) are prepared on a sapphire substrate. Using e-beam lithography, Ar milling and evaporation, Cr/Au electrodes are deposited onto the flakes. Next, the heterostructure is milled away into the micro-bridge structure as shown in Fig. 7.17a via e-beam lithography and Ar milling. After fabrication, all three devices are wire bonded and cooled down in a dilution refrigerator. Figure

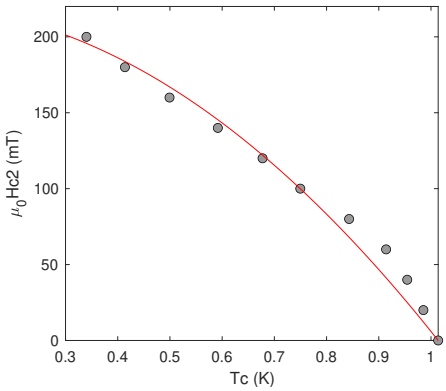

Figure 7.18: Transition temperature at various external fields.

7.17b shows temperature dependence of the four-probe resistance at various out of plane magnetic fields ranging from 0 to 200 mT. After plotting the T_c as a function of external magnetic field we extract $H_{c2}(0)$ = 220 mT by fitting

$$H_{c2}(T) = H_{c2}(0)\left(1 - \left(\frac{T}{T_c(0)}\right)^2\right). \tag{7.5}$$

From the relation $H_{c2} = \frac{\phi_0}{2\pi\xi^2}$ where ϕ_0 is the flux quantum, we know that $\xi(T=0)$ = 38.7 nm. At T = 750 mK, the temperature at which we collected our data, ξ = 57.4 nm due to the temperature scaling of the coherence length, $\xi(T) = \xi_0\left(1 - \frac{T}{T_c}\right)^{-1/2}$.

Current vs. voltage (I-V) relation contains information about the nature of the superconductivity in a sample. Therefore we have taken I-V's as well as the differential resistances ($\frac{dV}{dI}$) at various temperatures and magnetic fields. The I-V's in the absence of external magnetic fields show non-linear relation with a flat zero-voltage drop trace as expected from a superconductor (see Fig. 7.19a). As the magnetic field is increased, the micro-bridge becomes more dissipative and the I-V relation approaches a linear, Ohm's law behavior. Using the I-V relation and the $\frac{dV}{dI}$ relation in Fig. 7.19a (top and bottom) the $\frac{dV}{dI}$ as a function of V is plotted in Fig. 7.19b. In Fig. 7.19c, a single cross section of the heat map in Fig. 7.19b is plotted on top and a zoom-in of it is plotted below.

There are many sharp changes in the slope of the I-V which manifest as sharp peaks and troughs in the $\frac{dV}{dI}$ vs. I as well as $\frac{dV}{dI}$ vs. V. Since the microbridge has a width that is a multiple times larger than ξ, we expect that these features are not due to the Andreev reflections but rather due to domains of dissipation in the superconducting microbridge. There have been many reports on kinks in the I-Vs of superconducting microbridges since the 1970s [69–73]. The dimensions of those microbridges are comparable to our device, therefore we expect that similar "hot spots" occur in our microbridge causing paths of dissipation.

After characterizing the microbridge, its coherence length and field dependence

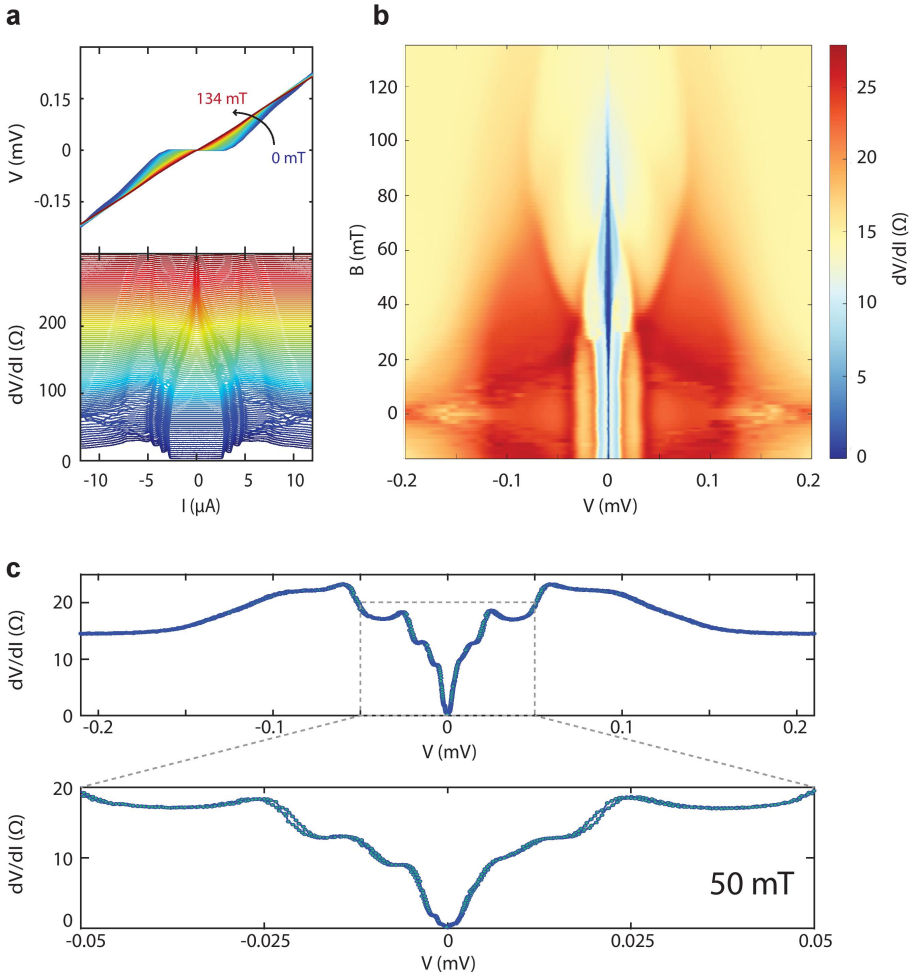

Figure 7.19: **a** I-V traces at 0 to 134 mT external fields (top) and $\frac{dV}{dI}$-I traces at 0 to 134 mT external fields displaced vertically for easier visualization (bottom). **b** Heat map of the $\frac{dV}{dI}$ as a function of voltage and external field. **c** $\frac{dV}{dI}$ as a function of bias voltage at 50 mT external field (top) and a zoom-in of the trace (bottom).

of the critical current I_c, we compare the results from our single crystal van der Waals superconductors to those of De Simoni *et al.* [58]. Using the side gates shown in Fig. 7.17a which are also made from the same flake, we apply electric fields in order to pinch off the supercurrent in the microbridge. Figure 7.20a-b show the I-V's and their corresponding $\frac{dV}{dI}$'s while applying various side gate voltages (V_s) at 0 mT and 100 mT. However, no significant changes in the I_c are observed even at $\pm$ 60 V. This can be clearly seen in Fig. 7.20c where I_c's are plotted as a function of V_s. There are small varations in the I_c's however, these variations are on the order

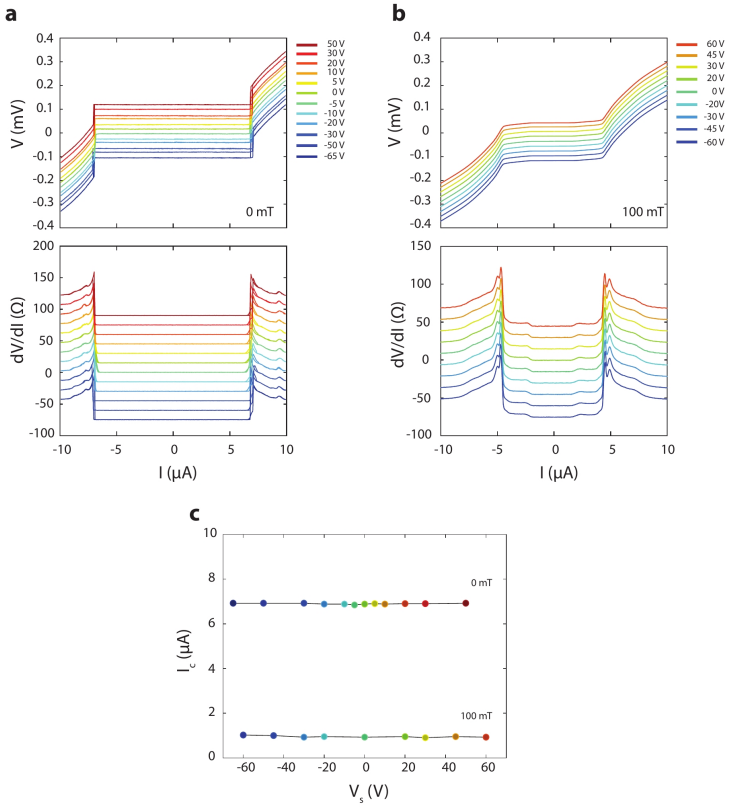

Figure 7.20: Independence to side gate. *I-V* traces (top) and $\frac{dV}{dI}$ (bottom) at various side gate voltages, taken with **a** in 0 mT external magnetic field and **b** 100 mT external magnetic field. Traces are displaced for visual aid. **c** Critical current plotted as a function of side gate voltage showing no effect.

of the leakage current we measured at ~ 0.5 nA/V_S. Similar independence to the side gate voltage are observed in all three of our 2H-TaS_2 devices.

In order to carefully compare the systems where the field tunability is observed with our devices, we list the relevant parameters in Table 7.1. Our device parameters are comparable to those listed in Ref. [58, 63, 64, 74–76] which all showed significant field tuning of the critical current. At the time of writing this thesis, our current hypothesis is that this is due to the difference in the crystallinity of our samples to theirs and the difference in material. In all of those devices reported, samples are fabricated by evaporation which means that the devices fabricated in this manner are highly polycrystalline with many grain boundaries. We speculate that the polycrystallinity could potentially have an impact on the superconducting

behavior of the devices, since every grain boundary is a center of broken crystal symmetry which could be susceptible to field effect. If this is the true, then the grain boundaries would behave as weak links, causing the entire device to become a mesh of many parallel S-s'-S which may be tuned to be S-n-S by field effect or oxidation. It has been demonstrated that granular superconductors behave as Josephson junction arrays, the critical current of which can be controlled by an external electric field [77, 78]. In our case, our bulk 2H-TaS_2 single crystals are synthetically grown and the flakes are mechanically exfoliated from bulk crystals. This ensures that the entire device, including the side gates themselves are made of a single crystal without any grain boundaries. In this picture, the electric field cannot penetrate into the superconductor to destroy the critical current.

Recently, works from Golokolenov *et al.* [75], Ritter *et al.* [74] and Alegria *et al.* [76] argued that the origin of the apparent suppression of the critical current through side gating is likely due to quasi particle excitation from highly energetic electrons leaking from the side gates into the superconducting bridge. In particular, Golokolenov *et al.* [75] showed a similar field effect tunability of the critical current in polycrystalline V devices that follow a Fowler-Nordheim field emission model. These works provide a step forward in understanding this controversial issue of field effect tunability in superconducting bridges. In contrast, our devices do not show any suppression of the critical current even when our leakage currents are nearly three orders of magnitude larger than those of De Simoni *et al.* and Golokolenov *et al.*, which suggests that the Fowler-Nordheim model alone is not sufficient to capture the overarching phenomena.

We believe that additional experiments should be conducted on non-layered single crystalline superconductors to confirm the effects of crystallinity and leakage currents on the suppression of the critical current. Due to the anisotropic nature of the superconducting order parameter in van der Waals superconductors, $\xi_{in-plane}$ are quite different to the $\xi_{out-of-plane}$. If this experiment is performed on a single crystalline, isotropic superconductor, then we would be able to directly compare the results to the works by De Simoni *et al.* which will shine light on the mechanism through which the field effect manifests. Additionally one should consider performing the gating experiments using ionic liquids which allows the application of high electric fields in the absence of the leakage of high energy electrons. If the critical current is unaffected while gating via ionic liquids, then the suppression seen by De Simoni *et al.* is likely due to high energy electrons from the gate leaking into the bridge as well. If the critical current is still suppressed while employing ionic liquid gating, then one can conclude that the suppression of the critical current can arise due the field effect through the grain boundaries.

	Ti[58]	Al [58]	V[62, 64]	Al-Cu-Al [63]	TiN[74]	V [75]	Ti [76]	2H-TaS_2 (this work)
T_c (K)	0.41	1.5	3.6	1.5	3.7	4.18	-	1-1.2
I_c (uA)	11	12	250	5.8	45	-	0.1	3-8
$\xi_{ab}(0)$ (nm)	100	63	-	-	-	40	-	38.7
λ_L (nm)	900	310	-	-	-	-	-	450
t (nm)	30	11	60	30	20	30	30	37-39.3
w (nm)	200	30	110	200	80	30	60	160-600
l (nm)	545	5000	180	800	2000	30	>1000	1000
R_N (Ω)	45	320	-	-	1600	-	1400	7-25
H_c (mT)	127	-	-	-	3.5		700	60-200
gate	both sides	back	single side	single side	single side	both sides	single side	both sides
I_{leak} (A)	$\sim 10^{-15}$	$\sim 10^{-11}$	-	$\sim 10^{-11}$	$\sim 10^{-7}$	$\sim 10^{-11}$	$\sim 10^{-10}$	$\sim 10^{-8}$
crystallinity	poly	poly	poly	poly	poly	poly	poly	single

Table 7.1: Comparison of the relevant parameters in Ref. [58, 63, 64, 74–76] to those of this work.

Appendix.

A. Methods

Device fabrication

A flake of 2H-TaS_2 and subsequently, hBN are transferred onto a pre-patterned sapphire substrate using polydimethyl siloxane (PDMS) [11] (Fig. A.1a). Positive e-beam resist (PMMA) and electron discharge layer (Electra 92) are spincoated on the sample. Using Raith EBPG 5000+ at 100 keV, electrode pattern is exposed. After development, the sample is subjected to a gentle Ar mill, which removes the hBN and exposes the 2H-TaS_2. The sample is then moved to an evaporation chamber without breaking the vacuum, where Cr/Au (1 nm/ 65 nm) are evaporated (Fig. A.1b). PMMA/ Electra are spincoated once more for the second e-beam exposure which defines the etch mask. Using the same Ar milling system, the device is milled into the bridge shape (Fig. A.1c). Figure A.1d shows a scanning electron microscopy image (also with a layer of Electra) of one of the devices (device 1).

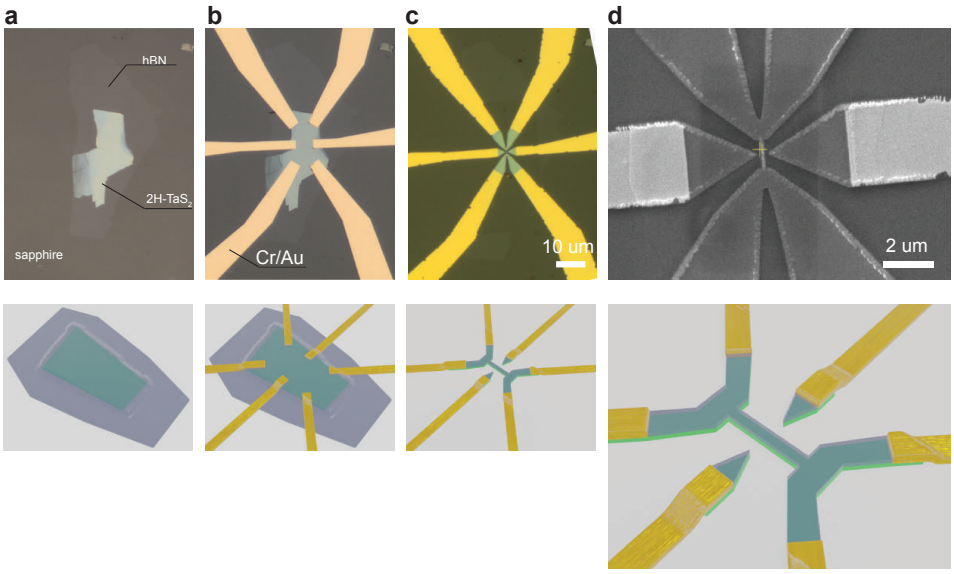

Figure A.1: Microscopy images (top) and corresponding illustration (bottom) of the fabrication procedure. **a** A 37 nm thick flake of 2H-TaS_2 is stamped on sapphire and encapsulated with 16 nm hBN. **b** After e-beam lithography and Ar milling, electrodes are deposited on 2H-TaS_2. **c** Using e-beam lithography and Ar milling, the flake is defined into the bridge shape. **d** Scanning electron microscopy image of the device after completing the fabrication procedure.

B. Measurement

RT

After fabrication, the samples are cooled down in a Leiden cryogenic dilution fridge. The resistance is measured while cooling down, to detect the superconducting tran-

sition. A lock-in technique sourcing 100 nA at 17.777 Hz in the circuit configuration shown in Fig. 1 of the main text is used.

I-V and *dV/dI-V*

Once at a set temperature, a d.c. current is sourced and a digital multimeter (DMM) is used to read the d.c. voltage drop across the bridge. In addition to the d.c., a small a.c. current from a lock-in at 77.777 Hz is used to simultaneously measure the dV/dI. Gate voltages are applied using Keithley 2410 high voltage source meter.

C. Superconducting transition of devices 1-3

In this section, the characterization results of all three devices are presented. In Fig. C.1, SEM images of each devices and their superconducting transitions are shown. All three devices have T_c of ~1 K which is slightly higher than those reported [68, 79]. The device geometry including the bridge width and the distance to the side gates are listed in Table 7.1. $I-V$ and dV/dI characterizations of individual devices are presented in respective subsections.

	Flake Thickness	Bridge Length	Bridge Width	Distance to gate	T_c	T_{IV}	T_{gate}
Dev 1	37 nm	1 µm	150 nm	150 nm	1.25 K	1 K	0.92 K
Dev 2	39.3 nm	1 µm	300 nm	355 nm	1.01 K	0.75 K	0.6 K
Dev 3	39.3 nm	1 µm	434 nm	425 nm	1.07 K	0.8 K	0.7 K

Table 7.1: Geometries and T_c of all three devices. T_{IV} refers to the temperatures at which the magnetic field dependence of $I-V$ and dV/dI are taken. T_{gate} refers to the temperature at which the gate dependence measurements of $I-V$ and dV/dI are taken

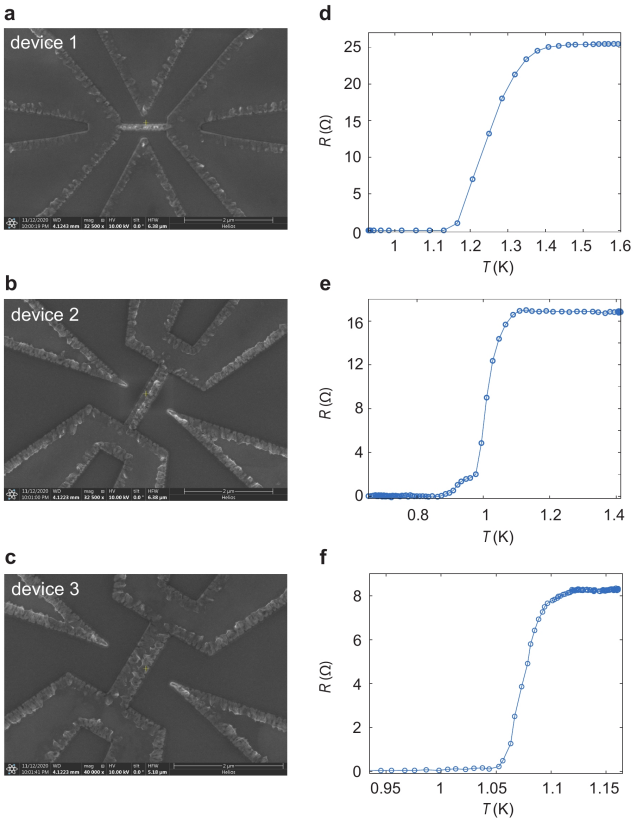

Figure C.1: **a-c** Scanning electron microscopy (SEM) images of devices 1,2 and 3 each with varying bridge dimensions. **d-f** *R-T* plots of corresponding devices showing the superconducting transitions.

Characterization of device 1

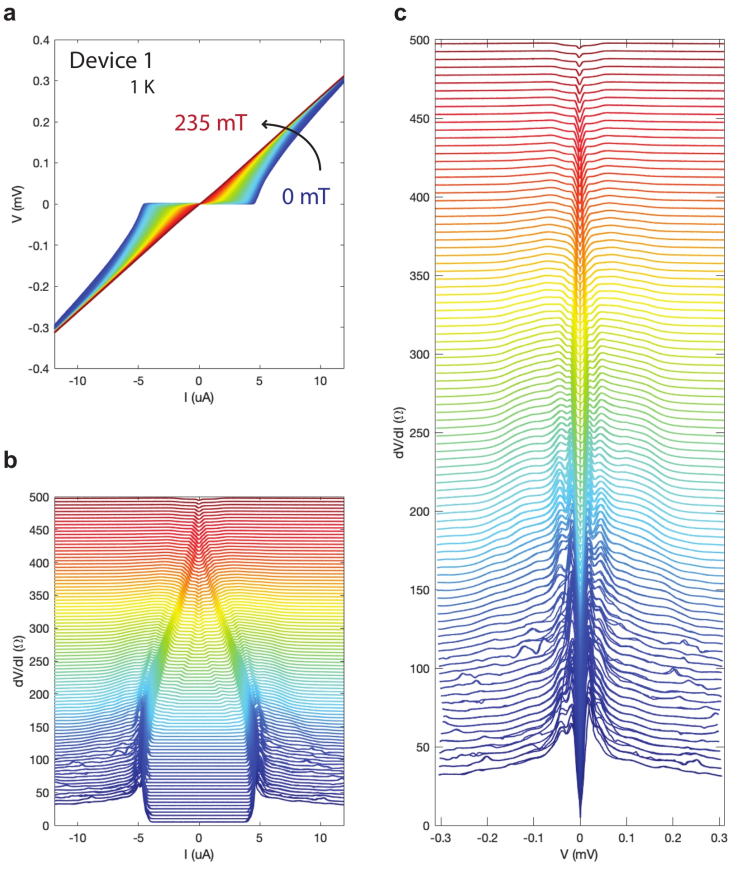

Figure C.2: *I-V* and dV/dI characterization of device 1. **a** $I-V$ as a function of magnetic field. **b** Differential resistance dV/dI vs. I at various magnetic fields. Plots are displaced vertically for better visualization. **c** dV/dI vs voltage derived from **b**.

Characterization of device 2

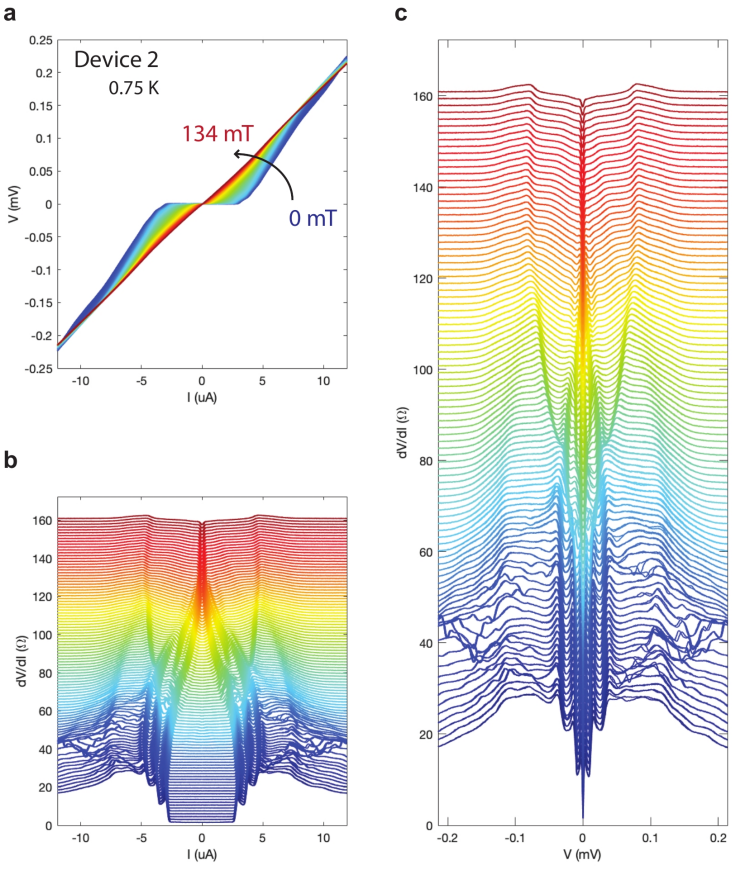

Figure C.3: *I-V* and dV/dI characterization of device 2. **a** $I-V$ as a function of magnetic field. **b** Differential resistance dV/dI vs. I at various magnetic fields. Plots are displaced vertically for better visualization. **c** dV/dI vs voltage derived from **b**.

Characterization of device 3

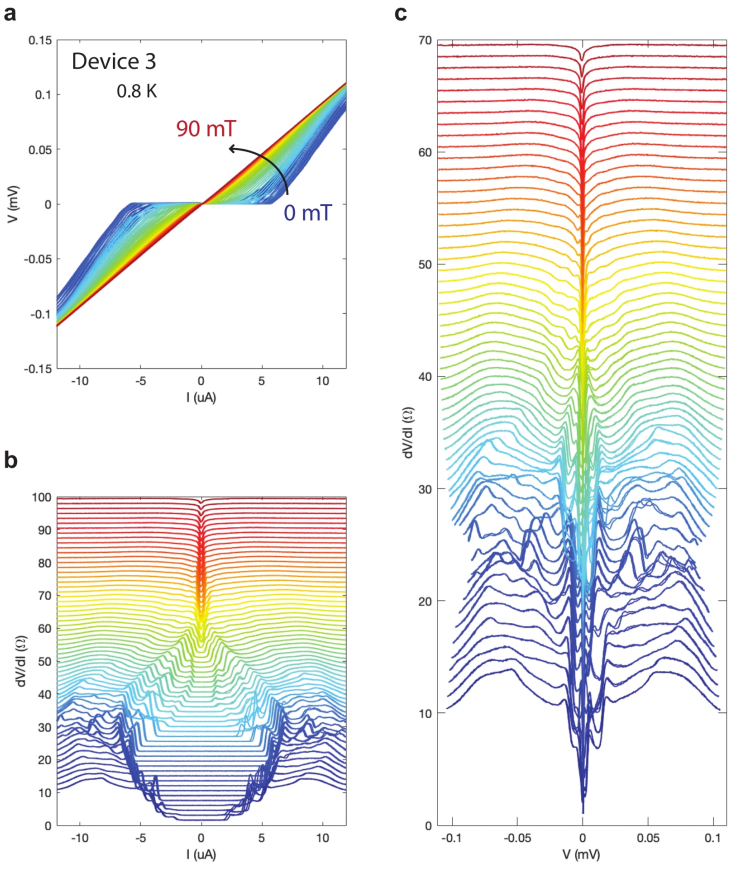

Figure C.4: *I-V* and dV/dI characterization of device 1. **a** $I-V$ as a function of magnetic field. **b** Differential resistance dV/dI vs. I at various magnetic fields. Plots are displaced vertically for better visualization. **c** dV/dI vs voltage derived from **b**.

D. Excess current

In this section, we extract the excess current I_{exc}, which is often associated with a weak link behavior, from devices 1-3 and plot their behavior as a function of external magnetic field. Figure D.1 shows $I-V$(top) and dV/dI-I plots (bottom) of device 1 at 1 K subjected to external magnetic fields of 0 mT, 95 mT and 157 mT. Using the extreme values, linear fits are performed in both the negative and positive regions. Where this line crosses the x-intercept is often referred to as I_{exc}. It can be observed that I_{exc} decreases with an applied magnetic field. The I_{exc} values at each magnetic field are extracted for each device and plotted in Fig. D.2.

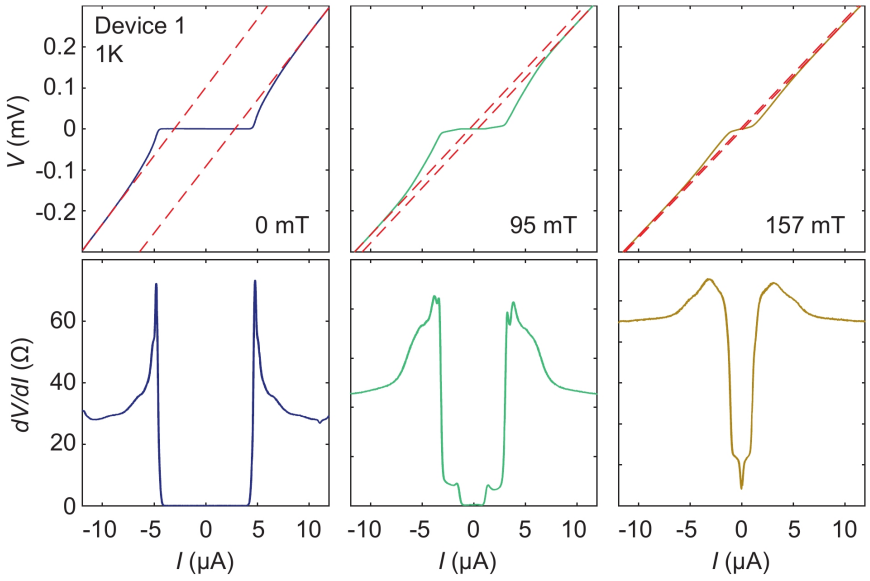

Figure D.1: Excess current in device 1 changing with external magnetic field. Top: $I-V$ plots. Dashed red lines indicate the line fits showing the excess current at the x-intercept. Bottom: Corresponding dV/dI-I plots.

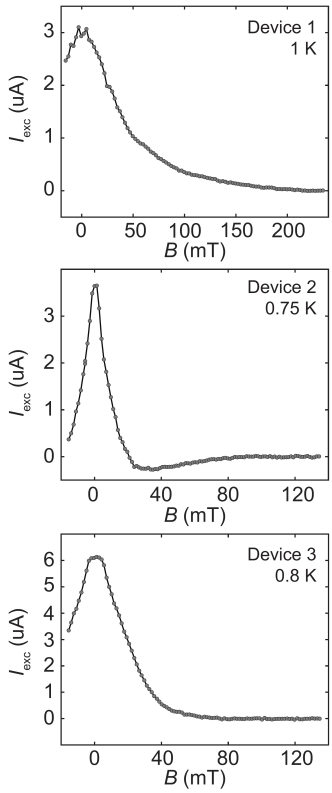

Figure D.2: Magnetic field dependence of I_{exc} in device 1 (top), device 2 at (middle) and device 3 at (bottom).

E. Gate independence devices 2,3

In the main text, we presented the results of independence to gate in device 1, which has the narrowest bridge width and the smallest gap (Table 7.1). In this section, the gate-independence of I_c in devices 2 and 3 are presented. In Fig. E.1a $I-V$ and dV/dI-I of device 2 at 50 mT and 0.6 K are shown. Gate voltages ranging from -60 V to 60 V are applied yet there is negligible differences between the plots. Similar data from device 3 at 0 mT and 0.7 K are shown in Fig. E.1b. Likewise, gate voltages from -40 V to 40 V are applied, but does not show noticeable differences between the plots.

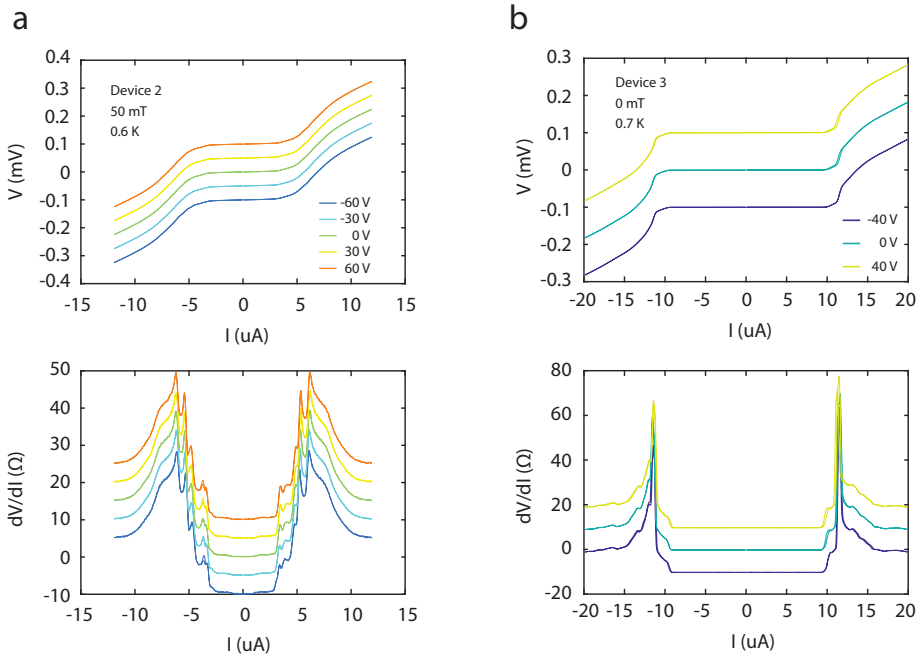

Figure E.1: Gate independence of the critical current in devices 2 and 3. Top: $I-V$ at various side gate voltages. Bottom: dV/dI-I at various side gate voltages. **a** Device 2 at 50 mT. **b** Device 3 at 0 mT. Plots are displaced vertically for easier visualization.

References

[1] D. Lu, D. J. Baek, S. S. Hong, L. F. Kourkoutis, Y. Hikita, and H. Y. Hwang, "Synthesis of freestanding single-crystal perovskite films and heterostructures by etching of sacrificial water-soluble layers," *Nature materials*, vol. 15, no. 12, pp. 1255–1260, 2016.

[2] D. Ji, S. Cai, T. R. Paudel, H. Sun, C. Zhang, L. Han, Y. Wei, Y. Zang, M. Gu, Y. Zhang, *et al.*, "Freestanding crystalline oxide perovskites down to the monolayer limit," *Nature*, vol. 570, no. 7759, pp. 87–90, 2019.

[3] H. S. Kum, H. Lee, S. Kim, S. Lindemann, W. Kong, K. Qiao, P. Chen, J. Irwin, J. H. Lee, S. Xie, *et al.*, "Heterogeneous integration of single-crystalline complex-oxide membranes," *Nature*, vol. 578, no. 7793, pp. 75–81, 2020.

[4] V. Harbola, S. Crossley, S. S. Hong, D. Lu, Y. A. Birkhölzer, Y. Hikita, and H. Y. Hwang, "Strain gradient elasticity in $SrTiO_3$ membranes: Bending versus stretching," *Nano letters*, vol. 21, no. 6, pp. 2470–2475, 2021.

[5] S. S. Hong, M. Gu, M. Verma, V. Harbola, B. Y. Wang, D. Lu, A. Vailionis, Y. Hikita, R. Pentcheva, J. M. Rondinelli, and H. Y. Hwang, "Extreme tensile strain states in $La_{0\cdot7}Ca_{0\cdot3}MnO_3$ membranes," *Science*, vol. 368, no. 6486, pp. 71–76, 2020.

[6] R. Xu, J. Huang, E. S. Barnard, S. S. Hong, P. Singh, E. K. Wong, T. Jansen, V. Harbola, J. Xiao, B. Y. Wang, S. Crossley, D. Lu, S. Liu, and H. H. Y., "Strain-induced room-temperature ferroelectricity in $SrTiO_3$ membranes," *Nature communications*, vol. 11, no. 1, pp. 1–8, 2020.

[7] B. Peng, R.-C. Peng, Y.-Q. Zhang, G. Dong, Z. Zhou, Y. Zhou, T. Li, Z. Liu, Z. Luo, S. Wang, *et al.*, "Phase transition enhanced superior elasticity in freestanding single-crystalline multiferroic $BiFeO_3$ membranes," *Science advances*, vol. 6, no. 34, p. eaba5847, 2020.

[8] D. Davidovikj, D. J. Groenendijk, A. M. R. Monteiro, A. Dijkhoff, D. Afanasiev, M. Šiškins, M. Lee, Y. Huang, E. van Heumen, H. S. J. van der Zant, *et al.*, "Ultrathin complex oxide nanomechanical resonators," *Communications Physics*, vol. 3, no. 1, pp. 1–6, 2020.

[9] N. Manca, G. Mattoni, M. Pelassa, W. J. Venstra, H. S. J. van der Zant, and A. D. Caviglia, "Large tunability of strain in WO_3 single-crystal microresonators controlled by exposure to H_2 gas," *ACS applied materials & interfaces*, vol. 11, no. 47, pp. 44438–44443, 2019.

[10] D. H. Blank, M. Dekkers, and G. Rijnders, "Pulsed laser deposition in twente: from research tool towards industrial deposition," *Journal of physics D: applied physics*, vol. 47, no. 3, p. 034006, 2013.

[11] A. Castellanos-Gomez, M. Buscema, R. Molenaar, V. Singh, L. Janssen, H. S. J. Van Der Zant, and G. A. Steele, "Deterministic transfer of two-dimensional materials by all-dry viscoelastic stamping," *2D Materials*, vol. 1, no. 1, p. 011002, 2014.

[12] A. P. Mackenzie and Y. Maeno, "The superconductivity of Sr_2RuO_4 and the physics of spin-triplet pairing," *Reviews of Modern Physics*, vol. 75, no. 2, p. 657, 2003.

[13] Y. Maeno, S. Kittaka, T. Nomura, S. Yonezawa, and K. Ishida, "Evaluation of spin-triplet superconductivity in Sr_2RuO_4," *Journal of the Physical Society of Japan*, vol. 81, no. 1, p. 011009, 2011.

[14] A. P. Mackenzie, T. Scaffidi, C. W. Hicks, and Y. Maeno, "Even odder after twenty-three years: The superconducting order parameter puzzle of sr 2 ruo 4," *npj Quantum Materials*, vol. 2, no. 1, pp. 1–9, 2017.

[15] S. Benhabib, C. Lupien, I. Paul, L. Berges, M. Dion, M. Nardone, A. Zitouni, Z. Q. Mao, Y. Maeno, A. Georges, *et al.*, "Ultrasound evidence for a two-component superconducting order parameter in Sr_2RuO_4," *Nature physics*, vol. 17, no. 2, pp. 194–198, 2021.

[16] S. Ghosh, A. Shekhter, F. Jerzembeck, N. Kikugawa, D. A. Sokolov, M. Brando, A. P. Mackenzie, C. W. Hicks, and B. J. Ramshaw, "Thermodynamic evidence for a two-component superconducting order parameter in Sr_2RuO_4," *Nature Physics*, vol. 17, no. 2, pp. 199–204, 2021.

[17] A. P. Mackenzie, J. A. N. Bruin, R. A. Borzi, A. W. Rost, and S. A. Grigera, "Quantum criticality and the formation of a putative electronic liquid crystal in $Sr_3Ru_2O_7$," *Physica C: Superconductivity*, vol. 481, pp. 207–214, 2012.

[18] J. J. Randall and R. Ward, "The preparation of some ternary oxides of the platinum metals," *Journal of the American Chemical Society*, vol. 81, no. 11, pp. 2629–2631, 1959.

[19] A. Callaghan, C. W. Moeller, and R. Ward, "Magnetic interactions in ternary ruthenium oxides," *Inorganic Chemistry*, vol. 5, no. 9, pp. 1572–1576, 1966.

[20] B. Sohn, B. Kim, S. Y. Park, H. Y. Choi, J. Y. Moon, T. Choi, Y. J. Choi, T. W. Noh, H. Zhou, S. H. Chang, *et al.*, "Emergence of robust 2d skyrmions in $SrRuO_3$ ultrathin film without the capping layer," *arXiv preprint arXiv:1810.01615*, 2018.

[21] D. J. Groenendijk, C. Autieri, T. C. van Thiel, W. Brzezicki, J. R. Hortensius, D. Afanasiev, N. Gauquelin, P. Barone, K. H. W. van den Bos, S. van Aert, *et al.*, "Berry phase engineering at oxide interfaces," *Physical Review Research*, vol. 2, no. 2, p. 023404, 2020.

[22] G. Kimbell, P. M. Sass, B. Woltjes, E. K. Ko, T. W. Noh, W. Wu, and J. W. A. Robinson, "Two-channel anomalous hall effect in $SrRuO_3$," *Physical Review Materials*, vol. 4, no. 5, p. 054414, 2020.

[23] L. Wang, Q. Feng, H. G. Lee, E. K. Ko, Q. Lu, and T. W. Noh, "Controllable thickness inhomogeneity and berry curvature engineering of anomalous Hall effect in $SrRuO_3$ ultrathin films," *Nano letters*, vol. 20, no. 4, pp. 2468–2477, 2020.

[24] J. Matsuno, N. Ogawa, K. Yasuda, F. Kagawa, W. Koshibae, N. Nagaosa, Y. Tokura, and M. Kawasaki, "Interface-driven topological Hall effect in $SrRuO_3$-$SrIrO_3$ bilayer," *Science Advances*, vol. 2, no. 7, p. e1600304, 2016.

[25] L. Wang, Q. Feng, Y. Kim, R. Kim, K. H. Lee, S. D. Pollard, Y. J. Shin, H. Zhou, W. Peng, D. Lee, *et al.*, "Ferroelectrically tunable magnetic skyrmions in ultrathin oxide heterostructures," *Nature materials*, vol. 17, no. 12, pp. 1087–1094, 2018.

[26] G. Koster, L. Klein, W. Siemons, G. Rijnders, J. S. Dodge, C.-B. Eom, D. H. A. Blank, and M. R. Beasley, "Structure, physical properties, and applications of $SrRuO_3$ thin films," *Reviews of Modern Physics*, vol. 84, no. 1, p. 253, 2012.

[27] F. Pizzocchero, L. Gammelgaard, B. S. Jessen, J. M. Caridad, L. Wang, J. Hone, P. Bøggild, and T. J. Booth, "The hot pick-up technique for batch assembly of van der waals heterostructures," *Nature communications*, vol. 7, no. 1, pp. 1–10, 2016.

[28] K. Kim, M. Yankowitz, B. Fallahazad, S. Kang, H. C. P. Movva, S. Huang, S. Larentis, C. M. Corbet, T. Taniguchi, K. Watanabe, *et al.*, "van der waals heterostructures with high accuracy rotational alignment," *Nano letters*, vol. 16, no. 3, pp. 1989–1995, 2016.

[29] M. Schultz, S. Levy, J. W. Reiner, and L. Klein, "Magnetic and transport properties of epitaxial films of $SrRuO_3$ in the ultrathin limit," *Physical Review B*, vol. 79, no. 12, p. 125444, 2009.

[30] Y. Kats, I. Genish, L. Klein, J. W. Reiner, and M. Beasley, "Large anisotropy in the paramagnetic susceptibility of $SrRuO_3$ films," *Physical Review B*, vol. 71, no. 10, p. 100403, 2005.

[31] F. Bern, M. Ziese, A. Setzer, E. Pippel, D. Hesse, and I. Vrejoiu, "Structural, magnetic and electrical properties of $SrRuO_3$ films and $SrRuO_3$/$SrTiO_3$ superlattices," *Journal of Physics: Condensed Matter*, vol. 25, no. 49, p. 496003, 2013.

[32] Š. Masys and V. Jonauskas, "A first-principles study of structural and elastic properties of bulk $SrRuO_3$," *The Journal of chemical physics*, vol. 139, no. 22, p. 224705, 2013.

[33] T. Kiyama, K. Yoshimura, K. Kosuge, Y. Ikeda, and Y. Bando, "Invar effect of srru o 3: Itinerant electron magnetism of ru 4 d electrons," *Physical Review B*, vol. 54, no. 2, p. R756, 1996.

[34] C. 'E. d. Guillaume, "Research on nickel steels. expansion at high temperatures; electrical resistance," *CR Acad. Sci*, vol. 125, no. 235, p. 18, 1897.

[35] M. van Schilfgaarde, I. A. Abrikosov, and B. Johansson, "Origin of the invar effect in iron–nickel alloys," *Nature*, vol. 400, no. 6739, pp. 46–49, 1999.

[36] A. Grutter, F. Wong, E. Arenholz, M. Liberati, and Y. Suzuki, "Enhanced magnetization in epitaxial $SrRuO_3$ thin films via substrate-induced strain," *Journal of Applied Physics*, vol. 107, no. 9, p. 09E138, 2010.

[37] J. Liu, Y. Feng, R. Tang, R. Zhao, J. Gao, D. Shi, and H. Yang, "Mechanically tunable magnetic properties of flexible $SrRuO_3$ epitaxial thin films on mica substrates," *Advanced Electronic Materials*, vol. 4, no. 4, p. 1700522, 2018.

[38] P.-H. Xiang, N. Zhong, C.-G. Duan, X. Tang, Z. G. Hu, P. X. Yang, Z. Q. Zhu, and J. H. Chu, "Strain controlled metal-insulator transition in epitaxial $NdNiO_3$ thin films," *Journal of applied Physics*, vol. 114, no. 24, p. 243713, 2013.

[39] G. Yong, R. M. Kolagani, S. Adhikari, W. Vanderlinde, Y. Liang, K. Muramatsu, and S. Friedrich, "Thermal stability of $SrTiO_3/SiO_2/Si$ interfaces at intermediate oxygen pressures," *Journal of Applied Physics*, vol. 108, no. 3, p. 033502, 2010.

[40] O. Matsuda, M. C. Larciprete, R. L. Voti, and O. B. Wright, "Fundamentals of picosecond laser ultrasonics," *Ultrasonics*, vol. 56, pp. 3–20, 2015.

[41] R. J. Dolleman, D. Davidovikj, S. J. Cartamil-Bueno, H. S. van der Zant, and P. G. Steeneken, "Graphene squeeze-film pressure sensors," *Nano letters*, vol. 16, no. 1, pp. 568–571, 2016.

[42] L. Veyrat, C. Déprez, A. Coissard, X. Li, F. Gay, K. Watanabe, T. Taniguchi, Z. Han, B. A. Piot, H. Sellier, *et al.*, "Helical quantum hall phase in graphene on $SrTiO_3$," *Science*, vol. 367, no. 6479, pp. 781–786, 2020.

[43] W. Qing-Yan, L. Zhi, Z. Wen-Hao, Z. Zuo-Cheng, Z. Jin-Song, L. Wei, D. Hao, O. Yun-Bo, D. Peng, C. Kai, *et al.*, "Interface-induced high-temperature superconductivity in single unit-cell fese films on $SrTiO_3$," *Chinese Physics Letters*, vol. 29, no. 3, p. 037402, 2012.

[44] J. Hu, J. Gou, M. Yang, G. J. Omar, J. Tan, S. Zeng, Y. Liu, K. Han, Z. Lim, Z. Huang, *et al.*, "Room-temperature colossal magnetoresistance in terraced single-layer graphene," *Advanced Materials*, vol. 32, no. 37, p. 2002201, 2020.

[45] S. A. Lee, J.-Y. Hwang, E. S. Kim, S. W. Kim, and W. S. Choi, "Highly oriented $SrTiO_3$ thin film on graphene substrate," *ACS applied materials & interfaces*, vol. 9, no. 4, pp. 3246–3250, 2017.

[46] H. Miyazaki, S. Odaka, T. Sato, S. Tanaka, H. Goto, A. Kanda, K. Tsukagoshi, Y. Ootuka, and Y. Aoyagi, "Inter-layer screening length to electric field in thin graphite film," *Applied Physics Express*, vol. 1, no. 3, p. 034007, 2008.

[47] R. J. Dolleman, D. Davidovikj, H. S. J. van der Zant, and P. G. Steeneken, "Amplitude calibration of 2D mechanical resonators by nonlinear optical transduction," *Applied Physics Letters*, vol. 111, no. 25, p. 253104, 2017.

[48] J. Lee, Z. Wang, K. He, R. Yang, J. Shan, and P. X.-L. Feng, "Electrically tunable single-and few-layer MoS_2 nanoelectromechanical systems with broad dynamic range," *Science advances*, vol. 4, no. 3, p. eaao6653, 2018.

[49] C. J. Shearer, A. D. Slattery, A. J. Stapleton, J. G. Shapter, and C. T. Gibson, "Accurate thickness measurement of graphene," *Nanotechnology*, vol. 27, no. 12, p. 125704, 2016.

[50] L. Tian, A. Vasudevarao, A. N. Morozovska, E. A. Eliseev, S. V. Kalinin, and V. Gopalan, "Quantitative piezoelectric force microscopy: Influence of tip shape, size, and contact geometry on the nanoscale resolution of an antiparallel ferroelectric domain wall," *arXiv preprint arXiv:0802.2900*, 2008.

[51] J. Y. Jo, Y. S. Kim, T. W. Noh, J.-G. Yoon, and T. K. Song, "Coercive fields in ultrathin $BaTiO_3$ capacitors," *Applied physics letters*, vol. 89, no. 23, p. 232909, 2006.

[52] Y. Gagou, J. Belhadi, B. Asbani, M. El Marssi, J.-L. Dellis, Y. I. Yuzyuk, I. P. Raevski, and J. F. Scott, "Intrinsic dead layer effects in relaxed epitaxial $BaTiO_3$ thin film grown by pulsed laser deposition," *Materials & Design*, vol. 122, pp. 157–163, 2017.

[53] L.-W. Chang, M. Alexe, J. F. Scott, and J. M. Gregg, "Settling the "dead layer" debate in nanoscale capacitors," *Advanced Materials*, vol. 21, no. 48, pp. 4911–4914, 2009.

[54] X. L. Li, B. Chen, H. Y. Jing, H. B. Lu, B. R. Zhao, Z. H. Mai, and Q. J. Jia, "Experimental evidence of the "dead layer" at $Pt/BaTiO_3$ interface," *Applied Physics Letters*, vol. 87, no. 22, p. 222905, 2005.

[55] M. E. Lines and A. M. Glass, *Principles and applications of ferroelectrics and related materials*. Oxford university press, 2001.

[56] S. Tanifuji, Y. Aota, S. Kameda, T. Takagi, and K. Tsubouchi, "Discussion of millimeter wave FBAR with very thin AlN film fabricated using MOCVD method," in *2009 IEEE International Ultrasonics Symposium*, pp. 2170–2173, IEEE, 2009.

[57] T. Ishidate and S. Sasaki, "Coupled acoustic modes in tetragonal $BaTiO_3$," *Journal of the Physical Society of Japan*, vol. 56, no. 12, pp. 4214–4217, 1987.

[58] G. De Simoni, F. Paolucci, P. Solinas, E. Strambini, and F. Giazotto, "Metallic supercurrent field-effect transistor," *Nature nanotechnology*, vol. 13, no. 9, pp. 802–805, 2018.

[59] A. D. Caviglia, S. Gariglio, N. Reyren, D. Jaccard, T. Schneider, M. Gabay, S. Thiel, G. Hammerl, J. Mannhart, and J.-M. Triscone, "Electric field control of the $LaAlO_3/SrTiO_3$ interface ground state," *Nature*, vol. 456, no. 7222, pp. 624–627, 2008.

[60] Y. Cao, V. Fatemi, S. Fang, K. Watanabe, T. Taniguchi, E. Kaxiras, and P. Jarillo-Herrero, "Unconventional superconductivity in magic-angle graphene superlattices," *Nature*, vol. 556, no. 7699, pp. 43–50, 2018.

[61] E. Sajadi, T. Palomaki, Z. Fei, W. Zhao, P. Bement, C. Olsen, S. Luescher, X. Xu, J. A. Folk, and D. H. Cobden, "Gate-induced superconductivity in a monolayer topological insulator," *Science*, vol. 362, no. 6417, pp. 922–925, 2018.

[62] F. Paolucci, G. De Simoni, P. Solinas, E. Strambini, C. Puglia, N. Ligato, and F. Giazotto, "Field-effect control of metallic superconducting systems," *AVS Quantum Science*, vol. 1, no. 1, p. 016501, 2019.

[63] G. De Simoni, F. Paolucci, C. Puglia, and F. Giazotto, "Josephson field-effect transistors based on all-metallic Al/Cu/Al proximity nanojunctions," *ACS nano*, vol. 13, no. 7, pp. 7871–7876, 2019.

[64] C. Puglia, G. De Simoni, N. Ligato, and F. Giazotto, "Vanadium gate-controlled josephson half-wave nanorectifier," *Applied Physics Letters*, vol. 116, no. 25, p. 252601, 2020.

[65] M. Rocci, G. De Simoni, C. Puglia, D. D. Esposti, E. Strambini, V. Zannier, L. Sorba, and F. Giazotto, "Gate-controlled suspended titanium nanobridge supercurrent transistor," *ACS nano*, vol. 14, no. 10, pp. 12621–12628, 2020.

[66] X. Xi, L. Zhao, Z. Wang, H. Berger, L. Forró, J. Shan, and K. F. Mak, "Strongly enhanced charge-density-wave order in monolayer $NbSe_2$," *Nature nanotechnology*, vol. 10, no. 9, pp. 765–769, 2015.

[67] L. S. Farrar, M. Bristow, A. A. Haghighirad, A. McCollam, S. J. Bending, and A. I. Coldea, "Suppression of superconductivity and enhanced critical field anisotropy in thin flakes of FeSe," *npj Quantum Materials*, vol. 5, no. 1, pp. 1–7, 2020.

[68] E. Navarro-Moratalla, J. O. Island, S. Manas-Valero, E. Pinilla-Cienfuegos, A. Castellanos-Gomez, J. Quereda, G. Rubio-Bollinger, L. Chirolli, J. A. Silva-Guillén, N. Agraït, *et al.*, "Enhanced superconductivity in atomically thin TaS_2," *Nature communications*, vol. 7, no. 1, pp. 1–7, 2016.

[69] T. M. Klapwijk and T. B. Veenstra, "Superconducting Al microbridges with reduced self-heating," *Physics Letters A*, vol. 47, no. 5, pp. 351–352, 1974.

[70] M. Octavio, W. Skocpol, and M. Tinkham, "Improved performance of tin variable-thickness superconducting microbridges," *IEEE Transactions on Magnetics*, vol. 13, no. 1, pp. 739–742, 1977.

[71] A. J. Rimberg, T. R. Ho, C. Kurdak, J. Clarke, K. L. Campman, and A. C. Gossard, "Dissipation-driven superconductor-insulator transition in a two-dimensional josephson-junction array," *Physical review letters*, vol. 78, no. 13, p. 2632, 1997.

[72] M. Stuivinga, T. M. Klapwijk, J. E. Mooij, and A. Bezuijen, "Self-heating of phase-slip centers," *Journal of low temperature physics*, vol. 53, no. 5, pp. 673–683, 1983.

[73] W. J. Skocpol, M. R. Beasley, and M. Tinkham, "Self-heating hotspots in superconducting thin-film microbridges," *Journal of Applied Physics*, vol. 45, no. 9, pp. 4054–4066, 1974.

[74] M. F. Ritter, A. Fuhrer, D. Z. Haxell, S. Hart, P. Gumann, H. Riel, and F. Nichele, "A superconducting switch actuated by injection of high-energy electrons," *Nature communications*, vol. 12, no. 1, pp. 1–6, 2021.

[75] I. Golokolenov, A. Guthrie, S. Kafanov, Y. A. Pashkin, and V. Tsepelin, "On the origin of the controversial electrostatic field effect in superconductors," *Nature Communications*, vol. 12, no. 1, pp. 1–7, 2021.

[76] L. D. Alegria, C. G. Bøttcher, A. K. Saydjari, A. T. Pierce, S. H. Lee, S. P. Harvey, U. Vool, and A. Yacoby, "High-energy quasiparticle injection into mesoscopic superconductors," *Nature Nanotechnology*, vol. 16, no. 4, pp. 404–408, 2021.

[77] T. S. Orlova, B. I. Smirnov, and J. Y. Laval, "Effect of an electric field on the i–v curves of $DyBa_2Cu_{3-x}O_y$/1 wt% Pt HTSC ceramics," *Physics of the Solid State*, vol. 43, no. 6, pp. 1007–1011, 2001.

[78] D. Domínguez, C. Wiecko, and J. V. José, "Critical current enhancement due to an electric field in a granular d-wave superconductor," *Physical review letters*, vol. 83, no. 20, p. 4164, 1999.

[79] J. A. Wilson, F. Di Salvo, and S. Mahajan, "Charge-density waves and superlattices in the metallic layered transition metal dichalcogenides," *Advances in Physics*, vol. 24, no. 2, pp. 117–201, 1975.

8

8

Conclusion

This thesis deals with both the applications and fundamental studies of van der Waals and complex oxide membranes. In this chapter, we summarize the key results from individual chapters and the outlook.

8.1. Introduction and Methods

We began by giving an overview of the field of 2D materials in Chapter 1 in both fundamental properties as well as their potential applications in microelectromechanical systems (MEMS).

In Chapter 2 we discussed the methods in which the 2D materials are fabricated in the lab. Various exfoliation and transfer methods are discussed. In the case of complex oxides, pulsed laser deposition is introduced as well as the recently developed technique of releasing epitaxially grown layers.

8.2. Application of Graphene in pressure sensing

Next we moved on to the application of graphene membranes in capacitive pressure sensors. In Chapter 3 we demonstrated the high performance capacitive pressure sensor made from two layers of graphene suspended over 10000 cavities in SiO_2/Si. Through modelling, we discovered that only a small fraction of the suspended graphene drums contribute to the pressure sensing. Although the yield of suspended graphene is nearly 99%, there are many pathways through which the gases move in and out of the cavities resulting in an actual yield of 25% of the 10000 drums actually contributing to the pressure sensing. Despite this, our graphene based pressure sensor out-performed the state-of-the-art silicon based pressure sensor per area.

In Chapter 4 we addressed the issue of leakage in suspended graphene devices. By studying the leakage time constant extracted from the time-dependent resonance frequency of graphene membranes, we observed a leakage time constant on the order of 20 seconds immediately after the fabrication of the graphene drum. Using the sealing technique we developed, this leakage time constant increased by 4 orders of magnitude. This work demonstrated that capacitive pressures sensors made of graphene still have large room for improvements.

8.3. Fundamental studies of phase transitions by temperature dependent nanomechanics

In Chapter 5 and Chapter 6 we probed the phase transitions in antiferromagnetics 2D materials and charge density wave (CDW) materials.

In Chapter 5 we showed that the phase transition can be probed by measuring the temperature dependent resonance frequencies of suspended membranes. At the transition temperature, the resonance frequency shows discontinuities which arise due to the discontinuities in the thermal expansion coefficient. By careful analysis, we translated this into the specific heat. Finally using the back gate to electrostatically strain the membrane, we tuned the transition temperature of $FePS_3$.

In Chapter 6 the CDW transitions are studied more closely in 2H-TaS_2 and 2H-$TaSe_2$. Using the method from Chapter 5 we studied their phase transition as well as the effect of degradation on the transition temperature of 2H-TaS_2. Surprisingly we observed an enhancement of the transition temperature by more than 50 K by simply exposing the sample to air for prolonged durations thereby degrading the

crystal.

8.4. Outlook

The Outlook Chapter contains some of the currently on-going works which are yet to be published. These projects require more work in understanding and performing additional measurements in order to reach the publication stage.

The Outlook Chapter of this dissertation mainly deals with a new class of quasi-2D material; the free-standing complex oxides. We first characterized an itinerant ferromagnet, $SrRuO_3$ in its free-standing form using magnetotransport. After characterization we showed the effect of geometric deformation by using the Si substrate to electrostatically pull on the membrane.

Next, we tested the pressure sensing abilities of suspended complex oxides by measuring their pressure dependent resonance frequencies. We observed that by simply annealing in air, we are able to promote stronger chemical bonds between the substrate and the membrane causing a nearly hermetic seal. This self-sealing may be a key to improving the hermeticity of ultra thin pressure sensors.

Using 2D materials and free-standing complex oxides in a van der Waals heterostructure - to our knowledge - for the first time, we fabricated and characterized a bulk acoustic resonator working in the membrane mode. Using optothermal, electrostatic and piezoelectric excitations, we were able to vibrate the membrane. Unlike the other two excitation modes, we observe ferroelectric switching in the piezoelectrically driven case.

Finally we end the Outlook Chapter by showing the results of gate independence of supercurrent in single crystal monolithic micro bridges made from 2H-TaS_2 flakes. Recent discovery showed complete suppression of supercurrent in polycrystalline superconductors by field effect. In our work we tested this experiment on a single crystal superconductor of similar properties and showed that the supercurrent is unaffected by the side gates.

Acknowledgements

These four years have been the most intense years of my life. I spent incredible amounts of hours physically at work trying make use of this incredible opportunity as much as possible while I was at this incredible institute. TU Delft is world-famous for the world-class infrastructure, but what people may not know is that this institute has the world-class atmosphere and a collection of people who make it that way. If I were allowed, I would write many chapters about all the people I need to thank and that would probably outweigh the scientific content of this dissertation. Following is only the abstract, which - as in scientific writing - does not capture all the details.

I start this list with my two promotors who made it possible for me to pursue this PhD. I have been blessed with the best bosses ever. It took me a whole year to call you by your names instead of your titles, but **Peter** and **Herre**, I am grateful for your passionate supervision throughout the four years. Both of you have let me explore wild and perhaps useless ideas which you guys gave me plenty of signals of danger about. Still, you guys supported my decisions nonetheless and I was able to explore many different areas of condensed matter physics thanks to you. I've become a much better researcher through these successes and failures and I have you guys to thank!

Peter, to this day, I still wonder sometimes what made you hire me for this position. I thank the deities that aligned the stars, the lack of traffic in the morning and the good cup of coffee you had before sending me the offer that day. I didn't have much to show for during my masters, yet you gave this oblivious master student from half way across the world a chance to experience the wonderful life of doing a PhD in your group. I am grateful for your support, supervision and patience. I had multiple mental breakdowns during the later half of my degree, and talking to you always helped me realize that I am on a good track and I can finish on time. I am grateful that you always checked on my happiness first rather than the progress of my projects. You made me feel always welcomed for discussions regarding science or personal problems and made me feel like an important constituent of the group. Thanks to your impeccable leadership and genuine care towards every individual researcher, the groups in TNW and 3mE will flourish and produce many scientific breakthroughs.

Herre, it took me a while to realize that behind the critical scientific comments, you had genuine interest in the well being of your students. I am grateful that you spent the energy to respond to my emails during one of my mental breakdowns and immediately invited me for a chat the next morning to hear what I had to say. You have an amazing gift of finding the relevant questions and categorizing important facts from the not so important ones. You are awfully active for someone with a fully white hair. I hope you don't have any more accidents and hope you beat Peter

at tennis one day!

Next I would like to thank the people who had to comb through this dissertation, **the defence committee**. I am honoured and grateful to have the world experts on MEMS, 2D materials and complex oxides to evaluate my dissertation. I look forward to meet you all at my defence - albeit virtual. Here, I address the committee members in no particular order:

Harold, in our brief discussion during your visit to Delft, I was amazed that someone with such contributions to the scientific community could be so humble. Thank you for being the driving force of the field of complex oxides. In particular, I am a direct beneficiary of your work on free-standing complex oxides. My work will not have been possible without your discovery! Thank you for being on my committee and I'm sorry about the awkward timing of the defence.

Dear Professor **Sabina** (do you still not like me calling you that?). I had the pleasure of knowing you as a colleague and as a friend. Of all the projects we interacted on, SingaFun was the best! I'm grateful for the experiences I had with you both scientifically and abroad. I hope you become as nurturing of a Professor as you are in friendship. Thank you very much for taking the responsibility of being my committee member. Great wishes in building up your group.

Max, thank you for the great work you and your group is doing towards the graphene flagship. Whenever I give a presentation in Delft or abroad, it is always a pleasure to boast about all the different activities our work-package is doing - many of which are from your group. Thank you for accepting to be on the committee and I hope to see more crazy graphene based devices from your group!

Andres, the legendary post doc of QN. I have you to thank for inventing the transfer technique which was essential for this thesis. In the recent years we have collaborated during the quarantine and we have a few papers together! Working with you is always fun because you are such a creative scientist. Thank you for being one of my committee member. I hope we can keep in touch throughout the years!

Professor Sarro, although we have never met, you have kindly accepted to be on my defence committee. I hope I don't make you regret your decision! I look forward to our meeting.

Yaroslav thank you for enlightening me through discussions and meetings. I benefited so much from your expertise in several of my projects. We run into each other a lot during our coffee breaks and I'm going to miss that! Thank you for being the reserve member of my committee!

Again, I thank the committee members for taking your time to read my thesis and to examine me during the defence. My apologies for the weird defence time.

Next are my predecessors **Dejan** and **Robin**. You guys have been so productive during your PhD, I constantly found myself comparing myself to you. **Dejan** you are an amazing scientist with a warm and humanly personality. The scientific community is surely missing out with you in industry. Thanks for the free late night consultation, although you probably charge people a lot for that now. I hope the very best for you and Magdalena. **Robin**, you paper-writing machine! I can't be-

lieve you were able to write more than 10 first-author papers during your PhD while strictly working a nine-to-five schedule. Over the past few years I had the haunting image of your publications list to thank for driving myself so hard. I still think that I got less done in much more time... Good luck twisting your graphene!

Next, my scientific partner and office mate, **Makars**. We started on the very same day, and I am even a few years older than you but you have impressed me with your breadth of knowledge. Over the years, I felt that I learned a lot by talking to you, watching you work and bouncing off ideas on your big brain. We make a great team and have a lot of papers to show for it. No matter which path you take in academia, I believe you are going to be a successful PI. If you can't, there is no way that I can, so for my sake, please be successful! Best of luck in your Postdoc and I hope you enjoy SG as much as I have!

Maurits, **Gabriele** the new work horses of the Steeneken lab. You have very different backgrounds yet you have caught up to my level of understanding in a matter of half a year. You guys are critical thinkers, are already much better than me at simulations and are quickly becoming independent researchers. Your PhD paths look much brighter than mine so I hope you enjoy it just as I have mine!

Dong Hoon, you are a humble and modest scientist but I know that you have immense knowledge in your head. The pandemic has slowed down the rate of progress, but you will still have many exciting results. Don't work too hard though, your family needs to enjoy your company!

Next is my dear army of students. **Hugo** when you joined, I was an unprepared supervisor, but thankfully you did not need my fragile input as you quickly became an independent researcher. Your work on measuring gas permeation through nanopores in graphene has allowed us to publish the results in Nature Comms. Your work ethics (working long hours and even during the weekends) has put up a high standard for the other students who I've supervised. Outside of work you are such a hospitable person. I wish we had more beers after work. I hope industry is treating you well!

Rijk it was an interesting experience for me to supervise you. You must have had troubles being between two different groups during your MEP. In the end your contribution on making the hydrogen sensing setup has allowed continuation of the project. Good luck in the industry.

Roderick, I am so grateful that you are an independent researcher. You are hard working, get things done and everytime I meet you, you have new results to show. You are a very meticulous researcher and have a pleasant personality. I had the pleasure of being present during one of your eureka moments but you will have had the success even without my supervision. Good luck wrapping up your thesis!

Ulderico, you too-muscular-to-be-a-physicist physicist. We only worked on the project for a couple months together, but you have done so much in that two months. You have now started your PhD, and sounded a bit worried. But don't worry. You are way more knowledgeable than when I started my PhD and look! I'm about to finish it! I have no doubt that you will be successful and will get far.

Kasper, it's a shame that we just started working together as I write this. I think you have a beautiful project ahead of you and I hope I can still be of help.

Katya, technically you are not my student, but nonetheless, I enjoyed training you and working with you in the cleanroom. You are very humble of your knowledge and are very hard working. Sara still talks about our dinner together sometimes. You've made quite the impression on her!

Marnix, you were struggling in the beginning but at the end of your MEP, you managed to produce amazing results on graphene based microphones. Good luck in your next career path!

Bachelor projects are always a risk. They have to be accomplishable which is difficult to foresee in science. Unfortunately, **Otman**, your project was very difficult to start with, exfoliating monolayers of 3 atom thick crystals and stacking them together on top of a cavity. Luckily we changed the topic just in time for you to have some results to finish the degree with. I hope you still enjoyed working with complex oxides and the cryostat. **Tijmen** and **Willemijn**, your projects fortunately ended up in a publication, which is a part of this thesis as well. I am thankful for your contributions to the project!

Next, my collaborator on the other side of the campus, **Farbod**. I was able to witness your transition from assistant to associate professor and I have no doubt you will continue to be successful. You are a driven, passionate scientist and also understanding of the difficulties of experimental research. At the time, it was frustrating to fit the unfittable data even with your help, but in hindsight it is an enjoyable memory for me.

Abhilash, the guy doing all sorts of wavy maps with a cantilever! I hope the defence-preparation process is going smoothly for you. Good luck with the career after PhD!

Irek and **Ata**, you guys are amazing. I never can understand when you guys talk about mechanics, gas permeation, non-linear dynamics and magnetic levitation. This list keeps growing! You guys are already very strong scientists and you have your Nature Comms to prove it!

Ali I'm glad you are participating in the journal club. Looking forward to a theorist's perspective on the 2D materials!

Arthur, the theorist postdoc. I hope you have a fruitful postdoc period in Delft!

Hadi, welcome back to the mechanical side of graphene! Your presentation on wrinkled CVD graphene and ultra low E left quite an impression on me. I hope you have many papers working in DMN!.

Richard, as I told you before, during my first year, I was always wondering "who is that guy always asking the smartest questions during the werkbespreking?". You seemed to know everything! Starting from the QN Christmas potluck (which still hasn't returned), I got to know you a little better. It is always so nice to have a discussion with someone with such enthusiasm for science. I hope you hold on to it!

Andrea Cupertino, before you joined, I had the pleasure to have a look at your CV and I was quite intimidated by your experience. You have an impressive scientific history and you are on your way to make even more! Aside from the science, it's always a pleasure to talk to you about anything. After a couple years of frustrating cleanroom work, you are getting amazing results! Congrats and keep up the

good work!

Dongil, your work on using machine learning to optimize spider web resonators is impressive! Good luck with the publication process and I hope you enjoy your time in Delft!

Minxing, for someone with such a different background you are becoming a very strong experimentalist. You are working on many risky and exciting project. It's nice to see that you are coming up with very interesting solutions to your very difficult problems. Don't over work yourself and good luck!

Gerard, you are often very quiet, but when you speak, you ask the most critical questions. Whenever I needed your consultation on technical details or on supervising a BEP project, you didn't hesitate to lend your hand. Thank you for this. You've been getting a lot of recognition for your work in collaboration with ASML! Good luck with this exciting project and many other crazy projects!

Martin Robin you are a great scientist and a great person. You have a way to effortlessly communicate with co-workers which is an ability I lack. Together with **Ruben** we started collaborating on a project and I hope you and I can benefit from it!

Ruben you and Martin have built an amazing setup! I hope you can milk many many papers from it!.

Matthijs de Jong I'm looking forward to your superradiance to come to fruition! Enjoy the rest of your PhD!.

Curry, you are always so positive and always smiling even though you are working crazy hours. It's a pleasure to interact with you. You already have many interesting results and are writing two papers in your second year! You will have a successful PhD!

Amy, it was nice to develop a research direction with you. It was unfortunate that the project didn't finish as anticipated but I hope you still enjoyed your visit. I hope you are doing well back home.

Sten, one thing Robin said before leaving was "If you want to work and publish on realistic applications of graphene, you need to work with Sten" (paraphrased). It was true! Your work on transfer free graphene is ground breaking and will greatly benefit all of us one day. **Roberto**, I hope you are the one to initiate this graphene revolution! Best of luck and I hope the cleanroom tools never break while you are working on your projects.

Maria Roodenburg and **Dorine**, Peter's group runs smoothly thanks to your efforts. Thank you for all the nice interactions!

The plant-whisperer **Satadal**. Your work on Si photonics was very interesting. Your interview presentation left a strong impression on me. Now you are using those devices to talk to plants! Good luck on the remainder of your post-doc!

Masoud, I have so much respect for you for doing another Postdoc abroad while you already have a PI position and already lead a group at home. We had an interesting project together but unforunate circumstances have made it difficult for us to continue. I hope you enjoyed your postdoc experience and I hope your group in Iran appreciate having you back. Stay in touch!

Oscar, my friend, the expert cook of the Mexican cuisine (you told me you

cooked the Mole wrong, but it was still good!). I miss randomly running into you in the third floor corridor and in the cleanroom. I hope you are enjoying your new career in ASML!

Pascal you have left such a legacy in the van der Zant lab. I wish I had interacted with you much more while you were here. We still send each other interesting papers but it's not the same as bothering you in person. I hope you're ready for your life long career as a PI. You are great at managing multiple students, so I suspect that you will have no problem leading your new army of students!

Nikos the legendary one man research group! It's quite amazing how much you have accomplished during your PhD. Whenever someone asks me how to make devices, I tell them "ask Nikos" out of habit. You have taught me so much even though you are not my predecessor. Congratulations again on having Adam and I hope your career transitions are smooth.

Andrea Caviglia, the leader of the Quantum Foundry. I am grateful that you have let me explore the growth and measurement of free standing complex oxides. Through this experience, you provided your supervision, even though I am not a part of your group and involved me in several projects. It is always great to talk to you thanks to your positivity and enthusiasm for any minor results. Talking to you restarts the fire in my scientific engines. I am always in awe when you talk about condensed matter physics. I have made it my goal to one day understand all the things you say and hopefully hold an intellectual conversation about physics with you. You have an amazing group with amazing setups and hard working amazing people. I hope you keep up your scientific output!

Thierry my teacher, mentor and a friend. You have taught me how to grow my own samples using the PLD, how to say 'no' sometimes, how to use a cryostat and how to stay positive even through scientifically tough times. You have an incredible breadth of knowledge fit for much more than a PhD student and you have unbelievably long work hours far extending past mine. Academia will be missing out if you don't continue on this path, but the industry is lucky to have you. (Thank you for being my translator)

Edouard, my other teacher, mentor and the postdoc supervisor I never had. You have also taught me how to use the cryostat, the PLD, gave me ideas, research directions and was a sounding board for the later half of my degree. You never shy away when anyone asks for help and this may be a disadvantage for you and I. I have learned to refuse, but I think you still suffer from helping out others at the cost of your own time. I learned so much from talking to you and working with you. Some of our crazy ideas didn't work, but I'm still glad we tried them out. I don't know where you will end up next, but I'm sure whoever works with you will benefit from working with you.

Ludwig it's unfortunate that your project didn't give the results you intended, but it's great to see that you are capable to fill and operate the Morgan by yourself! Enjoy your future careers and thank you and Ulderico for initiating the bouldering activity!

Patrick with the most amazing last name. You are the most pleasant person to talk to; so easy going and never negative. I wish I could keep calm as you do so well.

Good luck exfoliating and torturing all sorts of complex oxide films!

Mattias the next leader of the optics group. Your idea on BTO sounds very interesting! It's a shame that I couldn't be a part of it thanks to this long book, but I will still be enjoying it once the results are out and published. Speaking of, finish up your NPS!

Yildiz you had one of the most toughest PhD projects and you managed to produce beautiful results with **Edouard**. Even with so many setbacks such as the accident, the pandemic and the samples not superconducting, you still managed to finish the project. Congratulations and good luck in your future careers!

Victoria, you started working on a tough project where the measurement setup had to be dismantled every other day. Yet you still managed to reproduce the extremely high hydrogen sensitivity while making samples for other projects. Good luck in your future endeavours!

João, I get reminded of the wise words you said in my first year. At the time, I didn't quite realize but towards the end of my PhD, I fully understand what you meant. Thank you!

Luigi, Gentle and humble artist of the vdW nano pillars! Best of luck in the next step of your career!

Giordano Mattoni I only had a short interaction with you but I wish that it was longer. I have directly benefited from your work on building and configuring the PLD, the Navy and your growth of WO_3. You are a wizard on coding and science and I wish you the best of luck!

Mafalda you were actually the first one to train me on the PLD. It is a very complicated process so it was difficult to digest the information but you were very patient. Thank you and I hope you enjoy consultancy!

Dirk, thanks to you and **Dejan**, I was able to step a foot into the world of complex oxides. You guys have let me be a part of your ground breaking work on complex oxide resonators, which I am grateful for. Good luck with your career at Shell!

Dima, the legendary postdoc who built the optics lab from scratch. Best of luck in starting your group and I will keep an eye on your future publications!

Jorrit, a great scientist leaving academia. It's always been a pleasure to interact with you. I wish you good luck whichever industry you choose to work in!

Maria El Abbassi the mother of all PhDs. I first thought you were a cold and goal driven person. Boy was I wrong. I found out too late that you were the most kind, nurturing mentor figure with the utmost patience for students. I'm gonna miss our interactions, the teas, s***ty coffee and 4 hour long barbecues. Keep in touch, whichever company you are working in. Best of wishes with the recovery!

Chunwei my neighbour and a fellow student of McGill Physics. Beyond the emotionless demeanour, you are a kind, caring and passionate person. Perhaps your zealousness towards humanity has driven you away from academia, but I think you hold a lot of knowledge and experience. I can tell by the amount of people asking for your help on a daily basis. Thank you for making me my favourite Taiwanese noodle dish and I hope you lead a peaceful life away from academia. Try to enjoy the rest of your PhD!

Luca. Sara always asks about the friend who lost all his weight. She says she

felt bad that you weren't able to enjoy any food during the barbecues. I hope you stay healthy and enjoy the rest of your PhD!

Jasper you have an extremely interesting and interdisciplinary project. I look forward to seeing your results in future papers! **Thomas** I heard that you are working with an extremely challenging molecule. Best of luck with your project! **Damien**, it was a pleasure to be working together on a paper with you. I envy your level of theoretical understanding. Good luck with the rest of your PhD! **Jacqui**, **Tristan** and **Sebastian** my new office mates. You guys are so hard working, I don't have any doubts you will have a successful PhD. **Sergeii**, you are super motivated and hard working even on the weekends. I'm sure your hard work will pay off. Keep it up, and good luck!

Toeno, my mentor. I sincerely appreciate that you take the role of a mentor seriously. Having regular meetings with you have helped me on several occasions. Directly venting my problems and listening to your guidance helped of course, but just the thought of having someone to talk to in case of academic and political problems relieved a lot of the anxieties. Thank you very much. You have an amazing lab with amazing people. I hope you a successful and swift track to full professorship!

Brecht, I was impressed by your presentation during the interview process as well as your work ethics in the cleanroom and your perseverance in the face of failures. Now you have become a master in the cleanroom. Good luck with the rest of your PhD!

Joris it's always a pleasure to talk to you. You are always such an up-beat guy even through the times of COVID and slow progress. Hope you keep up the positivity throughout your PhD!

Michael you give great talks during werkbespreking! Your new setup looks intense. I hope you get some fruitful results from the monster!

Samer my fellow comrade in plaid! It's always a pleasure to talk to you. I appreciate all the sincere advice on the thesis and academia you have given me and I'm grateful that you participate in the 2D journal club. I hope you keep your positivity and interest in 2D materials. Let's keep in touch !

Kavli staff, every graduating PhD in experimental physics needs to have a section for the wonderful Kavli staff. One of the biggest reasons for me to apply to TU Delft at the end of my masters was because of the world class cleanroom. Now, after working in the cleanroom for 4 years, I know that the staff make it the world class facility! I deeply respect the work ethics of all of you. Your drive for maintaining order, best working conditions and listening to the concerns of the users make Kavli nanolab the most pleasant cleanroom in the world to work in. In particular, I thank you **Charles** for all the interesting conversations in the cleanroom. You are such a nice person to work with and a pleasant character to get along with. I also thank **Marc** not only for being the operation manager through the COVID crisis and still maintaining a safe yet manageable work flow, but also being an ear that listens to concerns and understanding the frustrations of a PhD student in his final year.

Allard, thank you so much for maintaining the AFMs in tip top shape! They were central pieces of equipments for the work in this thesis!

Tino, the guy with the cool tatoo. Thank you for taking care of our labs, es-

pecially during the time when Montana broke. Thanks to your dedication, I could perform my experiments in multiple labs without delay!

Qing and **Ting**, the colleagues I met while slaving away in the cleanroom! **Qing** I haven't met your kitty yet, but I envy that you have one! You are always working so hard in the cleanroom. Due to the unfortunate restrictions in the cleanroom we don't meet so often anymore, but I hope you have a wonderful PhD and a wonderful life with the kitty! **Ting**, a cleanroom guru from QuTech. I'm glad that you participate in our 2D journal club. Although you don't work with 2D materials at the moment, you have such a deep relationship with graphene you will get used to the current frontiers when you switch back to the field! Good luck finding your next position and I hope you make it as a PI!

Marc Westig my former office mate, the crazy German postdoc. Many people think **Holger** is crazy, but I saw the crazy in you long time ago! When I heard that you had left academia I was in shock. You are the most knowledgeable, hard working post doc with crazy ideas and methodical choice of words, I knew you were made for science. I'm glad to hear that you are enjoying the life in industry. Please do keep in touch!

Holger thanks for answering our questions on multiple Andreev reflections via text! Your work in Nature Comms was very helpful as a guide for the work Thierry and I are working on! I hope you are enjoying the industry!

Sergi Pud, when I was becoming obsessed with authorships and first author papers, your advice helped me a lot. Good luck leading your own group!

Felix, you have such a beautiful PhD thesis, it sparked a flame of artistry in a lot of the remaining PhDs. Congratulations with Felicitas and with your new career!

Adrian my theorist friend! It's a big decision to transition from theory to experiments and I have great respect for you for doing that. I can't imagine transitioning from experimental physics to theory! Good luck with your experiments!

Sarwan, you and I gave our very first werkbesprekings on the very same day. It was pleasant to talk to you whenever we met, but I think you were stuck in the lab or the gym the rest of the time. Hope you have a smooth transition into industry!

Byoung moo, my only (used to be) Korean colleague in the department. I remember thinking "this guy is fricking smart. I have to learn everything he knows" when you gave your werkbespreking. Every time I walked by your office on the weekend, I could see that you were already working by the time I arrive and you were still working when I left. Crazy guy. Good luck transitioning in to industry!

Alkisti Sara and I miss you a lot! You made us feel so welcomed in all the social events I attended in my first year. Your sarcastic jokes and warm hospitality has really enlightened our first year in Europe. I hope you are enjoying industry!

Christina we had a difficult student to "co-supervise" together, but we endured! I know that you have left academia for your passion. I hope you enjoy it!

Mathijs Garming our collaboration happened coincidentally. I got in touch with you to ask for a sample of ITO on glass to test an idea. We ended up speaking about our respective research and now we are working on two projects together! Your measurement technique is amazing! I know that you are also very close to graduation. Good luck preparing for your dissertation!

et al. I'm trying my best to re-live my four years at TU Delft to think of everyone to thank. But knowing my small brain, I am likely forgetting someone important. If I had an interaction with you, our interaction probably shaped the person that is me right now. And for that, I thank you.

TU Delft

External

Samuel and **Javi**, we met when I was a new PhD student still. You guys came by to do a week of measurements and I kept you hostage in my lab during that entire week. I'm sorry you couldn't see more of Delft! After the intense week of measurements, we had beer together and I still think fondly of that day. I visited you guys in my trip to Valencia and you guys greeted me so kindly. You guys have impressive list of publications and I know that this is only the beginning. Best of luck in your post doc!

Angelo Di Bernardo, we had an intense 4 months of interaction but you have left a strong impression. It was an exciting time working with you. You seem to have had a successful grant application. I hope the project works out!

Prof. Hilke, this thesis would not have been possible if it wasn't for you. You gave me a chance to change myself from a lazy bachelor student to a hard working master student. You taught me how to be a good researcher and showed me how fun research can be. I am grateful for your kind supervision.

Dr. Wayne Yang, I have too many things to say, I don't think I can fit them in this book. You were my supervisor during my bachelor project in Canada and we are both in Delft for a PhD. You had a profound influence on my scientific career and also my mental health. I don't think we will land in the same institute in our post docs, but our paths will cross. I've never met anyone more observant, critical and methodical. You will be a great, successful AND passionate leader one day. Don't forget about our promise about sending our bad PhD students to each other's group for some tough lovin.

Auntie and Uncle. Sara and I still talk about the way you treated us like family. We had the most amazing time in Singapore and had the kind of food which we will never be able to enjoy again in our lifetimes. You have the smartest bunch of children I have ever seen. Still amazing to think that every one of them are either a physicist or a mathematician. I hope you are keep healthy! @Uncle, I miss our night drinking cognac and whiskey! I miss that night more than the Michelin star food you bought us. Keep healthy so we can one day meet again and enjoy some good drinks!

Scott, one of the few methods to unwind the week in my PhD years was watching RM with you. I am grateful that we are still in contact after high school and that we are both in research (in one form or another). I wish you a good career in physical engineering and lets hang out over some chicken, pizza, RM and games!

Mom, **Dad** words can't describe how grateful I am to be your son. (David, are you reading this? if you are reading this, please translate for them so they catch the nuances entirely.) You sacrificed so much, by leaving your success, a house, family

and network in South Korea just so that David and I can lead a better life in Canada. I can't imagine the types of decisions you must have made. You have raised me with your infinite yet strict love and I am forever grateful. I will stop here, since David will be reading this and I don't want him to see my soft side.

Gramma, I miss you very much (David, please again here). You've raised me when Mom and Dad were busy trying to make a living to provide us with food and clothes and a place to live and a chance to move to a better country. You were my second mother from when I could crawl to when I went off to university. You have the best heart and the purest soul. I wish you a long and healthy life. I will stop here again.

David, I'm so proud of what you've accomplished in the recent years. Mom, Dad, gramma and I were very worried about you for one or two years, but you quickly changed back. And now you are leading a healthy life, working diligently towards your goal and striving to be a good son to mom, dad and gramma. I think Joey has a positive influence on you. I hope you guys have a happy life together.

The last section of this book is reserved for the most powerful person in my life and her (now mine as well) family. **Sara's parents**, I am grateful that you trusted me enough to drag Sara along on this journey. First, I convinced her to move from Nova Scotia - where you are - to Quebec. Now she's half way across the world. Every time I visit you, you treat me like your own and I'm grateful for that. I wish you health and happiness!

Finally **Sara**, this journey could not have been possible if it wasn't for you. I can't believe you put up with me being at work 60-100 hour a week, plus bringing work home. I keep telling you that this is only temporary and will stop after the PhD phase, but ... sorry from what I've seen, this only gets worse. I wished that we could travel and explore more areas in Europe, but this pandemic has messed up our plans on travelling and our other plan. No matter. I am looking forward to the journey ahead no matter where we are in the world.

Curriculum Vitæ

Martin Lee

17-05-1991 Born in Seoul, South Korea.

Education

2004–2009 Clayton Heights Secondary
British Columbia, Canada

2009–2015 Undergraduate in Physics
McGill University, Montreal, Quebec, Canada
Thesis: Graphene based Midi Controller
Supervisor: Prof. Michael Hilke

2015–2017 Master in Physics
McGill University, Montreal, Quebec, Canada
Thesis: Graphene: Transfer Methods and Applications
Supervisors: Prof. Michael Hilke
Prof. Walter Reisner

2017-2021 PhD. Applied Physics
Technische Universiteit Delft, Delft, The Netherlands
Thesis: Applied and fundamental studies of vibrating 2D membranes
Promotors: Prof. dr. Peter G. Steeneken
Prof. dr. ir. Herre S. J. van der Zant

List of Publications

32. M. Abrahams, **M. Lee** et al., *Squeeze film based graphene microphone*, (manuscript in preparation).

31. P. Blah, E. Lesne, **M. Lee** et al., *Magneto transport of freestanding $SrRuO_3$ membranes*, (manuscript in preparation).

30. **M. Lee**, E. Lesne, T. C. van Thiel, M. Šiškins, P. Blah, U. Filippozzi, P. G. Steeneken, A. D. Caviglia, H. S. J. van der Zant, *Electrostatic manipulation of magnetism in suspended $SrRuO_3$*, (manuscript in preparation).

Chapter 7

29. C. Liu, R. J. Dolleman, **M. Lee**, M. Šiškins, H. S. J. van der Zant, P. G. Steeneken, G. J. Verbiest *Tension-controlled Thermodynamics in Graphene Resonator Based on Acoustic Phonons Scattering*, (manuscript in preparation).

28. M. M. S. Fakhrabadi, Z. Tang, **M. Lee**, M. Šiškins, A. Turchanin, H. S. J. van der Zant, P. G. Steeneken, G. J. Verbiest, *Nanomechanical characterization of self-assembly based free-standing carbon nanomembranes*, (manuscript in preparation).

27. **M. Lee**[*], T. C. van Thiel[*], S. Mañas-Valero, E. Coronado, Y. M. Blanter, P. G. Steeneken, A. D. Caviglia, T. M. Klapwijk, H. S. J. van der Zant, *Single-crystal van der Waals superconductor microbridge and gate independence*, (manuscript in preparation).

Chapter 7

26. **M. Lee**, J. R. Renshof, K. J. van Zeggeren, Maurits J. A. Houmes, E. Lesne, M. Šiškins, T. C. van Thiel, M. R. van Blankenstein, A. D. Caviglia, H. S. J. van der Zant, P. G. Steeneken, *Nanomechanics of ferroelectric switching in suspended van der Waals - complex oxide heterostructures*, (manuscript in preparation).

Chapter 7

25. M. W. H. Garming, I. Gerward C. Weppelman, **M. Lee**, T. Stavenga, P. Kruit, J. P. Hoogenboom, *Ultrafast Scanning Electron Microscopy with sub-micron optical pump resolution*, (manuscript in preparation).

in preparation

– – – – – – – – – – – – – – – – – – – –

in print

24. **M. Lee**, M. Robin, R. Guis, U. Filippozzi, D. H. Shin, T. C. van Thiel, S. Paardekooper, J. R. Renshof, H. S. J. van der Zant, A. D. Caviglia, G. J. Verbiest, P. G. Steeneken, *Self-sealing complex oxides resonators*, arxiv, (submitted 2021).

Chapter 7

23. M. Šiškins, E. Sokolovskaya, **M. Lee**, S. Mañas-Valero, D. Davidovikj, E. Coronado, H. S. J. van der Zant, P. G. Steeneken, *Tunable strong coupling of mechanical resonance between spatially separated $FePS_3$ nanodrums.*, arxiv, (submitted 2021).

22. M. Šiškins, S. Kurdi, **M. Lee**, B. J. M. Slotboom, W. Xing, S. Mañas-Valero, E. Coronado, S. Jia, W. Han, T. van der Sar, H. S. J. van der Zant, P. G. Steeneken, *Nanomechanical probing and strain tuning of the Curie temperature in suspended $Cr_2Ge_2Te_6$ heterostructures*, arxiv, (submitted 2021).

21. J. López-Cabrelles, S. Mañas-Valero, I. J. Vitórica-Yrezábal, M. Šiškins, **M. Lee**, P. G. Steeneken, H. S. J. van der Zant, Guillermo Mínguez Espallargas, E. Coronado, *Chemical design and magnetic ordering in thin layers of 2D MOFs*, arxiv, (accepted 2021).

20. D. Afanasiev, J. R. Hortensius, M. Matthiesen, S. Mañas-Valero, M. Šiškins, **M. Lee**, E. Lesne, H. S. J. van der Zant, P. G. Steeneken, B. A, Ivanov, E. Coronado, A. D Caviglia, *Controlling the anisotropy of a van der Waals antiferromagnet with light*, Science Advances **7**, 23 (2021).

19. **M. Lee**[*], M. Šiškins[*], S. Mañas-Valero, E. Coronado, H. S. J. van der Zant, P. G. Steeneken, *Study of charge density waves in suspended 2H-TaS_2 and 2H-$TaSe_2$ by nanomechanical resonance*, Applied Physics Letters **118**, 193105 (2021).

Chapter 6

18. W. Zhang, Q. Zhao, C. Munera, **M. Lee**, E. Flores, J. E. F. Rodrigues, J. R. Ares, C. Sanchez, J. Gainza, H. S. J. van der Zant, J. A. Alonso, I. J. Ferrer, T. Wang, R. Frisenda, A. Castellanos-Gomez, *Integrating van der Waals materials on paper substrates for electrical and optical applications*, Applied Materials Today **23**, (2021).

17. J. Azpeitia, R. Frisenda, **M. Lee**, D. Bouwmeester, W. Zhang, H. S. J. van der Zant, F. Mompean, M. Garcia-Hernández, A. Castellanos-Gomez, *Integrating superconducting van der Waals materials on paper substrates*, Materials Advances, (2021).

16. A. Keskekler, O. Shoshani, **M. Lee**, H. S. J. van der Zant, P. G. Steeneken, F. Alijani, *Tuning nonlinear damping in graphene nanoresonators by parametric-direct internal resonance,* Nature Communications **12** 1099, (2021).

15. M. Šiškins, **M. Lee**, D. Wehenkel, R. van Rijn, T. W. de Jong, J. R. Renshof, B.C. Hopman, W. S. J. M. Peters, D. Davidovikj, H. S. J. van der Zant, P. G. Steeneken, *Sensitive capacitive pressure sensors based on graphene membrane arrays,* Microsystems & Nanoengineering **6**, 102 (2020).

Chapter 3

14. E. Whiteway, **M. Lee**, M. Hilke, *Real Space Raman Spectroscopy of Graphene Isotope Superlattices*, Physical Review B **102**, 23 (2020).

13. I. E. Rosloń, R. J. Dolleman, H. Licona Solera, **M. Lee**, M. Šiškins, H. Lebius, L. Madauß, M. Schleberger, F. Alijani, H. S. J. van der Zant, P. G. Steeneken, *High-frequency gas effusion through nanopores in suspended graphene*, Nature Communications **11**, 1 (2020).

12. **M. Lee**, A. Mazaheri, H. S. J. van der Zant, R. Frisenda, A. Castellanos-Gomez, *Drawing WS_2 thermal sensors on paper substrates,* Nanoscale (2020).

11. D. Davidovikj,D. J. Groenendijk, A. M. R. V. L. Monteiro, A. Dijkhoff, D. Afanasiev, M. Šiškins, **M. Lee**, Y. Huang, E. van Heumen, H. S. J. van der Zant, A. D. Caviglia, P. G. Steeneken, *Ultrathin complex oxide nanomechanical resonators*, Communications Physics **3**, 1 (2020).

10. E. Whiteway, **M. Lee**, M. Hilke, *Graphene Isotope Superlattices with Strongly Diminished Thermal Conductivity for Thermoelectric Applications*, ACS Applied Nano Materials **3**, 9 (2020).

9. A. Mazaheri, **M. Lee**, H. S. J. van der Zant, R. Frisenda, A. Castellanos-Gomez, *MoS_2-on-paper optoelectronics: drawing photodetectors with van der Waals semiconductors beyond graphite,* Nanoscale (2020).

8. M. Šiškins[*], **M. Lee**[*], S. Mañas-Valero, E. Coronado, Y. M. Blanter, H. S. J. van der Zant, P. G. Steeneken, *Magnetic and electronic phase transitions probed by nanomechanical resonance,* Nature communications **11**, 1 (2020).

Chapter 5

7. S. Caneva, M. D. Hermans, **M. Lee**, A. Garcia-Fuente, K. Watanabe, T. Taniguchi, C. Dekker, J. Ferrer, H. S. J. van der Zant, P. Gehring, *A mechanically tunable quantum dot in a graphene break junction,* Nano letters **20**, 7 (2020).

6. M. Šiškins, **M. Lee**, F. Alijani, M. R. van Blankenstein, D. Davidovikj, H. S. J. van der Zant, P. G. Steeneken, *Highly anisotropic mechanical and optical properties of 2D layered As_2S_3 membranes,* ACS nano **13**, 9 (2019).

5. **M. Lee**, D. Davidovikj, B. Sajadi, M. Šiškins, F. Alijani, H. S. J. van der Zant, P. G. Steeneken, *Sealing graphene nanodrums,* Nano letters **19**, 8 (2019).

Chapter 4

4. **M. Lee**, T. A. Vuong, E. Whiteway, X. Capaldi, Y. Zhang, W. Reisner, C. S. Ruiz-Vargas, M. Hilke, *From 2D to 3D: Graphene molding for transparent and flexible probes,* Applied Physics Letters **114**, 4 (2018).

3. R. J. Dolleman, D. Lloyd, **M. Lee**,J. S. Bunch, H. S. J. van der Zant, P. G. Steeneken, *Transient thermal characterization of suspended monolayer MoS_2,* Physical Review Materials **2**, 11 (2018).

2. K. L. M. Elder, M. Seymour, **M. Lee**, M. Hilke, N. Provatas, *Two-component structural phase-field crystal models for graphene symmetries,* Philosophical Transactions of the Royal Society A: Mathematical, Physical and Engineering Sciences **376**, 2113 (2018).

1. J. Qu, **M. Lee**, M. Hilke, X. Liu, *Investigating the impact of SEM chamber conditions and imaging parameters on contact resistance of in situ nanoprobing,* Nanotechnology **28**, 34 (2017).

* These authors contributed equally